TECHNISCHE
UNIVERSITÄT
WIEN
Vienna University of Technology

DISSERTATION

Probing Low-Mass Dark Matter with CRESST-III -

Data Analysis and First Results

Ausgeführt zum Zwecke der Erlangung des akademischen Grades eines
Doktors der Naturwissenschaften

unter der Leitung von

Prof. Dr. Jochen Schieck
Atominstitut (ATI)

eingereicht an der Technischen Universität Wien
Fakultät für Physik

von

Martin Stahlberg

Matrikelnummer: 01634376

Wien, am 17. Februar 2020

Kurzfassung

Die Suche nach der Dunklen Materie ist eines der interessantesten Themen der modernen Physik. Obwohl die Existenz dieser Materieform durch astronomische Beobachtungen impliziert wird, gibt es bis heute keinen schlüssigen Nachweis durch eines der zahlreichen Experimente. Während das Forschungsgebiet stetig wächst, geraten leichte Teilchen, die das klassische WIMP-Szenario ersetzen, zunehmend in den Fokus. Diese Arbeit präsentiert eine Analyse von Daten aus der ersten Phase von CRESST-III, einem unterirdischen Experiment zum direkten Nachweis von Partikeln der Dunklen Materie, die mit instrumentierten $CaWO_4$-Kristallen interagieren sollen. Unter Verwendung von Daten, die zwischen Mai 2016 und Februar 2018 gesammelt wurden, wird eine Obergrenze für den Wirkungsquerschnitt der spinunabhängigen sowie spinabhängigen elastischen Streuung von Partikeln der Dunklen Materie an den Kernen des Zielvolumens (O, Ca und W) bestimmt. Ergebnisse von vier Detektoren mit Schwellen für Rückstoßenergien nahe dem Entwurfsziel von 100 eV werden der erwarteten Sensitivität des CRESST-III-Experiments gegenübergestellt, und die stärkste Ausschlussgrenze wird mit Resultaten anderer direkter Suchexperimente verglichen. Ein Überblick über die beobachteten Untergrundprozesse wird gegeben, sowie ein Vergleich mit früheren CRESST-Messungen. In diesem Zusammenhang wird ein neuartiger Ansatz für die Energierekonstruktion untersucht, der die Signalsättigung im Übergangskantensensor berücksichtigt. Durch die Untersuchung von Kernrückstoßereignissen mit einer Minimalenergie von 30,2 eV wird gezeigt, dass CRESST in einzigartiger Weise zur Suche nach leichten Teilchen geeignet ist, und zukünftige Phasen des Experiments eine noch höhere Empfindlichkeit erreichen können. Die Analyse verwendet einen Software-Triggeralgorithmus, der auf dem gesamten aufgezeichneten Datenstrom arbeitet, und das zuvor verwendete Hardware-Triggerschema ersetzt. Dieser Ansatz ermöglicht die Definition von Detektorschwellen basierend auf einem Güteparameter, insbesondere als Funktion einer beobachteten Anzahl von Rauschereignissen. Auf dem Datenstrom wird zudem eine Signalsimulation durchgeführt, mit der die Auswirkung jedes Analyseschnitts auf die Überlebenswahrscheinlichkeit von Signalereignissen studiert wird.

"Specialization may be a great temptation for the scientist.
For the philosopher, it is the mortal sin." (Sir Karl Popper)

Contents

1 Preface

Dark matter is one of the most puzzling topics of physics today. While its existence seems logical and is implied by astronomical evidence, results from dark matter detection experiments remain inconclusive. The field of dark matter physics is growing rapidly, and opening up towards lighter particles, which provide an alternative to the more and more disfavored standard WIMP scenario. This work presents an analysis of data from the first phase of CRESST-III, an underground experiment aimed at direct detection of dark matter particles interacting in an instrumented $CaWO_4$ target volume. Using data collected between May 2016 and February 2018, an upper limit on the cross-section for spin-independent as well as spin-dependent elastic scattering of dark matter particles off the target nuclei (O, Ca, and W) is extracted. A comparison of four detectors achieving nuclear recoil energy thresholds near the design goal of 100 eV with the projected performance of CRESST-III is given, and the strongest exclusion limit is checked against results from other direct search experiments. An overview of observed backgrounds is provided, and compared to earlier CRESST measurements; in this context, a novel approach for the energy reconstruction is explored, which accounts for signal saturation in the transition edge sensor. Via examination of nuclear recoil events with energies as low as 30.2 eV, it is shown that CRESST is uniquely suited to explore the low-mass dark matter particle regime, and future phases of the experiment should yield even more sensitivity. This work employs a software trigger on the complete recorded datastream, replacing the previously used hardware triggering scheme. It enables the definition of detector thresholds based on a figure of merit, namely as a function of allowed noise triggers. A signal simulation on the stream is also performed, which is used to assess the effect of each analysis cut.

2 Dark Matter

The concept of "dark matter" is as old as the theory of gravity itself. After Isaac Newton presented his *Philosophiae Naturalis Principia Mathematica* in 1687, speculations arose about astronomical objects which would predominantly interact via gravitation, emit little to no visible light, and be therefore invisible to the observer. In the late 18th century, Pierre-Simon Laplace in France and John Michell in England independently performed calculations for massive objects capable of gravitationally "trapping" light - a simplistic idea of a black hole under the assumption of light "corpuscules" [1]. Michell even proposed a way of detecting these objects via orbiting luminous matter, and postulated the existence of double star systems where one star is "invisible". He concluded that an estimate for the amount of unseen stellar matter could be given by identifying the number of such systems [2].

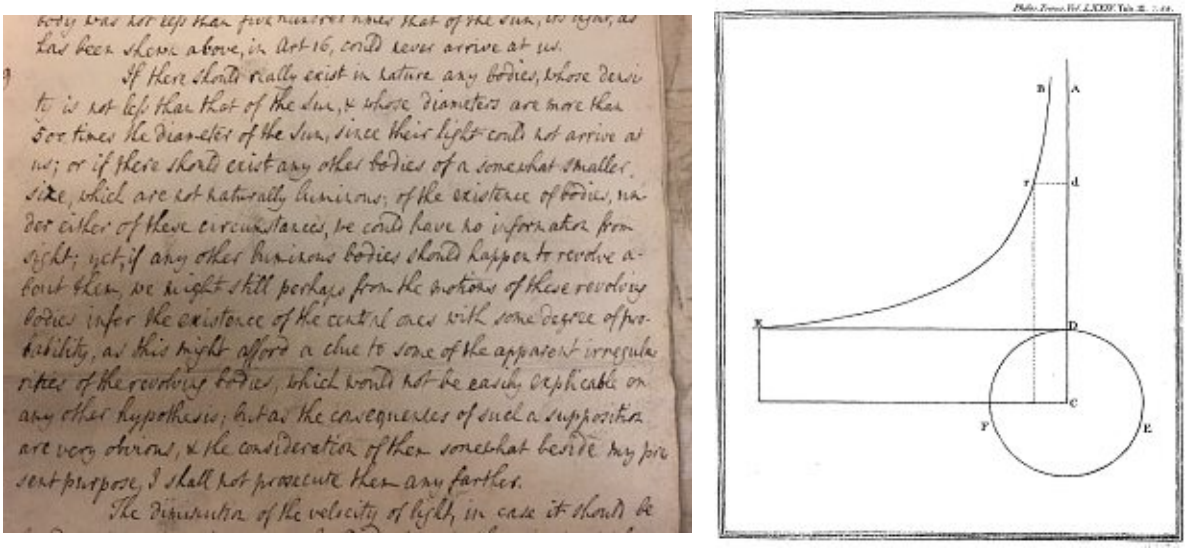

Figure 2.1: Left: John Michell's postulation of "not naturally luminous bodies" in a letter from 1784 [2]; 500 is the number of times the velocity of light exceeds the velocity v_e of a body falling from infinity to the the surface of the sun. Right: v_e illustrated in Michell's diagram (a detailed explanation can be found in [1]).

2.1 Inference from Astrophysical Phenomena

Today, the possibilities of astronomical observations extend far beyond visible light, and the term *dark matter* is commonly used for a hypothetical form of matter which explains several gravitationally observed phenomena. Henri Pointcaré used the expression for non-luminous stellar matter in 1906, when discussing Lord Kelvin's dynamical calculation of the total mass of the Milky Way. Kelvin had described the galaxy as an ideal gas, and predicted a velocity dispersion for stars which was comparable to the one inferred from telescopes [3]. Pointcaré concluded that there should be more luminous than dark stellar matter [4]. Later, astronomers such as Kapteyn and Oort adopted the term and refined the process of determining the amount of dark matter in the Milky Way [5].

In 1933, Fritz Zwicky found a contradiction between his work and that of Edwin Hubble, who had previously estimated the mass of the Coma galaxy cluster via the number of observed galaxies and their luminosity [6]. Zwicky instead studied the velocities of the galaxies, and used the virial theorem to derive the mass of the cluster, which was more than 500 times higher than Hubble's mass [7]. Zwicky's explanation was that a huge amount of additional, non-luminous matter was present in or between the galaxies. As his approach via the virial theorem depends on the assumption of the cluster galaxies being gravitationally bound, his claims were met with doubt at first. Beginning in 1970 [8], Rubin et al. published evidence for a similar effect in single spiral galaxies [9]: The velocity of stars as a function of their distance to the center of the galaxy does not follow the relation $v \sim \sqrt{1/r}$ as one would expect from the law of gravity and the condition for stable orbits, but instead stays flat at higher distances. This observation has been confirmed for many more galaxies since (cf. Figure 2.2). A suggested explanation is the presence of a so-called *halo*, consisting of gravitationally interacting, non-visible matter, and extending far outside the visible disk.

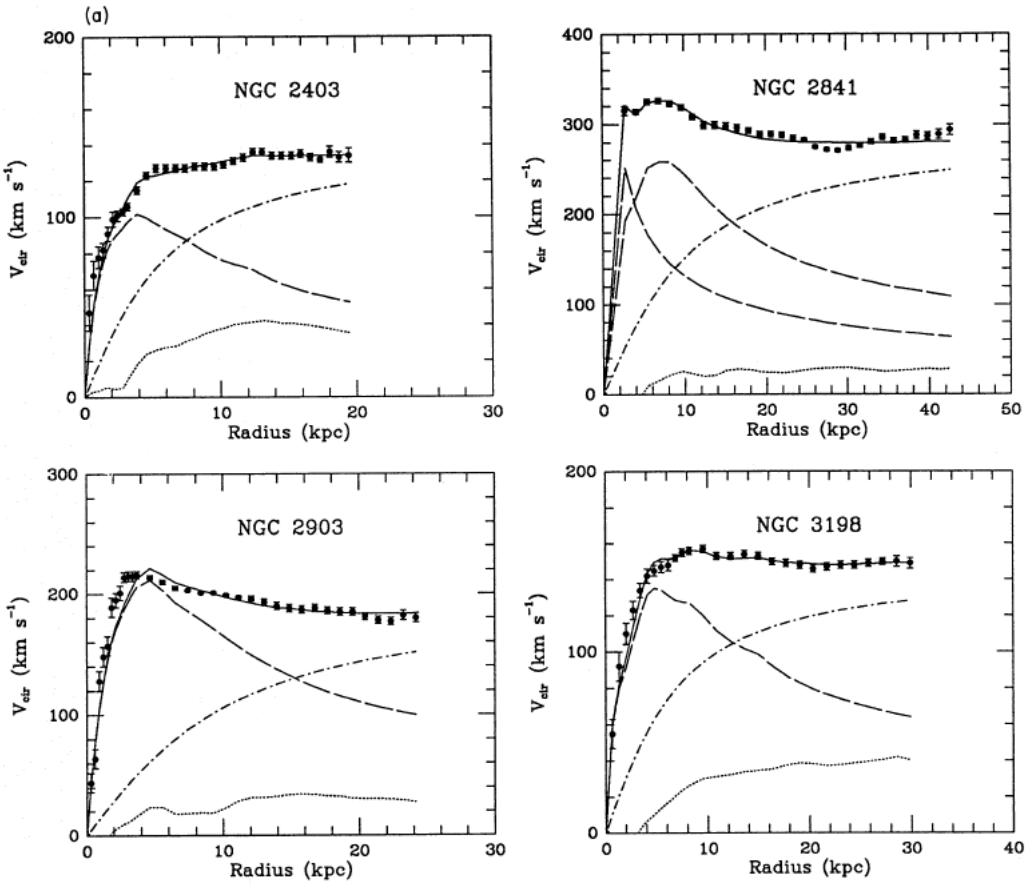

Figure 2.2: Rotation curves for different spiral galaxies, taken from Begeman et al. (1991) [10]. Measured velocities as a function of distance to the galactic center are indicated as dots, and fitted contributions from a disk (falling component, dashed line), intergalactic gas (dotted line), and a halo (rising component, dash-dotted line) are shown.

A general parametrization of dark matter halo profiles is given by

$$\rho(r) = \frac{\rho_0}{(\frac{r}{R_s})^{\gamma}(1+(\frac{r}{R_s})^{\alpha})^{(\beta-\gamma)/\alpha}} \text{ [11]}, \tag{2.1}$$

where r is the distance to the center of a galaxy, and $\rho(r)$ is the dark matter density at this distance. R_s is the scale radius, and ρ_0 is the dark matter density at the center. These parameters are individual for each galaxy. A widely used halo model with $\alpha = \gamma = 1$ and $\beta = 3$ is the *Navarro-Frenk-White* profile, which was motivated by galaxies from N-body simulations [12](cf. Section 2.3.2).

2.1.1 Galaxy Cluster Mergers

The characteristics of galaxy cluster mergers are another astronomical observation consistent with the existence of dark matter. Employing *gravitational lensing*, a concept first theorized by A. Einstein, the presence of dark matter distributions was established for several such objects. The gravitational field around massive objects or large accumulations of matter results in a warping of space-time, which produces an apparent bending of trajectories for light from stars in the background. This process allows measuring the mass of the object, or a mass distribution in space. The latter can then be compared to the distribution of visible objects in optical images, or a luminosity distribution, and x-ray images. In the past, the merger of two galaxy clusters 1E 0657-558 ("bullet cluster") was studied in several publications (e.g. [13], [14], [15]). Its mass distribution is shown in Figure 2.3 in blue, and apparently the visible matter is arranged around two dense centers of dark matter.

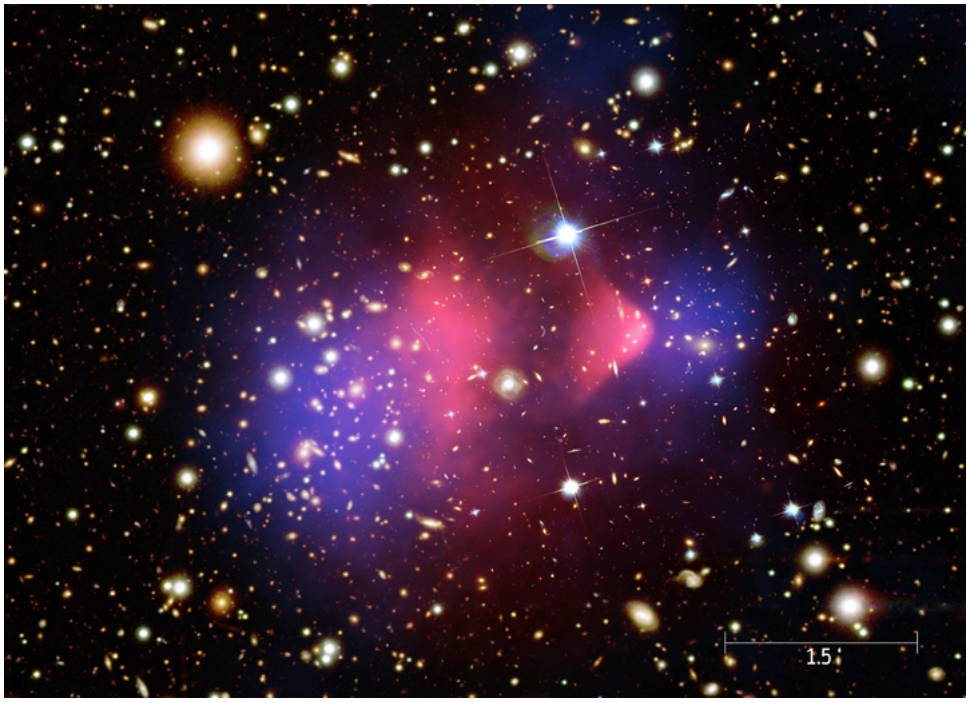

Figure 2.3: Optical and x-ray (red) image of the cluster 1E 0657-558, as well as a mass distribution obtained via gravitational lensing (blue) [16].

The x-ray image (shown in red) however tells a different story: As the right cluster traversed the other, loosely bound interstellar gas was stripped off due to electromagnetic interaction, which now trails behind, forming a bullet-like shape. Apparently, dark matter present in both clusters has little to no interaction with the interstellar gas, since both mass distributions

did not influence each other. This could either be explained by compact dark matter objects behaving similar to stars, or by a halo of non-baryonic particles, or both.It can also be argued that dark matter must have a low self-interaction, otherwise the shape of its mass distribution would be more complex, i.e. the two mass centers would look deformed.
While this appears compelling, a similar analysis for the cluster Abell 520 (Figure 2.4) contradicts the simple picture [17]: Here, a large amount of dark matter was left behind in the middle after the merger (blue), coinciding with the distribution of the interstellar gas (green), but not with the galaxies (orange). This would suggest either different types of dark matter ("sticky" and "non-sticky"), or a completely different explanation through modified gravitation.

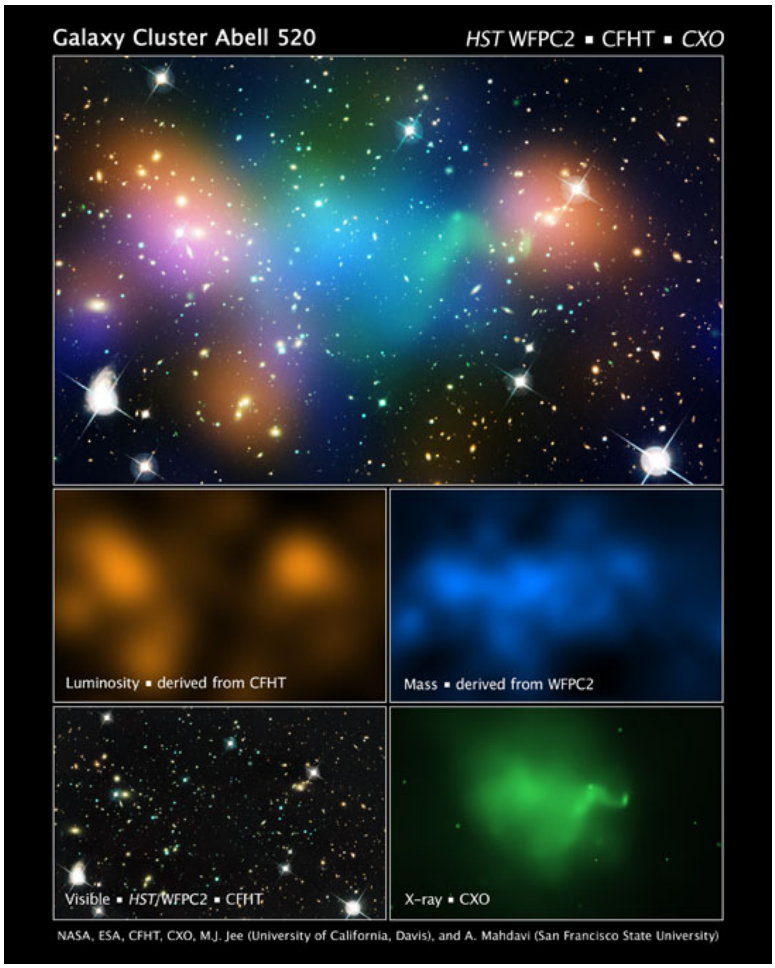

Figure 2.4: Images of the galaxy cluster Abell 520 taken in visible light and x-ray range (green), in addition to luminosity (orange) and lensing mass (blue) distributions. An overlay of all three mass distributions is shown on top [17].

2.2 Description in General Relativity

In order to explain the phenomena described in the previous sections, a cosmological model accounting for the presence of dark matter must be developed, and the main steps are motivated here. The only known interaction in which dark matter partakes is gravitation; therefore, the starting point for a cosmological model which includes it is Einstein's theory of general relativity. Following the postulate of mass-energy equivalence, Einstein's field equations relate a mass-energy distribution to a proportional curvature of space time caused by its gravity:

$$G_{\mu\nu} = \kappa T_{\mu\nu} \tag{2.2}$$

The *Einstein tensor* $G_{\mu\nu}$ parametrizes the curvature of space time, while the *stress-energy tensor* $T_{\mu\nu}$ describes the density and flux of energy and momentum in spacetime; $\kappa = \frac{8\pi G}{c^4}$ is the *Einstein constant* and G is Newton's gravitational constant. $G_{\mu\nu}$ is chosen such that $\nabla_\nu G^{\mu\nu} = 0$, to satisfy the energy and momentum conservation condition $\nabla_\nu T^{\mu\nu} = 0$ on the right side:

$$G_{\mu\nu} = R_{\mu\nu} - \frac{1}{2} g_{\mu\nu} R, \tag{2.3}$$

with the *Ricci tensor* $R_{\mu\nu}$, which is a contraction of the *Riemann curvature tensor* with the metric tensor $g_{\mu\nu}$. A second contraction yields the *Ricci scalar* R. The Einstein tensor thus only depends on the metric. An additional constant term proportional to the metric tensor can be added on the right side without violating the requirements for the Einstein tensor. This yields the form

$$\frac{8\pi G}{c^4} T_{\mu\nu} = R_{\mu\nu} - \frac{1}{2} g_{\mu\nu} R + \Lambda g_{\mu\nu}, \tag{2.4}$$

where Λ is the *cosmological constant*. The *Robertson-Walker metric* implements the condition of an isotropic, homogenous and expanding universe, and yields a diagonal metric tensor $g_{\mu\nu}$, where the line element ds in spherical coordinates (r, θ, ϕ) is defined as

$$ds^2 = dt^2 - a^2(t) \left[\frac{dr^2}{1 - kr^2} r^2 (d\theta + sin^2(\theta) d\phi^2) \right]. \tag{2.5}$$

The value of k denotes the curvature of spacetime and can take values between -1 and 1. $a(t)$ is the time-dependent scale parameter which describes the expansion of the universe.

(2.6)

2.2.1 The Friedmann Equation

Inserting the Robertson-Walker metric 2.5 into 2.4 yields the *Friedmann equation* for the 0 component, if $\frac{\dot{a}}{a}$ is identified with the *Hubble constant* H. This equation describes the energy and matter content in the universe:

$$H^2 = \left(\frac{\dot{a}}{a}\right)^2 = \frac{8\pi G}{3}\rho - \frac{kc^2}{a^2} + \frac{\Lambda}{3} \tag{2.7}$$

With $\Omega_m = \frac{8\pi G}{3H^2}\rho$, $\Omega_k = \frac{kc^2}{a^2H^2}$ and $\Omega_\Lambda = \frac{\Lambda}{3H^2}$, this can be rewritten as

$$1 = \Omega_m + \Omega_\Lambda - \Omega_k \tag{2.8}$$

The different terms denote different fractions. In particular, the term Ω_Λ describes an energy contribution from the cosmological constant, and Ω_k gives the contribution due to the curvature of the universe. Ω_m then comprises all gravitationally interacting matter in the universe. By modifying Ω_m, the effect of dark matter can now be taken into account. No further assumptions apart from having mass are made so far about the nature of dark matter; it is in particular not necessary for dark matter to be baryonic or non-baryonic, or to be particle-like at all.

2.2.2 Interpretation of Different Terms - The ΛCDM Model

Naively, one should be able to estimate Ω_m by measuring its individual components:

$$\Omega_m = \Omega_b + \Omega_r \tag{2.9}$$

The terms Ω_r and Ω_b account for the radiation and the baryonic matter in the universe, respectively. Experimentally, values for Ω_m, Ω_b and Ω_Λ can be derived from the Cosmic Microwave Background (CMB), which will be discussed in section 2.3.1. The most accurately measured values are $\Omega_m = 0.309$, $\Omega_b = 0.049$ [18][1], and $\Omega_\Lambda = 0.691$. $\Omega_r = 5.38 \cdot 10^{-5}$ [20] is dominated by the energy contained in the CMB, and its value is derived directly from the CMB temperature. With these values, the equation above is not fulfilled, i.e. the components Ω_b and Ω_r do not add up to Ω_m. This necessitates the introduction of another mass term Ω_c:

$$\Omega_m = \Omega_b + \Omega_r + \Omega_c \tag{2.10}$$

[1] An arXiv pre-print of the more recent 2018 data is available [19].

This component cannot be attributed to the cosmological constant or the curvature of the universe; it behaves like gravitationally interacting, non-luminous matter. Using the values from above, we obtain

$$\Omega_c = 0.26. \tag{2.11}$$

This means that there is about five times as much dark matter in the universe as there is luminous matter (the sum of Ω_b and Ω_r), and the vast majority of the universe is thus dark. For non-baryonic particle dark matter, two scenarios have been suggested which describe the extreme cases: "hot" and "cold" dark matter, where the former describes light, relativistic particles, and the latter corresponds to heavy, non-relativistic particles [21]. As the dark matter component Ω_c needs to be cold to explain observed structures in the universe today (cf. Section 2.3.2), the formulation of the Friedman equation with cosmological constant and a dark matter component is called the *Lambda Cold Dark Matter* (ΛCDM) model.

2.3 Measurements of ΛCDM Parameters

Several astronomical observations have implications for dark matter properties: Parameters of the ΛCDM model can be extracted from characteristics of the Cosmic Microwave Background, models of structure formation in the early universe, or calculations for nucleosynthesis following the Big Bang. This list is not complete, as there are more approaches such as galaxy redshift surveys, type Ia supernova distance measurements, and analysis of absorption spectra of galaxies and quasars ("Lyman-alpha forest"). An overview can be found e.g. in [11]. In this section, three sources will be briefly introduced, which provide the strongest constraints.

2.3.1 Fluctuations of the Cosmic Microwave Background

According to our current understanding, the CMB is a remnant of the Big Bang, and was released about 380,000 years later [22]. During the period of recombination, formerly single protons and electrons formed atoms, which were no longer able to scatter thermal radiation, and the universe became transparent. Although the CMB was observed as early as 1941 by Andrew McKellar [23], it was first recognized and studied by Arno Penzias and Robert Wilson in 1965 [24]. At the time of decoupling, the universe essentially consisted of a hot gas, and its density and therefore temperature variations were "frozen" into the pattern of the CMB. After cooling down, the CMB photons now exhibit a nearly isotropic black body spectrum with $T_\gamma = 2.7255 \pm 0.0006K$ [25], and anisotropies on the scale of 10 ppm. As the initial

density fluctuations depend on the interaction and the proportion of the different matter components (baryonic matter, dark matter, and radiation), we can infer information about the dark matter content of the universe by studying the power spectrum of the anisotropies. To this end, CMB measurements from satellite experiments such as COBE, WMAP and Planck are usually modelled with a spherical harmonics expansion:

$$T(\theta,\phi) = \sum_{lm} a_{lm} Y_{lm}(\theta,\phi) \tag{2.12}$$

As an example, the ratio between the first and second peak in Figure 2.5 can be used to obtain the fraction of baryonic matter Ω_b. Independently, the dark matter fraction Ω_c can be derived from the third peak. The data was taken by the Planck satellite experiment [18].

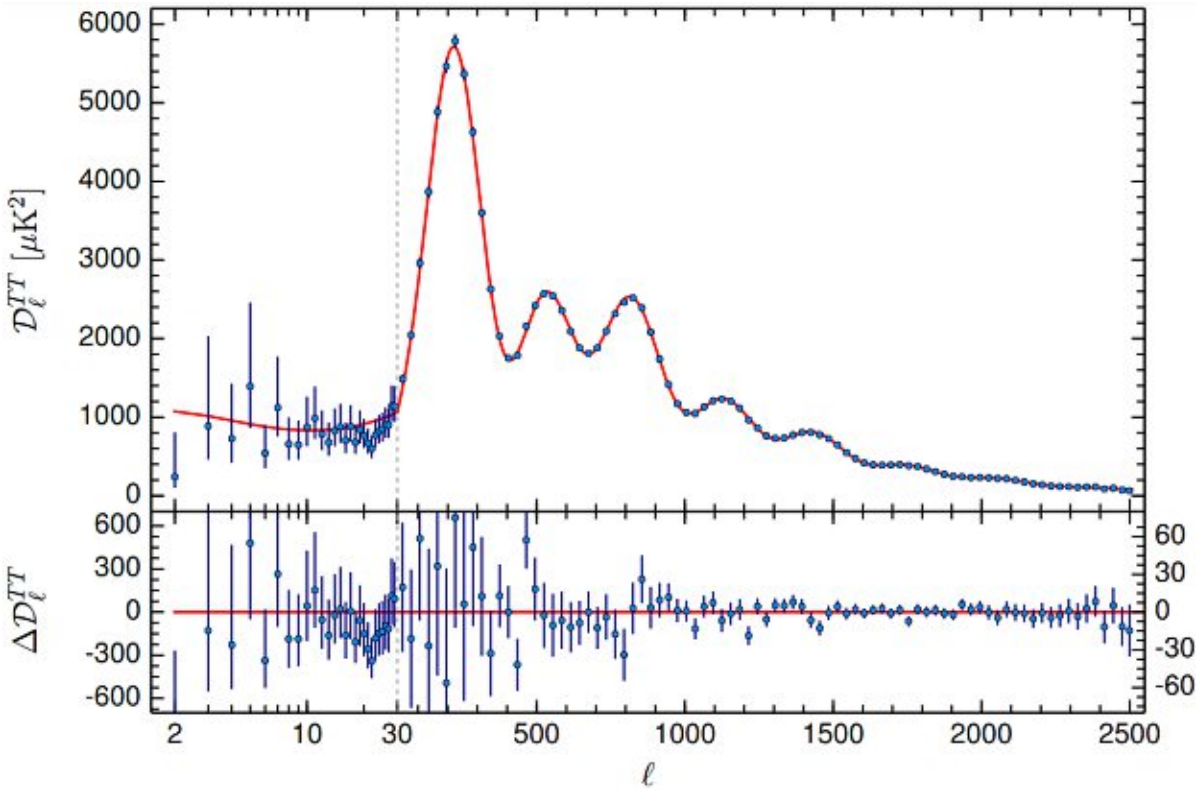

Figure 2.5: CMB power spectrum after decomposition into spherical harmonics; The value D_l^{TT} gives the power summed for each multipole l [18], and the residuals ΔD_l^{TT} are given in the lower panel. At $l = 30$, the horizontal axis changes from logarithmic to linear, and the scale of the vertical axis in the lower panel decreases.

2.3.2 Structure Formation in the Early Universe

Additional hints for dark matter come from considerations about structure formation in the early universe, where one needs to account for the fact that most of the matter is actually dark (cf. Section 2.2.2). Generally, structure formation can be described by two scenarios. "Hot" dark matter with relativistic particle velocities would decouple from baryonic matter and radiation early, and wash out density fluctuations, which results in a top-down scenario: large-scale structures like superclusters collapse first due to gravity, with the subsequent formation of smaller objects like galaxies. "Cold" dark matter, on the other hand, would cause the formation of small structures from initial density fluctuations first, as it consists of heavy, non-relativistic particles. This would mean a bottom-up scenario, which is consistent with surveys of the galaxy distribution as a function of redshift (and therefore, time) [26]. A growing number of N-body simulations such as the Millenium Simulation Project [27], as well as hydrodynamic simulations such as Illustris [28] and EAGLE [29] correctly reproduce this distribution using the latter model, in which cold dark matter structures act as "scaffolding" for ordinary matter distributions [30]. While early simulations focused only on dark matter, as it has the largest contribution to Ω_m, more recent ones simulate baryonic matter as well.

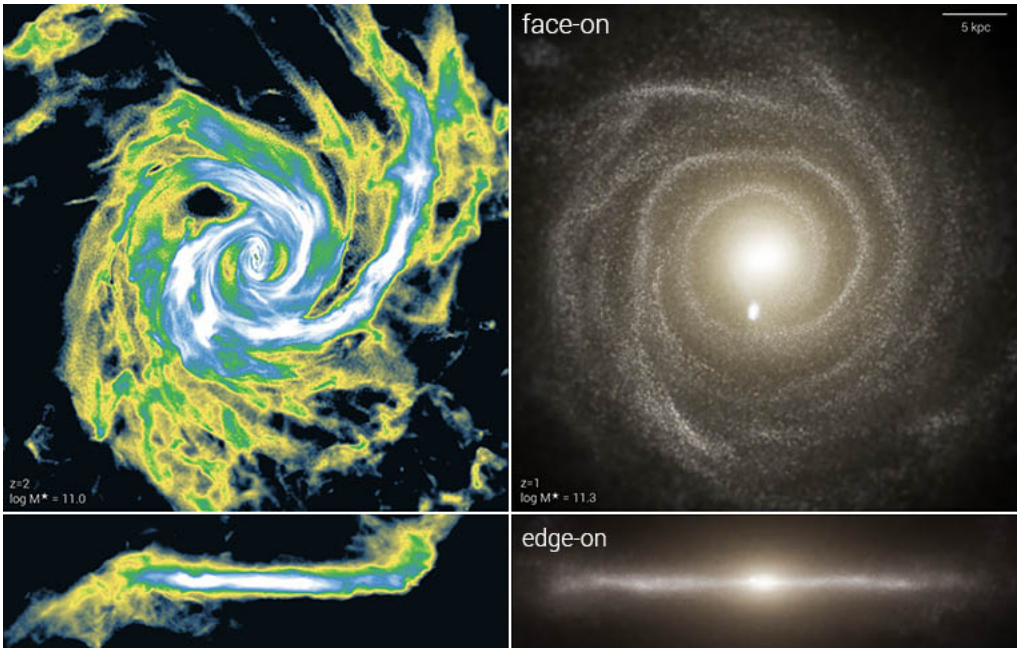

Figure 2.6: Simulated Milky Way mass analog disk galaxy from the Illustris TNG50 simulation. Left: gas distribution at z=2, Right: stellar distribution at z=1 [28].

2.3.3 Big Bang Nucleosynthesis

During the process of *primordial Nucleosynthesis* or *Big Bang Nucleosynthesis*(BBN) at the beginning of the universe, heavier nuclei formed from protons and neutrons, starting with Deuterium, which then further combined to ^{4}He. The amount of remaining Deuterium is an indicator for the baryon density n_b, as a smaller density leads to a lower D production rate. Measuring the Deuterium content of the universe today and using the photon density n_γ, one can calculate n_b and thus Ω_b. A similar argument can be made for the ratio ^{7}Li/H and ^{3}He/H, the latter of which yields the most precise constraint [20]:

$$\Omega_b h^2 = 0.0225 \pm 0.0015 \tag{2.13}$$

(h is the value of the Hubble constant relative to 100 $\frac{\text{km}}{\text{s Mpc}}$). Figure 2.7 shows a comparison between the baryon density obtained from BBN and results from the CMB. There is a disagreement between the results for ^{7}Li/H and other ratios as well as the CMB result; the observed amount of ^{7}Li is a factor three too low. This is called the "Cosmological Lithium Problem".

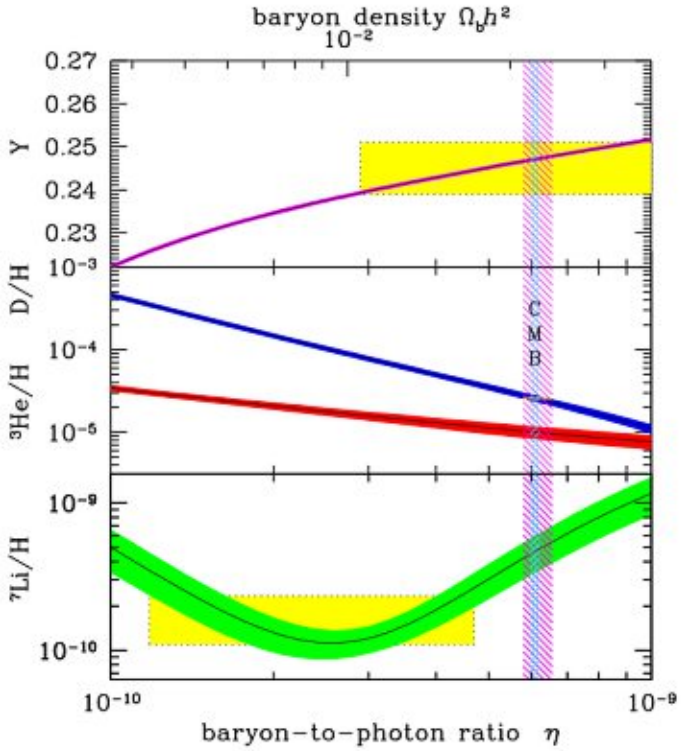

Figure 2.7: Estimation of the baryon density n_b from the ratio of light nuclei produced in big bang nucleosynthesis [20].

2.4 Proposed Explanations for Dark Matter

Many candidates for dark matter have been suggested, including known particles from the Standard Model of particle physics, as well as particles from extended models such as supersymmetry (SUSY). Today, it is commonly accepted that dark matter cannot be explained through the Standard Model of particle physics alone. An overview can be found in [31] and [32]; however, the main candidates are briefly discussed here. In order to be consistent with the phenomena presented in the previous section, any dark matter explanation must account for the absence of light; in case of new particles, they must be effectively stable, i.e. have a relatively long life time with respect to the age of the universe, or at least their number density must be constant. At the end of this section, alternative scenarios are considered.

2.4.1 MACHOs

Massive Compact Halo Objects are very dense accumulations of baryonic matter, such as black holes and neutron stars, which do not emit light. Any determination of Ω_b solely based on luminous baryonic matter would be insensitive to these objects, and therefore underestimate the amount of baryonic matter in the universe. However, previously discussed ΛCDM analyses of the CMB do not rely on the luminosity of baryonic matter, but instead on its gravitational interaction, and are thus sensitive to Ω_m and Ω_b independently. Though some dark objects have been identified via gravitational lensing, in particular black holes, the total number of these objects is too low to account for the missing mass. BBN provides an additional confirmation that only a small fraction of the dark matter in the universe stems from MACHOS [31].

2.4.2 Neutrinos

The mass density contribution from neutrinos is usually considered as part of Ω_r; due to the relativistic speed and extremely low masses of neutrinos, they can only explain Ω_m in a "hot" dark matter scenario, which contradicts the observed structure evolution, as discussed before. Another problem is the required mass per neutrino, which would be around 1 eV and thus much higher than the current upper limit on the sum of the neutrino masses of around 0.2 eV [20].

2.4.3 WIMPs

A popular candidate for dark matter are *Weakly Interacting Massive Particles (WIMPs)*. Such particles would be able to annihilate pair-wise into basically massless particles, which in turn could interact with the cosmic plasma in the early universe and be in thermal equilibrium at the beginning. As the universe cools and expands, their energy becomes too low to produce WIMP pairs, leading to a "freeze out" of the WIMPs. The theoretical WIMP self-annihilation cross section matter is constrained by today's observed dark matter relic density; it roughly matches the scale of the weak intraction (≈pb), which is often called the "WIMP Miracle". Using Fermi theory, i.e. assuming weak interaction, one arrives at a particle mass between ≈100 GeV-1 TeV [32]. In the past, the idea of WIMPs was in particular important in the context of *supersymmetry*: This concept adds a bosonic partner to each fermion, and a fermionic partner to each boson, respectively. In the minimal supersymmetric model (MSSM), each particle from the Standard Model with an R-parity $P_R = -1$ is assigned a new partner with $P_R = 1$. R-partity is conserved, and thus the lightest supersymmetric particle has to be stable, and is a candidate for dark matter. In MSSM, this would be the lightest of four *neutralinos* χ_i, superpositions of photino and zino, which are the superpartners of photons and Z bosons, with two higgsinos (superpartners of the Higgs boson). Thus, the dark matter particle in question would be a WIMP. Since MSSM is already strongly constrained by results from the LHC experiments [33] [34], the supersymmetric WIMP is disfavoured as a dark matter candidate nowadays.

2.4.4 Axions/ALPs

Theoretically, the Lagrangian of Quantum Chromodynamics allows for a CP-violating term, which would give rise to a magnetic dipole moment of the neutron. Since there is no "natural" reason for this term to cancel out, but the dipole moment is excluded below $2.9{\cdot}10^{-26}$ e cm [35], the non-observation of CP violation in the strong interaction is known as the *strong CP problem*. It can be solved by introducing the *Peccei-Quinn* symmetry, which breaks below a certain scale. The Goldstone theorem then implies a new particle due to spontaneous symmetry breaking, which has been named *Axion*. This particle is massless for a perfect symmetry (Nambu-Goldstone boson), but has a non-zero mass in case of an approximate symmetry (pseudo Nambu-Goldstone boson), and could thus account for the dark matter in the universe. Different models and couplings result in a wide range of particle masses, which can be constrained in case of a dark matter axion, where a distinction is usually made for post-inflation and pre-inflation axion creation models. In general, SM-extending particles

motivated by spontaneous symmetry breaking are subsumed under *Axion-like* particles (ALPs). ALPs as dark matter candidates do not necessarily solve the strong CP problem.

2.4.5 Sterile Neutrinos

As neutrino oscillations are incompatible with the massless Standard Model neutrinos, one suggested explanation for their observation is the existence of right-handed, *sterile* neutrinos. These would not interact with other Standard Model particles except gravitationally, and can only be observed via mixing and subsequent detection as regular flavoured neutrinos. This allows for the generation of neutrino masses via a Dirac mass term in the Lagrangian. If an additional Majorana mass term is introduced, implying that sterile neutrinos (and neutrinos) are their own antiparticles, the eigenvalues of the mass-mixing matrix are inversely proportional, which leads to expected large masses for the sterile neutrinos, and very small masses for the regular neutrinos. This is called the *see-saw* mechanism. Detection of sterile neutrinos would only be possible via an enhanced rate of regular neutrinos due to mixing.

2.4.6 Asymmetric Dark Matter (ADM)

Similar to the observed asymmetry between antimatter and matter in the universe today, there might be an asymmetry between dark matter particles and antiparticles. This would mean that the dark matter relic density is not defined by the annihilation cross section as in the standard WIMP case, but by the asymmetry. Relating the asymmetries in both the dark and the visible sector produces a dark matter particle mass which is comparable to that of the proton [36].

2.4.7 Modified Gravity

Galactic rotation curves can be explained easily through Modified Newtonian Dynamics (MOND), assuming a non-linear relation between the gravitational force F_G acting on an object of mass m, and its experienced acceleration a:

$$F_G = \tilde{F}_N = m\mu\left(\frac{|a|}{a_0}\right)a \tag{2.14}$$

Here, $\tilde{F}_N$ denotes the modified version of Newton's second law. The function $\mu(\frac{|a|}{a_0})$ must be chosen such that Newtonian behavior is reproduced at high accelerations ($\frac{|a|}{a_0} >> 1$), and a new behavior is obtained for low accelerations ($\frac{|a|}{a_0} << 1$). a_0 is thus a constant describing the

characteristic acceleration at which MOND becomes dominant. Today, several versions of MOND theories exist, including tensor-vector-scalar gravity (TeVeS), which is a relativistic extension of the model [37]. TeVeS can explain gravitational lensing, but needs additional assumptions and fine-tuning to avoid unphysical phenomena such as superluminal motion. The behavior of galaxy mergers and anisotropies of the CMB can hardly be explained by modified gravity at all, and MOND theories have yet to produce a complete cosmological model. A detailed overview on phenomenological problems of MOND is given in [38].

2.5 Detection Methods

Three approaches to detect dark matter have been suggested and pursued: *Direct detection* via interaction processes of dark matter particles with particles from the Standard Model, *indirect detection* via Standard Model particles in final states of dark matter annihilations or decays, and *production* of dark matter at particle colliders. Figure 2.8 illustrates the different detection channels.

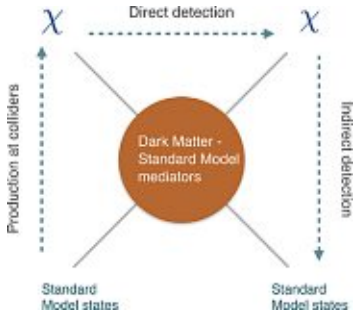

Figure 2.8: Detection and production channels for dark matter interacting with Standard Model particles; Standard Model as well as additional mediators are considered [39].

2.5.1 Direct Detection

If a species of dark matter particles is not only gravitationally interacting, but interacts also weakly via another force, processes such as elastic and inelastic scattering off a detector target material can be used to prove its existence. The signal seen in an ideal experiment then depends on the cross-section of the respective process, as well as the amount of dark matter particles penetrating the detector, and the amount of detector material employed. In reality, detector properties such as detection threshold and resolution also play an important role. This section briefly describes the different classes of direct detection experiments; the most recent physics results are summarized in Figure 2.10, which gives upper limits on the cross section for spin-independent, elastic scattering of dark matter particles off nuclei. A detailed overview on the current experimental landscape can be found in [40]. As will be shown in section 3.2, apart from the duration of data taking, the sensitivity of an experiment to dark matter interactions is determined by three key characteristics: the recoil energy threshold, the choice of the target material, and the distinction between signal and background events. In this work, emphasis is put on nuclear recoils as signal, although very light (sub-GeV) dark matter particles can also deposit detectable energies in recoils off electrons [41, 42]. Background discrimination is achieved in many experiments through the use of multiple readout channels; in scintillating materials, nuclear recoils feature a reduced light output

compared to e^- recoils, γ and α events, a behavior known as *quenching* [43]. Thus, the amount of scintillation light measured for an interaction can act as a discriminator, while another channel (ionization or phonon/heat signal) is used to assess the total deposited recoil energy.

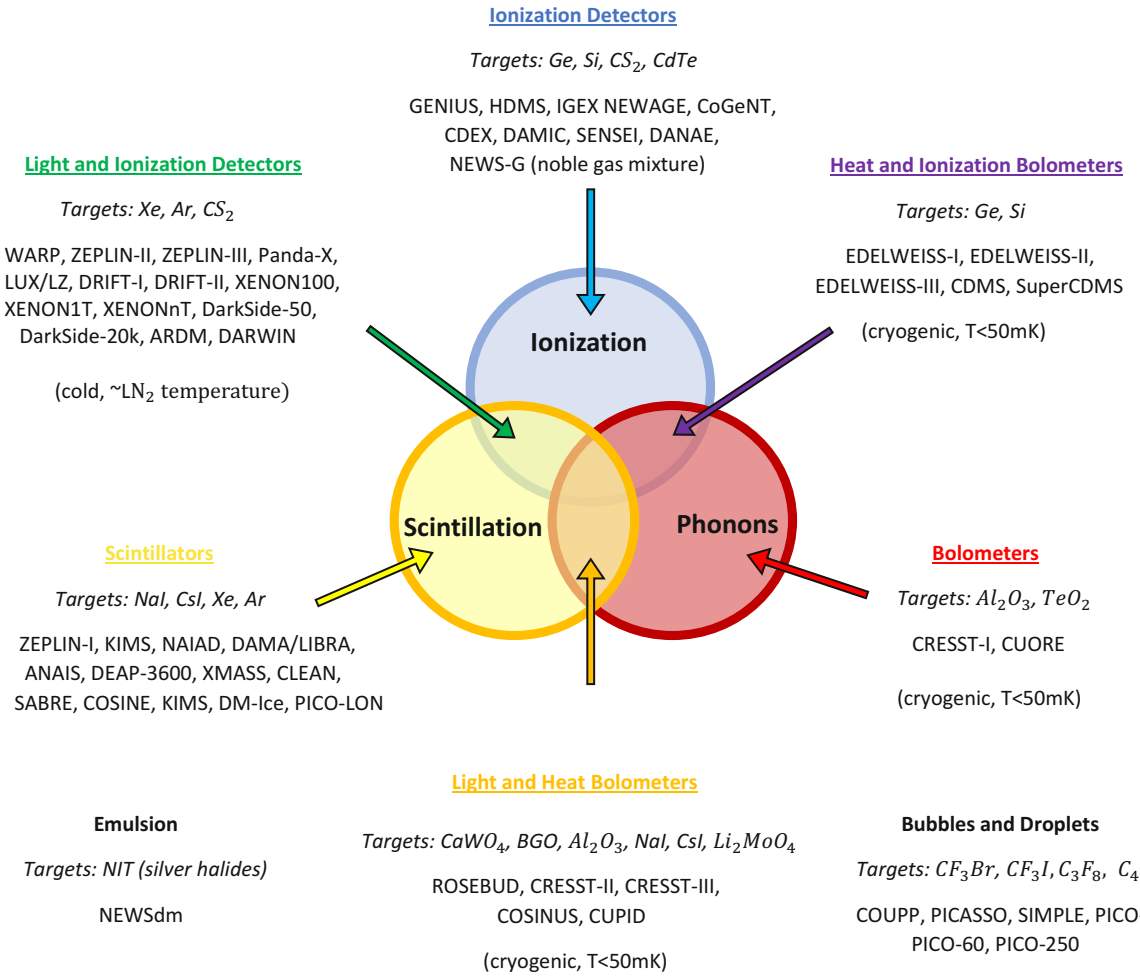

Figure 2.9: Different direct detection experiments, sorted by detection mechanism. Experiments with multiple signal channels for one event are located in the "overlap" regions. NEWAGE, DRIFT, and NEWSdm are directional searches, which also aim at measuring the direction of the recoiling nucleus.

2.5.1.1 Liquid Noble Gas Experiments

Experiments such as XENON [44], LUX [45], and PandaX [46] employ liquid Xe as target material for elastic scattering off nuclei. If an interaction happens inside the detector, which is realized as a dual-phase time projection chamber, primary scintillation light is created, and recorded by photomultiplier arrays at the top and bottom of the tank. This gives the horizontal position of the interaction. Secondary scintillation light due to ionization is created at the interface between Xe gas and liquid Xe by the drifting charges. The time delay of the second signal is exploited to determine the vertical position of the primary interaction. Its absolute location is then used to veto events near the tank walls and define an inner fiducial volume. Backgrounds due to the surrounding laboratory or the tank itself are limited to the vicinity of the tank borders because of the self-shielding effect of liquid Xe. A discrimination between electron and nuclear recoils is possible through the analysis of the ratio between the two signals, since electron recoils produce more scintillation light. The significant advantage of such experiments is an easy scalability; increasing exposure per time unit simply requires a larger tank and more liquid. XENON typically achieves energy thresholds of a few keVee [47][2], and in its current phase XENON1T employs one tonne of liquid scintillator as fiducial volume, while the total amount of liquid Xe is 3.5 tonnes. The next phase XENONnT is planned to extend the latter to 8.3 tonnes [48]. The liquid Xe has to be purified constantly in order to reach the desired charge yield at the applied field [44].
Liquid Argon is often considered an alternative to Xenon because of its lower price, which outweighs the lower density (Xe: 131.29 u, Ar: 39.95 u), although this benefit is in part mitigated by the need for low-background Ar which was not exposed to cosmogenic activation. It has also been shown that liquid Ar allows for pulse shappe discrimination in the scintillation light signal, enabling further background suppression [49]. The Darkside-50 experiment at LNGS instruments 46kg of liquid Argon, and its successor Darkside-20k is envisaged to feature 20 tonnes [50]. Today, liquid noble gas experiments provide the most stringent exlusion limits for dark matter particles with masses above ~1 GeV.

2.5.1.2 Bubble Chambers

Bubble chambers feature superheated liquids, such as C_3F_8 in the PICO-60 experiment at SNOLAB [51]. An energy deposition in the target material results in the formation of a bubble, which in turn causes detectable acoustic oscillations. As electron recoils have an

[2] Electron-equivalent energy: for a nuclear recoil of 1 keVee, the energy deposited in scintillation light is the same as for an electron recoil of 1 keV; the nuclear recoil energy is obtained via multiplying by the quenching factor (see Section 3.4.1).

extremely low probability for bubble creation ("nucleation"), they can be neglected as a background; α interactions can be identified by their different signal characteristics. Events are triggered optically by cameras, which are also used for tracking to identify events near the detector walls [51]. While the achievable threshold is on the same scale as for liquid noble gas experiments (3.3 keV for PICO-60), the focus of such experiments lies on the choice of target materials which are sensitive to spin-dependent scattering (see section 3.2).

2.5.1.3 Cryogenic Detectors

Detecting phonon signals from elastic scattering processes inside a target material requires the possibility for phonons to propagate through it. This can be achieved with a crystal target, commonly in combination with a highly sensitive thermometer such as a transition edge sensor (TES) (see section 3.3.3). The resulting detector can then be operated either as a bolometer measuring an energy flux, or as a calorimeter which integrates and gives the total deposited energy. Additionally, the target crystal may be grown from a scintillating material, which adds another readout channel allowing for the discrimination of different event classes such as electron and nuclear recoils. In order to measure the scintillation light, a second crystal with another TES is usually employed. While this setup can yield extremely low recoil energy thresholds, the growth of radiopure crystals and their instrumentation are delicate processes and do not easily allow for tonne-scale target masses and thus large exposure. Due to the low nuclear recoil energy threshold, this type of experiment yields the best sensitivity for dark matter particle masses below ~1 GeV. This work presents results from CRESST-III, Phase One with $CaWO_4$ as target material. Other examples for cryogenic experiments include CUORE (TeO_2) and the upcoming COSINUS (NaI) and NUCLEUS ($CaWO_4$ and Al_2O_3)[3]; EDELWEISS, CDEX and CoGeNT use Ge as target material, while SuperCDMS employs Ge and Si.

[3] CUORE and NUCLEUS are not aimed at the detection of dark matter.

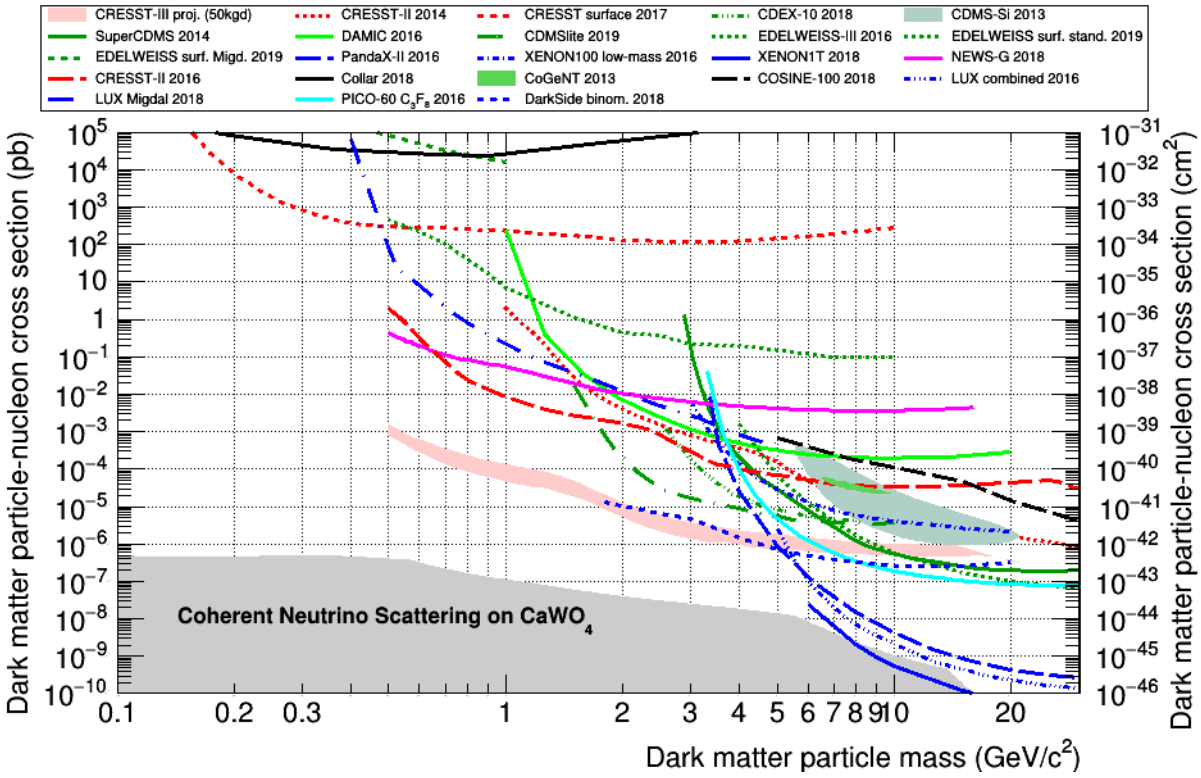

Figure 2.10: Results from different dark matter direct detection experiments. An upper limit on the cross section for spin-independent elastic scattering of dark matter particles off nuclei is given as a function of assumed dark matter particle mass. Limits from XENON1T [52], XENON100 [53], PandaX [54], DarkSide [55], LUX [56, 57], EDELWEISS [58, 59], SuperCDMS [60], CDMSlite [61], DAMIC [62] and CDEX-10 [63] are shown. Liquid noble gas experiments based on xenon or argon are represented by blue colors, while silicon or germanium based solid state detector experiments are depicted in green. Results from COSINE-100 (NaI, dashed black line) [64], Collar (H, black line) [65], NEWS-G (Ne + CH_4, magenta) [66] and PICO (C_3F_8, cyan) [67] are also shown, along with positive evidence reported by CDMS-Si [60] and CoGeNT [68]. Results from CRESST-II obtained with the detectors TUM40 [69] and Lise [70] are depicted as red dashed lines; the top red dotted line corresponds to a surface measurement performed with a gram-scale Al_2O_3 detector [71]. All results represent upper limits at 90 % confidence level, apart from the CoGeNT (99 %) and CDMS signals. The gray area indicates the cross section below which background events due to coherent scattering of neutrinos off $CaWO_4$ are expected [72].

2.5.2 Indirect Detection

An excess in cosmic radiation could be an indication for dark matter, and quantifying such an excess would reveal information about the characteristics of dark matter particles. While charged particles are deflected on their way to earth due to interstellar magnetic fields, directional information from neutral particles may be correlated with specific objects in the sky. An excess of cosmic photons or neutrinos from a certain direction coinciding with the known location of a dark matter distribution in the universe would indicate that Standard Model particles can be produced through annihilations of dark matter particles. While dark matter distributions can be mapped via graviational lensing, the main problems here are discrimination between dark-matter annihilation signals and other sources, as well as detection efficiency for photons/neutrinos. Based on data from the Large Area Telescope (LAT) onboard the Fermi satellite, an excess of gamma rays from the galactic center of the Milky Way was reported and disputed by various groups [73]. The origin of this excess is yet unknown; if it is interpreted as a dark matter signal, the properties of the dark matter particle depend strongly on the assumed model [74].

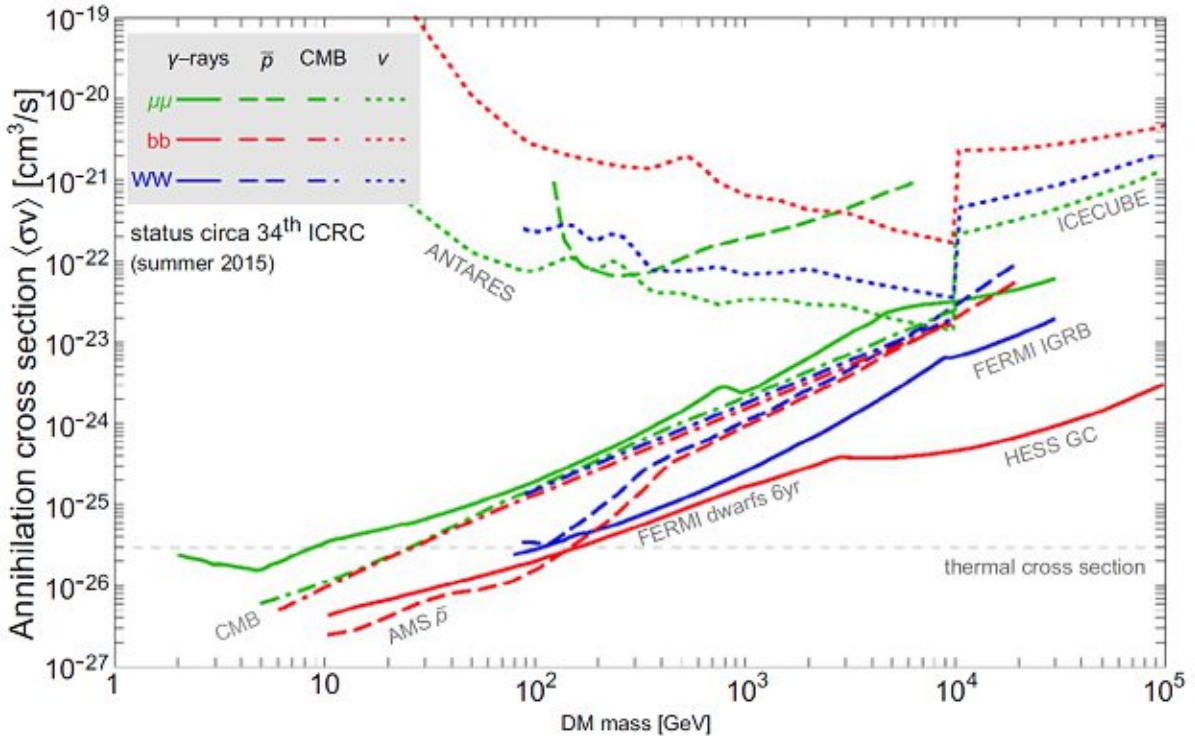

Figure 2.11: Current upper limits from several indirect searches [39]. Different dark matter annihilation channels into SM particles are indicated via different colors.

2.5.3 Production at Colliders

The "freeze-out" mechanism implies that above a certain center-of-mass energy, dark matter particles can be produced in annihilations of Standard Model particles. If this happens in a collider experiment, the energy carried by dark matter could not be detected in the final state, if the current upper limits for interaction cross-sections are taken into account. This means that final states with *missing energy* would be an indication for dark matter production, if they can be safely separated from other events where Standard Model particles, e.g. neutrinos, escape the detectors [75]. Similarly, *appearance* events with two jets in opposing directions without a preceding track can be due to dark matter interactions. Since the last LHC upgrade, the ATLAS and CMS experiments operate at high center-of-mass energies of $\sqrt{s} \sim 13\,\text{TeV}$; examples for current analyses are shown in figure 2.12. As in indirect searches, the result is only valid for certain assumptions on the interaction, e.g. which type of mediator partakes. In both of the two cases described above, it is impossible to verify that a newfound particle has the necessary life time to account for dark matter.

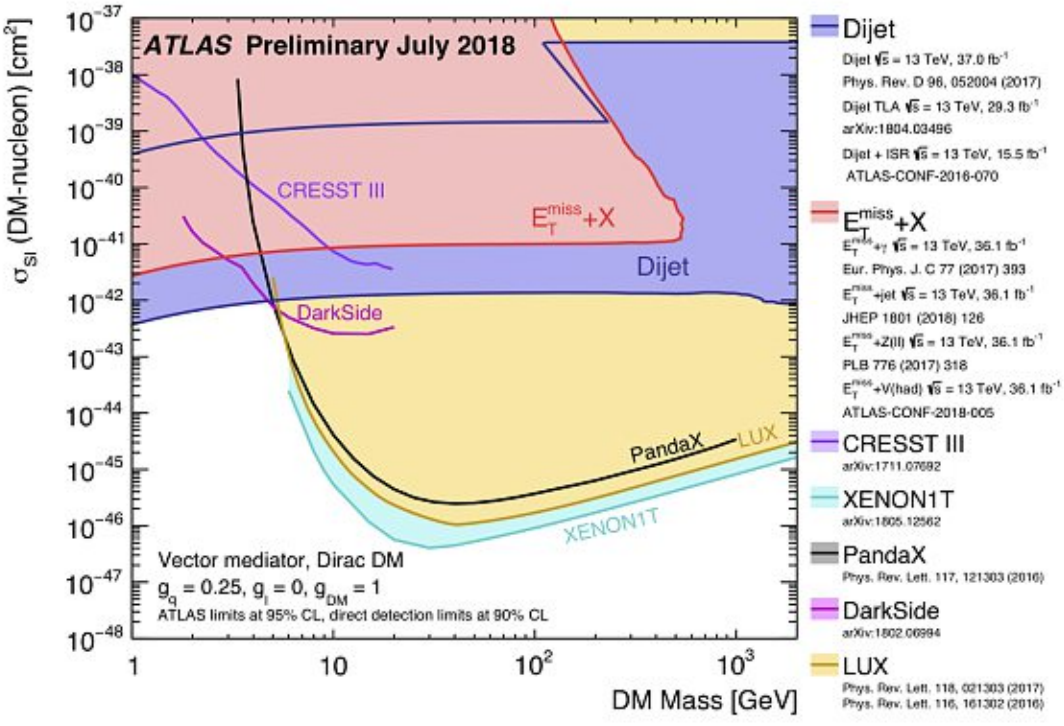

Figure 2.12: Current upper limits on spin-independent scattering from the ATLAS detector for a vector mediator; several analyses are indicated, together with results from direct detection experiments (Image: ATLAS Collaboration/CERN) [76].

3 Dark Matter Search with CRESST

This work describes a direct dark matter search; naturally, this requires a signal expectation for dark matter in an earth-bound detector, as well as a description of the interaction processes, both of which are given in the next sections. A detailed description of the experimental setup follows, and finally the framework to extract information on the properties of dark matter is introduced.

3.1 Dark Matter in the Milky Way

In order for us to directly detect dark matter, it must be present in our galaxy and, more specifically, on earth. However, the velocity dispersion curve of the Milky Way has proven to be difficult to measure accurately. This is due to the relative movements of earth, the solar system, and the stars which are observed, as well as obscuring gas in the galactic disk. Additionally, the local dark matter density at the position of the earth varies with the assumed halo model. Figure 3.1 shows the Milky Way's rotation curve as measured by Gaia DR2 [77] in comparison to previous results. An overview on different models and calculated values for the dark matter density at the position of the sun based on this data is given in [78], with values for $\rho_{DM,\odot}$ between 0.3-0.4 GeV/cm^3. Simulations of Milky Way analogues using an NFW halo profile (cf. Section 2.1) give 0.37-0.38 GeV/cm^3, which is consistent.

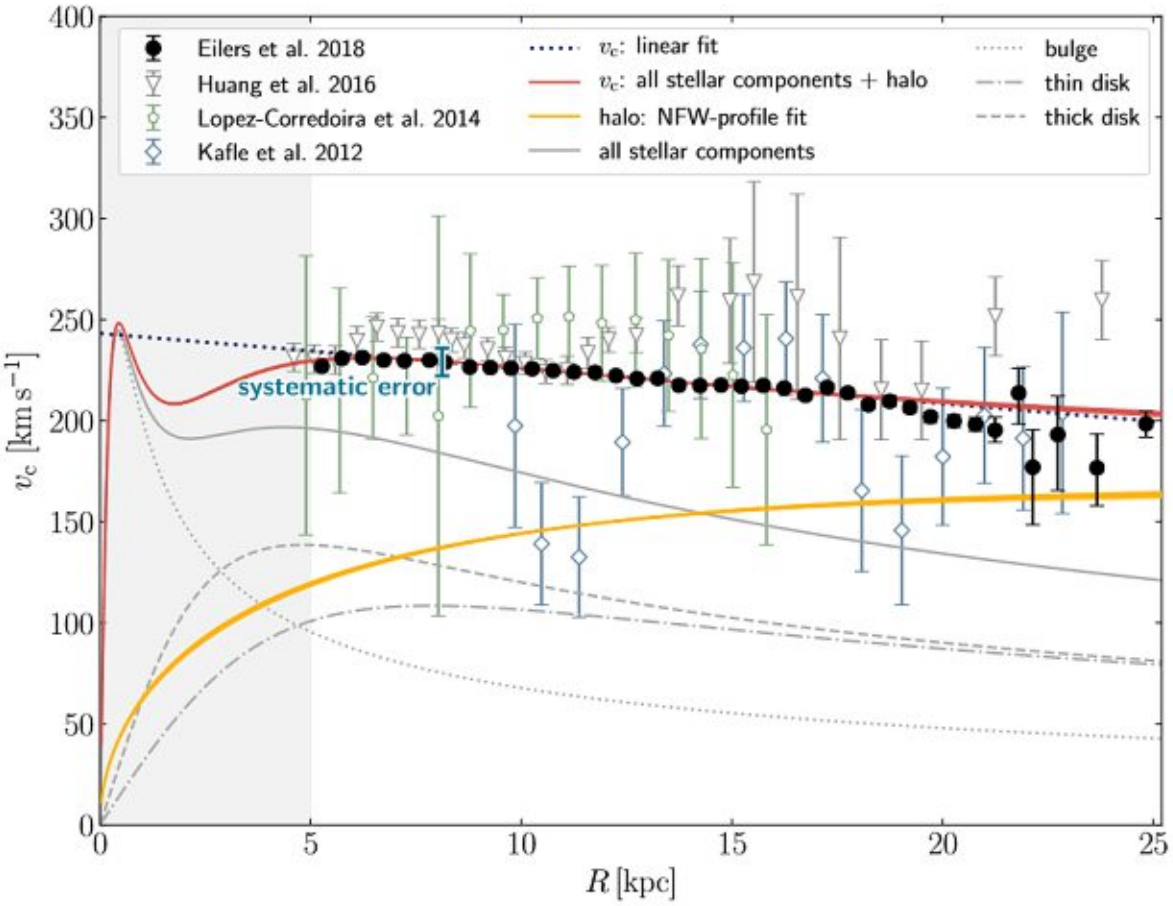

Figure 3.1: Circular rotation curve of the Milky Way measured with Gaia DR2 [77] (black dots) - observed velocity as a function of distance from the galactic center. A sum of several components (red) was fitted: a galactic bulge (gray dotted line), a thin and a thick disk (dash-dotted and dashed gray lines), as well as a NFW dark matter halo (yellow). The blue error bar gives a systematic uncertainty of 3 % at the position of the sun, and the blue dotted line represents a linear fit. Figure taken from [77].

As a comparison of this work to other experimental results requires the use of the same model,

$$\rho_{DM,\odot} = \rho_{DM,\text{earth}} = 0.3\,\text{GeV/cm}^3 \tag{3.1}$$

will be assumed, which is a common value in dark matter searches. The corresponding halo is non-rotating and isothermal in the galaxy, and features a Maxwellian velocity distribution.

3.2 Expected Signal

Due to the low expected velocities of cold dark matter particles, the effective interaction with target nuclei is elastic scattering. Spin-independent scattering is illustrated in Figure 3.2 for the special case of MSSM: The dark matter particle $\tilde{\chi}_1^0$ (i.e. the neutralino) couples to a neutral scalar boson; in MSSM, this is one of the Higgs bosons h_0 and H_0. Alternatively, it could couple directly to a quark q and produce a squark $\tilde{q}$. For spin-dependent scattering, the scalar boson is replaced with a neutral vector boson such as the Z.

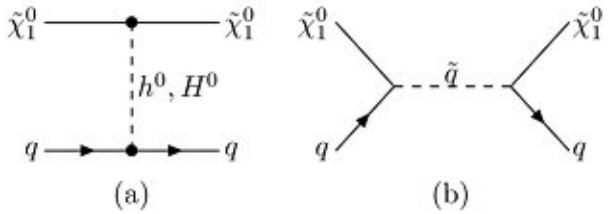

Figure 3.2: Processes contributing to spin-independent elastic scattering of a neutralino in the MSSM scenario [79]

3.2.1 Expected Event Rate

In the context of direct dark matter searches, it is often convenient to normalize the expected event rate to the amount of detector material employed. With a hypothetical halo of dark matter present in our galaxy, the rate of interactions R per mass unit is proportional to the dark matter flux Φ, the interaction cross section $\sigma_{\chi N}$, and the total number of target nuclei N_T divided by the target mass m:

$$R_N \sim \Phi_\chi \cdot \sigma_{\chi N} \cdot \frac{N_T}{m}, \tag{3.2}$$

N_T can be written as $N_T = \frac{m}{m_N}$, where m_N is the mass of a target nucleus. The flux Φ depends on the dark matter density ρ_χ, the mass of a dark matter particle m_χ, and its expected velocity $\langle v_\chi \rangle$.

$$\Phi \sim \frac{\rho_\chi}{m_\chi} \cdot \langle v_\chi \rangle \tag{3.3}$$

More accurately, dark matter particles should feature velocities v_χ which follow a Maxwell-Boltzmann distribution $f(\vec{v}_\chi)$ in the galactic rest frame, as mentioned in section 3.1. Consid-

ering only one direction relative to earth, this simplifies to a Gaussian distribution:

$$f(\vec{v}_\chi) = \frac{1}{\sqrt{2\pi}\sigma}\exp\left(-\frac{|\vec{v}_\chi|^2}{2\sigma^2}\right), \quad \sigma = \sqrt{\frac{3}{2}}v_0 \tag{3.4}$$

The asymptotic speed v_0 is approximated with the local circular speed $v_0 \approx 220\,\mathrm{km/s}$ [80][1] (the rotational speed of the local system), and gives the velocity dispersion σ. For a detector located on earth, $\vec{v}_\chi$ has to be corrected by the movement $\vec{v}_E$ of earth relative to the galactic rest frame, i.e. $f(\vec{v}_\chi) \rightarrow f(\vec{v}_{\chi E}) = f(\vec{v}_\chi + \vec{v}_E)$, where

$$|\vec{v}_E| \approx 231\,\mathrm{km/s} + 15\,\mathrm{km/s}\cdot\cos\left(\frac{2\pi}{1\,\mathrm{yr}}(t-t_0)\right) \text{ [82]} \tag{3.5}$$

$|\vec{v}_E|$ considers the peculiar motion of the sun, and earths orbit around it. t_0 corresponds to June 2$^{\mathrm{nd}}$; the equation above implies that the flux of dark matter in this model varies with time and has a maximum on this date. With sufficient statistics, time modulation analysis of the total event rate may be perfomed, which is a common approach in experiments with limited background discrimination [83]. Using the above modifications, and introducing an energy-dependent cross section $\sigma_{\chi N}(E_R)$, the differential recoil rate $\frac{dR_N}{dE_R}$ per unit of target mass is given by

$$\frac{dR_N}{dE_R} = \frac{1}{m_N}\frac{\rho_\odot}{m_\chi}\int_{v_{min}}^{v_{esc}} v_{\chi E} f(\vec{v}_{\chi E})\frac{d\sigma_{\chi N}}{dE_R}(E_R, v_{\chi E})d^3 v_{\chi E}, \tag{3.6}$$

where v_{min} is the minimum velocity to produce a recoil energy $\geq E_R$, and v_{esc} is the galactic escape velocity. At $v_{esc} \approx 544\,\mathrm{km/s}$ [84], dark matter particles (and any other objects) are able to escape the gravitational potential of the Milky Way; it is therefore the maximum observable relative velocity. v_{min} is a detector property, which is determined by the recoil energy threshold. In the non-relativistic case of cold dark matter ($v_{\chi N} << c$), the recoil energy E_R can be calculated for a simple two-body scattering process as

$$E_R = \frac{\mu^2 v_{\chi E}^2}{m_N}(1 - cos\theta), \quad \mu = \frac{m_\chi m_N}{m_\chi + m_N}, \tag{3.7}$$

with the reduced mass μ, which depends on the target nucleus mass m_N and the dark matter particle mass m_χ. θ is the scattering angle. In equation 3.6, the differential cross section can

[1] A slightly higher, updated value of $v_0 \approx 230\,\mathrm{km/s}$ is available [81]; in this work, 220 km/s is used to stay consistent with other dark matter experiments and previous CRESST publications.

be decomposed into a spin-dependent (SD) and a spin-independent (SI) part:

$$\frac{d\sigma}{dE_R} = \frac{d\sigma_{SD}}{dE_R} + \frac{d\sigma_{SI}}{dE_R}. \tag{3.8}$$

Using the formalism of [11], each component can be expressed as

$$\frac{d\sigma_x}{dE_R} = \frac{\sigma_{0,x}}{E_{R,max}} F_x^2(q), \quad E_{R,max} = \frac{\mu^2 v_{\chi E}^2}{m_N}, \tag{3.9}$$

with the *nuclear form factor* $F_x(q)$ for a given momentum transfer $q^2 = 2m_N E_R$ and process $x \in \{\text{SD,SI}\}$. The energy $E_{R,max}$ is the maximum recoil energy for a given relative velocity, and $\sigma_{0,x}$ corresponds to scattering off a point-like nucleus. In the spin-independent case, the cross section is determined by the coupling strengths to protons f^p and neutrons f^n, as well as the nuclear mass number A and proton number Z:

$$\sigma_{0,SI} = \frac{4\mu^2}{\pi}(f^p Z + f^n(A-Z))^2. \tag{3.10}$$

This results in a scaling with A^2 if $f^p \approx f^n$. The form factor is given by the fourier transform of the mass distribution for the target nucleus; an analytic expression was given by Helm [85] using a spherical Bessel function $j_1(qr_n)$:

$$F(q) = 3\frac{j_1(qr_n)}{qr_n} e^{-(qs)^2/2} \tag{3.11}$$

Following [86], model-independent form factors for O and Ca and the Woods-Saxon form factor for W are used in this work instead. For the differences between the factors, the reader is referred to [86]. In the spin-dependent case, the cross section depends on the total nuclear spin J and the spin expectation values for the neutron and proton group $\langle S_n \rangle$ and $\langle S_p \rangle$. Two coupling constants a^p and a^n incorporate the contribution of each quark to the respective nucleon.

$$\sigma_{0,SD} = \frac{8\mu^2}{\pi}(a^p < S_p > + a^n < S_n >)^2 \frac{(J+1)J}{J^2} \tag{3.12}$$

In the simplest model, pairs of nucleons cancel out in terms of spin and angular momentum, and only nuclei with odd mass numbers feature a non-zero cross section, which is determined by the single unpaired proton or neutron. Since the spin-dependent form factor only couples to the spin, and not to the mass distribution as in the SI case, it varies only little with q, and can be considered constant (i.e. equal to one) for low recoil energies. We obtain the final

differential recoil rate

$$\frac{dR_x}{dE_R} = \frac{\rho_\odot}{m_\chi \mu^2} \sigma_{0,x} F_x^2(q) \int_{v_{min}}^{v_{esc}+v_E} \frac{f(\vec{v}_{\chi E})}{v_{\chi N}} d^3 v_{\chi E} \tag{3.13}$$

The integral implies that

$$\frac{dR}{dE_R} \sim e^{-\frac{E_R}{E_c}}, \quad E_c = \frac{2\mu^2 v_0^2}{m_N}; \tag{3.14}$$

therefore we expect an exponentially falling spectrum in recoil energy. The decay constant can then be used to obtain the dark matter particle mass m_χ, while the cross section can be inferred from the total scale. In case no signal is measured, the recoil spectrum for a given σ and m_χ may be calculated, and an exclusion limit can be derived via comparison to the observed spectrum. Figure 3.3 shows nuclear recoil energy spectra for a $CaWO_4$ target obtained with the above formula for dark matter particle masses of 10, 50 and 100 GeV; "Bumps" for the contributing elements O, Ca, and W are visible. The assumed cross section for spin-independent scattering is 10^{-8} pb.

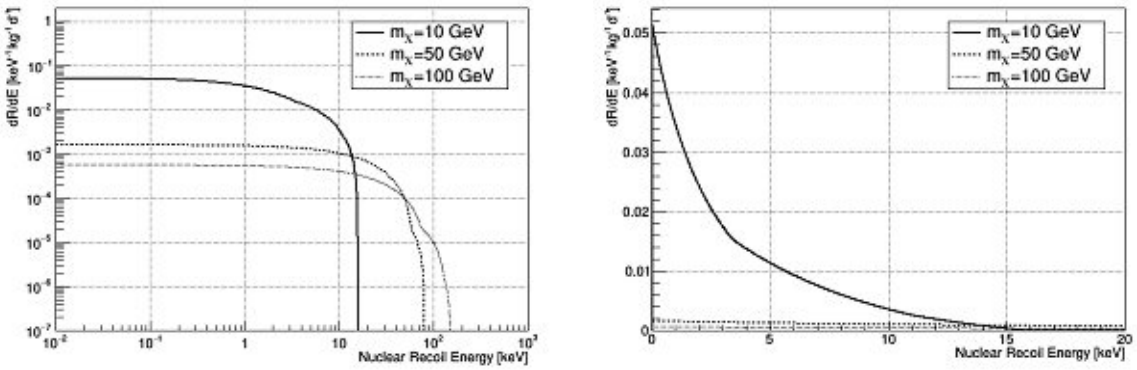

Figure 3.3: Nuclear recoil energy spectrum for spin-independent scattering off $CaWO_4$, calculated for three different dark matter particle masses and a cross section of 10^{-8} pb. Left: Double-logarithmic scale; Right: Linear scale. The kinks are due to contributions from different target nuclei (O, Ca, and W).

3.3 THE CRESST EXPERIMENT

Operational in different configurations since 1999 [87], CRESST (Cryogenic Rare Event Search with Superconducting Thermometers) represents one of the earliest attempts to directly detect dark matter. Instrumented target crystals are used to measure energy depositions from traversing particles - Al_2O_3 as well as $CaWO_4$ were the most prominent target materials in the main experiment, but measurements were carried out also with a variety of other substances (recently e.g. Li_2MoO_4, [88]). As motivated in the previous sections, target materials for direct detection experiments should feature a high atomic number to increase the number of possible interactions. At the same time, a low atomic number yields sensitivity to smaller recoil energies for kinematic reasons, and thus sensitivity to low-mass dark matter particles; this is one of the reasons for using compounds of different elements. Since other causes for energy depositions in the detector apart from dark matter particles need to be vetoed or avoided, experiments must be performed in an extremely low-background environment, and with a reliable background identification method. CRESST is located in the Laboratori Nazionali del Gran Sasso underground facility, which provides a water-equivalent rock overburden of 3600 m [89] and removes cosmic radiation to a large extent (cf. Section 3.3.7). The experiment meets the second requirement through the use of additional small silicon-on-sapphire (SOS) wafers suited for the absorption of scintillation light, which provide a second detector channel for each module. As the fraction of scintillation light produced depends on the type of interaction, this allows to discriminate between dark matter-like nuclear recoils and e^-/γ events. The readout in each channel is realized via a transition edge sensor (TES), which is operated at extremely low temperatures around 15 mK. Different detector module designs have been implemented and tested, including different holding schemes for the crystals, as well as additional carrier crystals for the TES. This work focuses on data obtained in the first phase of CRESST-III; in the following section, the experimental layout and technical principles of CRESST are briefly sketched.

3.3.1 Dilution Refrigerators

In order to reduce thermal noise, cooling of the detector modules is necessary. CRESST employs a dilution refrigerator, which is based on the following principle: In the mixing of liquid ^{4}He and ^{3}He at low temperatures below ≈870 mK, a spontaneaous separation of two phases occurs. One *concentrated phase* contains practically only ^{3}He, while the other, superfluid *dilute* phase contains ≈93 % ^{4}He due to quantummechanical effects. Mixture is taken from the dilute phase, and part of its ^{3}He is separated and again added to the

concentrated phase. ^{3}He will then cross the phase boundary from the concentrated to the dilute phase, which consumes heat, and a net cooling is achieved. In practice, a dilution refrigerator consists of the *mixing chamber* itself, a *still heater* used to separate the extracted mixture into ^{4}He liquid and ^{3}He vapor, a *condensor line* for the ^{3}He to re-condense, and heat exchangers, where the mixture coming from the bath is used to pre-cool the condensed ^{3}He before it enters the mixing chamber again. This is a closed system, where the He mixture is constantly recycled. The ^{3}He condensor is coupled to a pre-cooling system via a heat exchanger; in the CRESST cryostat, this is implemented via a 1 K ^{4}He bath, which is vacuum pumped and filled through a capillary from another 4.2 K ^{4}He bath. Although recycling of the pre-cooling fluid in a closed loop is possible and realized for other cryostats, this is not the case for CRESST. An external ^{4}He recycling system with a liquefier is used, and liquid ^{4}He as well as liquid nitrogen for additional thermal insulation have to be refilled in intervals of ≈48-72 h. Pre-cooling with liquid gases, the so-called "wet" cryostat design, is still common nowadays, but is gradually being replaced by "dry" cryostat concepts, which feature a pulse tube pre-cooling system. The main caveat of using "dry" cryostats for low-energy measurements is the introduction of vibrations due to the pulse tube; these vibrations could propagate to the extremely sensitive detectors and artificially increase the energy threshold (see e.g. [90]). On the other hand, "dry" cryostats do not need the 1 K ^{4}He bath described above, which was shown to produce vibrations in "wet" cryostats.

3.3.2 Experimental Layout

The detector array or "carousel", consisting of a copper support structure with several mounting slots for detectors, is situated in the center of the experimental setup at the lower end of the cryostat. It is connected to the mixing chamber via a 1.5 m long Cu rod ("cold finger") which transports the cooling power. In Figure 3.4, the complete installation is shown, and several layers of shielding are indicated. The outermost is made of polyethylene and aimed at neutrons from the surrounding rock. A Pb layer and a Cu layer follow; both materials feature relatively high atomic numbers and efficiently remove γs. Generally, Cu is available with a higher purity and in particular less radioactivity than Pb; the combination of both materials limits the additional neutron background induced by heavy radioactive isotopes in the lead. To remove the remaining neutrons, another, innermost layer was added, which consists of polyethylene.

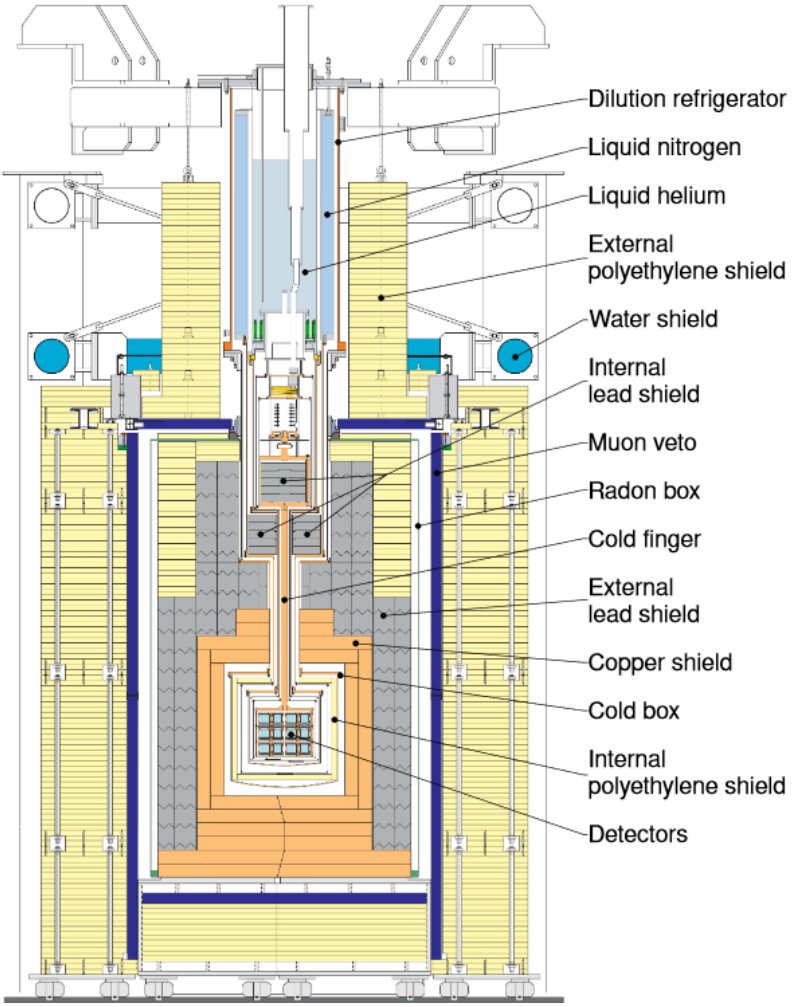

Figure 3.4: CRESST cryostat with detector carousel and shielding [91]. From the innermost to the outermost layer, the carousel is surrounded by polyethylene, copper, lead and again polyethylene shields.

3.3.3 Transition-Edge-Sensors (TES)

Any energy deposition in a crystal leads to the creation of phonons, which are subsequently collected at a TES sensor; these extremely sensitive thermometers are thin films of superconducting materials. In the transition between superconducting and normal conducting state, a small change in temperature corresponds to a detectable change in electrical resistance (cf. Figure 3.5); this means that the sensitivity of the detector improves with the steepness of the transition.

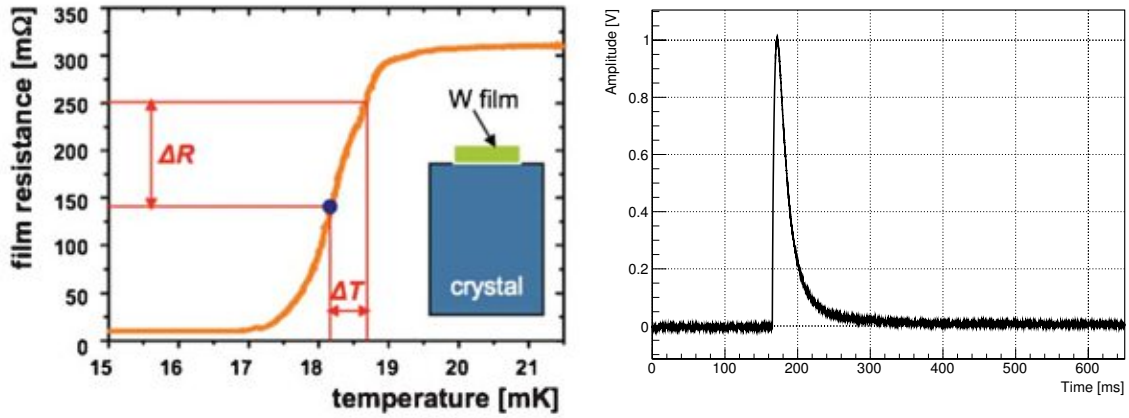

Figure 3.5: Left: Resistance curve as a function of temperature for a W film used in a CRESST TES; the transition temperature is ~18-19 mK. The TES (green) working point is set in a steep region on the lower half of the curve, and any energy deposition in the target crystal (blue) results in a measured temperature change ΔT. Figure taken from [92]. Right: Typical pulse shape measured by a SQUID; the signal decay is rather slow and takes several hundred 100 ms.

CRESST TESs are W thin films with additional small Al panels, the so-called *phonon collectors*, which are added to enhance the propagation of phonons from the main absorber crystal into the TES. A typical TES is sketched in Figure 3.6. For CRESST, the transition temperatures lie around 15 mK. Each TES is paired with an electrically decoupled heater film, which is evaporated on the crystal, and is used to set a working point for each detector individually independent of the carousel temperature. Obviously, the sensor cannot work if the transition temperature of the TES lies below the carousel temperature; therefore, each TES must be characterized by measurements before being introduced to the experimental setup. Increasing reproducibility and sensitivity of TES sensors is an important ongoing research topic for CRESST.

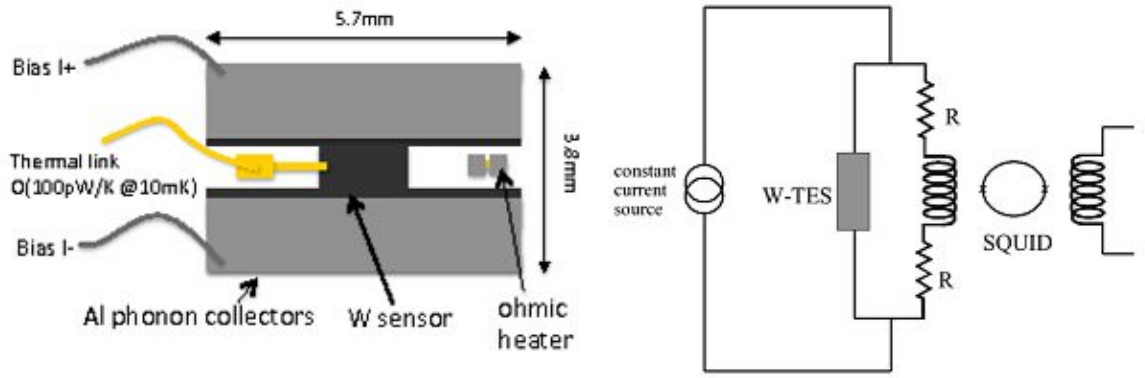

Figure 3.6: Left: Sketch of a CRESST W transition edge sensor [93]; the two bias current contacts as well as the heater film are indicated. A gold wire is used for the thermal link to the heat bath. Right: Simplified readout scheme via a SQUID. [94]

Each sensor is read out via a Superconducting Quantum Interference Device (SQUID) (cf. Figure 3.6, right), which serves as an amplifier [95]. An exception is made for instrumented holding stick TESs (see Section 3.3.5), where one SQUID is used for all three iSticks of a module in parallel. The typical pulse shape is illustrated in Figure 3.5 (right): Pulses display a short rise time (~1 ms) and decay very slowly (~100-300 ms). Signal formation is discussed in detail in Section 4.2.2.

3.3.4 Definition of a Working Point

The CRESST cryostat achieves a minimum temperature of ~7 mK at the carousel, which allows to set the operation point of each TES sensor above this value via an individual ohmic heater. For a given applied bias current, the transition of a TES is measured in the following way: A large voltage step is repeatedly injected via the heater. Starting from above the transition (i.e. in the normal conducting regime with high heating power), the constant DAC heating is then incrementally decreased while measuring the reconstructed step height. If the superconducting state is reached, the height does not increase anymore. The *working point* is defined for the TES in a similar manner: heater pulses with different heights are sequentially injected, and the constant heating is gradually reduced, starting from above the transition. This is illustrated in Figure 3.5 for a CRESST-III detector and two different injected amplitudes. The reconstructed pulse height first increases from zero to a maximum value, and subsequently decreases again as the superconducting state is approached. From the upper part of the transition (i.e. on the right flank in Figure 3.5), a region is selected where the pulse height curve of the lower injected amplitude is steep and the reconstructed pulse

height is high, resulting in maximal sensitivity. As the example curve in Figure 3.5 shows, the typical transition is not entirely "smooth", therefore a working point in close proximity to a "bump" has to be avoided. Using a feedback loop, the detector is kept in its working point throughout the measurement: *Control pulses* with a fixed amplitude are periodically injected into each crystal via the heater, and a comparison of their reconstructed pulse height with a predefined setpoint causes the quasi-constant TES heating to be increased or decreased to maintain a stable detector response over time.

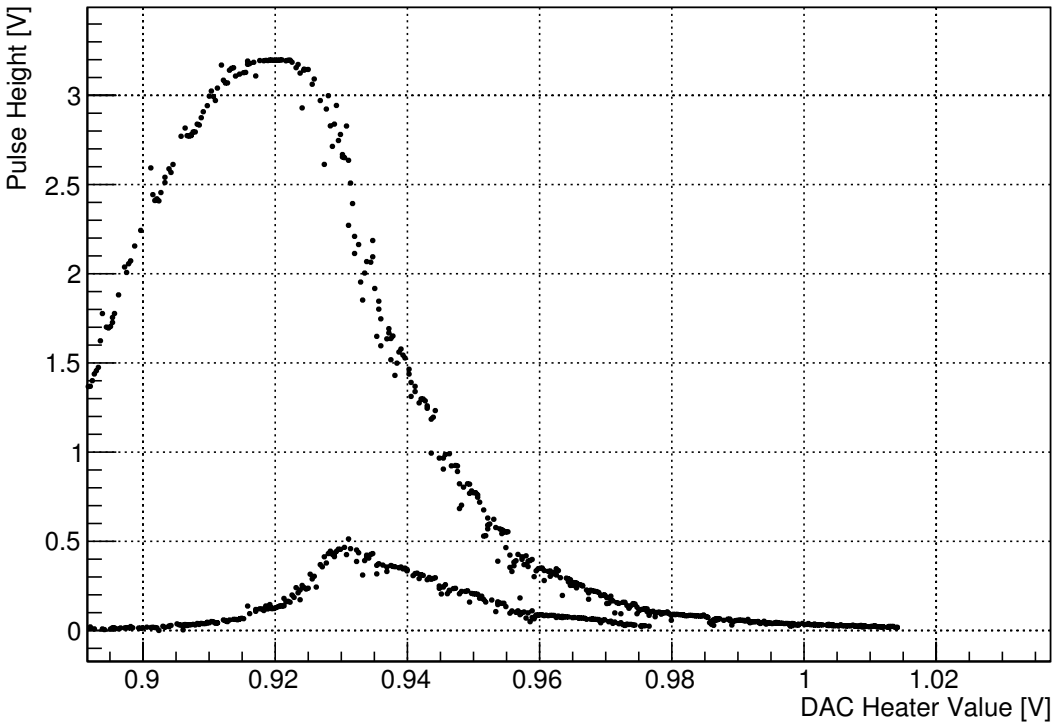

Figure 3.7: Heater sweep for detector B in CRESST-III; heater pulses with two different amplitudes were injected.

3.3.5 CRESST-III Detector Design

With CRESST-III, the focus shifted to the detection of low recoil energies. According to the detailed model for phonon collection in cryogenic particle detectors developed in [96], initial non-thermal phonons of high frequency created by a recoil thermalize at the crystal surface with a characteristic time constant τ_c. It was shown that the achievable recoil energy threshold E_{th} is proportional to τ_{film}, the characteristic time constant for phonon absorption in the thermometer, and inversely proportional to τ_c:

$$E_{\text{th}} \propto \frac{\tau_{\text{film}}}{\tau_c} \tag{3.15}$$

τ_c is proportional to the mean free phonon path length, which in case of a cubic crystal is proportional to the side length d; as τ_{film} is proportional to the volume $V \propto d^3$ of the crystal, we obtain

$$E_{\text{th}} \propto d^2 \propto m^{\frac{2}{3}} \tag{3.16}$$

for a crystal of mass m with fixed density, where the volume can vary [97]. Therefore, smaller detectors are more suitable for low mass dark matter search. A CRESST-III detector module typically consists of a ~24 g $CaWO_4$ crystal of (20x20x10) mm^3, paired with a SOS light detector, which has a volume (20x20x0.4) mm^3. The crystal is secured in its location via three $CaWO_4$ holding sticks, which have a length of 12 mm, a diameter of 2.5 mm, and a rounded tip, where the radius is about 2-3 mm. These sticks are also instrumented with a TES for readout and denoted "iSticks"; additional similar sticks, which hold the light detector, are not instrumented. The absorber crystal is transparent to its own scintillation light, which is a prerequisite in order for the light detector to measure it. Therefore, little to no signal is expected in the $CaWO_4$ iSticks for interactions in the main absorber, and they can be used as a veto[2]. The detector module is placed in a copper housing made of highly radiopure copper, and the inner surface is covered with highly reflective Vikuiti foil, which also scintillates. A design scheme is given together with an image of a CRESST-III module in Figure 3.8.

[2] Propagation of phonons from the main absorber to an instrumented holding stick will create a signal at higher energies.

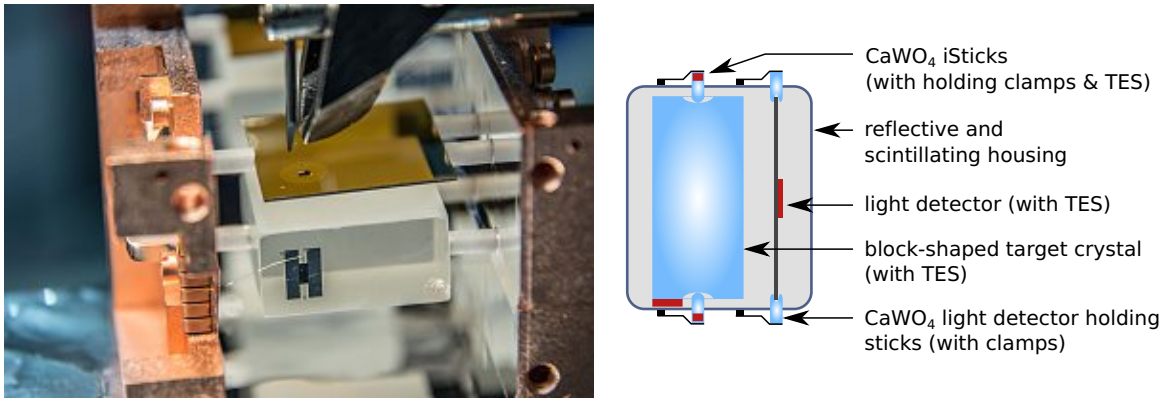

Figure 3.8: Image (left) and sketch (right) of a CRESST-III type detector module; the main $CaWO_4$crystal and the SOS light detector are held by instrumented $CaWO_4$ sticks, and the whole system is encompassed by the reflective foil and copper housing. The image also shows the bonding process, where a gold wire is used to connect the TES to the heat bath.

In the first phase of CRESST-III, ten modules of the aforementioned type were operated. Out of these, four are analyzed in this work, which exhibit a nuclear recoil energy threshold close to or below the design goal of 100 eV [98]. Exact masses for each absorber crystal are listed in table 3.1; the modules are called A, B, E, and J. Each $CaWO_4$ target crystal was cut from an ingot, grown from the cleanest commercially available materials at TU Munich [99], which is listed in Table 3.1.

Module	Mass of absorber crystal [g]	Crystal ingot [99]
A	23.6	TUM56
B	24.5	TUM73-1
E	24.5	TUM73-4
J	23.9	TUM56

Table 3.1: Exact absorber crystal masses for modules A, B, E and J in CRESST-III, Phase One.

3.3.6 Electronics

Three main circuits are used in the experiment: One to measure pulses in the TES, one to apply constant heating and inject heater pulses into the crystal, and one for providing the necessary bias current for the SQUID. All are indicated in Figure 3.9, which gives an overview on used electronic components. A sampling interval of 0.04 ms was used in this work, with a total number of samples per hardware-triggered record window of $2^{14} = 16384$. This results in a record size of 655.36 ms. One quarter of each record window lies before the trigger timestamp; this is the so-called pre-trigger range of each pulse used to later assess the baseline in

analysis. On the right side of Figure 3.9, a second readout strand (black) connected to the SQUID electronics is depicted, which yields a continuous detector stream in addition to the hardware-triggered pulses; both for the continuous stream and the triggered pulses, voltages are sampled with transient digitizers at a resolution of 16 bits. Analysis of the stream is performed in software and will be discussed in Section 4.1. A detailed description of the SQUID electronics can be found in [95], while an overview on the readout process is provided in [100].

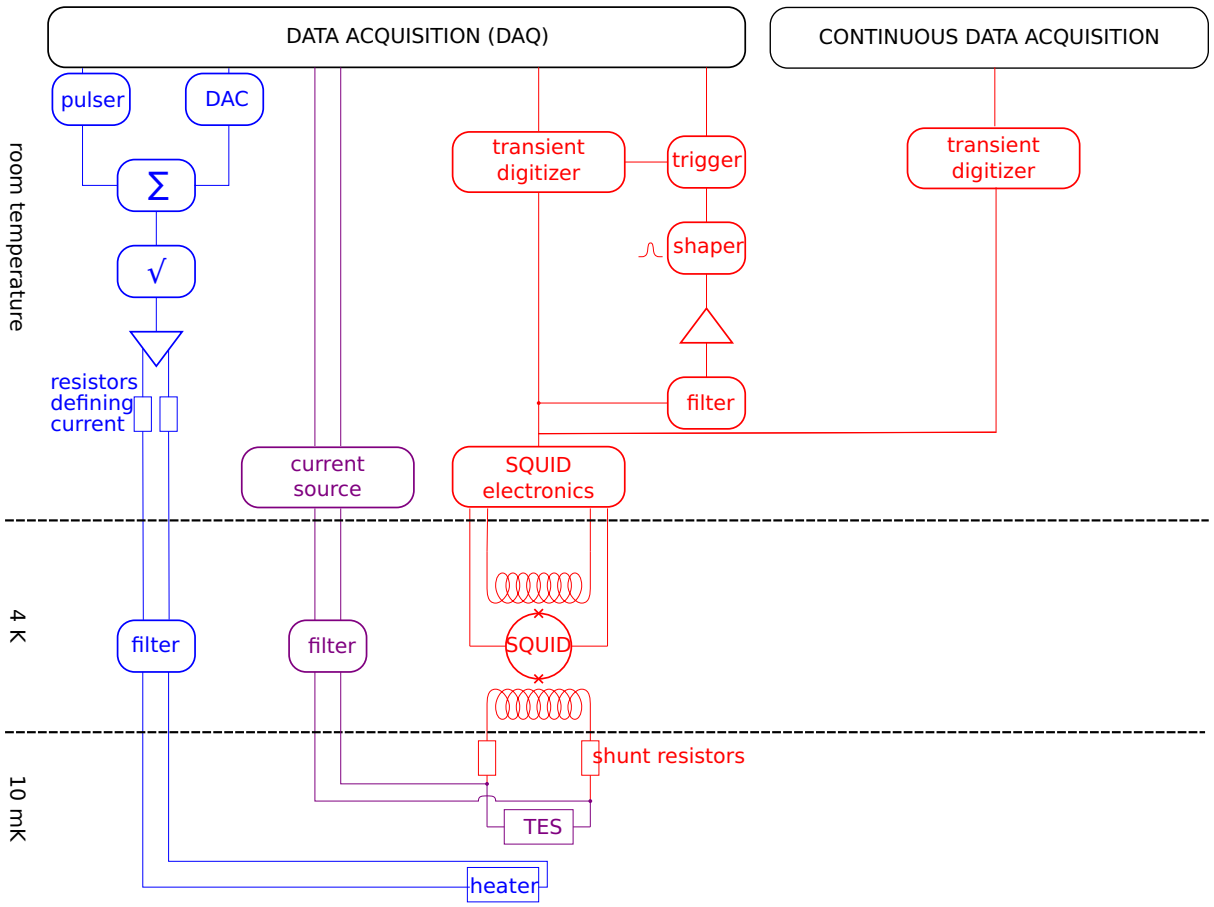

Figure 3.9: Block diagram illustrating the electronics used in CRESST-III [100]. The left, blue-colored part shows the circuit used to inject heater pulses into the crystal, while the violet circuit provides the bias current. The red part describes the readout electronics. All three circuits are managed by the dataacquisition (black). On the right side, components necessary for the additional continuous dataacquisition are displayed. Figure modified from [101].

3.3.7 Muon Veto Panels

Due to the rock overburden, the muon flux is reduced by a factor 10^6 compared to the surface, resulting in only ~1/ (m^2h) in the underground laboratory [102]. To veto remaining muon events, the CRESST cryostat is surrounded by a layer made of 20 muon panels (see Figure 3.4), which consist of plastic scintillators read out by photomultipliers. The geometrical coverage lies at 98.7% [94], where the remainder is due to the requirement of an opening for the cryostat at the top. In case of a trigger in one of the panels, all panels are read out. The information from the panels is then used to remove cryodetector events within a certain time interval around a muon panel event (cf. section 5.3.7). While the scintillator itself features a rise time of several ns [103], the photomultiplier has a typical time resolution of ~15 ns, which is still much smaller than the rise time in a TES (~ ms).

3.4 Light Yield and Band Description

As described in Section 3.3.5, three readout channels are available in a CRESST-III type detector module: The signal from the absorber crystal, the scintillation light collected in the SOS light detector, and the energy deposited in any of the instrumented holding sticks. Although all channels are read out via TES sensors and thus phonons are measured, the term "phonon channel" generally denotes the signal measured by the absorber crystal in this work. The presented analysis is aimed at events taking place in the main crystal, but it is also possible to use the light detector crystal as a target, and exploit its lower mass and thus detection threshold (cf. Section 3.3.5) [104].

For a given amount of energy deposited in the phonon channel, the measured amount of scintillation light is used to discriminate between different event classes: Due to quenching, recoils off electrons and γs interacting with them will produce more light than recoils off nuclei. The ratio between light and phonon signal is denoted *light yield* (LY); it is compared to the total deposited energy. As there are three target nuclei in the material (O, Ca, and W), three bands are expected in addition to an electron band and one for γ events populated by monoenergetic peaks. Under normal measuring conditions in the underground laboratory, nuclear recoil bands are scarsely populated, and thus a neutron calibration with an AmBe source placed inside the outer polyethylene and lead shielding is usually performed in CRESST. This calibration also enhances the density in the electron band. Figures 3.11 and 3.10 show a bandfit based on such a measurement for detector A in CRESST-III, Phase One; the light yield is compared to the energy deposited in the phonon channel, instead of the

total deposited energy. The difference between both quantities is discussed in Section 4.5. Bands for nuclear recoils off O, Ca, and W are depicted in red, violet, and green, respectively. For each band, the mean line (solid), and 90 % contours (dashed) are indicated. Recoils off electrons are shown described by the blue band, and the mean line for γ events is illustrated in light blue. It is important to note here that the parameters for cosmogenic γ peaks cannot be deducted from this short dataset: their (very low) activities scale with measuring time (cf. Section 5.13). However, there is a fluorescence line of Cu at 8.05 keV, which was observed in earlier CRESST phases.

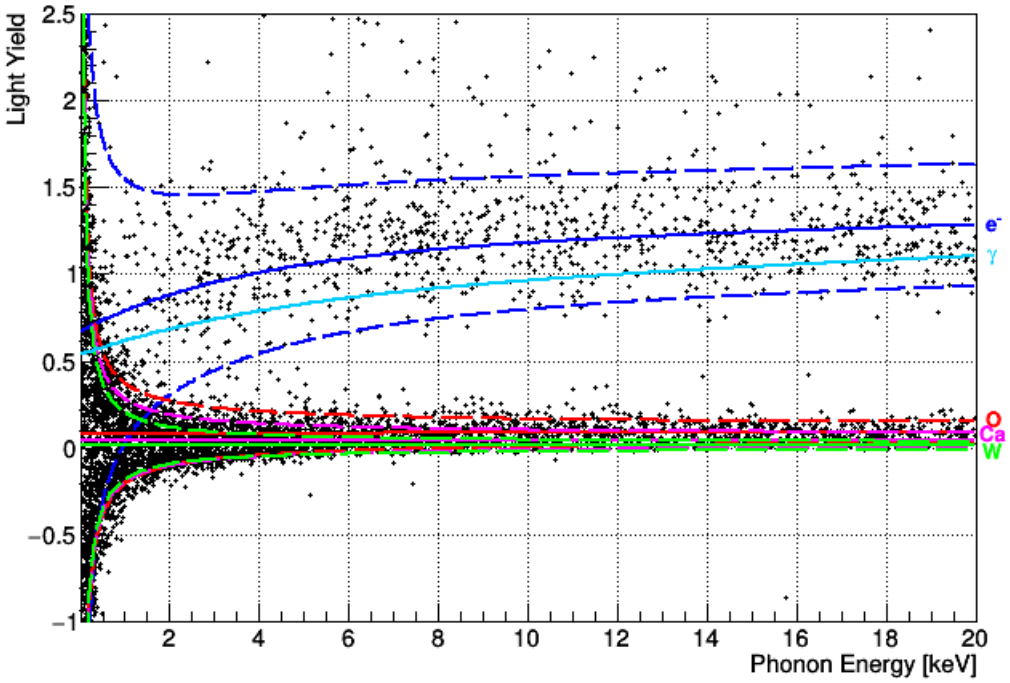

Figure 3.10: Examples for fitted recoil bands in the light yield versus phonon energy plane, using data from the neutron calibration of detector A in CRESST-III, Phase One. An electron recoil band (blue) is shown, together with the mean line of the γ band (light blue), and three quenched nuclear recoil bands for O (red), Ca (purple) and W (green). The four bands are indicated by their respective mean line and 90 % contours. Excess light events are also visible above the e^- band. Parameters for the bands and spectra are listed in tables 8.1 and 8.2.

3.4.1 Parametrization of Recoil Bands

An understanding of the recoil bands is necessary to identify possible dark matter event candidates. The analytic description used in this work was implemented in [105], and is based on earlier work [86] [101] [106]; this section gives a short overview. For computing reasons,

bands are parametrized in the light versus phonon energy plane, i.e. L vs E. Exemplary data and fitted bands are shown in Figure 3.11; it is the same data with the same parameters as in Figure 3.10.

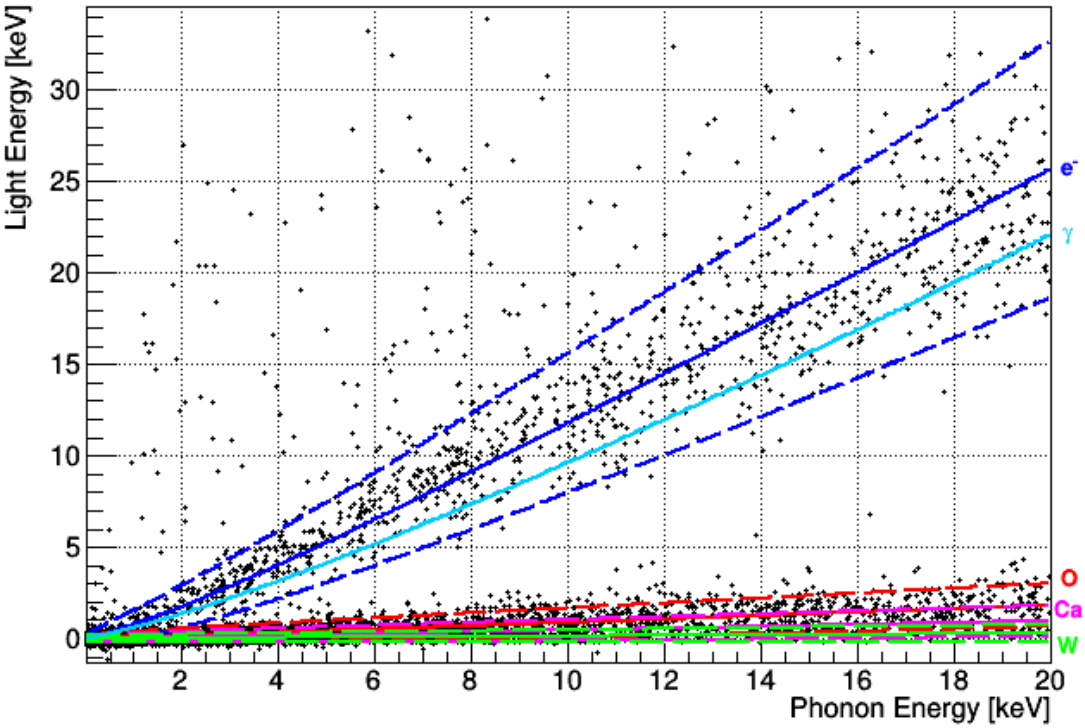

Figure 3.11: Examples for fitted recoil bands in the light versus phonon energy plane, using data from the neutron calibration of detector A in CRESST-III, Phase One. An electron recoil band (blue) is shown, together with the mean line of the γ band (light blue), and three quenched nuclear recoil bands for O (red), Ca (purple) and W (green). The four bands are indicated by their respective mean line and 90 % contours. Excess light events are also visible above the e^- band. Parameters for the bands and spectra are listed in tables 8.1 and 8.2.

Each band is described by an energy dependent mean line $L(E)$ and a Gaussian width $\sigma(L(E))$, which are then combined into a density function. This is motivated as follows: At high energies, the Poissonian generation of many scintillation photons is well described by a Gaussian function, and at low energies, the light detector resolution also behaves Gaussian-like. The energy deposited in the light detector for electron recoils L_e as a function of the phonon energy E is modeled via a polynomial of degree two, which considers a linear energy dependence factor L_0 plus a quadratic term to account for non-linearity (L_1). At low energies, the band is bent down due to non-proportionality of the produced scintillation light. This is

included via an exponential decay with parameters L_2 and L_3 [107].

$$L_e(E) = (L_0 E + L_1 E^2)\left[1 - L_2 \exp\left(-\frac{E}{L_3}\right)\right] \tag{3.17}$$

In γ interactions, secondary low-energy electrons are created, and their summed energy is smaller than the inital γ energy due to the combined non-proportionality; the mean line of this band L_γ lies slightly shifted to lower energies with respect to the electron band. Again, a polynomial of degree two is used to describe the dependence on the initial electron energy (parameters $Q_{\gamma,1} < 1$ and $Q_{\gamma,2} \sim 0$). The electron mean line is thus evaluated at a slightly lower energy:

$$L_\gamma(E) = L_e(E[Q_{\gamma,1} + EQ_{\gamma,2}]). \tag{3.18}$$

The nuclear recoil bands x for $x \in$ {O,Ca,W} are parametrized based on the electron recoil band:

$$L_x(E) = (L_0 E + L_1 E^2) \cdot \varepsilon LY_x \cdot \left[1 + f_x \exp\left(-\frac{E}{\lambda_x}\right)\right]. \tag{3.19}$$

with the parameters LY_x, λ_x and f_x, which describe energy dependent quenching for different target nuclei [106]. Since the scintillator non-proportionality effect is due to the stopping power for electrons in $CaWO_4$ [107], it is not present for nuclear recoils. The quenching of bands relative to the electron band varies slightly between different modules; in [106], it was shown that this can be described with an empirical factor ε for each module, which proportionally shifts all nuclear recoil bands.

	LY_x	f_x	λ_x
O	0.0739 ± 0.000019	0.7088 ± 0.0008	567.1 ± 0.9
Ca	0.0556 ± 0.00073	0.1887 ± 0.0022	801.3 ± 18.8
W	0.0196 ± 0.0022	0	∞

Table 3.2: Material-dependent quenching factors LY_x and band parameters f_x,λ_x; these constants were determined in [106].

The resolution of the light detector is parametrized as

$$\sigma_L(L) = \sqrt{\sigma_{L,0}^2 + S_1 L + S_2 L^2}, \tag{3.20}$$

and for the phonon detector the formula

$$\sigma_P(E) = \sqrt{\sigma_{P,0}^2 + \sigma_{P,1} E} \tag{3.21}$$

is used. The linear energy dependence in the light channel (parameter S_1) is motivated by

the Poisson statistics of scintillation photons; the empirical quadratic term proportional to S_2 accounts for additional effects. Similarly, $\sigma_{P,1}$ is an empirical factor which is usually small (cf. Table 8.1). Combining both resolutions, the width of a light band as a function of phonon energy can then be geometrically motivated as

$$\sigma_x(E) = \sqrt{\sigma_L^2(L_x(E)) + \left(\frac{dL_x(E)}{dE}\Big|_E\right)^2 \sigma_P^2(E)}, \tag{3.22}$$

where the derivative $\frac{dL_x}{dE}(E)$ is evaluated for a given energy E:

$$\frac{dL_e(E)}{dE} = \left[(L_0E + L_1E^2)\frac{L_2 e^{-\frac{E}{L_3}}}{L_3}\right] + \left[(L_0 + 2L_1E)(1 - L_2e^{-\frac{E}{L_3}})\right]. \tag{3.23}$$

Above the e^-/γ band, a distribution of events with a higher light to phonon energy ratio is visible in many detector modules. These *excess light* events were studied in [86], where they were attributed to electrons, which hit the scintillating foil and produce additional scintillation light. A phenomenological formula for the density distribution was found:

$$\rho_{ex}(E,L) = El_{amp} \cdot \exp\left(-\frac{E}{El_{dec}}\right) \cdot \frac{1}{2El_{width}} \cdot \exp\left(-\frac{L}{El_{width}} + \frac{\sigma_{L,e}^2}{2El_{width}^2}\right) \cdot \left[1 + \mathrm{erf}\left(\frac{L}{\sqrt{2}\sigma_{L,e}} - \frac{\sigma_{L,e}}{\sqrt{2}El_{width}}\right)\right], \tag{3.24}$$

where $\sigma_L(L_e(E)))$ was abbreviated as $\sigma_{L,e}$. This describes an exponentially decreasing density function, which starts at the mean line of the electron band, and was convolved with a Gaussian function to account for the detector resolution. Opposed to [86] and following [105], an independent amplitude El_{amp} is used instead of a fraction of the electron band. The remaining density functions for all the other bands are modeled as Gaussian distributions - again due to the Poisson statistics of scintillation photons - around the respective mean line $L_x(E)$ for a given energy, using the width $\sigma_x(E)$ (Equation 3.22). Therefore, the probability density distribution for observing an event with measured energies (E,L) in a given band x is written as:

$$\rho_x(E,L) = \frac{\frac{dN}{dE}(E)}{\sqrt{2\pi}\sigma_x(E)} \exp\left(\frac{(L - L_x(E))^2}{2\sigma_x^2(E)}\right) \tag{3.25}$$

In a next step, the expected differential recoil energy spectra for each event class are defined.

The empirical background model for the electron band is a constant plus a linear term,

$$\frac{dN_e}{dE}(E) = P_0 + EP_1, \tag{3.26}$$

while γ peaks are parametrized individually, as they are due to characteristic radiation from detector materials

$$\frac{dN_{\gamma,x}}{dE} = \frac{1}{\sqrt{2\pi}\sigma_p(M_x)} \exp\left(-\frac{(E-M_x)^2}{2\sigma_p^2(M_x)}\right). \tag{3.27}$$

Here, M_x is the mean value for a given peak x. The assumed spectrum for each neutron band x in case of a neutron source is an exponential function with decay constant D_x and initial amplitude F_x,

$$\frac{dN_x}{dE}(E) = F_x e^{-\frac{E}{D_x}}, \tag{3.28}$$

and the signal spectrum follows a similar model:

$$\frac{dN_s}{dE}(E) = F_s e^{-\frac{E}{D_s}}. \tag{3.29}$$

The exact description of all recoil bands now enables the formulation of a signal expectation, as well as background discrimination as long as bands are separated. This is discussed in the following section.

3.5 Extraction of Exclusion Limits

Contrary to other fields of particle physics, backgrounds in dark matter searches can often not be reliably attributed to a certain process, or modelled with sufficient accuracy. Especially when probing low recoil energies, as in the case of CRESST, new backgrounds can appear, and procedures for the calculation of exclusion limits need to account for this. Two approaches are used in this work: Yellin's optimum interval method and a likelihood calculation. For the optimum interval method, results from a bandfit are used to define an acceptance region, in which all observed events are treated as dark matter candidate events. In this way, events obviously belonging to e.g. the electron or γ band can be removed where the bands are well separated. For the likelihood method, the signal spectrum is included directly in the band fit.

3.5.1 Maximum Gap and Optimum Interval Method

The simplest and most conservative way of obtaining an upper limit on the interaction cross section in the presence of an unknown background is estimating the number of expected signal events in the experimental range, and then comparing to the observed number of events via Poisson statistics. Yellin methods improve this approach by considering the predicted shape of the signal energy spectrum. Figure 3.12 illustrates Yellin's maximum gap method: Between two observed events of energies E_i and E_{i+1}, there is a gap. The size of the gap is calculated by integrating over the recoil energy spectrum $\frac{dN}{dE}$. Following [108], the probability C_0 of the maximum gap of size $x_i = \int_{E_i}^{E_{i+1}} \frac{dN}{dE} dE$ being smaller than x is given by

$$C_0(x,\mu) = \sum_{k=0}^{m} \frac{(kx-\mu)^k e^{-kx}}{k!} \left(1 + \frac{k}{\mu - kx}\right), \tag{3.30}$$

where μ is the total expected number of events. m is the greatest integer smaller than μ/x. By adjusting the cross section σ and thus μ such that $C_0(x,\mu) = 0.9$, one can obtain an upper limit at 90% confidence level [108].

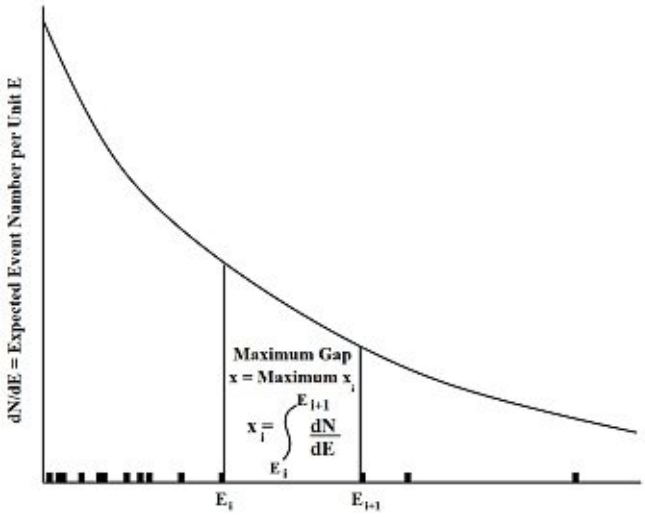

Figure 3.12: Exemplary recoil energy spectrum dN/dE for a cross section σ and Yellin's maximum gap. Figure taken from [108].

Since only one gap is used to find the upper limit in the end, the non-zero probability of fluctuations and thus of observing one event becomes a problem for large numbers of background events in a spectrum. This can be overcome by considering *optimum intervals* instead, such that the probability $C_n(x,\mu)$ that all intervals with $\leq n$ events have their expected number of events $\leq x$ becomes maximal. Effectively, this increases the statistics in the maximum

interval compared to the maximum gap. The upper limit now gives the cross section σ at which $C_{max}(x,\mu)$ is higher than would be expected from 90% of random experiments with that cross section in the absence of background [108] [109].

3.5.2 Accounting for Background: The Likelihood Approach

The likelihood function $\mathscr{L}$ gives the plausibility of a set of parameters θ for a given observation O. It is obtained from the probability function P by fixing the observed values and treating the parameters θ as variables. If $P(O|\theta)$ describes the probability of observing O, given θ, then:

$$\mathscr{L}(\theta|O) = P(O|\theta) \tag{3.31}$$

This is not to be confused with the posterior probability $P(\theta|O)$, which is the probability that the model θ is true, given an observation O. Maximizing $\mathscr{L}(\theta|O)$ such that $\mathscr{L}(\theta_{bf}|O) \geq \mathscr{L}(\theta|O)$ for each θ gives the best-fit model θ_{bf} for an observation O. For a set of measurements or datapoints O_i, the probability function P can be generalized, if they are assumed to be described by the same probability density function ρ:

$$\mathscr{L}(\theta|O) = \prod_{i=1}^{N} \rho(O_i|\theta). \tag{3.32}$$

In the most simple case, a normalized density is assumed, i.e. $\int \rho(O|\theta)dO = 1$, since a measurement will always yield some result. An extension of this model was proposed by Fermi, and motivated by Orear in 1958 [110]; this is the *extended likelihood model*. It allows the normalization to depend on the parameters, and introduces a penalty if the number of expected events ν for a given model θ deviates from the observed number of events. We consider infinitely small bins, such that only 0 or 1 events are observed in a bin Δx. Using Poisson statistis with an expectation value $\lambda = \rho(O)\Delta x$ for the two cases, and in the limit of infinitely small bins, we obtain

$$\mathscr{L}(\theta|O) = e^{-\nu} \prod_{i=1}^{N} \rho(O_i|\theta), \qquad \nu = \int \rho(O|\theta)dO \tag{3.33}$$

with the number of expected events ν. A detailed review of the method, and the cases where it is applicable, can be found in [111]. In most cases, the *log-likelihood* function $\ln(\mathscr{L}(\theta|O))$ is used, since it can be decomposed into summands, and has its maximum at the same value of θ because $ln(x)$ increases monotonously. Among other advantages, this avoids a multiplication of errors originating from limited machine precision. Numerically, minimizing

the negative log-likelihood function is easier than computing the maximum directly.

$$\ln(\mathscr{L}(\theta|O)) = \ln\left(e^{-\nu}\prod_{i=1}^{N}\rho(O_i|\theta)\right) = -\nu + \sum_{i=1}^{N}\ln(\rho(O_i|\theta)) \tag{3.34}$$

3.5.3 Confidence Levels

To assess the deviation of a given model $\theta_{excl} = m_\chi, \sigma_{\chi,excl}, \vec{\vartheta}_{excl}$ from the best fit value $\theta_{best} = m_\chi, \sigma_{\chi,excl}, \vec{\vartheta}_{excl}$ for a fixed mass m_χ, the *likelihood ratio* λ is defined

$$\lambda(m_\chi) = \frac{\mathscr{L}\left(m_\chi, \sigma_{\chi,excl}, \vec{\vartheta}_{excl}|O\right)}{\mathscr{L}\left(m_\chi, \sigma_{\chi,best}, \vec{\vartheta}_{best}|O\right)} = \frac{\mathscr{L}_{excl}}{\mathscr{L}_{best}} \tag{3.35}$$

According to Wilk's theorem, in the limit of an infinite number of measurements, the value $-2\ln(\lambda)$ is χ^2-distributed. Therefore,

$$q = \begin{cases} -2\ln(\lambda(m_\chi)) & \lambda > 0 \\ 0 & \lambda \leq 0 \end{cases} \tag{3.36}$$

is defined. A value q_{test} can now be compared to the values of a half χ^2 distribution $F_n(x)$, with n the number of degrees of freedom, to assess the probability of observing a test statistic which is at least as extreme. This is quantified by the p-value

$$p = \int_{q_{\text{test}}}^{\infty} F_n(q)\,dq. \tag{3.37}$$

The relevant χ^2 distribution here has only one degree of freedom ($n = 1$), since the only free parameter introduced by the signal hypothesis is the cross section.For example, if $q = 1.64$, this would correspond to a p-value of 10 %. Finally, to obtain the upper limit cross section σ_{excl} for a 90 % confidence level, i.e. a probability of 10 % to observe a higher cross section if σ_{best} is the true value,

$$\ln(\mathscr{L}_{excl}) = \ln(\mathscr{L}_{best}) - \frac{q}{2} \tag{3.38}$$

is used.

4 Data Analysis

This chapter describes analysis techniques which were applied to extract dark matter exclusion limits, as well as detector characteristics. Any analysis is based on a set of recorded pulses, which have to be extracted using a trigger condition. The raw data is then subjected to quality cuts, amplitude reconstruction, and energy calibration, and the combined energy information from the light and phonon channels is finally used to search for dark matter candidate events. In Section 3.3.6, the hardware triggering scheme which provides a first, preliminary dataset was introduced. It uses a hardware Bessel filter which allows the setting of a threshold trigger, with hardly any possibility of adaptation to a specific signal pulse shape; in addition, a software trigger is used in this work, which will be discussed in the following section.

4.1 Continuous Datastream

Historically, storing the complete datastream from each detector was unfeasible in CRESST due to the available electronic components. Instead, a hardware trigger was applied, and triggered pulses were stored, while the rest of the data were discarded. Consequently, if the threshold for a given channel was discovered to be not optimal after datataking, this could not be adjusted. In [112], this practice was complemented with the more modern approach of storing the complete stream, and the trigger condition was implemented in software instead of hardware. This means that the trigger threshold for each detector can be optimized after datataking with respect to a figure of merit - in this case, the rate of noise triggers, i.e. fluctuations of the baseline exceeding the threshold. A thorough description of the method can be found in [100]; an excerpt from the continuous datastream recorded with the phonon channel of module A in CRESST-III is shown in Figure 4.1.

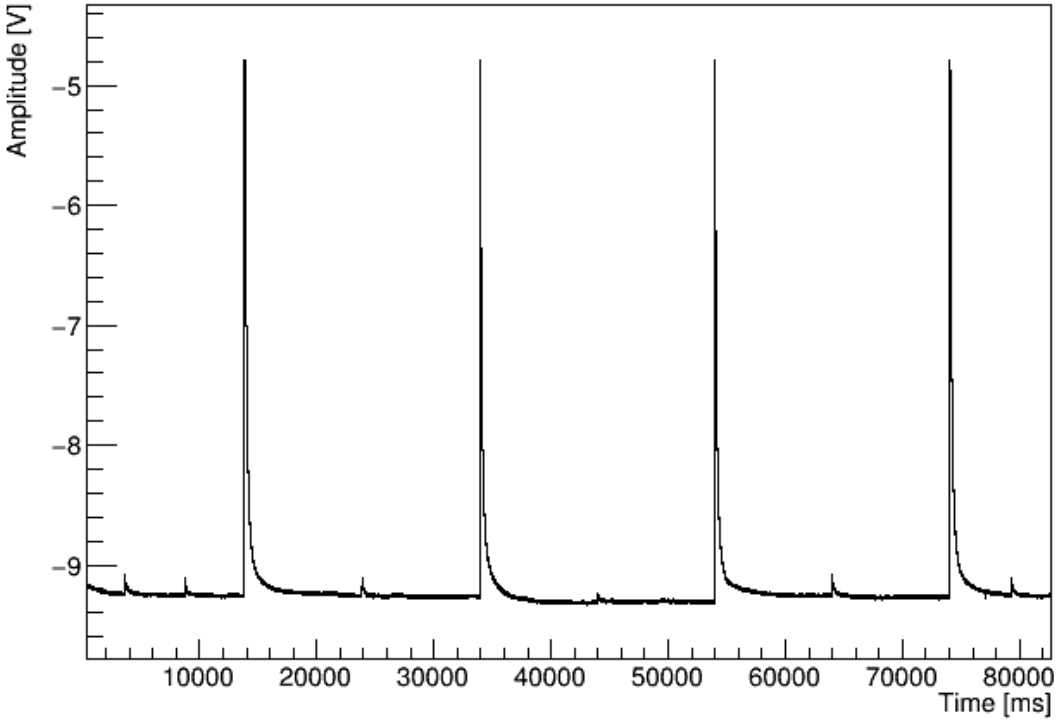

Figure 4.1: Excerpt from the continuous datastream of detector A in CRESST-III, Phase One. Heater pulses to control the detector operating point are periodically injected at intervals of 20 s; between them, smaller test pulses and particle pulses are visible.

4.1.1 Optimum Threshold Triggering

Instead of triggering on the raw stream, the optimum filter (cf. section 4.2.3) is used to obtain a filtered stream. A set of records is randomly drawn from the measuring period, and a threshold trigger is then applied to each (filtered) record. The number of triggered events is recorded as a function of different thresholds (cf. Figure 4.2).

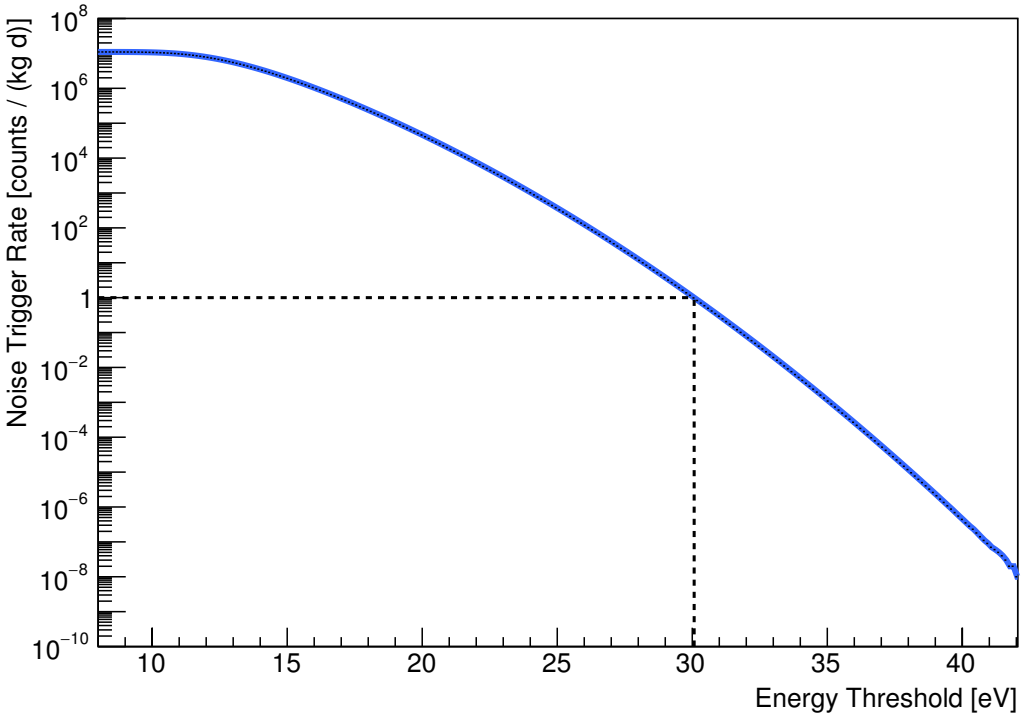

Figure 4.2: Number of observed noise triggers as a function of the chosen recoil energy threshold in eV for the phonon channel of detector A. The chosen threshold for one count per kgd is shown as a dashed line; it is 30.1 eV.

This measurement is used to set a threshold for a given number of noise triggers per time interval, which is chosen to be 1 noise count per kg and day. Instead of minimizing the number of noise triggers, a lower threshold could also be chosen and the method could be used to describe the expected number of such events analytically, and incorporate this into the likelihood formalism of section 3.5.2. Potentially, this could yield further sensitivity to low-mass dark matter particles. However, this work will explore the basic approach.
For all pulses extracted from the continous stream, the same readout window as for hardware-triggered pulses is used, i.e. 16384 samples.

4.1.2 Survival Probability - Continuous Stream Simulation

Since most of the stream is empty due to the low-background environment in the CRESST setup, the continuous datastream also provides a new way of determining the analysis efficiency, i.e. the probability of signal events surviving the analysis. By superimposing signal-like pulses onto the stream and processing the result in the analysis chain, all effects such as

removal due to quality cuts, random coincidences with muon panel events, test or control pulses, and pileup with other signal pulses can be accounted for, as well as effects from filtering, triggering and varying baseline conditions. The number of remaining events relative to the number of injected events then gives the *survival probability* for signal events, which can even be studied after each analysis step. Figure 4.3 illustrates the method for detector E in CRESST-III, Phase One, and shows the surviving fraction of signal events after analysis cuts as a function of injected energy. A discrete set of amplitudes was simulated. The applied analysis cuts are explained in detail in section 5.3.

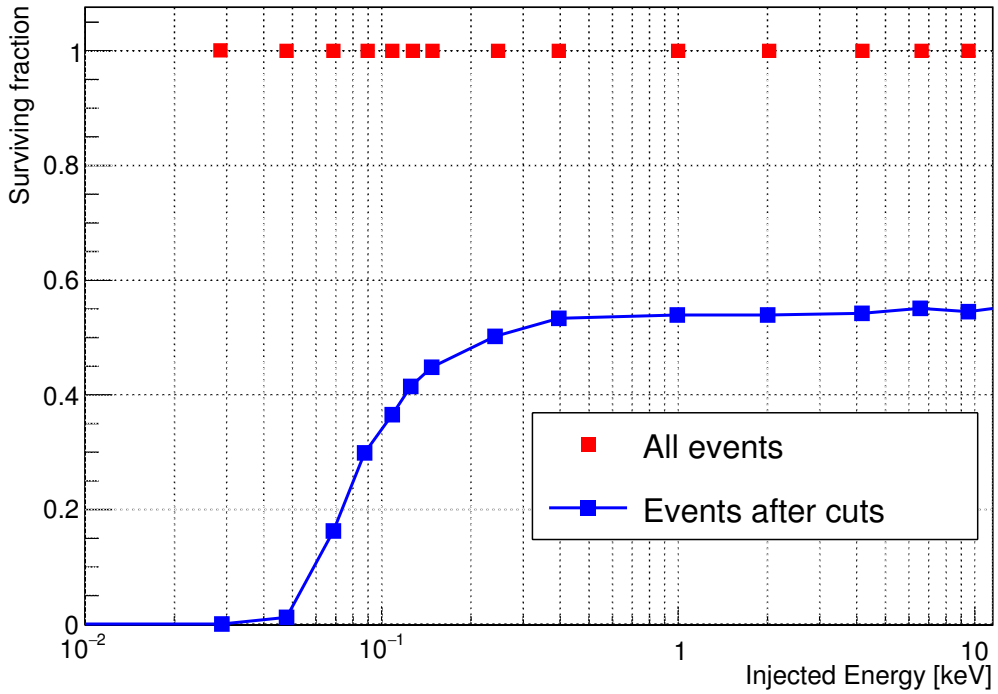

Figure 4.3: Survival probability for simulated signal events in detector E in phase one of CRESST-III after analysis cuts. A discrete set of amplitudes was injected, and the number of events surviving was normalized to the number of simulated events for each amplitude.

Traditionally, the survival probability was evaluated using a set of hardware-triggered empty baselines, which had limited statistics due to the fact that each empty baseline increased the effective detector dead-time - usually, one empty baseline was recorded per 10 minutes of measuring time. The amount of simulated events on the continuous stream is chosen such that events do not overlap, i.e. the length of the record window determines the statistics. Removing this constraint would decrease reconstruction efficiency due to pile-up.

4.1.3 Modeling of Expected Recoil Energy Spectrum

So far, an analytic description of the expected energy spectrum for nuclear recoils dN/dE was considered in Section 3.2. The calculation of upper limits requires integration over spectra convolved with the detector resolution; using a simulated spectrum requires less assumptions though it is computationally more expensive. Obviously, the recoil spectrum depends on the dark matter particle mass and interaction cross section; a simulation on the continuous stream thus has to be performed for each given mass and cross section. In [113], a flat energy spectrum was simulated, and later reweighted according to different signal expectations. The reconstructed energy spectrum already includes the detector resolution. It was shown in [113] that both methods, i.e. an analytic Gaussian description of the detector resolution and the simulation of a continuous energy spectrum, yield compatible results. In this work, the same continuous spectrum simulation is used for one detector module, while an analytic model with a discrete simulation only for the survival probability is used for the others.

Simulation and Energy Reconstruction

The energy reconstruction in a given analysis chain assigns a corresponding energy to the measured pulse height for particle events; conversely, it also assigns a corresponding pulse height for a given energy in case of a simulation on the stream. This means that a different reconstructed energy will be assigned to the same simulated event when processed in a different analysis chain - in particular, if a different standard event (cf. Section 4.2.1) is used for reconstruction than was used for simulation.
Consider the case of a flat energy spectrum discussed before: If only a finite set of energies and thus amplitudes is simulated to sample the spectrum, each amplitude will be reconstruced at an energy different from the original (simulated) one, but interpolation can be performed and the resulting spectrum is still flat. If a continuous energy spectrum was simulated on the other hand, the conservation of the spectral shape is not guaranteed. If events are to be reweighted, differences beween the expected spectrum before cuts in the new analysis chain and the original simulated spectrum must be accounted for. This will be discussed in detail in Section 5.9.

4.2 Energy Reconstruction

In order to determine the deposited energy of a cryogenic detector event, two steps are necessary: Firstly, an amplitude estimator has to be defined for the pulse, and secondly, the conversion function from this estimator to the deposited energy has to be obtained. This factor may be derived from either dedicated calibration measurements, or from peaks of known origin which appear in the energy spectrum (cf. Section 4.3). In addition, injected heater pulses with known amplitudes are used to adjust for small variations of the detector response with time.

4.2.1 Standard Event Fit

Standard event fitting is a straightforward approach to amplitude estimation, and is well-established in cryogenic particle detection experiments. The procedure described here follows [114]. Pulses originating from the same event type (e.g. nuclear recoil) are assumed to feature the same pulse shape, where the height of the pulse changes with the deposited energy. The energy for a given pulse can thus be obtained via a fit of this defined pulse shape or *standard event* (SEV), where the scale is a free parameter. SQUIDs do not feature a constant stable baseline, but can change between a number of discrete states, if the deposited energy in an event is high enough ("flux quantum loss"); therefore, a model for the baseline of each individual pulse also has to be defined. In this work, a combination of a constant and a linear term is used. Mathematically, the fit is then carried out in two steps: Shifting the standard event to the onset of the pulse, and scaling. In both steps, the best agreement is found by minimizing the RMS between standard event samples and pulse samples.

Truncated Fit

If the signal in the TES starts to saturate, (cf. section 3.3.5), the pulse shape of a given event type changes, until complete saturation is reached. To guarantee the linearity of the standard event fit amplitude as an energy estimator, only a subset of the pulse is used for fitting. This subset consists of samples with voltages above the baseline, but below a certain *truncation limit*; more specifically, the pulse range between the first and the last sample above the limit is discarded. Figure 4.4 shows a pulse with saturation effects to which the method was applied, using a standard event for this channel.

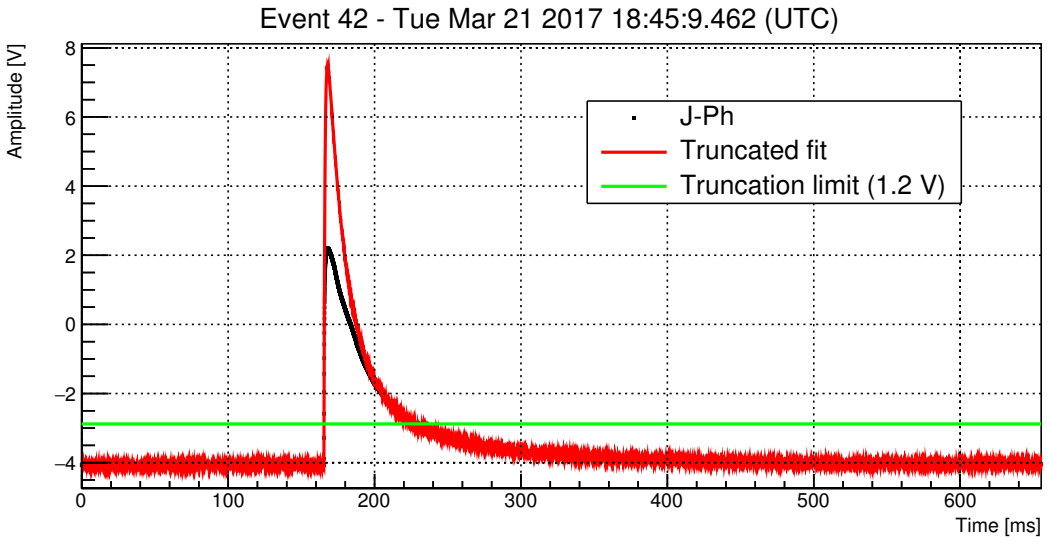

Figure 4.4: Example for a truncated fit in the phonon channel of detector J. The black pulse shows saturation effects and was fitted with the standard event (red) corresponding to the signal pulse shape. The truncation limit for this channel is 1.2 V, and is indicated by a green line.

Below the truncation limit, the pulse shape is assumed to be still consistent with the fitted standard event. The truncation limit is usually determined by a first untruncated fit to injected heater pulses, and a subsequent comparison of injected and reconstructed amplitude. This is illustrated in fig. 4.5. The value in reconstructed amplitude at which this relation starts to become nonlinear gives the truncation limit for each detector. As the result of the fit remains the same for pulses of low energies which completely lie below the truncation limit, an approximate determination of the limit is sufficient if one is mainly interested in the low-energy range. In this work, reconstructing the medium to high energy range is only necessary to observe calibration peaks and extract approximate calibration factors. A possible way to quantify the nonlinear behavior is given in Figure 4.6, where a truncation limit of 0.56 V is shown to correspond to a relative difference between the reconstructed amplitude and a linear model of 5 %. Using Figure 4.5, one would estimate this value 'by eye' to be around 0.6 V. The advantage of truncated fitting is the ability to reconstruct energies in spite of saturation, and thus cover a larger energy range.

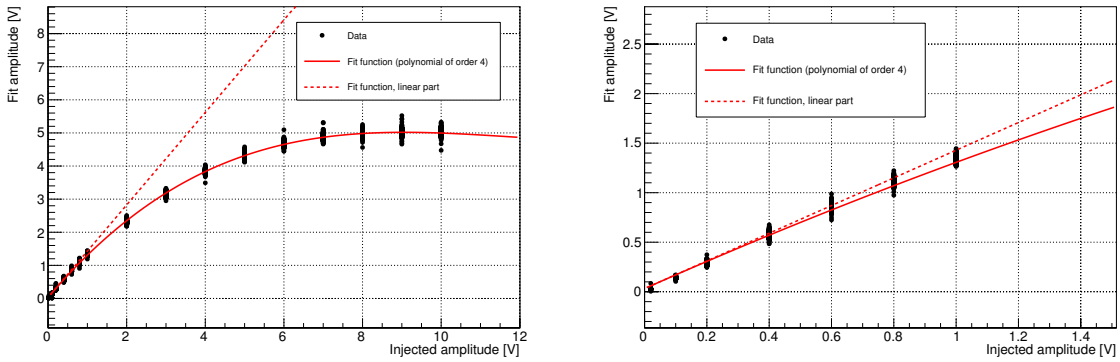

Figure 4.5: Resulting reconstructed amplitude from an untruncated fit of injected heater pulses versus injected amplitude for the phonon channel of module B (CRESST-III, Phase One); From the zoomed version on the right side, it is evident that for pulse heights below ~0.6 V, the relation between the two quantities is still linear.

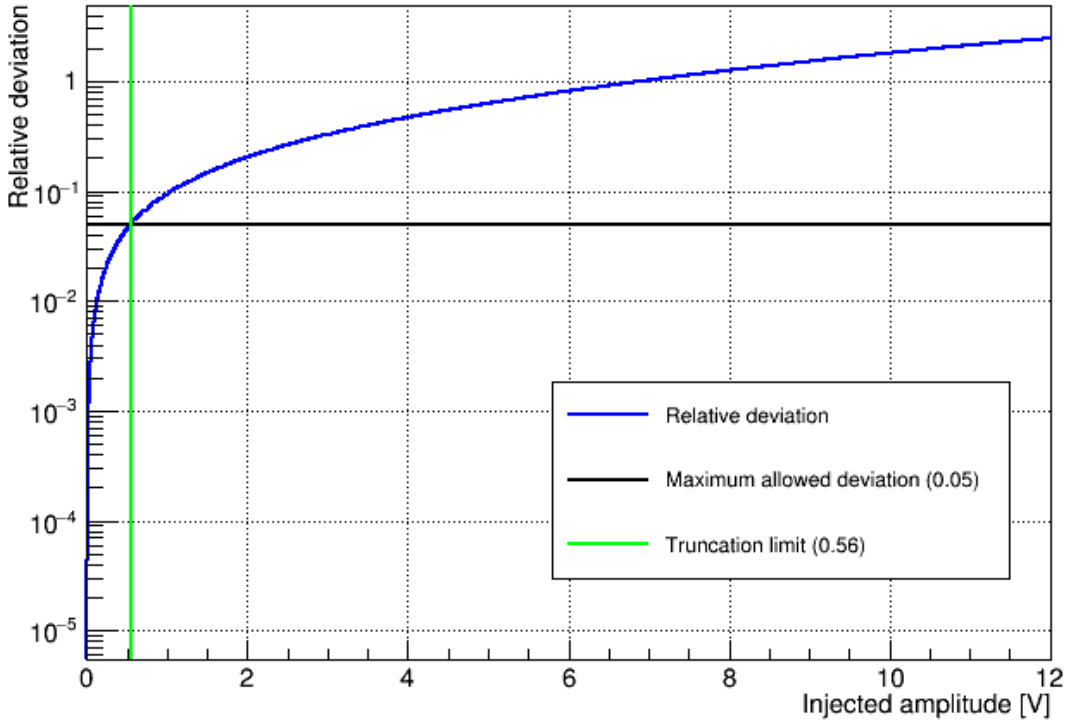

Figure 4.6: Extraction of a truncation limit for the phonon channel of detector B (CRESST-III, Phase One); the blue curve describes the relative difference between the fit function in Figure 4.5 and the linear part of that function. If a maximum deviation of 5 % is allowed, the resulting truncation limit is 0.56 V.

Figure 4.7 highlights two problems of the fitting method. Firstly, determining the onset of a pulse becomes impossible, if the number of samples in the rising flank which lie below the truncation limit is too small. Since the sampling frequency always stays the same, pulses of higher voltage and thus higher energy are more affected due to a steeper flank. This effect prevents amplitude reconstruction for high-energy pulses. An intuitive solution is a separate determination of the onset from the untruncated pulse, followed by a truncated fit with a fixed onset. However, this approach worsens the energy resolution at medium energies, where enough samples from the rising flank below the truncation limit are available. In Section 4.2.6 and 5.5, it is shown that the energy resolution for the phonon channel is anyhow determined by the optimum filter energy reconstruction; therefore, the effect due to the two-step fitting will be neglected in this work. The second problem of truncated fitting is remnant noise of the standard event. Since the standard event is created by averaging pulses (see next section) and scaled linearly during the fit, a mismatch between the scaled noise and the real noise occurs for pulses above a certain amplitude, because the real noise does not scale linearly with the pulse amplitude. In Figure 4.7, this effect is already well visible. It implies a scaling of the fit RMS with the pulse amplitude, which is illustrated in Figure 5.8 in section 5.3.3. While this obviously reduces the pulse shape discrimination power at high energies, it is in particular a problem when using scaled standard events for a signal simulation, as discussed in Section 4.1.2.

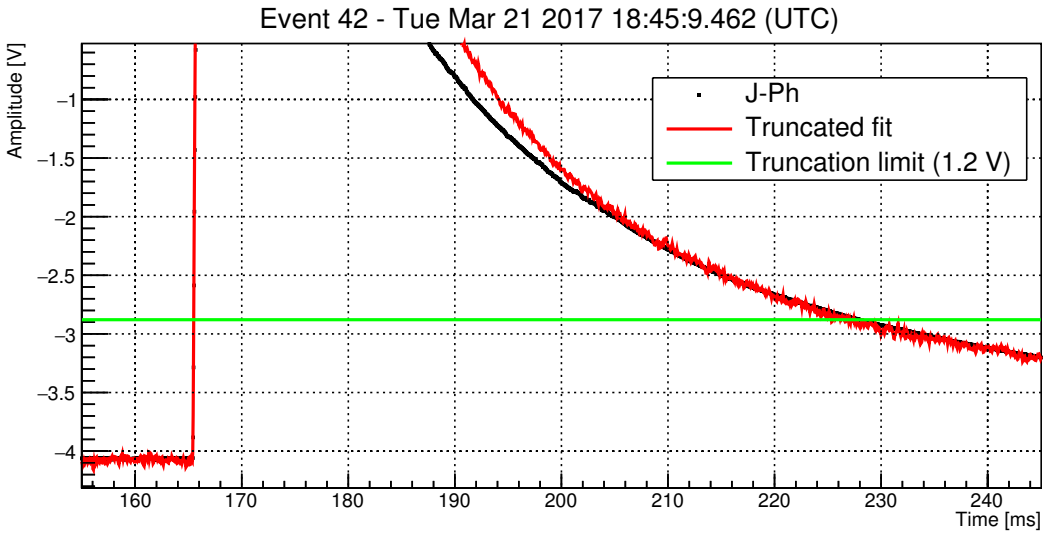

Figure 4.7: Zoomed version of Figure 4.4. Only two samples of the original pulse below the truncation limit are used by the fit to determine the onset; scaled noise on the standard event is visible.

Creation of Standard Events

For the creation of a standard event, a set of pulses is selected which is assumed to contain only one class of events. This sample is subsequently cleaned and its pulses are averaged, after a linear baseline model was subtracted, determined from the pre-trigger range of each pulse. If the events can safely be assumed to be monoenergetic, i.e. if they originate from a peak in the spectrum, unweighted averaging is sufficient; otherwise a weighting is necessary. Obviously, this needs another energy estimator, which is usually the result of a maximum search performed on a smoothed pulse; here, this raw pulse height is determined via a 50 sample running average. The averaged pulse will feature an increased signal-to-noise ratio compared to a single pulse, since baseline components without any phase relation to the signal are washed out. However, this is only true as long as they are unable to influence the relative position of the pulse in the record window, i.e. their amplitude lies below the trigger threshold. In this work, all standard events were created using a low-energy region of the respective detector below the truncation limit, where the observed background spectrum is flat. This results in reduced statistics of only $\sim 20-50$ original events and thus a larger noise scaling effect than in previous CRESST iterations, where observed γ peaks could be used. For the phonon channels, nuclear recoil events from an AmBe neutron calibration were used, while electron recoil events were used for the light channels. Different datasets will be discussed in Section 5.1. Each standard event is scaled such that its maximum amplitude is at 1 V.

4.2.2 Parametric Description

Apart from the empirical approach via a standard event, the pulse shape recorded by the TES can also be described in an analytic way [96]. In this model, initial high-frequency ($\sim$ 1.5 THz) *non-thermal* phonons are considered, which are successively converted into *thermal* phonons ($\sim$ 300 GHz). Signal contributions from both components are described with one amplitude parameter and one characteristic decay time each (A_n,τ_n and A_t,τ_t, respectively). The additional parameter τ_{in} describes a characteristic time constant of the thermometer itself depending on its dimensions and material and, most importantly, on the absolute temperature.

$$\Delta T(t) = \Theta(t-t_0)\left[A_n\left(e^{-\frac{t-t_0}{\tau_n}} - e^{-\frac{t-t_0}{\tau_{in}}}\right) + A_t\left(e^{-\frac{t-t_0}{\tau_t}} - e^{-\frac{t-t_0}{\tau_n}}\right)\right] \tag{4.1}$$

Here, $\Delta T(t)$ is the temperature rise relative to the heat bath, and t_0 is the onset time of the pulse. Apart from this model for a TES operated in *bolometric* mode, i.e. measuring the flux of non-thermal phonons ($\tau_{in} << \tau_n$), a *calorimetric* model measuring energy can also be defined:

$$\Delta T(t) = \Theta(t-t_0)\left[A_n\left(e^{-\frac{t-t_0}{\tau_{in}}} - e^{-\frac{t-t_0}{\tau_n}}\right) + A_t\left(e^{-\frac{t-t_0}{\tau_t}} - e^{-\frac{t-t_0}{\tau_n}}\right)\right] \tag{4.2}$$

The latter describes a case in which the rise time and amplitude of the fast component A_n are defined by the heat capacity of the thermometer and the absorbed energy. Both operating modes can be realized via a modification of τ_{in}. CRESST-III TESs are operated in calorimetric mode.

4.2.3 Optimum Filtering

The method of *optimum filtering* or *Gatti-Manfredi filtering*, reported first in [115], is another approach to energy estimation. It is frequently used in similar cryogenic experiments, e.g. [116], and provides a superior energy resolution. Any time series $v(t)$ can be expressed as a fourier backtransformation

$$v(t) = \frac{Q}{2\pi}\int_{-\infty}^{\infty} \mathscr{H}(i\omega)\mathscr{S}(\omega)e^{i\omega t}d\omega, \tag{4.3}$$

with the fourier transform $\mathscr{S}(\omega)$ of the signal $S(t)$ and the transfer function $\mathscr{H}(i\omega)$. Q is a normalization constant. In [115], it was shown that an optimal signal-to-noise ratio at the time of measurement t_m is achieved, if

$$\mathscr{H}(i\omega) = K\frac{\mathscr{S}^*(\omega}{\mathscr{N}(\omega)}e^{-i\omega t_m}, \tag{4.4}$$

where $\mathscr{N}(\omega)$ is the *noise power spectrum* (NPS) of the baseline, and K is another normalization constant. An NPS is obtained through addition of fourier-transformed baselines in fourier space, yielding a frequency histogram with a resolution determined by the sampling frequency of the original baselines.

Creation of Filters

If the signal $S(t)$ is assumed to be a multiple of a known pulse shape $S_0(t)$, i.e. $S(t) = a \cdot S_0(t)$, the filter $\mathcal{H}(i\omega)$ can be built from the fourier transform of $S_0(t)$. Each measured pulse is then fourier transformed and multiplied by the filter kernel; the backtransformation and comparison to the result for the original standard event yields the amplitude a. This is the same scaling which was assumed for the standard event fit in the previous section, therefore the fourier transform of the standard event is used in combination with the noise power spectrum to obtain an optimum filter for each detector. The constants Q and K are adjusted such that $a = 1$ for the original standard event. For simplicity, the time of the pulse maximum is set to 0. Figure 4.8 shows a standard event before and after the filter has been applied; Figure 4.9 shows the corresponding filter kernel in the frequency domain, and the representation of the standard event is given in Figure 4.10.

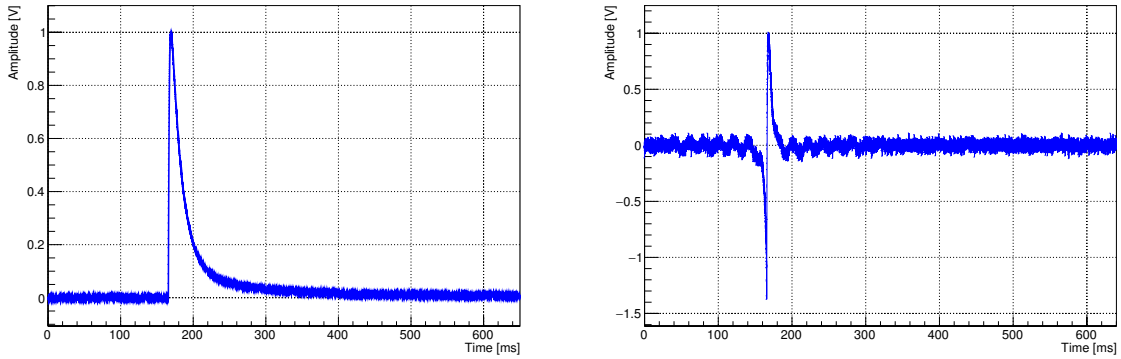

Figure 4.8: Standard event for the phonon channel of detector A before and after the filter kernel has been applied. The filter was scaled such that the resulting amplitude of the filtered standard event equals 1 V.

It is important to note that the description of the signal component in fourier space is only a good approximation as long as the pulse shape is not energy-dependent - it is in particular not valid for pulses suffering from saturation effects of the detector. This implies a linear relation of filter amplitude to energy only for pulses below a certain limit, which ideally corresponds to the truncation limit of the truncated fit. While the optimum filter method provides a superior energy resolution compared to truncated fitting thanks to the "removal" of the baseline, its linear range is therefore significantly smaller. In Section 4.2.6, it is shown that a combination of both methods is possible and yields a good result, i.e. features superior energy resolution as well as a larger dynamic range compared to the optimum filter alone.

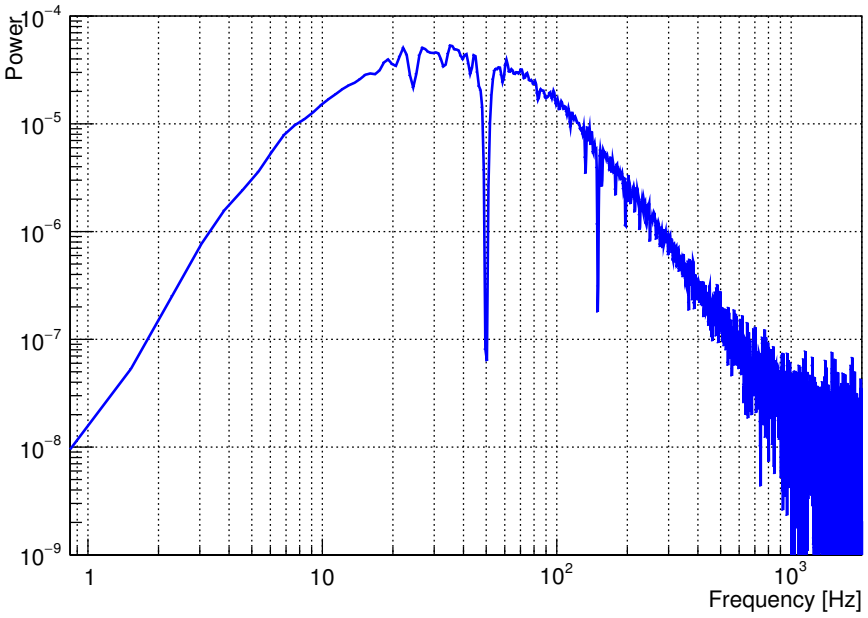

Figure 4.9: Optimum filter kernel for the phonon channel of module A in CRESST-III, Phase One. Prominent noise frequencies such as 50 Hz are removed.

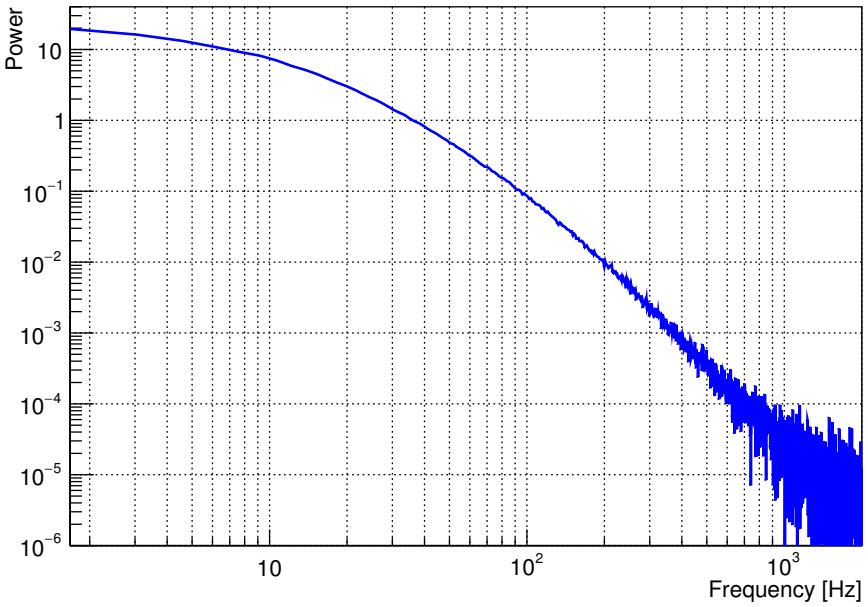

Figure 4.10: Representation of the standard event for the phonon channel of detector A in Fourier space; the frequency spectrum is used in combination with the noise power spectrum to obtain the filter kernel.

4.2.4 Description of Detector Response with Test Pulses

Using heater pulses with a defined input energy, which is linearly proportional to a set voltage due to the square rooter in the electronic circuit (see Section 3.3.6), small variations of the detector response with time can be corrected for, if we assume that the reconstructed height of these test pulses scales in the same way as the height of particle pulses. This is a reasonable assumption as long as the pulse shape remains constant with respect to injected energy, or if a truncated fit is used to reconstruct the amplitude. In practice, the reconstructed test pulse amplitude is mapped to the injected one using a separate spline for each (constant) injected amplitude, which describes the time dependence of the detector response for this amplitude only. Figure 4.11 illustrates this concept for seven different amplitudes; the smoothing is implemented via a Gaussian kernel with a width of 0.5 h, where the typical interval between two test pulses of the same injected amplitude is approximately 38 min.

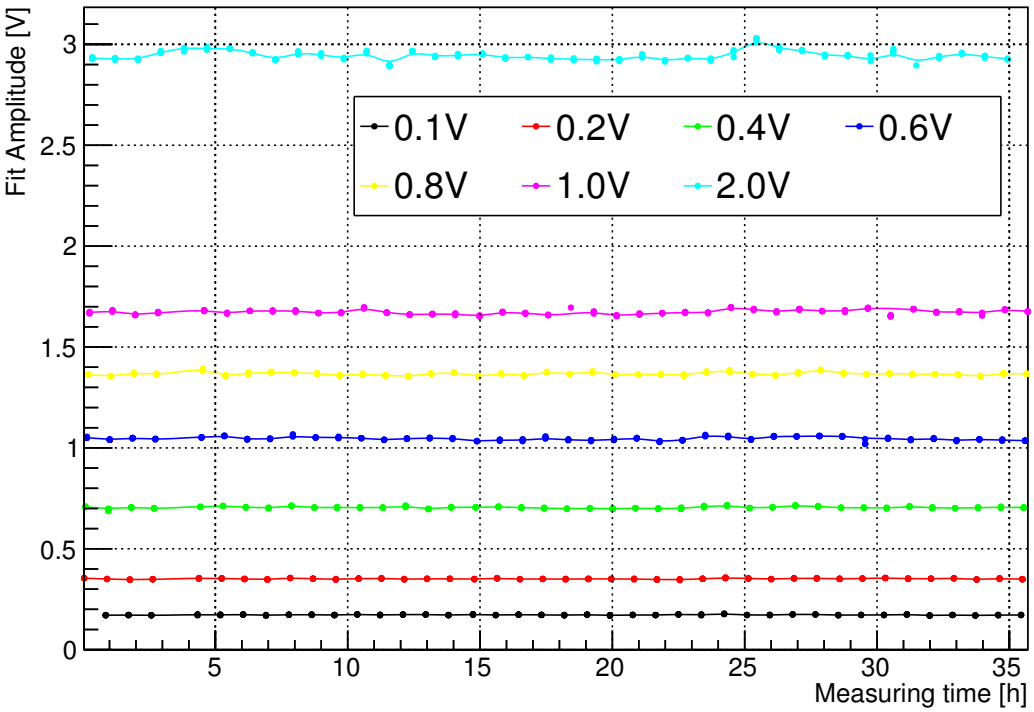

Figure 4.11: Reconstructed test pulse amplitude (fit) as a function of time in a continuous measuring interval. Pulses in the phonon channel of detector A from the training dataset in CRESST-III were used. Each injected amplitude (indicated in the legend) is described by a spline which was created using a Gaussian kernel with a width of 0.5 h.

For a measured particle event, each test pulse spline is then evaluated at the measured time, and an interpolation is performed which yields the *transfer function* at the time of the particle event. This function can then be evaluated at the reconstruced particle event amplitude to obtain the test pulse equivalent amplitude. Figure 4.12 shows the procedure for a set of four points representing the evaluated test pulse splines, and two different transfer functions: A cubic spline interpolation and a polynomial of order two. The impact of different choices will be discussed in the next section.

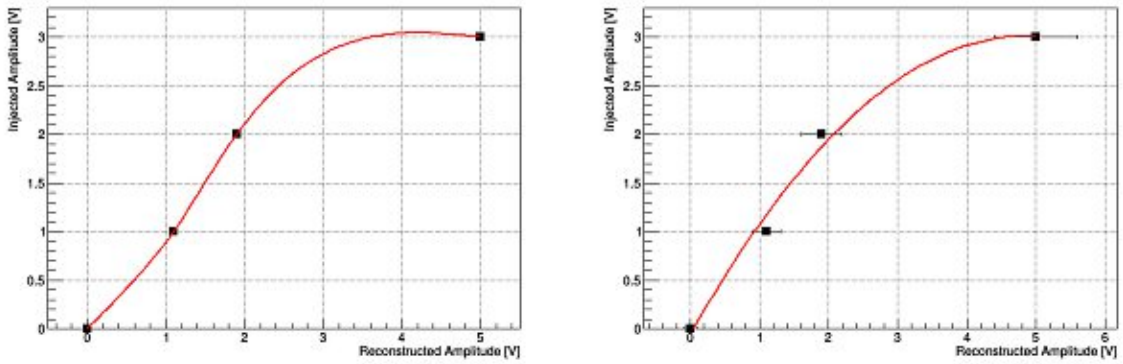

Figure 4.12: Left: Cubic spline interpolation for an arbitrary set of four points; no uncertainties are taken into account by the method. Between 2 V and 3 V injected amplitude, this approach yields an unrealistic transfer function, and a linear interpolation would give a better result; Right: Function interpolation (second degree polynomial) for the same points. Exemplary reconstruction uncertainties of 15 % are indicated and were taken into account by the fit.

In this way, a spectrum in test pulse equivalent amplitude is obtained, as displayed in Figure 4.15. An important effect of this method is the implicit second linearization step, as well as further enhancement of the dynamic detector range; this is due to the information about the injected voltage for each recorded test pulse. As the energy scale of a detector is not known a-priori, injected test pulse heights have to be chosen carefully in order to overlap with the linear range for particle events; this optimization step has to be performed at the beginning of each measurement campaign in CRESST.

4.2.5 Transfer Function

As described above, an interpolation between the results of the different test pulse splines has to be performed at the measuring time of a particle event. This transfer function can be obtained either via a polynomial fit or spline interpolation. Both methods including their advantages and disadvantages are briefly discussed here, and examples are shown in Figure 4.12. The differences between both methods are also well visible in Figure 4.13, which shows results for a continuous measuring interval from the neutron calibration of detector A in CRESST-III, where the number of entries is color-coded logarithmically. The reconstructed energy was obtained via spline interpolation. An exemplary evaluation of the test pulse splines at $t = 0$ and a linear extrapolation to higher energies from the two highest injected amplitudes shows a good agreement between the extrapolation and the spline result. When comparing both to a polynomial fit of ninth order, the latter shows an unrealistic extrapolation .

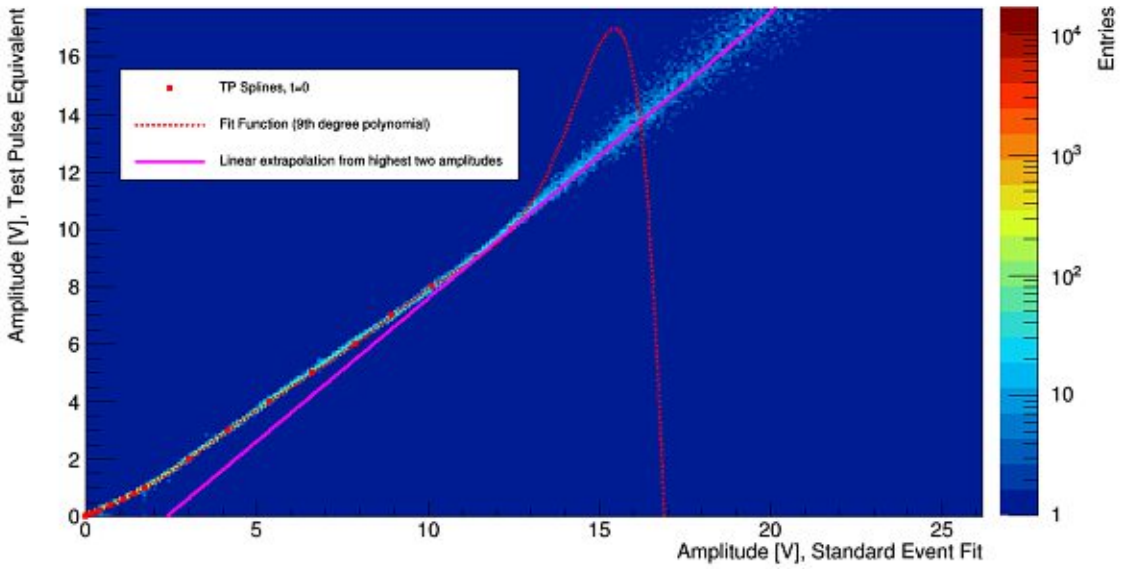

Figure 4.13: Obtained test pulse equivalent amplitude (y axis) for e^-/γ and neutron-induced events from the neutron calibration dataset of detector A (phonon channel) in CRESST-III, Phase One; spline interpolation was used. Red dots show exemplary reference values from test pulse splines evaluated at the beginning of the dataset. For comparison, a polynomial fit to these values is shown (red dashed line), and an extrapolation only using the two highest injected amplitudes is displayed in solid violet.

Polynomial Fit

A polynomial fit is less sensitive to outliers, i.e. large variations in the reconstructed amplitude for a given injected amplitude, than a spline interpolation, and uncertainties can be included for each injected amplitude. Additionally, deviations from the ideal, linear behavior can be somewhat quantified by the coefficients of the polynomial terms. The obvious disadvantage is the behavior of the polynomial outside the fitted region; here, the linear term is not even dominant anymore and the description of the detector response is not adequate.

Spline Interpolation

If spline interpolation is used to model the detector response, the border region features of a polynomial are avoided, and the transfer function model has less features. Less bias is introduced since no explicit functional model is assumed. This comes at the cost of higher sensitivity to outliers in reconstructed amplitude. Figure 4.13 illustrates that this approach is useful for extrapolation to high amplitudes. If the number of reference points is too low, a spline will yield unphysical results, just like a polynomial with too many degrees of freedom; This is demonstrated in Figure 4.12.

From Figure 4.13 it follows that spline interpolation yields a relatively robust result in the presence of sufficient points; it is therefore used as the standard transfer method in this work.

4.2.6 Conversion of Filter Amplitude to Standard Event Fit Amplitude

The optimum filter amplitude corresponds to the raw pulse height only in the very low energy region (linear region). If a measured pulse starts to saturate, the difference between the optimum filter amplitude and the measured pulse height will increase, as well as the difference between the optimum filter amplitude and the standard event fit amplitude of the same event. This becomes a problem if one wants to use fitted test pulses to describe the response of the detector as a function of time: While the fitted amplitude of test pulses scales in the same way as the fitted amplitude of particle pulses, this relation does not apply for the respective filter amplitudes due to the different pulse shapes. To circumvent this problem, the amplitude from the filter is first converted to an equivalent standard event fit amplitude before the test pulse information is included. From the neutron calibration, neutron-induced nuclear recoil events are selected and their standard event fit amplitude

is plotted as a function of the obtained trigger filter amplitude. A polynomial of ninth order is fitted to describe the conversion function (Fig. 4.14). This polynomial is then evaluated for all events in the background dataset. Above a certain filter amplitude value, a conversion is not possible anymore and the converted amplitude becomes meaningless. The resulting maximum values are given in section 5.5 for the phonon channel of each analyzed module.

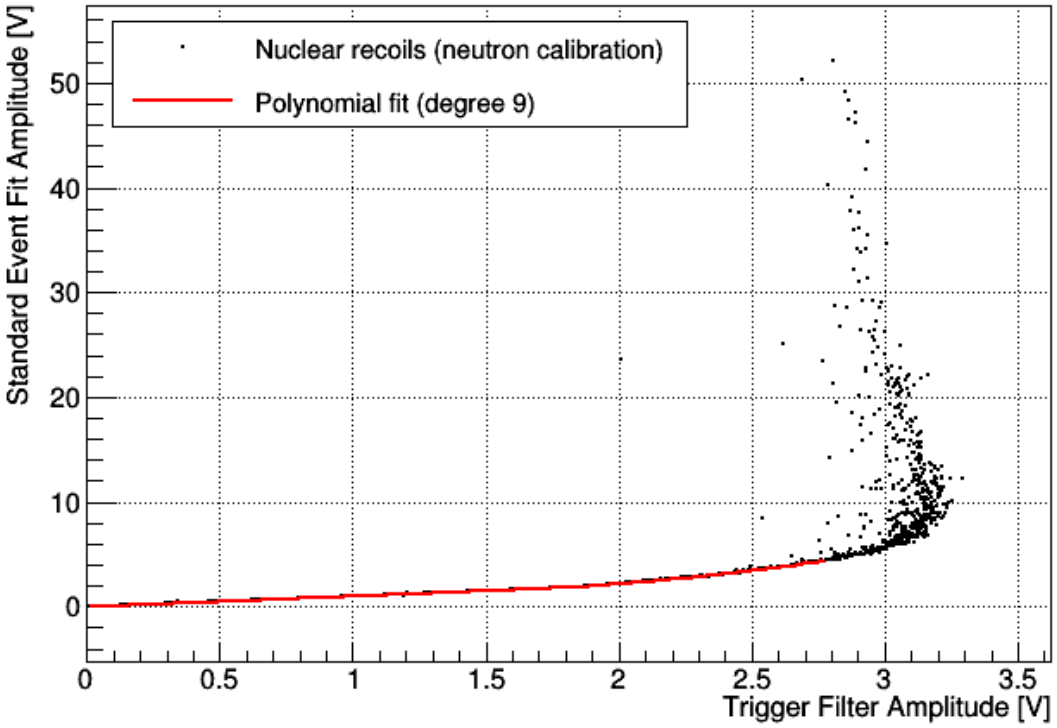

Figure 4.14: Conversion of filter amplitude to equivalent standard event fit amplitude for the phonon channel of detector E. Data from the neutron calibration of detector E was used, and the displayed events have been selected from the nuclear recoil bands. On the right, the energy cutoff is visible as the upper limit of the polynomial fit range (2.7 V).

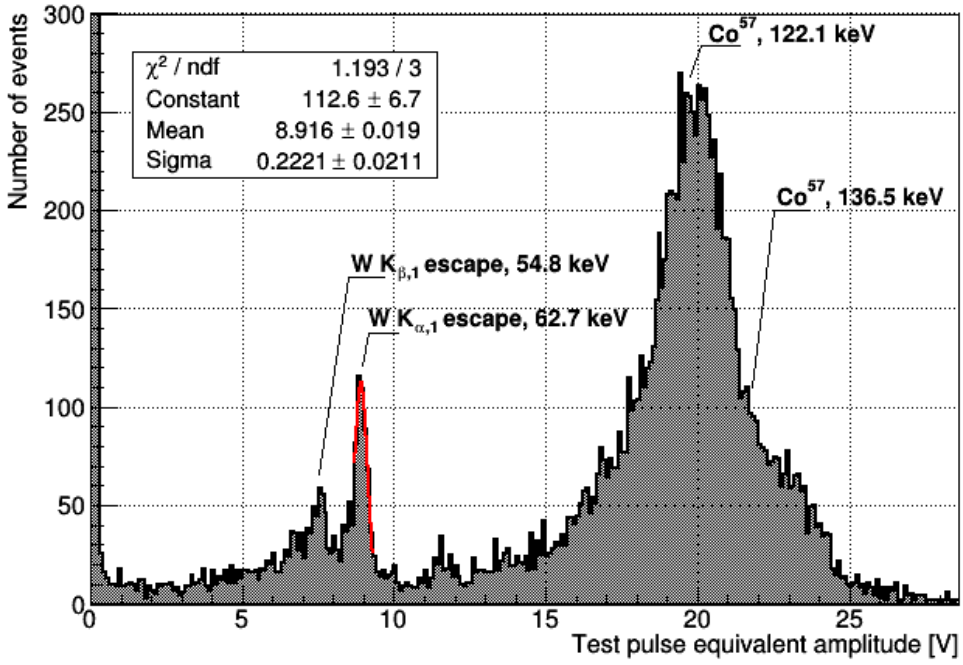

Figure 4.15: Spectrum from a Co^{57} γ calibration of detector A in equivalent test pulse amplitude; the energy scale could be inferred from the location of the known peak at 122 keV, or the W $K_{\alpha,1}$ and $K_{\beta,1}$ escape lines. An exemplary fit is shown for the $K_{\alpha,1}$ escape line (E=62.7 keV). The Gaussian-like, right side of the peak is used.

4.3 Obtaining the CPE Factor

In the last step, the spectrum in equivalent injected test pulse amplitude has to be scaled with the correct factor (denoted "Convert Pulse Height to Energy (CPE) factor" in accordance with previous CRESST work). From a Co^{57} calibration measurement, a first approximate value of the CPE factor is extracted using the positions of two 62.7 keV and 54.8 keV γ escape lines. These originate from 122 keV γs emitted by the Co^{57} source causing $K_{\alpha 1}$ and $K_{\beta 1}$ transitions in W, where the shell transition energy is lost. To allow for an energy reconstruction at these high energies, the use of the standard event fit amplitude instead of the optimum filter amplitude is necessary. As the resulting factor is only used as a first estimate, the difference between the two energy estimators is not crucial here. A fit to the $K_{\alpha 1}$ escape line is shown in Figure 4.15, which yields a conversion factor of 62.7 keV/8.916 $V_{inj,eq} \approx 7.93 \frac{keV}{V_{inj,eq}}$. Since these lines are usually already far above the linear range of a CRESST-III type phonon channel, the CPE factor is corrected by the position of a known low-energy γ line present in the background dataset which originates from cosmogenically activated ^{179}W (cf. Section 5.13.2).

4.4 Resolution Measurement with Test Pulses

Another use of heater pulses is the determination of the detector resolution. An example of this is shown in Figure 4.16, which displays the standard deviation in fit amplitude as a function of injected test pulse voltage for the phonon channel of detector A in CRESST-III, Phase One. This gives a rough estimate of the resolution as a function of energy, and the relation is approximately linear, implying that the relative resolution remains roughly constant. Figure 4.17 shows the converted filter amplitude for a test pulse injected near threshold; this method can be used to obtain the resolution at "zero" amplitude, and gives a value of ~1 mV. It is a more accurate result than the fit function from Figure 4.16, which gives roughly ~0.5 mV. Therefore, using an extrapolation results in an underestimation of the resolution.

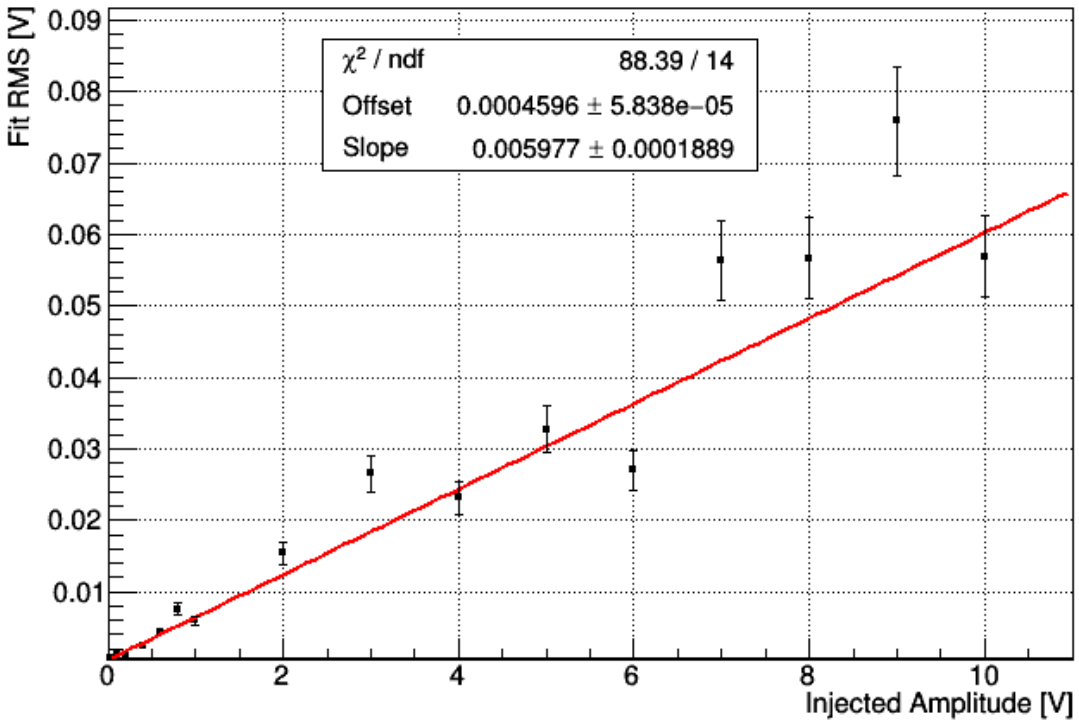

Figure 4.16: Standard deviation in fit amplitude for different injected test pulses for the phonon channel of detector A. One continuous measuring interval from the neutron calibration dataset in CRESST-III, Phase One was used. The red line is a linear fit function.

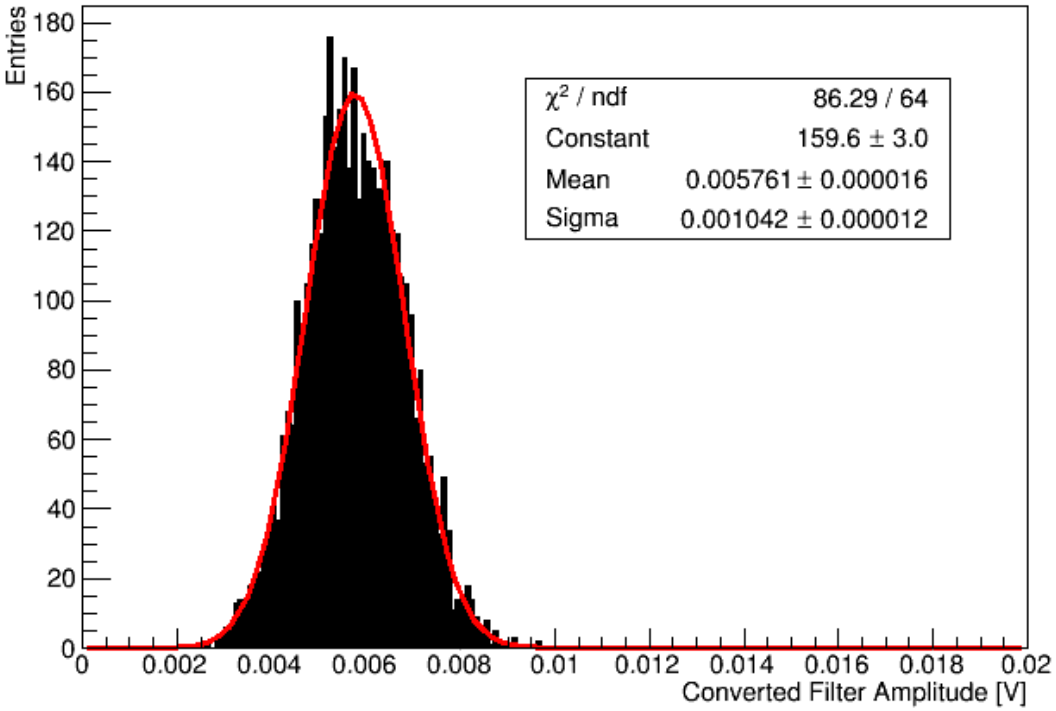

Figure 4.17: Extraction of the detector resolution for an injected test pulse with an amplitude near threshold in A-Ph. The filter amplitude was used and converted to an equivalent standard (particle) event fit amplitude; the resulting distribution was fitted with a Gaussian function, and its width gives the resolution in V.

4.5 Phonon Energy versus Total deposited Energy

In Section 3.4, the recoil band description along with a signal expectation and background model were motivated for the light yield versus E plane, where E is the total energy of an event. In a calorimetric measurement, energy which cannot be converted to scintillation light must remain in the phonon channel. This implies that for nuclear recoils, the relative amount of energy remaining in the phonon channel will be higher than for e^-/γ events. If the energy deposited in the phonon channel is used to approximate the total deposited energy, this means that nuclear recoil energies will be slightly overestimated, since the energy scale is calibrated to events in the e^- band. The total, event-type-independent deposited energy is defined using the following correction:

$$E = \eta E_l + (1-\eta)E_p = [1-\eta(1-LY)]E_p. \tag{4.5}$$

E_l and E_p are the energies measured in the light and phonon channel, and η describes the relative amount of produced scintillation light. In a previous phase of CRESST, $\eta \approx (6.6 \pm 0.4)\,\%$ was determined via a visible tilt of calibration γ lines in the LY-E_p plane [117]. For the present phase, the known lines from the Co^{57} calibration campaign as well as their corresponding W escape peaks lie well above the linear range of the detectors and extremely low statistics in the cosmogenically induced Hf lines (cf. Section 5.13) do not permit any determination of η. Since an overestimation of the phonon energy effectively reduces the sensitivity for low-mass dark matter by shifting the measured recoil spectrum to higher energies (cf. Section 3.2), it results in a more conservative dark matter exclusion limit (see also Section 5.11.4). The above correction is therefore not applied and the corresponding effect on the total deposited energy of an event is neglected.

5 Results - CRESST-III, Phase One

From the first data taking campaign of CRESST-III, four modules are selected which were shown [112] to exhibit a nuclear recoil energy threshold near the design goal of 100 eV: These modules are A, B, E, and J. In the following sections, phonon and light detectors of each module are denoted via the suffixes "-Ph" and "-L", respectively.

5.1 Datasets Used

Three different datasets have been processed for this work: An AmBe neutron calibration, a ^{57}Co γ calibration, and a background dataset without any source present. Approximately 20 % of the background data were used as a training set to define cuts and fix the energy calibration of the pulses, where the corresponding measuring intervals were selected randomly from the whole measuring period. The resulting measuring times and exposures, calculated using Table 3.1, are listed in table 5.1. In addition, Figure 5.1 shows the start and end dates for all datasets.

Module	^{57}Co calibration [kgd]	AmBe neutron calibration [kgd]	Training dataset [kgd]	DM dataset [kgd]
A	0.3852	0.8245	0.8481	5.4967
B	0.4000	0.8559	0.8044	5.4677
E	0.3999	0.8559	0.8804	5.7062
J	-	0.8349	0.5087	4.0372

Table 5.1: Raw exposures for different datasets and detectors

From the remaining background data, all training files are excluded. This dataset is referred to as the "dark matter" dataset. In every continuous measurement interval, the first and last event recorded in a detector channel mark the beginning and the end of the measuring period.

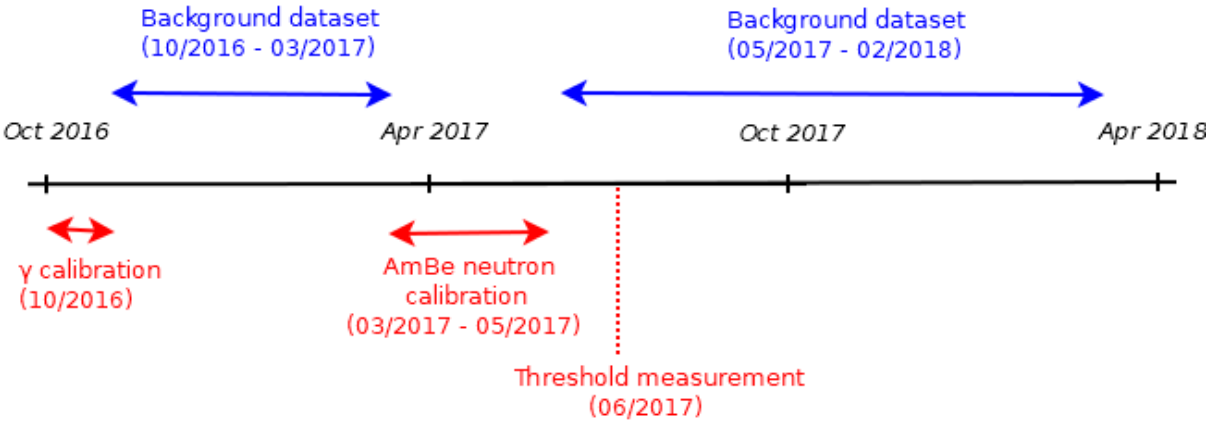

Figure 5.1: Start and end date for the datasets analyzed in this work: The ^{57}Co γ calibration, the AmBe neutron calibration and the two-part background dataset are indicated. The dedicated threshold measurement only required a very short interval of a few hours.

For detector J, the working point had to be changed to achieve a higher sensitivity; this change occured after the γ calibration, but before the neutron calibration. Therefore, the total exposure in the background dataset is lower, and the γ calibration cannot be used for this detector. Two analysis chains were established for each detector module to provide an independent cross check. One is discussed in this work, while the other can be found in [118]; results from the latter for detector A were also published in [88]. As explained in Section 4.3, low-energetic γ lines due to cosmogenic activation need to be used to verify the energy calibration in each detector. Since the statistics in these lines is limited, the full dataset above 100 eV was unblinded to cross-check the energy scale, after a detailed study and comparison of the analyses took place. No changes in the analysis chain established with the training dataset were made; only the CPE factor for conversion between test pulse equivalent amplitude and electron equivalent energy was adjusted by a few percent. Finally, the last part of the dataset below 100 eV was unblinded for each detector.

5.2 Analysis Workflow

In a first iteration, hardware-triggered data are used to obtain standard events (cf. Section 4.2.1) for each phonon and each light detector, as well as a noise power spectrum (cf. Section 4.2.3). The baselines used for the NPS were drawn periodically in intervals of 10 minutes. Each standard event is built out of events selected from the neutron recoil band in the neutron calibration dataset, to ensure the best possible similarity to potential dark matter recoils. For the standard events, only pulses within the linear range of each detector and well below the

truncation limit (see section 4.2.1) are used. The truncation limits are in turn determined by an untruncated fit of test pulses in each detector and are listed in table 5.2.

Channel	Truncation Limit [V]
A-Ph	0.6
A-L	0.3
B-Ph	0.7
B-L	2.5
E-Ph	0.8
E-L	0.8
J-Ph	1.2
J-L	0.3

Table 5.2: Truncation limits for different channels used for the standard event fit.

Using the standard events and noise power spectra, filters are built for each detector; each dataset is then retriggered, such that one noise trigger per kg of detector mass and day in the phonon channel of a module is expected (see Section 4.1.1). The analysis chain is then defined using the training dataset for each detector module. In table 5.3, the thresholds applied to the filtered stream are listed for each channel.

Channel	Trigger threshold [V]
A - Ph	0.0068
A - L	0.006
B - Ph	0.015
B - L	0.006
E - Ph	0.0107
E - L	0.002
J - Ph	0.0066
J - L	0.013

Table 5.3: Trigger thresholds in V for different channels operated in CRESST-III, Phase One. These thresholds are applied to the filtered stream in software.

5.3 Applied Cuts

Cuts are applied to both the dark matter dataset and the neutron calibration data for each detector to remove baseline artifacts, pile-up events which cannot be correctly reconstructed, events vetoed by the iStick or muon system, as well as periods of unstable detector operation. Additionally, coincidence of two or more cryogenic detector modules leads to the exclusion of the corresponding events from their respective datasets. An explanation for each cut and applied values for the dark matter dataset are given in the following sections.

5.3.1 Stability Cut

The operating point of the detector is monitored trough the use of control pulses. If the measured pulse height of two consecutive control pulses deviates from the average height by more than three standard deviations, an unstable time period is defined which will be excluded from the total measuring time. The period ends when the measured pulse height lies again within 3σ around the mean. For each channel, the corresponding values for mean and standard deviation are given in Table 5.4, along with the nominal set voltage used by the control loop.

Channel	Set Point [V]	Mean Control Pulse Height [V]	Standard Deviation σ [V]
A-Ph	4.5	4.4980	0.0299
A-L	1.4	1.3999	0.0062
B-Ph	4.5	4.4991	0.1058
B-L	0.95	0.9500	0.0029
E-Ph	3.0	2.9970	0.0332
E-L	0.35	0.3500	0.0012
J-Ph	5.35	5.3497	0.0088
J-L	1.1	1.1000	0.0030

Table 5.4: Mean control pulse heights and standard deviations for different channels.

5.3.2 Rate Cut

Since only constant backgrounds are measured plus a hypothetical dark matter component, the rate of events recorded in a detector should be roughly constant over time[1]. Figure 5.2 illustrates the recorded (=triggered) number of particle events for one data segment of detector E (left plot). An interval centered around each event is used to calculate the rate as a function of time, and mean value as well as standard deviation are determined for the training dataset. The resulting values are given for each detector module in Table 5.5.

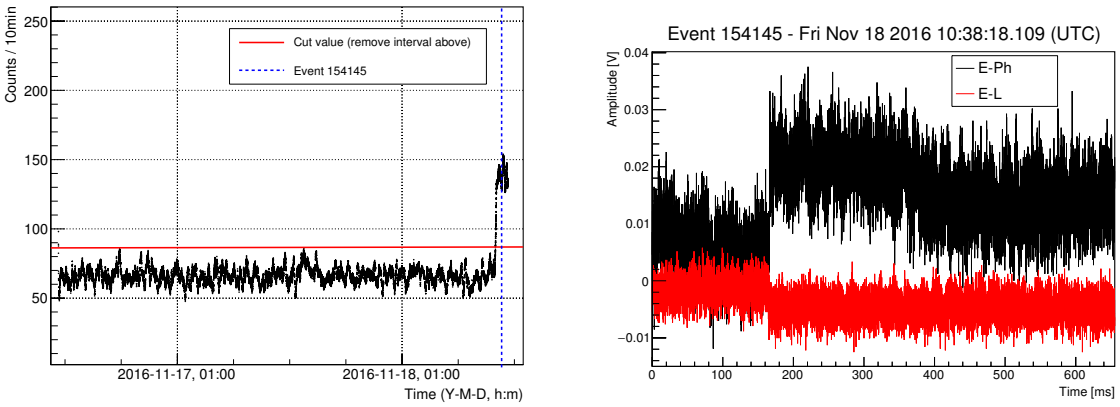

Figure 5.2: Left: Event rate of detector E as a function of time for a data segment from the training dataset. At the end, a period of high rate is visible, which is removed by the rate cut (red). Right: Jump event originating from the period of high rate (time indicated by the blue dashed line); both light (red) and phonon channel (black) show an instantaneous shift in opposite directions.

It is visible that the rate changes very suddenly towards the end of the segment in Figure 5.2; in such time intervals with high event rates, "jump" events are observed, which are most probably due to electromagnetic interference. An example event from the shown period, where both channels are affected, is displayed on the right side of Figure 5.2. Its exact time is also marked with a dashed blue line in the left plot. Since these events are only distinguishable from real pulses above a certain amplitude and could be misinterpreted as a dark matter signal, time intervals containing them are removed by a rate cut. If the number of recorded events in a time period deviates by more than 3 σ from the average, the whole period is removed. An interval size of 10 minutes was found to provide a good compromise between time precision and statistical sample size. This event class was observed most prominently in detectors J and E, and to a much lesser degree also in detector A, while detector B did not record such pulses. Each detector module may be influenced differently by a changing

[1] as long as no "dark matter bursts" are taken into account

magnetic field due to differences in the orientation of the TES sensors; this is an ongoing topic, and further tests are planned.

Module	Mean [counts per 10 min]	Standard deviation σ [counts per 10 min]	Mean [Hz]	Standard deviation σ [Hz]
A	47.7	3.0	0.080	0.005
B	29.1	2.9	0.049	0.005
E	50.3	12.3	0.084	0.021
J	25.6	5.2	0.043	0.009

Table 5.5: Mean trigger rate for particle events and standard deviation in modules A, B, E and J, determined from the training dataset. For each detector, intervals with a deviation greater than 3 σ from the average value were removed by the rate cut.

5.3.3 Quality Parameter Cuts

A set of quality parameters is determined for each measured event, which are used to remove pulses affected by pile-up or electronic features. Cut values are defined for each parameter, and listed in the following section.

Peak Position

For each pulse, a baseline is fitted in the pre-trigger range, i.e. in the region of the record window before the pulse onset. A linear model is assumed, and an RMS is calculated for this range of the record. Subsequently, a peak search algorithm is applied, which operates on a 50 sample average of the pulse. This search gives the *Pulse Height* in V and the *Peak Position* parameter in ms, describing the relative position of a triggered pulse inside the readout window. If a pulse is not at the correct position with respect to its readout window, the trigger was caused by a different signal, and energy reconstruction will not work properly. The peak position of all pulses is required to be within 160 ms to 180 ms after the start of the readout window. This interval was estimated from test pulses and simulated pulses and is found to be consistent for both; The same interval is used for all phonon channels. For light channels, this cut is not applied, since low energetic nuclear recoil events are not expected to feature a light signal at all (cf. Section 3.4.1), and would otherwise be cut randomly.

Voltage Spikes

Outlier high-voltage or low-voltage samples in a baseline have no particle physics origin and are due to the electronic readout components. They are not related to a recorded pulse, but may influence its energy reconstruction if present. An example "spike" event which triggered is shown in Figure 5.3. To exlude events with such features, the voltage difference between each two consecutive samples of a record is calculated, and the minimum difference is compared to the baseline RMS. The ratio between both is required to be greater than -150. The minimum is used instead of the maximum difference, because a real pulse may have an almost instant rise, but cannot have an instant decay (cf. Section 4.2.2).

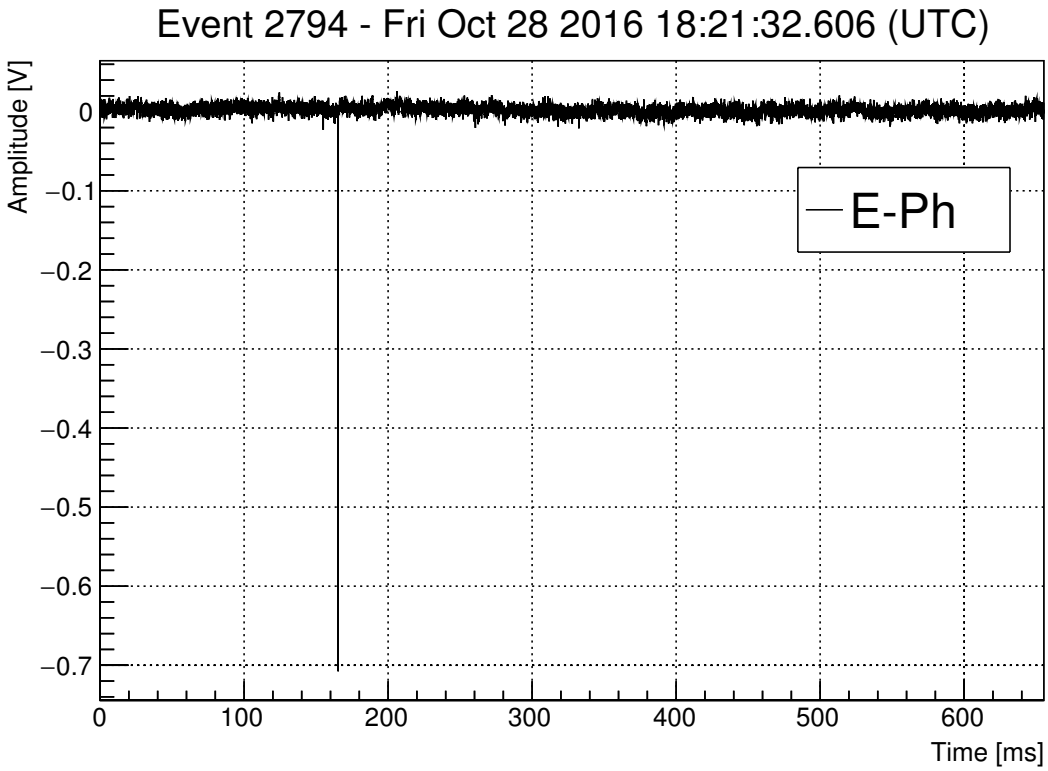

Figure 5.3: Example of a triggered "spike" event in the phonon channel of detector E. A single sample shows a significantly smaller voltage than the rest of the otherwise empty baseline.

Right-Left Baseline

Within a readout window of sufficient size, a pulse should relax back to the regular baseline; The last samples of a record should yield in average the same baseline as the first samples. If this is not the case, either the readout window was too small, i.e. the energy of the pulse was

too high and it has not yet fully decayed, or the baseline has changed during the recording. The difference between an average baseline calculated from the last 50 samples of a pulse and another calculated from the first 50 samples is evaluated as a function of pulse height. Below a certain pulse height, this value is constant, and all pulses decay within the readout window. All events displaying a difference significantly greater or smaller than this value and with a pulse height below the maximum are removed. The exact cut value varies for different channels and is given in Table 5.6. For detector J, two iterations were necessary due to the aforementioned "jump" events at low pulse heights. For detector B, the cut was not applied at all.

Channel	Cut value [V]	Maximum pulse height for cut [V]
A-Ph	0.0125	0.1
E-Ph	0.05	2.5
J-Ph	0.04	4
J-Ph	0.001	0.06

Table 5.6: Values for the right-left baseline cut in different channels. The right column gives the pulse height below which the cut is applied.

5.3.4 iStick Veto

If one of the instrumented sticks measures a pulse, this either means that the energy deposition of the corresponding event did not happen in the main absorber, or that phonons propagated from the absober crystal to the stick. In the former case, the event needs to be removed from the final sample. To account also for the latter case, the corresponding cut is defined using periodically recorded empty baselines instead of triggered pulses. Since the three instrumented sticks of each detector module have different characteristics and in particular different resolutions and thresholds, the optimum value for the cut is estimated from the pulse height spectrum of the iStick channel (all three sticks are read out via the same SQUID channel) by fitting a Gaussian function to the left side of the noise peak. At some point the Gaussian function does not describe the distribution on the right side anymore, which is where the optimal cut value lies. This is illustrated in Figure 5.4 for detector E. Table 5.7 lists cut values for all analyzed detector modules.

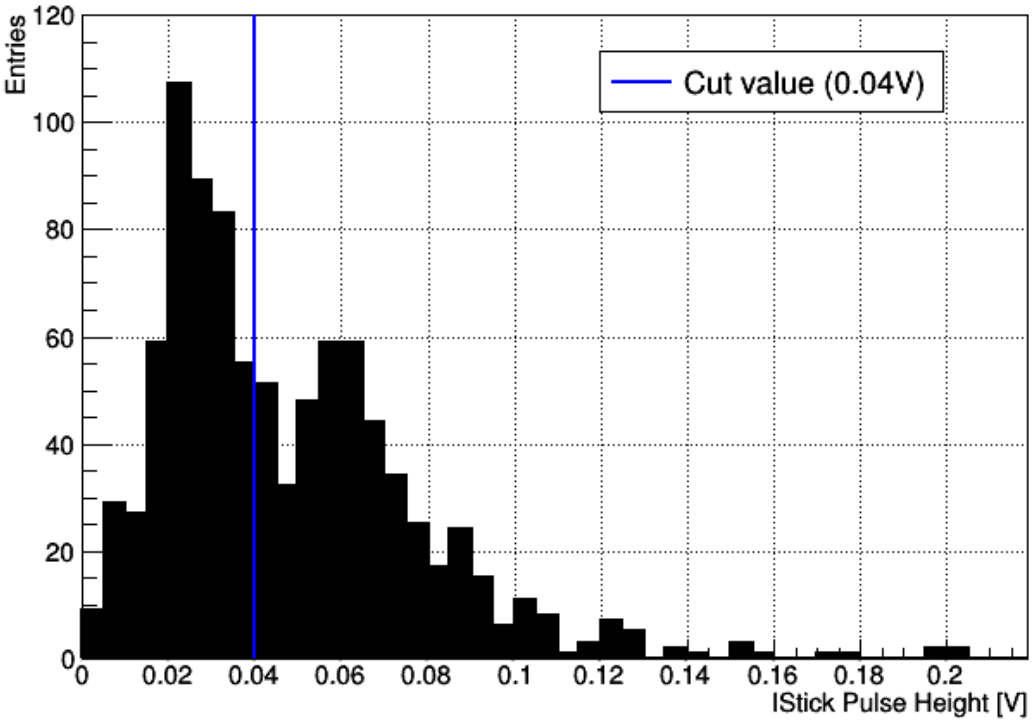

Figure 5.4: iStick pulse height distribution in the training dataset for detector E. The blue line indicates the cut value on the right flank of the noise peak; real pulses are considered to lie above this value.

Module	Cut value [V]
A	0.015
B	0.03
E	0.04
J	0.15

Table 5.7: iStick pulse height cut values for modules A, B, E, and J. Events where the pulse height in the iStick channel exceeded this value are removed from the dark matter dataset.

5.3.5 Filter Amplitude Ratio

The optimum filter trigger used to obtain the records requires a periodic filter function in fourier space. This means that for a given record, also information outside the actual readout window was used for triggering. This information is, however, not saved, but only the window itself. Since all later analysis of pulses is based only the samples within the record window, a

cross check is performed for simulated pulses: The same filter is applied again to the recorded pulse without the stream around it (instead, a flat baseline is assumed). Figure 5.5 shows the results for detector E; in general, the trigger filter is much more robust due to its increased amount of information. Especially at low energies, the filter which only operates on the record window is sensitive to artifacts and disturbances and assigns too high amplitudes to events. This confirms that using the trigger filter amplitude as energy estimator is a favorable choice. As a precaution, for all events in the background dataset, the resulting amplitude of the second filter is allowed to deviate from the amplitude of the trigger filter by no more than 5%.

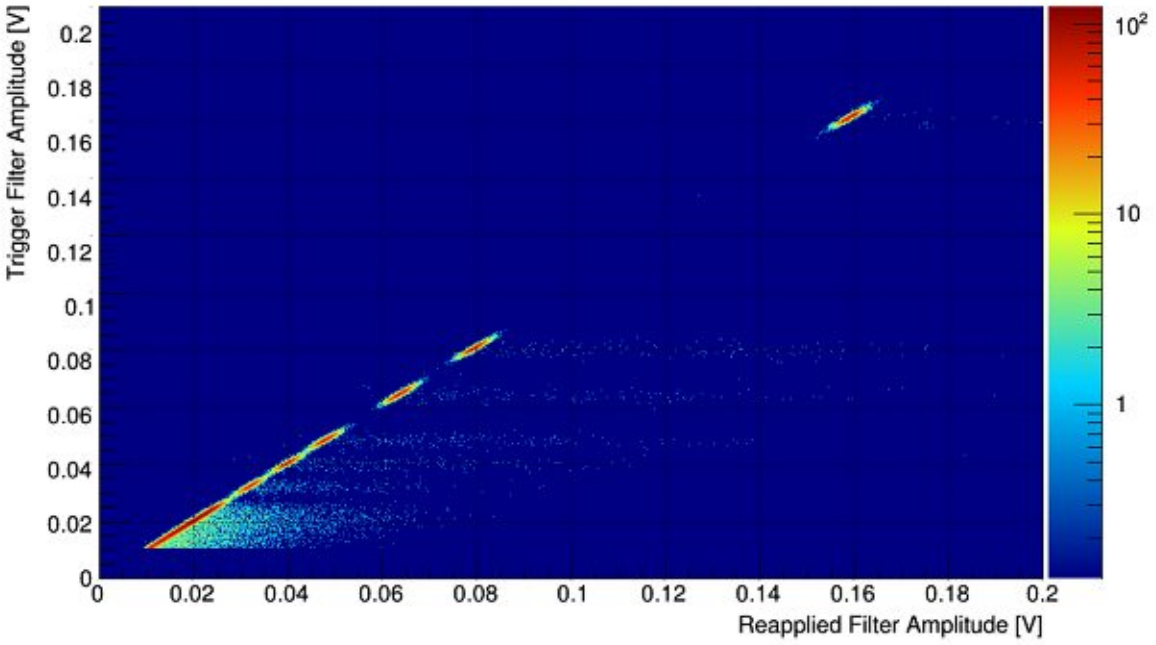

Figure 5.5: Amplitude of the trigger filter versus amplitude of the reapplied filter for simulated pulses on the phonon channel of detector E. Towards low energies, more amplitudes were simulated; in this region, the reapplied filter assigns a higher energy than the trigger filter for several events.

5.3.6 Pulse Shape Cuts

The standard events used for fitting and filtering define the ideal appearance of nuclear recoil (and e^-/γ) events in the main absorber crystal of a module, i.e. the ideal pulse shape in the light and phonon channel. Any event featuring pile-up or disturbances, or happening in another part of the detector, should be vetoed if its pulse shape in one channel is sufficiently different from the respective standard event for that channel. Considering e.g. events in one of the instrumented sticks, phonons propagating from the stick to the main crystal would cause a different pulse rise time in the phonon channel due to the different flux of non-thermal phonons (cf. Section 4.2.2). Three different RMS quantities used for discrimination are explained below.

Truncated Fit RMS

The truncated fit RMS serves as the most simple discrimination parameter. Figures 5.6 and Figure 5.7 illustrate the definition of the cut for the phonon channel of detector E: Simulated pulses, i.e. standard events scaled by different amplitudes, are superimposed onto the stream and subsequently reconstructed and fitted, where the RMS as a function of amplitude should be roughly constant (Figure 5.6). The ideal RMS distribution for pulses of the same injected amplitude would be Gaussian (Figure 5.7), but coincidence with other events and changing baseline noise produce a tail towards higher values. The RMS obtained for real pulses is then compared to the expected distribution; 5.8 shows the behavior at higher energies (here as a function of the fitted amplitude). At some point, simulated pulses are fitted differently than real pulses because they are not subject to saturation. Therefore, above the truncation limit, the RMS cut value is extracted from the real e^- and γ bands instead of the simulation. A truncated fit RMS cut is applied to both the phonon and the light channel of each module.

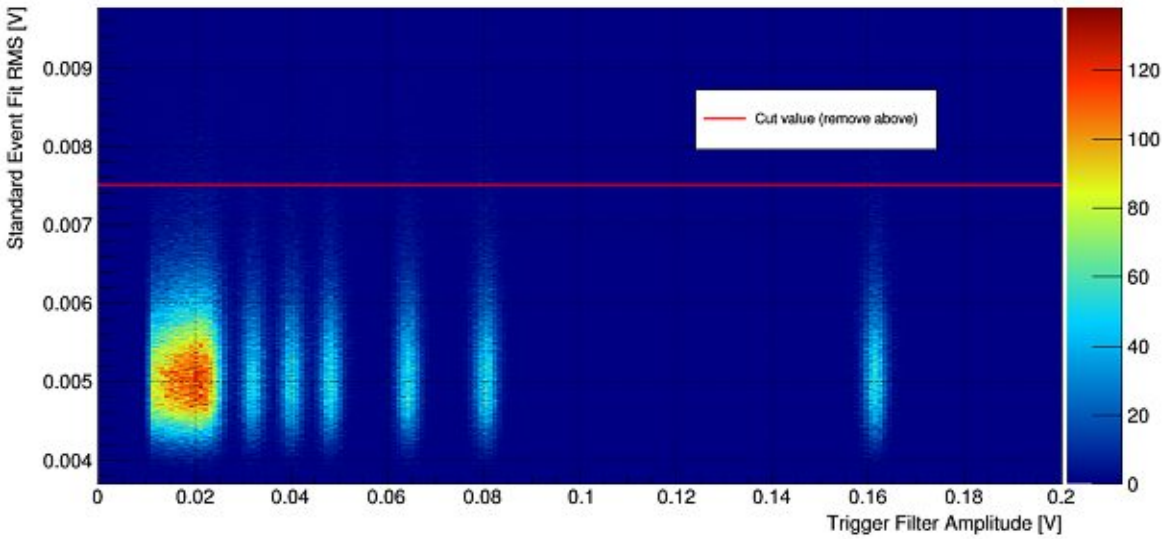

Figure 5.6: RMS from the standard event fit versus trigger filter amplitude for simulated pulses of different amplitudes. In this low amplitude range, the mean RMS is constant; the cut value for this detector is indicated via a red line. The simulation was performed on the training background dataset of detector E.

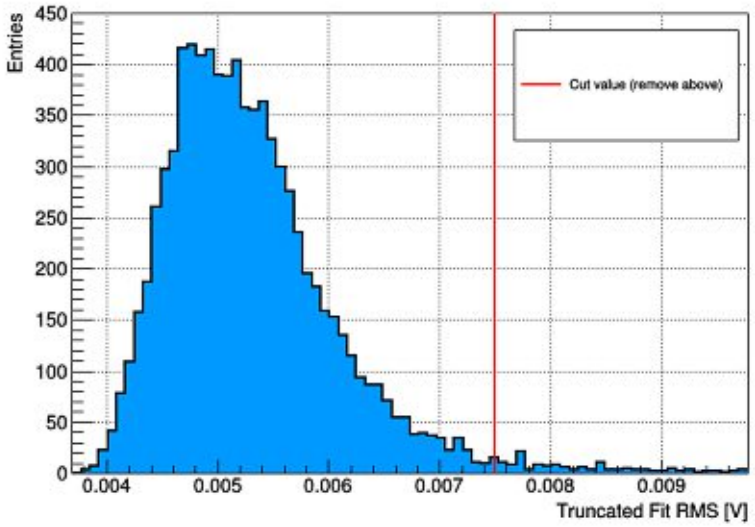

Figure 5.7: Truncated fit RMS for simulated pulses with a trigger filter amplitude of 0.08 V; a "slice" of Figure 5.6 is shown. The cut value is indicated via a red line.

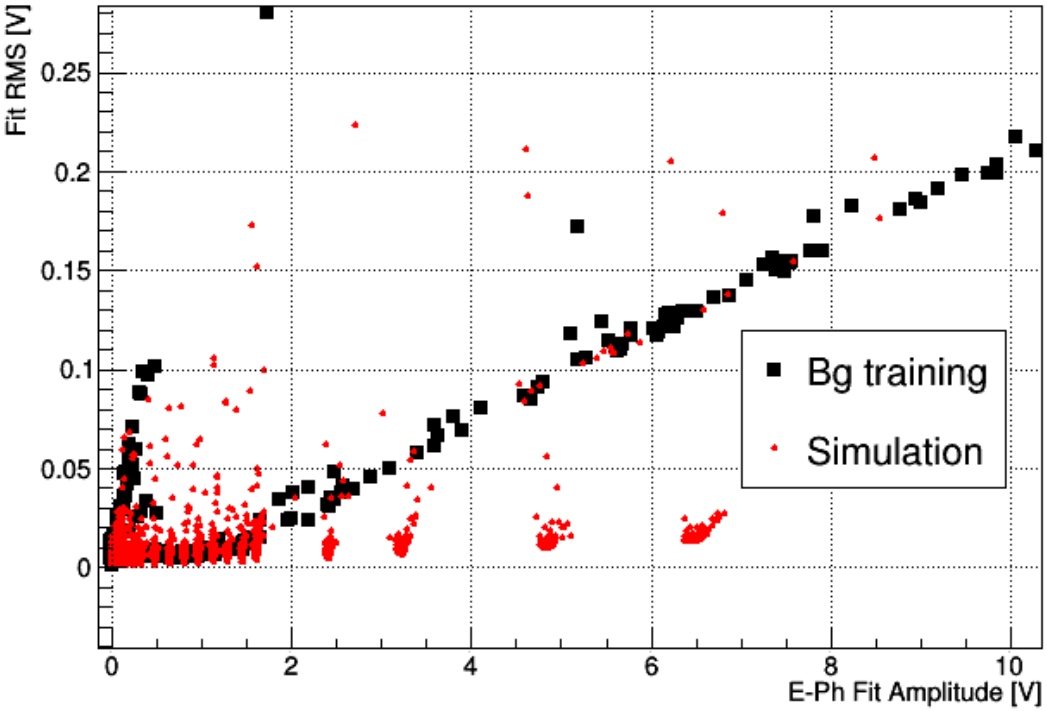

Figure 5.8: RMS from the standard event fit versus fitted amplitude for simulated pulses of different amplitudes (red), as well as real events (black) from the training set of detector E. At amplitudes above ~1 V, the distributions deviate due to the noise scaling effect.

Optimum Filter RMS

Reapplying the optimum filter to the record window (cf. previous section) also yields an RMS quantity. This is defined via the difference between each filtered pulse and a filtered standard event, which was scaled before by the resulting filter amplitude for the measured pulse. Figure 5.9 shows the reapplied filter RMS relative to the trigger filter amplitude for simulated pulses; again, this relation should be constant for low energies and thus amplitudes. Pulses with a significantly different pulse shape than the template used in the filter will be assigned a higher RMS, and can thus be removed - in Figure 5.9, the cut removes part of the "jump" event population in detector E (discussed in Section 5.3.2) coinciding with the simulation pulses. This distribution was not well visible in Figure 5.6; in comparison to the standard event fit RMS, the optimum filter RMS is less prone to a high noise relative to the signal, and therefore more reliable at lower energies.

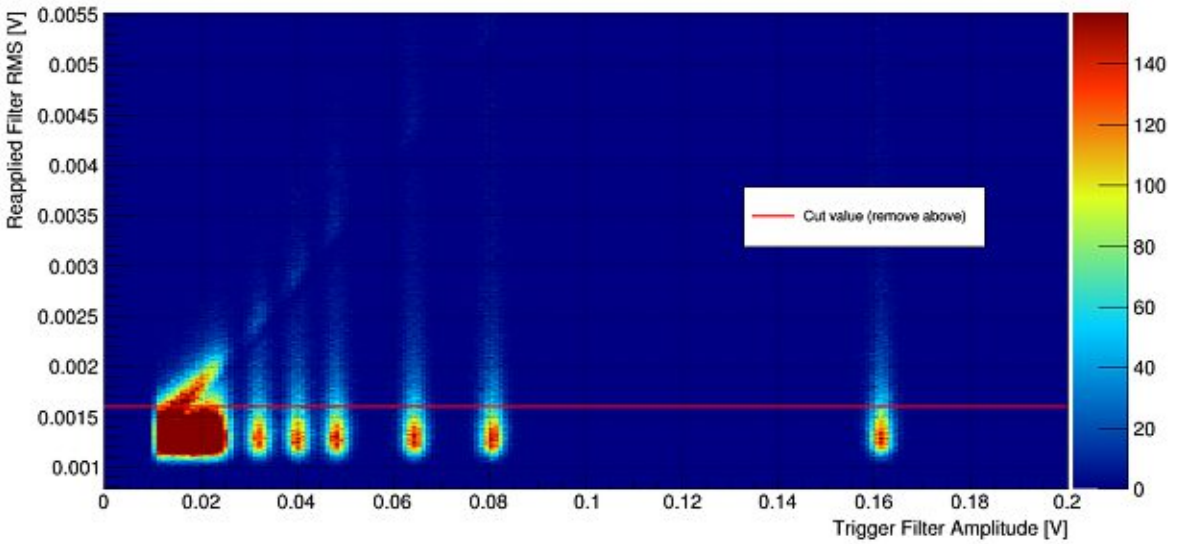

Figure 5.9: RMS of the reapplied optimum filter as a function of the trigger filter amplitude for simulated pulses of different amplitudes; the simulation was performed for the background dataset of detector E. At low energies, a population of events with linearly increasing RMS is visible; these are jump events.

Peak Filter RMS

Using a subset of the pulse and the filtered scaled standard event for the RMS calculation, i.e. a narrow region around the peak, emphasis can be put on characteristics of the pulse shape. In this case, the RMS is evaluated the same way as in the previous paragraph, but only for the region around the peak. This quantity was found to be most effective in the discrimination between "jump" events (cf. Figure 5.2) and real pulses, since no distinct maximum is visible for the former. In Figure 5.9, some of these events coincide with simulated pulses and are visible as an additional band at low energies.

5.3.7 Muon Veto

For each particle event, the time distance to the closest muon event recorded in one or more of the panels is calculated; The timestamp of each cryodetector event is corrected by the standard event fit result, i.e. the resulting position of the shifted SEV, where the SEV itself is defined such that its onset is exactly at the trigger position. If the time difference is negative, the timestamp of the muon event lies before the timestamp of the cryodetector event. Figure 5.10 shows the distribution of time distances, which follows an exponential model for values greater and smaller than zero, consistent with random coincidence. As no causal coincidence

peak is visible, the corrected timestamp of each cryodetecor event is conservatively required to be at least 10 ms after the last muon event and not closer than 5 ms to the next one. This is sufficient to exclude any real coincidence, since the typical rise time in a cryodetector is several ms (e.g. 0.8 ms-2.7 ms in tables 8.3 and 8.4), but will remove mostly uncorrelated events. Real coincidences are rare due to the low muon rate in the laboratory (cf. Section 3.3.7); almost all triggers in the muon veto are caused by ambient γs, and are thus also not self-correlated. A muon panel will always be faster in terms of signal formation than a cryodetector (cf. Section 3.3.7); the asymmetry of the window additionally accounts for the fact that a typical muon entering the detector should first trigger the veto.
The signal fraction which will be cut randomly and independent of energy can be estimated as follows: Assuming a constant muon veto trigger rate of 5.2 Hz, which is the usual observed value in CRESST-III, the probability P_c of a cryodetector event coinciding with at least one muon panel event in a window of 15 ms is

$$P_c = 1 - P(0) = 1 - \frac{\lambda^k}{k!} e^{-\lambda}|_{k=0} \quad , \qquad \lambda = 5.2\text{Hz} \cdot 0.015\text{s} = 0.078, \tag{5.1}$$

where $P(0)$ is the poisson probability of observing zero events in a time window of 15 ms, and λ is the expected number of muon panel events in this time window. This gives a probability of $P_c = 7.50\,\%$ for each cryodetector event to be vetoed randomly, consistent with the fraction of events removed by this cut, which is also $\approx 7.5\,\%$ for all detectors (cf. Section 5.9).

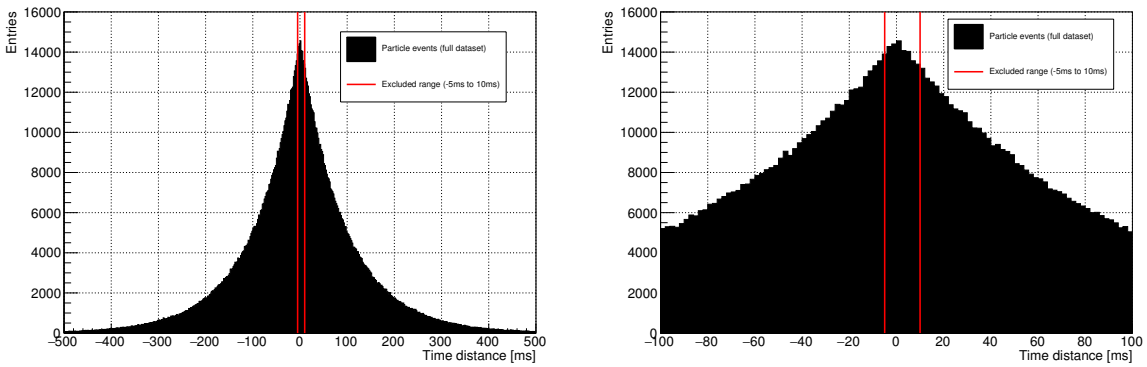

Figure 5.10: Time difference between cryodetector events and muon panel events. The cut value for the excluded range is indicated in red. Right: Zoom to small time distances.

As the time resolution of the muon panels is much better than that of the cryodetectors, coincidences between two opposing panels could be used to significantly improve the efficiency of the veto and avoid random coincidences with cryodetector events. However, this also

means less discrimination against cryodetector events due to muons getting "stuck" in the detectors, and neglects the geometrical coverage of the panels (opening for the cryostat at the top). Therefore, a reduced exposure is considered acceptable to avoid false signal positives from muon events. In Section 5.11, it will also be shown that the effect of an increased exposure on the exclusion limit is negligible in this work. The signal height could be used as an additional discriminator; this requires calibration of the panels, and a precise knowledge of the muon flux as well as the experimental setup, which could be acquired via simulation.

5.3.8 Cryodetector Coincidence

Interactions of a dark matter particle with more than one detector are highly unlikely. Instead, events where multiple modules triggered are probably due to muons traversing the experimental setup, or caused by radiogenic contamination of detector parts. In the first case, such events should already be removed by the muon veto. A cut is applied to each module to remove particle events, where an event in another detector coincidies within a window of [-10 ms,10 ms]. This range is sufficient to account for the time resolutions of both detectors. The time for each individual event is calculated in the same way as for the muon veto cut, i.e. the original trigger timestamp is corrected by the pulse fit result. As for the muon veto, an estimation of the resulting amount of random coincidences can be made: Considering the trigger rates determined for the rate cut (Section 5.3.2), a typical module triggers at ~0.07 Hz, where only particle events are considered. There is no additional contribution due to coincidence with injected heater pulses, since these are injected to all detectors simultaneously. For 10 modules, and using equation 5.1 with $\lambda = 0.07\text{Hz} \cdot 0.02\text{s} = 0.0014$, this gives a probability of 1.4 % for a recorded particle event to be vetoed randomly. The above approach neglects differences in trigger rates, and in particular the fact that channels can be "blind" if they move away from their operating point; this would reduce the number of randomly vetoed events significantly. Therefore, the obtained value gives an upper limit. In Section 5.9, where the combined effect of muon veto and cryocoincidence veto is depicted, the amount of simulation events removed due to cryodetector coincidence appears small. A cross check was performed, where the veto was only applied after all other selection criteria; for detector A, only four events out of ~5500 (no LY cut) in the final dataset were removed. This extremely small number can be understood when considering that real coincidences are more likely for high-energy events; these events are already removed by other cuts, and in particular by the limited energy range of the filter reconstruction (cf. Section 5.5).

5.3.9 Rise Time

For detector J, a population of events around ~ 6 keV with light yield values reaching from 0 to 1 contaminates the nuclear recoil band region (cf. Section 5.8). The population is visible in Figures 5.32 and 5.27. It was found that pulses from this event class show a different rise time; leaving τ_n and a scaling parameter for the amplitude free in a parametric two-component fit (described in detail in Section 4.2.2) while fixing all other parameters allows for a discrimination of these events. Figure 5.11 shows the fit result for τ_n as a function of energy for the phonon channel of detector J. As a precaution, the fit was performed also for the other detectors; no population of events with significantly deviating τ_n was found. The physical origin of this event class is unknown.

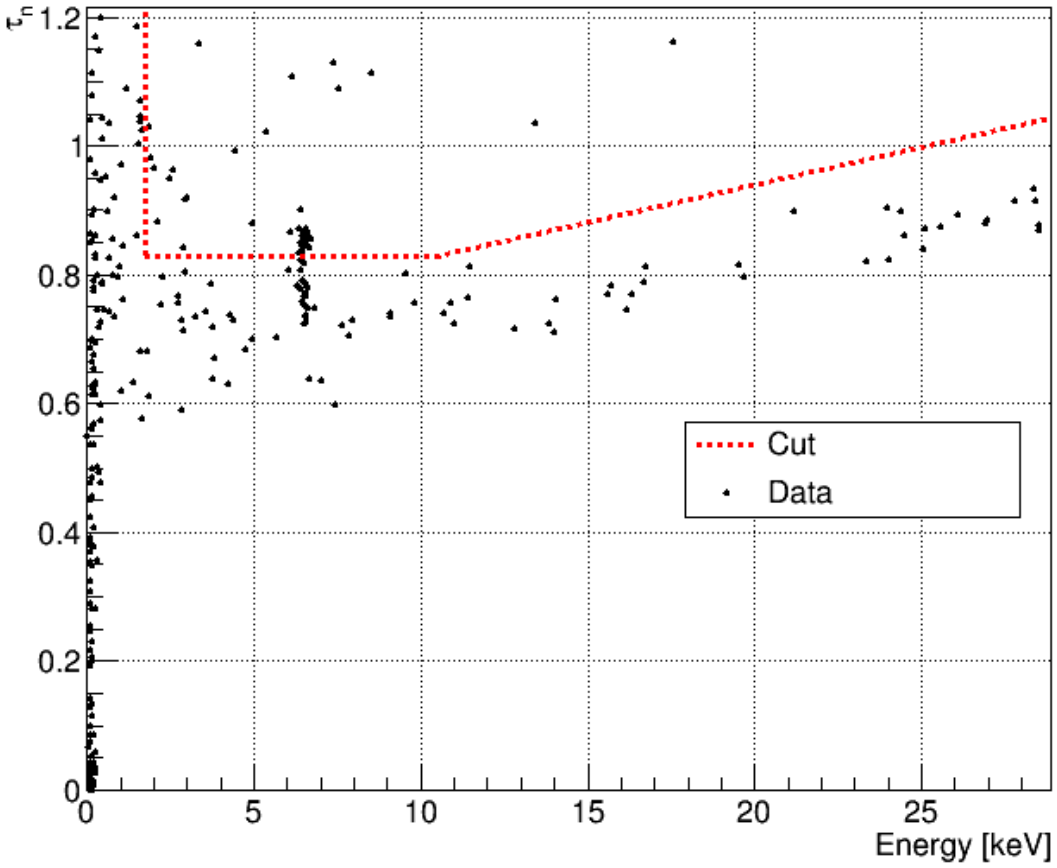

Figure 5.11: Distribution of the rise time τ_n as result of a parametric fit versus reconstructed energy for the phonon detector of module J. The event distribution around 6.5 keV features increased values of τ_n, and events above the dashed red line are removed. At higher energies, the rise time starts to increase; at low energies, the fit starts to fail and the rise time band widens.

5.4 Event Classes

Figure 5.12 shows the reconstructed (fit) phonon and light amplitudes for neutron calibration data of detector J. Multiple bands are visible, which can be explained by different event classes occuring in different parts of the detector. Neutrons recoiling in the main absorber show the lowest light to phonon amplitude ratio; the band above corresponds to e^- and γ events. Selecting only events with an instrumented stick amplitude above the noise results in the dataset highlighted in red. As mentioned in Section 3.3.5, all three absorber holding sticks are read out in parallel via the same channel. These events form three bands, and it is reasonable to assume that each band corresponds to hits in one of the three instrumented sticks.

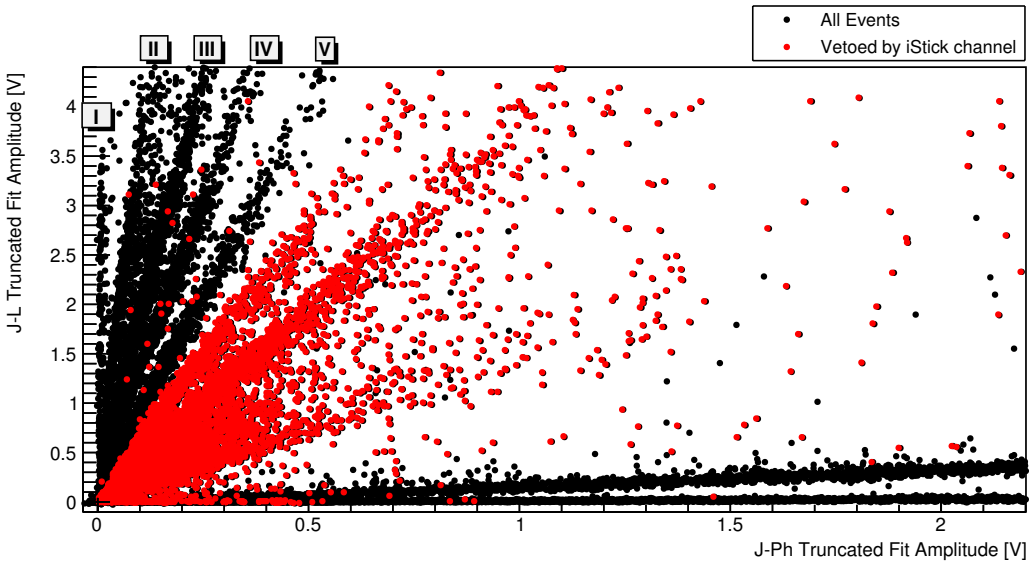

Figure 5.12: Light versus phonon channel amplitude after stability cut for neutron calibration data of detector J. Different bands are visible; the highlighted red events also show a signal in the iStick channel and can be vetoed. Events from the bands I-V are shown in Figure 5.13.

Five additional bands (labeled I-V in Figure 5.12) appear with an increasing light to phonon amplitude ratio. Since direct hits in the light detector will cause the highest light signal, the corresponding two bands I and II display the highest ratios. Band I features no signal in the phonon channel at all; these events are probably caused by hits in the Si part of the wafer, while band II corresponds to interactions in the Al_2O_3 crystal, where scintillation light is created and recorded by the main absorber crystal. The other three bands (III-V) can be attributed to hits in the non-instrumented light detector holding sticks. All of the former interpretations are solidified by Figure 5.13, which shows the pulse shape recorded in the light channel for events from all five bands: For bands I and II, the shape is identical, while it varies

for the bands III-V because of the different phonon propagation from each non-instrumented stick. This results in the removal of events from the bands III-V by the standard event fit RMS cut for the light detector channel. Events from bands I and II in turn show a significant deviation in the phonon channel pulse shape, and are removed by RMS cuts in this channel.

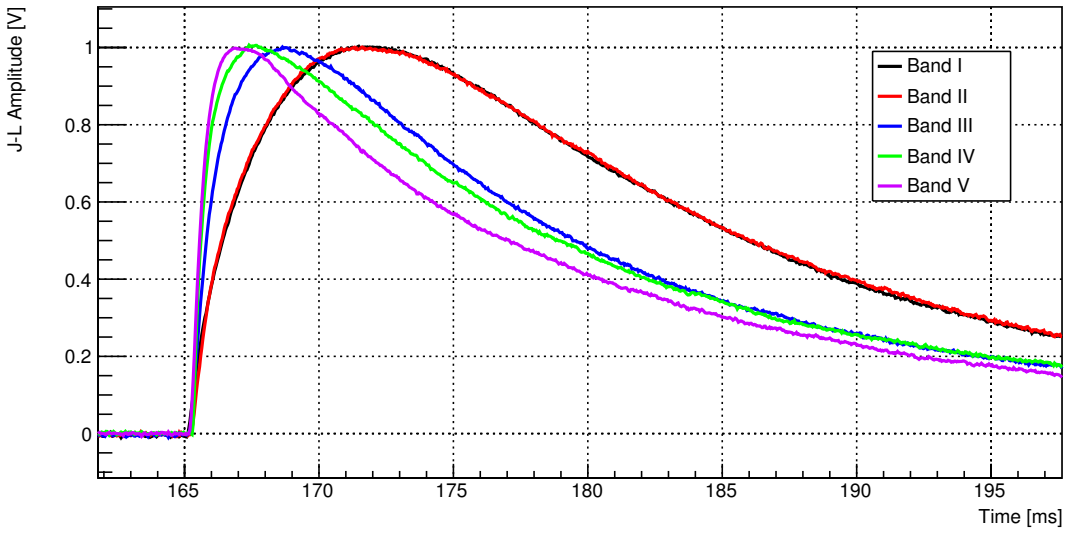

Figure 5.13: Events from five different bands in Figure 5.12; the pulse recorded in the light channel of detector J is shown. Events with the same pulse height were selected. The bands I and II represented by the black and red pulses feature the same pulse shape.

5.5 Energy Calibration

As energy estimator for the phonon channels, the amplitude of the trigger filter is used in this analysis, to achieve the best possible resolution at low energies. For the light detectors, the truncated fit is used instead, to allow for a larger dynamic range. A correlated version of the truncated fit is applied, where the phonon channel of a module is fitted first and defines the exact time of an event; the standard event in the corresponding light channel is then fixed at this position, and only scaled. To arrive at the energy of an event, several steps are necessary, which were already explained in Section 4.2. In particular, each event's filter amplitude in the phonon channel is first converted to an equivalent standard event fit amplitude (to increase the reconstructable energy range), before being adjusted using the detector's test pulse response evaluated at the time of the event. The conversion functions from filter amplitude to equivalent fit amplitude for each phonon channel, which are extracted from neutron calibration data via a polynomial fit, are illustrated in Figure 5.14 in this section and

Section 8.1 in the appendix. For module A, the phonon CPE factor (which converts test pulse equivalent amplitude to energy) was fine-tuned using the Hf M1 line (E=2.6 keV), while for the other modules, the L1 line (E=11.27 keV) was used. This is a consequence of the observed energy spectra and will be discussed in detail in Section 5.13. All CPE factors are listed in Table 5.8.

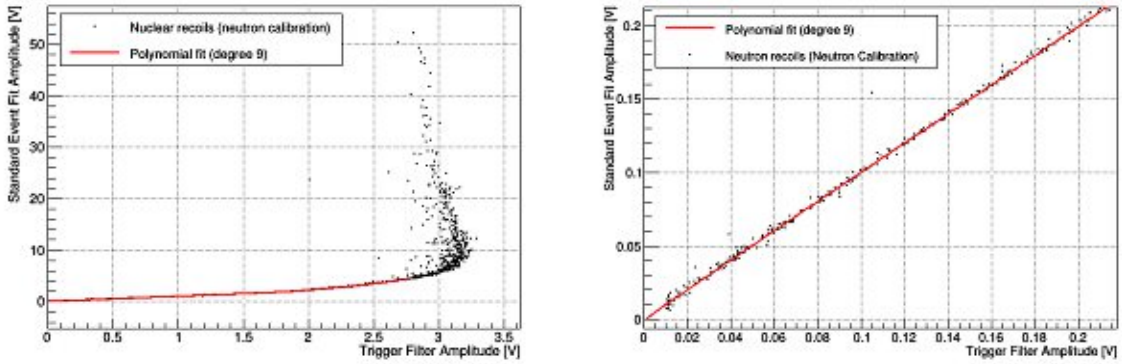

Figure 5.14: Conversion of filter amplitude to equivalent standard event fit amplitude for the phonon channel of detector E. Data from the neutron calibration of detector E was used, and the displayed events have been selected from the neutron bands. On the left, the energy cutoff is visible as the upper limit of the polynomial fit range (2.7 V); the right plot shows a zoom to low amplitudes.

Module	Phonon CPE [keV / $V_{TPE(conv.\ filter\ amp.)}$]	Light CPE [keV_{ee} / $V_{TPE(trunc.\ fit\ amp.)}$]
A	7.73	10.11
B	10.56	18.5
E	13.34	13.87
J	10.78	11.17

Table 5.8: Conversion factors from phonon and light test pulse amplitudes to energy for the modules A, B, E and J. For the light channels, the truncated fit amplitude is first converted to a test pulse equivalent (TPE) amplitude, and then calibrated. For the phonon channels, the filter amplitude is converted to equivalent fit amplitude, and then to TPE amplitude before calibration.

Due to saturation of pulses, which is not accounted for by the optimum filter, the reconstructed energy in the phonon channel of each module is limited; these limits are given in Table 5.9 both in filter amplitude and in equivalent fit amplitude. For detector J, the limiting factor is not the aforementioned effect, but a limited energy range of the simulation (see section 5.9).

Channel	Max. amplitude [V] (trigger filter)	Max. amplitude [V] (truncated fit)	Max. energy [keV]
A-Ph	4.1	5.8	20
B-Ph	4.3	4.8	33
E-Ph	2.8	4.4	29
J-Ph	7.5	14.2	50

Table 5.9: Maximum reconstructable filter amplitude and corresponding standard event fit amplitude for different channels.

5.6 Test Pulse Offset

An offset in the conversion between injected test pulse amplitude and reconstructed test pulse amplitude is observed in this phase of CRESST for the first time. This is illustrated in Figure 5.15, where a dedicated measurement was performed to study this effect in the phonon channel of detector A. Due to a problem with time stamps in this dataset, test pulses at low energies could only be identified when they triggered; therefore the number of points decreases towards lower amplitudes.

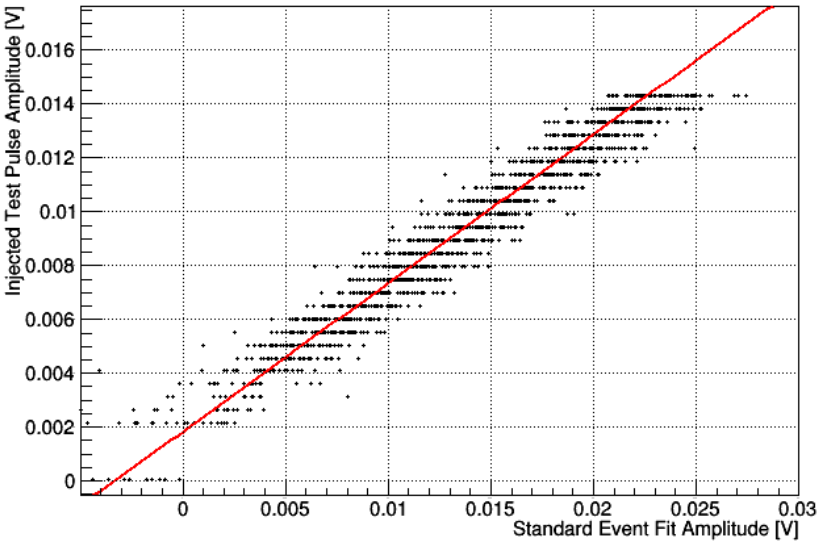

Figure 5.15: Dedicated measurement of test pulse offset in the phonon channel of detector A; reconstructed versus injected pulse height in V. The linear fit model gives an offset of 0.0018 V in injected amplitude.

The offset from the linear fit is 0.0018 V and is considered in the transfer function for this channel; other detectors do not display this effect. Two possible explanations are considered here: Intuitively, a minimum energy deposition might be required to cause a measurable pulse in the TES in the first place. This is entirely possible; however it is unclear why other detectors should not show this effect. It is more likely that the offset is caused by a piece of electronics; between the previous measuring campaign and the one discussed in this work, the method of scaling the injected test pulses was changed. As the pulser itself only allows for a certain number of different test pulse amplitudes, an external scaling via an additional DAC after the pulser was introduced. This enables the injection of more test pulses, but could also introduce scaled noise, which would worsen the accuracy. This method will be replaced in the next iteration of CRESST, and further test measurements are planned to study the effect. This will include in particular the injection of test pulses below the nominal detector threshold, which can be reconstructed using the known time stamp, allowing for an exact offset determination.

5.7 Light Yield and Bands

The light yield as a function of energy is depicted in the following section for the neutron calibration (figures 5.16-5.19) and the dark matter dataset (figures 5.21-5.28). For each module, a bandfit is performed according to section 3.4.1 in order to define an acceptance region for dark matter events to be used in Yellin's optimum interval approach, and to set up the likelihood model according to section 3.5.2. Each event is weighted with the signal survival probability at its respective energy (cf. Section 5.9).

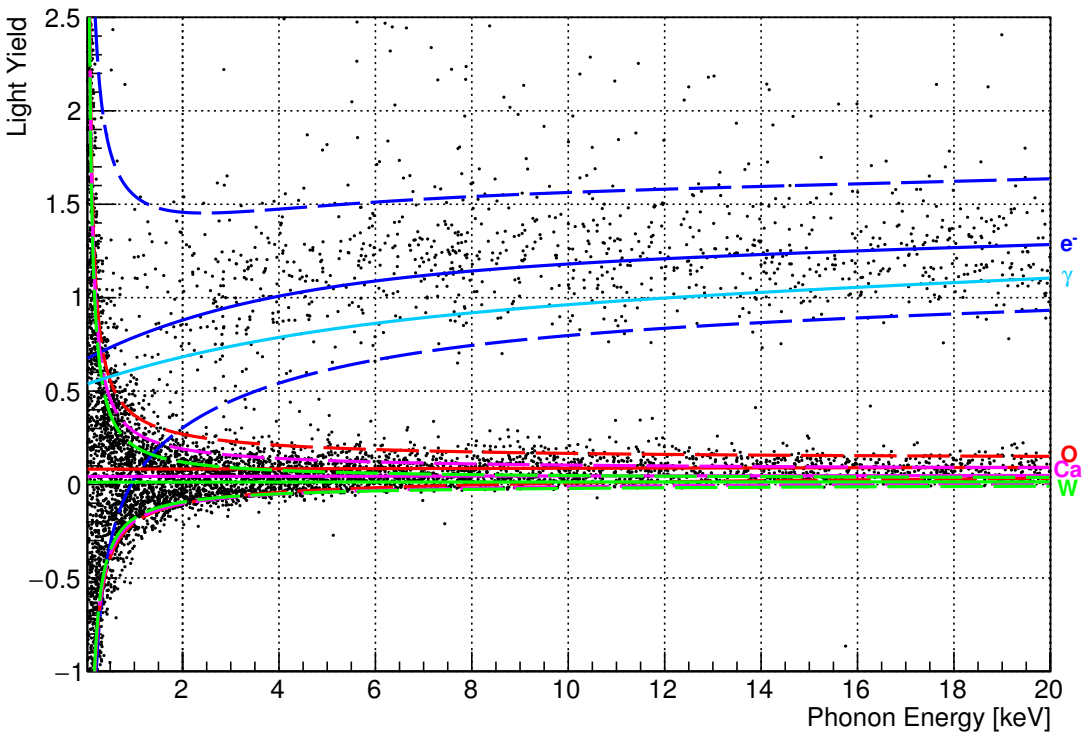

Figure 5.16: Bandfit and neutron calibration for detector A. The bands drawn are for recoils off electrons (blue), Oxygen (red), Ca (purple), and Tungsten (green). A mean line for γ events is shown in light blue.

The results of the bandfit are drawn additionally in each of Figures 5.16-5.27, where the blue, red, purple and green solid lines mark the mean lines of the electron, O, Ca and W recoil bands, respectively. The corresponding dashed lines of the same color denote the 90 % contours. The mean line for the γ band is given in light blue. In each fit, the electron band parameters were determined using both datasets for the respective detector, while the remaining nuclear recoil band parameters are only constrained by the neutron calibration.

The recoil spectra for each component are treated separately in each dataset (cf. Section 3.4.1), and the dark matter dataset gives the results for γ peaks. Section 8.2 lists all band and spectral parameters, and provides more information on the fitting procedure.

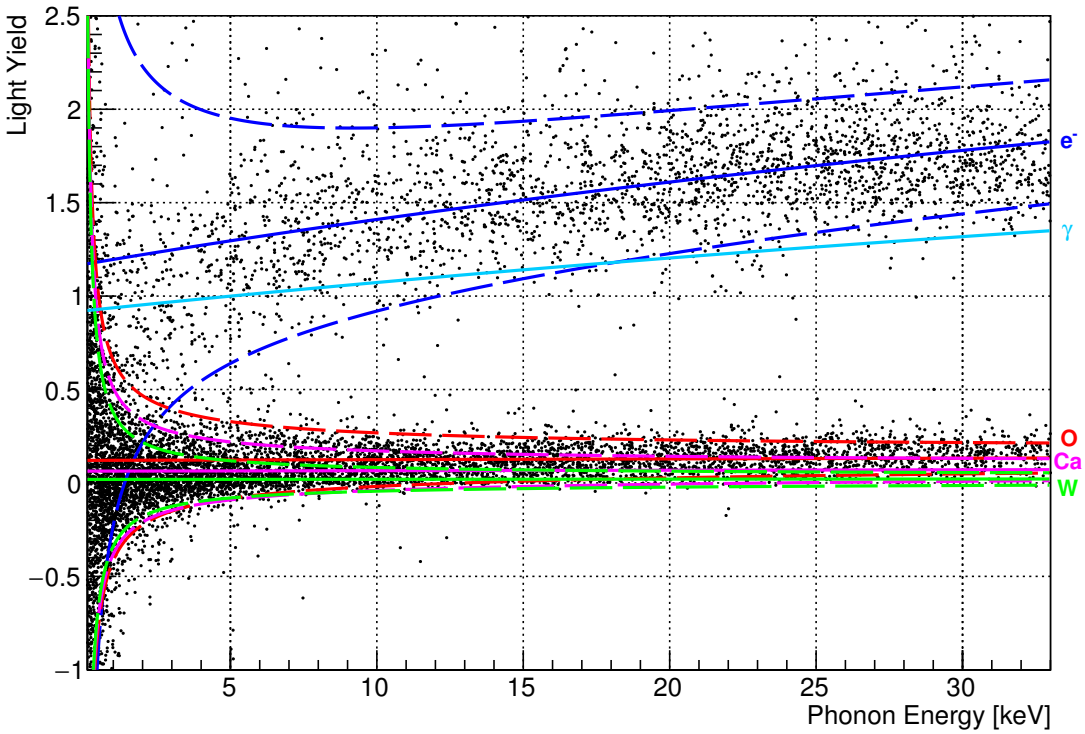

Figure 5.17: Bandfit and neutron calibration for detector B. The bands drawn are for recoils off electrons (blue), Oxygen (red), Ca (purple), and Tungsten (green). The mean line for γ events is shown in light blue.

Several events appear between the bands and below the nuclear recoil bands in the neutron calibration data; some outliers are to be expected, since only 90 % contours are shown. While events with a significantly negative light yield are usually due to artifacts in the light channel, events between the bands can be interpreted as coincidences between a nuclear recoil and an electron recoil, where the time between different interactions cannot be resolved. Another possibility are recoils off nuclei from contaminations, i.e. impurities in the crystal, although this is highly unlikely due to the low level of contaminants. In all detectors, excess light events are visible above the electron band.

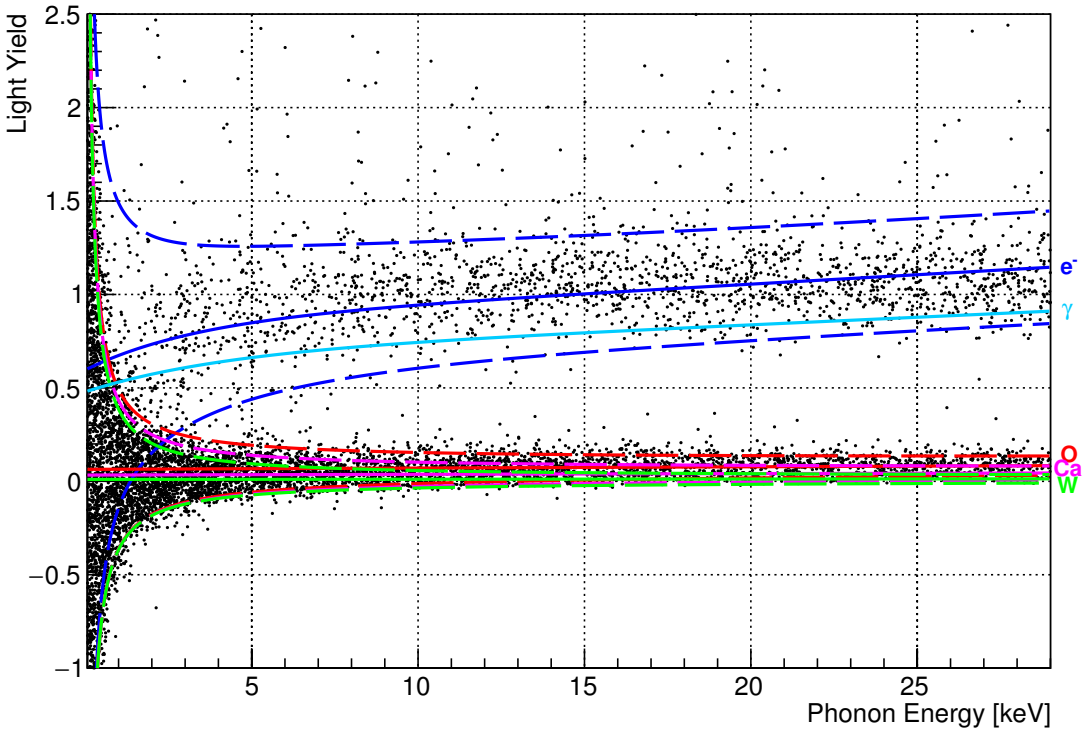

Figure 5.18: Bandfit and neutron calibration for detector E. The bands drawn are for recoils off electrons (blue), Oxygen (red), Ca (purple), and Tungsten (green). The mean line for γ events is shown in light blue.

Detector J (Figure 5.19) shows a strong nonlinearity in the resulting band model, which is due to the feature around 6 keV: events from the "line" force a larger width in LY of the electron band, which therefore incorrectly includes excess light events. This results in a larger nonlinearity, since the amount of excess light events decreases exponentially with energy. A cross check was performed for this detector, where all events between 5.5 and 8 keV were removed, and the survival probability, i.e. the number of events expected by the fit, was artificially set to zero for this region. The resulting electron band for detector J did not show a strong nonlinearity, and featured a smaller width, confirming the above explanation. It is shown overlaid with the modified neutron calibration data in Figure 5.20. This band description was not used in the limit calculation due to the modified signal survival probability; instead, the original bandfit result was used.

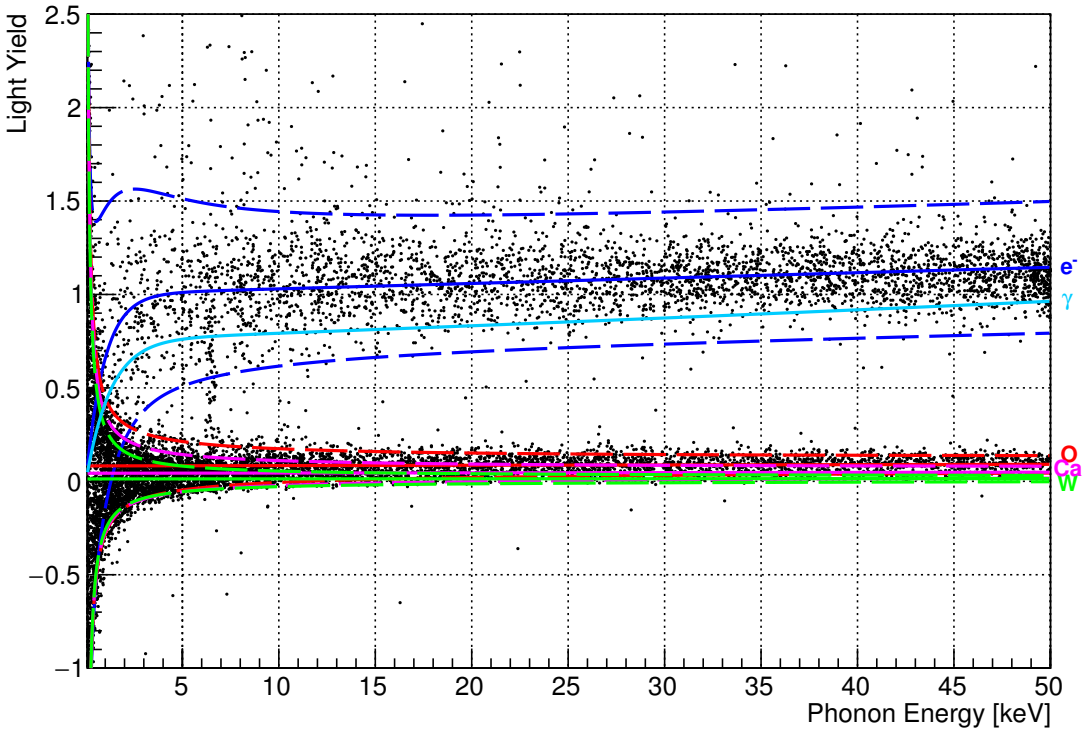

Figure 5.19: Bandfit and neutron calibration for detector J. The bands drawn are for recoils off electrons (blue), Oxygen (red), Ca (purple), and Tungsten (green). The mean line for γ events is shown in light blue.

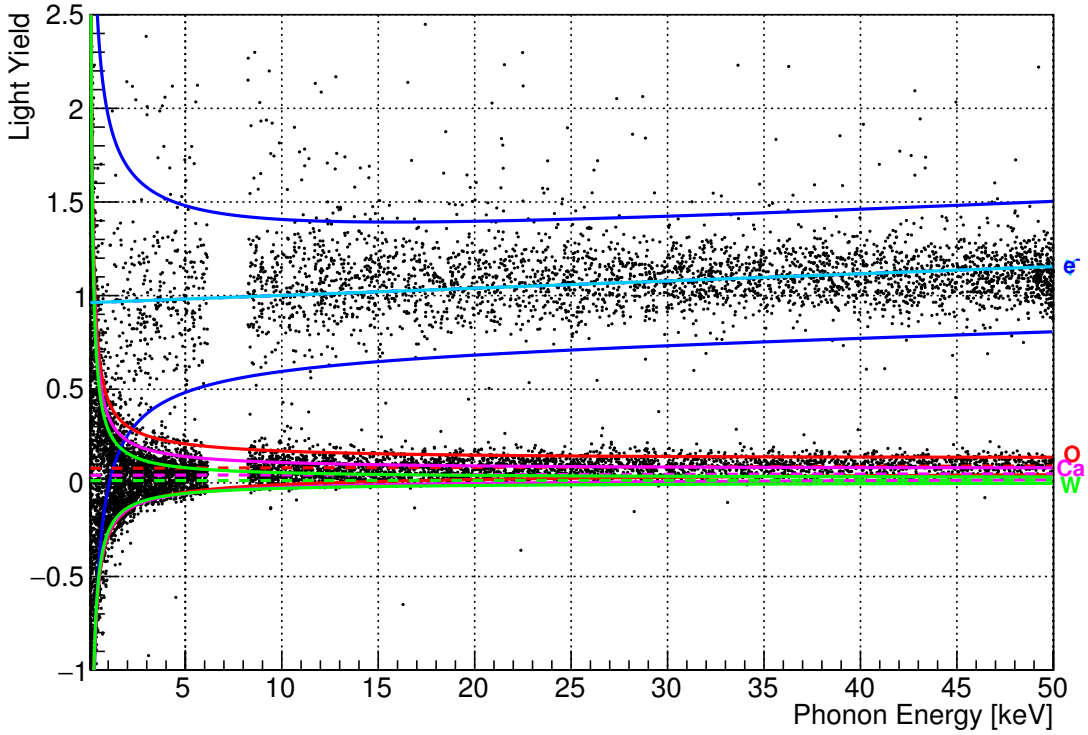

Figure 5.20: Modified bandfit and neutron calibration for detector J; the signal survival probability was set to zero between 5.5 and 8 keV. The bands drawn are for recoils off electrons (blue), Oxygen (red), Ca (purple), and Tungsten (green). mean line for γ events is shown in light blue.

For each dark matter dataset, the acceptance region for the Yellin limit calculation is indicated in yellow (Figures 5.21-5.28). It is defined by the 50 % O central line as upper limit and the 99.5 % W lower boundary as lower limit; this is discussed in Section 5.11. At low energies, the e^- and γ bands leak into the acceptance region, and an additional excess of events is visible in all detectors near the phonon channel threshold, which is inconsistent with the approximately constant density of the these bands. The low-energy region is highlighted in figures 5.22, 5.24, 5.26, and 5.28.

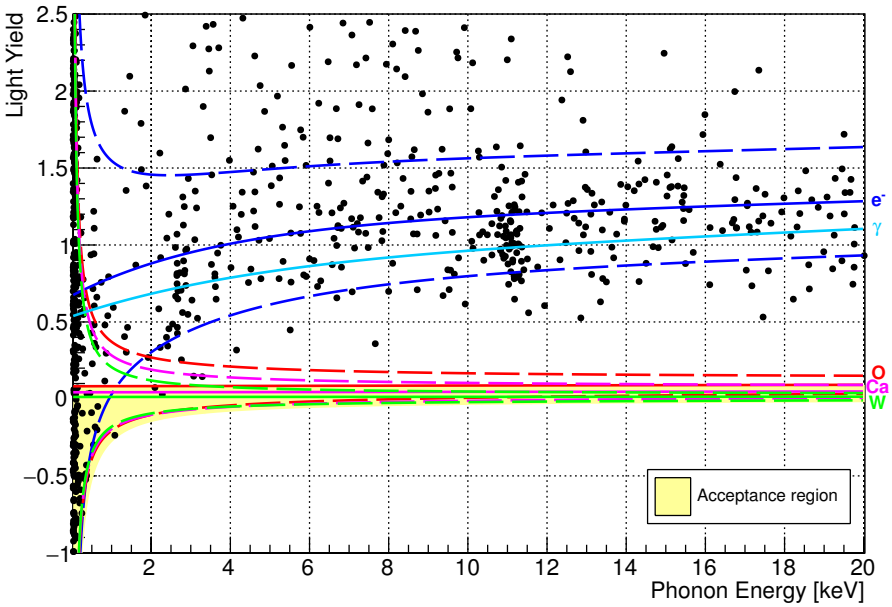

Figure 5.21: Bandfit and dark matter dataset for detector A. The bands drawn are for recoils off electrons (blue), Oxygen (red), Ca (purple), and Tungsten (green). The mean line for γ events is shown in light blue. The acceptance region used for Yellin limit calculations is depicted in yellow.

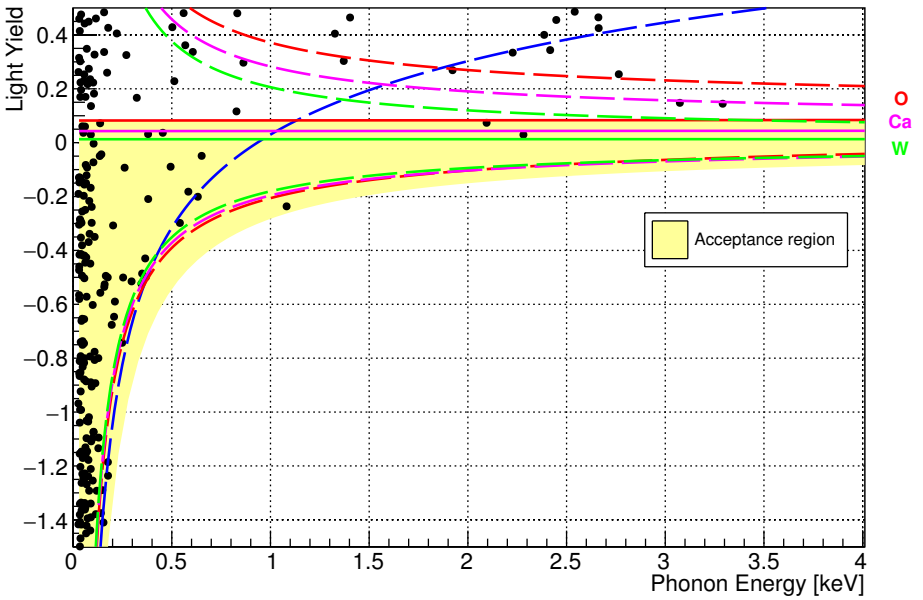

Figure 5.22: Zoomed version of Figure 5.21; the recoil energy range was chosen such that the most highly energetic events in the acceptance region are still visible.

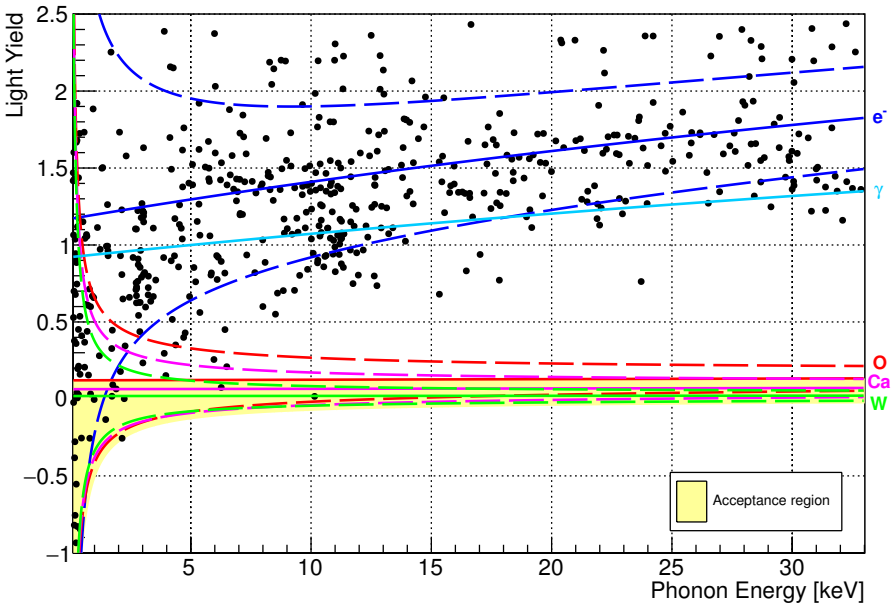

Figure 5.23: Bandfit and dark matter dataset for detector B. The bands drawn are for recoils off electrons (blue), Oxygen (red), Ca (purple), and Tungsten (green). The mean line for γ events is shown in light blue. The acceptance region used for Yellin limit calculations is depicted in yellow.

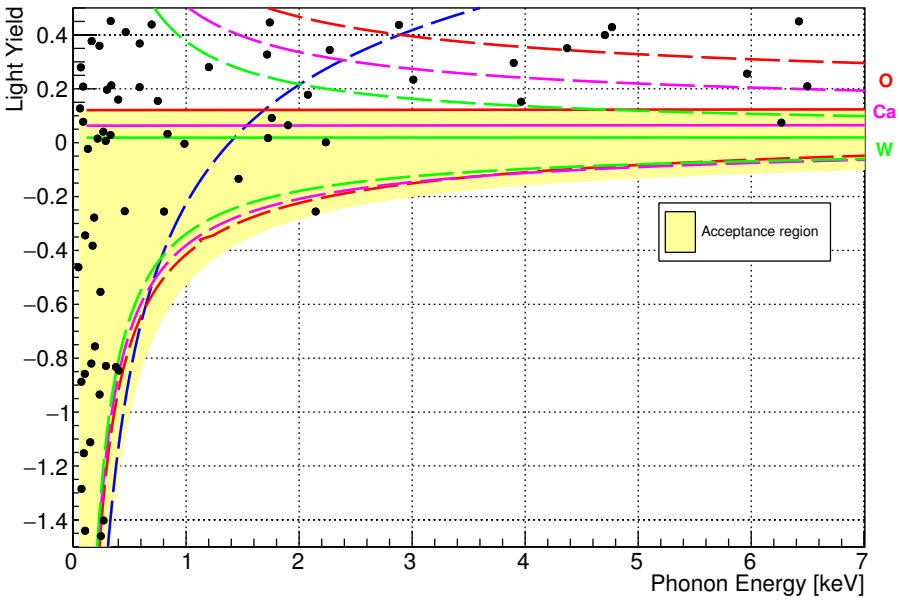

Figure 5.24: Zoomed version of Figure 5.23; the recoil energy range was chosen such that the most highly energetic events in the acceptance region are still visible.

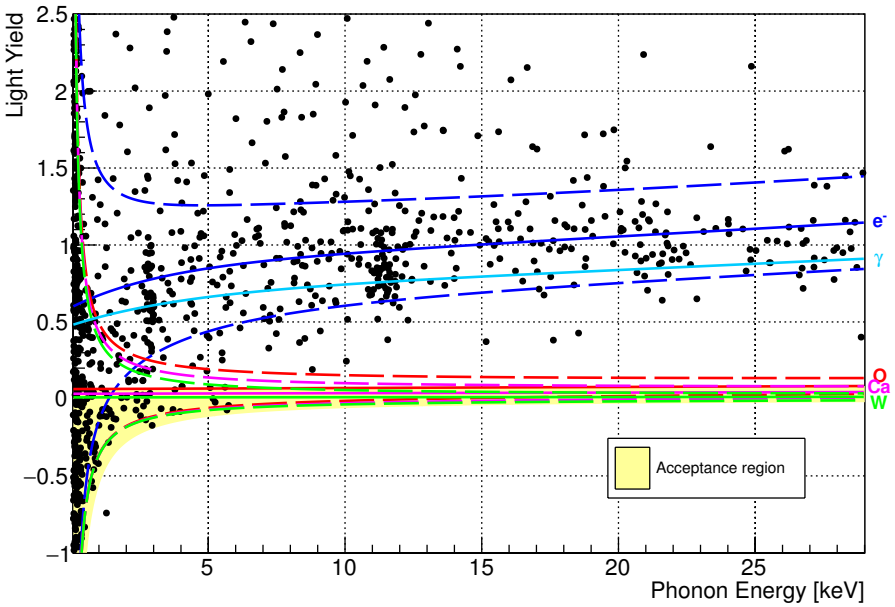

Figure 5.25: Bandfit and dark matter dataset for detector E. The bands drawn are for recoils off electrons (blue), Oxygen (red), Ca (purple), and Tungsten (green). The mean line for γ events is shown in light blue. The acceptance region used for Yellin limit calculations is depicted in yellow.

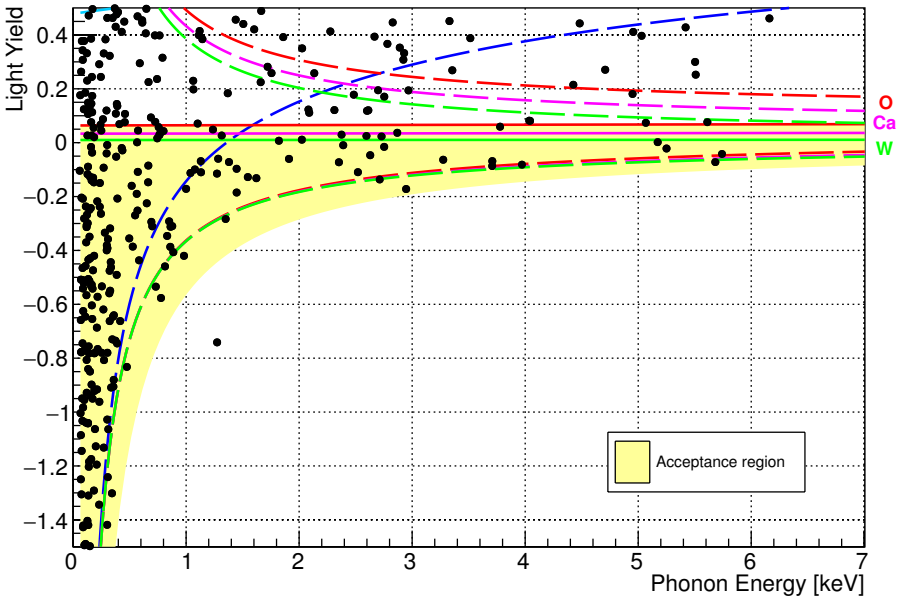

Figure 5.26: Zoomed version of Figure 5.25; the recoil energy range was chosen such that the most highly energetic events in the acceptance region are still visible.

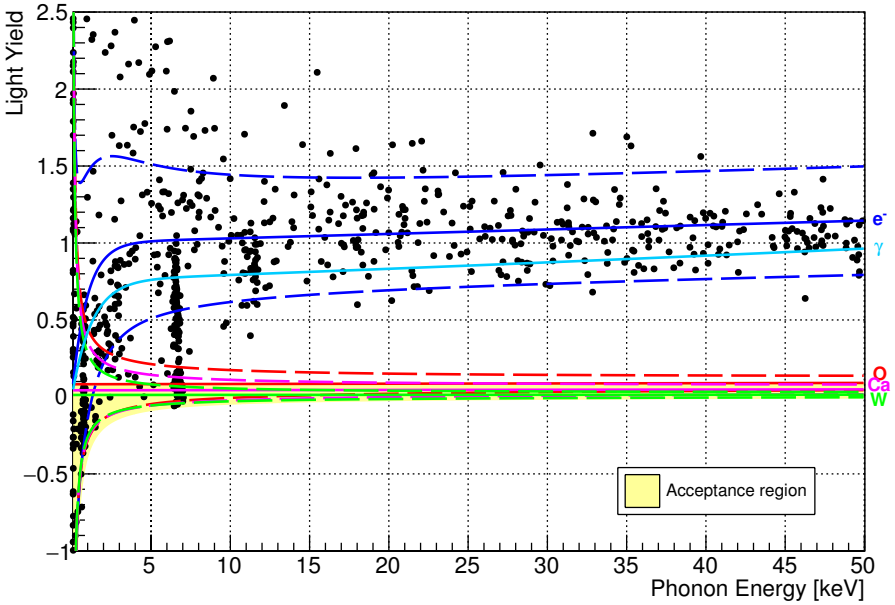

Figure 5.27: Bandfit and dark matter dataset for detector J. The bands drawn are for recoils off electrons (blue), Oxygen (red), Ca (purple), and Tungsten (green). The mean line for γ events is shown in light blue. The acceptance region used for Yellin limit calculations is depicted in yellow.

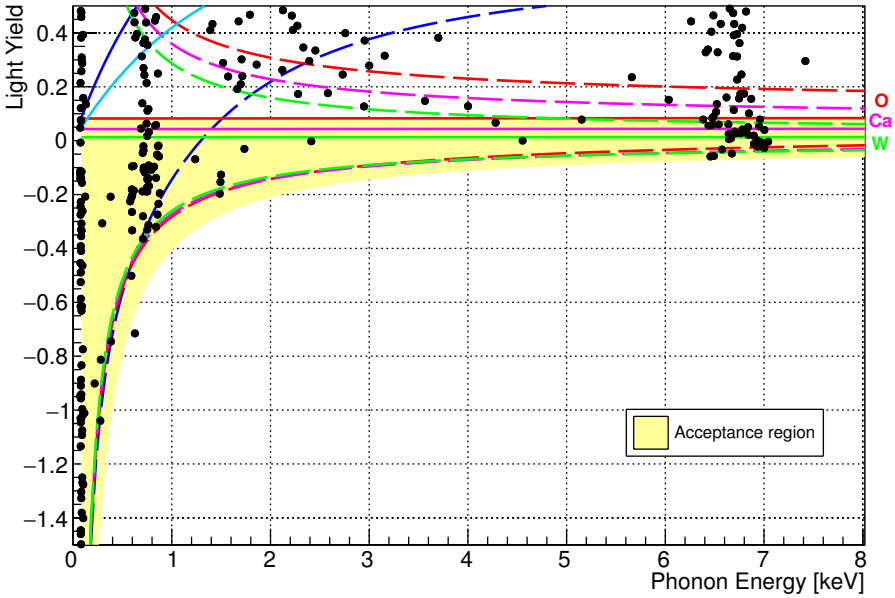

Figure 5.28: Zoomed version of Figure 5.27; the recoil energy range was chosen such that the most highly energetic events in the acceptance region are still visible.

5.8 Energy Spectra

A spectrum in phonon energy is given for each detector module, where events above a certain light yield are excluded (see caption for each module) in order to remove excess light events, and a binning of 0.1 keV was chosen. The cosmogenically induced Hf L1 (E=11.27 keV) and Hf M1 (E=2.6 keV) γ lines used for calibration are visible in all spectra. As the fit of these lines for calibration purposes was carried out separately from the bandfit, which also includes fit parameters for the background spectra (cf. Section 3.4.1), results of the latter can be used as a cross check. All lines included in the bandfit and their activities are given in Table 5.14 in Section 5.13. In the case of detector E, a known copper fluorescence line is visible clearly enough in the neutron calibration to be used for another calibration cross check. Its position is roughly consistent with the literature value of 8.048 keV. It should be emphasized that all the lines show very low statistics. The maximum energy in each spectrum is given by the upper limits on the trigger filter amplitude and the standard event fit amplitude.

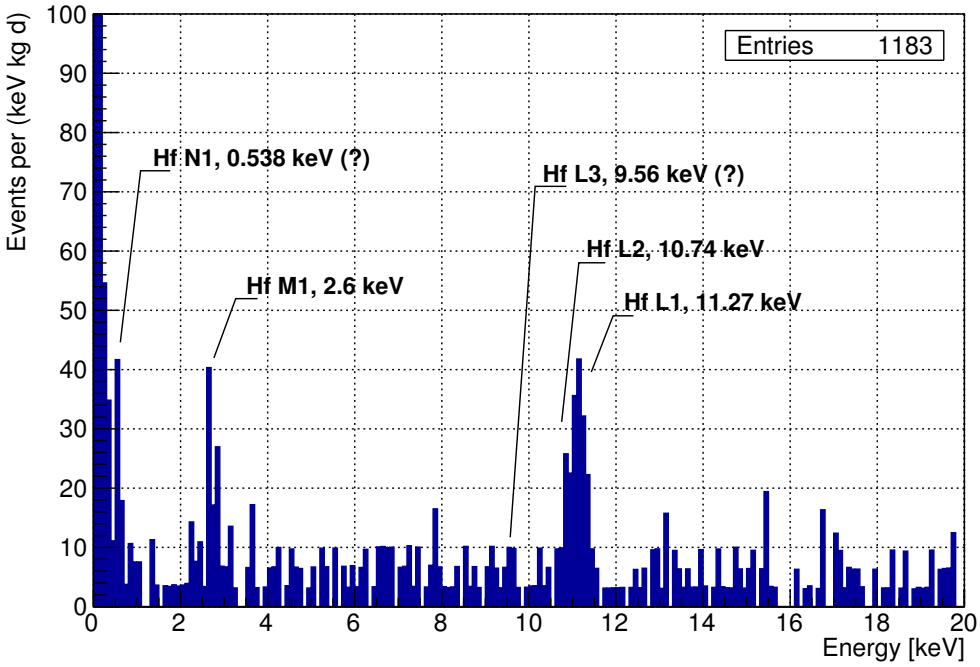

Figure 5.29: Background spectrum in detector A; events with a light yield below 1.6 were selected.

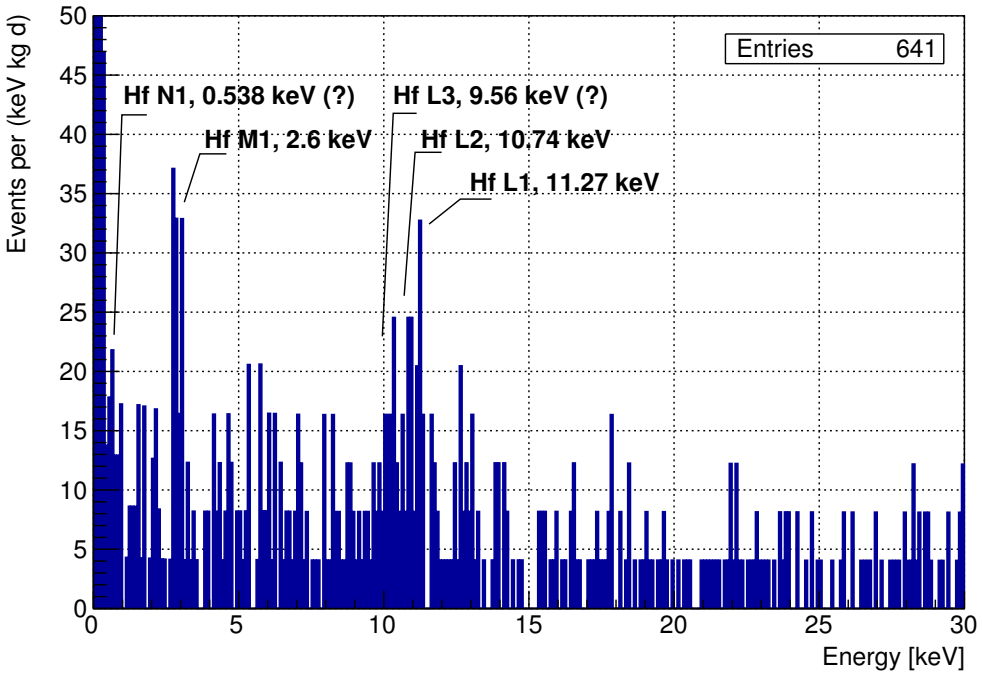

Figure 5.30: Background spectrum in detector B; events with a light yield below 2.5 were selected.

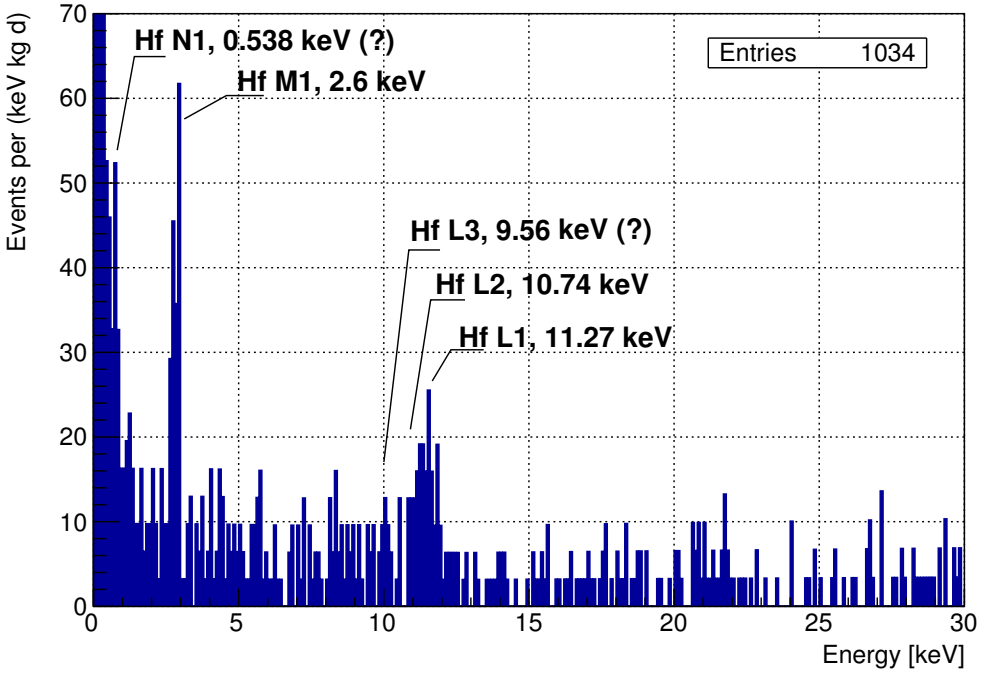

Figure 5.31: Background spectrum in detector E; events with a light yield below 1.5 were selected.

Another line below 1 keV appears in the detectors, the origin of which is unclear. A detailed discussion about possible background contributions is given in Section 5.13. The most prominent feature by far is an excess at low energies, which seems to be exponential in shape, and largely influences the dark matter exclusion limits; this will be analyzed in Section 5.12.1. In detector J, the phonon energy of the event population above 6 keV lies close to the lines from a ^{55}Fe γ source ($K_{\alpha,1}$=5.89875 keV, $K_{\alpha,2}$=5.88765 keV and $K_{\beta,1}$=6.49 keV) used in previous CRESST iterations for the calibration of light detectors. This could point to a leftover source as explanation, which is, however, very unlikely. The event population also shows a clear tilt in the light yield versus energy plane, which points to a γ origin (cf. Figure 5.27 and Section 3.4). The fact that also events without light occur and the difference in pulse shape are compatible with events occuring outside the detector and propagating into the absorber crystal; this is possible for anything hitting one of the absorber holding sticks, where the light would only enter the module through the transparent stick if the interaction happens near the wall. However, there is no signal in the stick channel for these events, which would only be possible if the corresponding stick did not work properly.

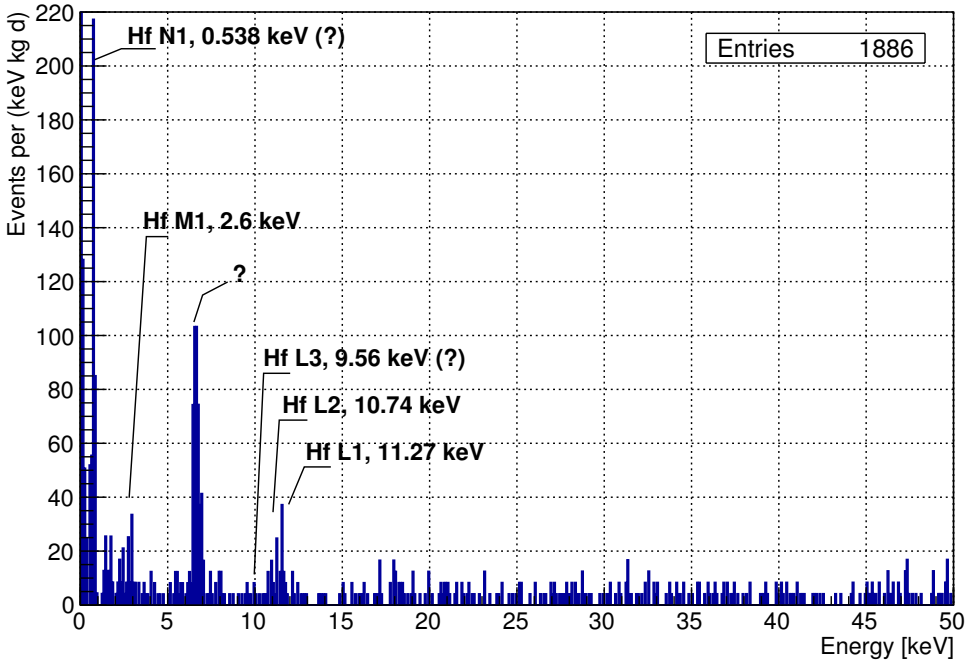

Figure 5.32: Background spectrum in detector J; events with a light yield below 1.5 were selected.

5.9 Survival Probability

As described in Section 4.1.2, a simulation of signal pulses is performed for all detectors using the recorded continuous stream. For detectors B, E and J, a fixed set of amplitudes is injected to the stream; for detector A, a flat energy spectrum is simulated in the interval [0-20]keV, where the upper value comes from table 5.9. The energy reconstruction used to determine the necessary pulse amplitudes originates from a different analysis chain [118] [119], therefore a cross check was performed to ensure that the reconstructed energy in this work matches the original injected energy reasonably well (cf. Section 4.1.2). This is illustrated in Figures 5.33 for surviving and 5.34 for removed events. Both show a systematic deviation above ~10 keV, i.e. the reconstructed energy is significantly larger than the injected one. Due to the fact that simulated pulses do not show saturation, the reconstruction assigns a higher energy, which explains this observation.

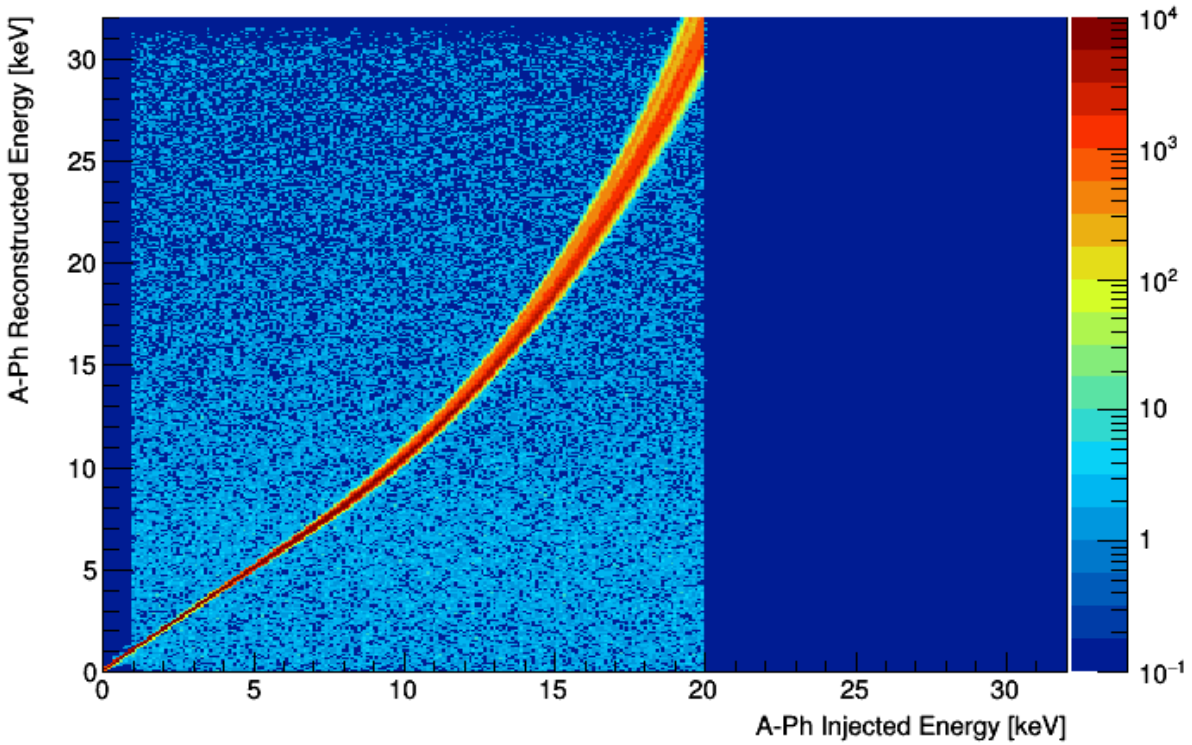

Figure 5.33: Reconstructed versus injected energy for the continuous stream simulation performed for the phonon channel of detector A. Only events surviving the selection criteria are considered.

Although a vast majority of events is reconstructed correctly, pile-up between simulated and real events results in some events where the reconstructed energy varies strongly from the injected one. In Figure 5.34, horizontal line-like structures are visible, which are due to coincidence of simulated pulses with test pulses. In such cases, the simulated pulse will get assigned the "energy" of the test pulse, if its amplitude is higher than that of the simulated pulse. Another feature at ~0.5 keV is caused by a filter effect due to control pulses; it is also visible in Figure 5.35 and will be discussed in the next section. If a simulated pulse did not trigger itself, but a small electronic feature caused the trigger to fire, the reconstructed amplitude will be close to zero. Since these events are typically removed by analysis cuts, their contribution is visibly reduced in the surviving event population (Figure 5.33). However, there are still pile-up events present, where the ratio between reconstructed and injected energy seems random. In both Figures, a cutoff is visible for pile-up events at a reconstructed energy of ≈30 keV. This is due to the saturating filter response for the coinciding real events; for the simulated pulses, the filter can still assign a higher amplitude as their pulse shape does not change.

As a further precaution, low-energy events below 1 keV where the reconstructed energy deviates by more than 5 % from the simulated one are removed, to circumvent the problem of survival due to pile-up with real events; more statistics at low energies would be needed to correctly model this effect and avoid "bumps" in the survival probability curve due to undersampling.

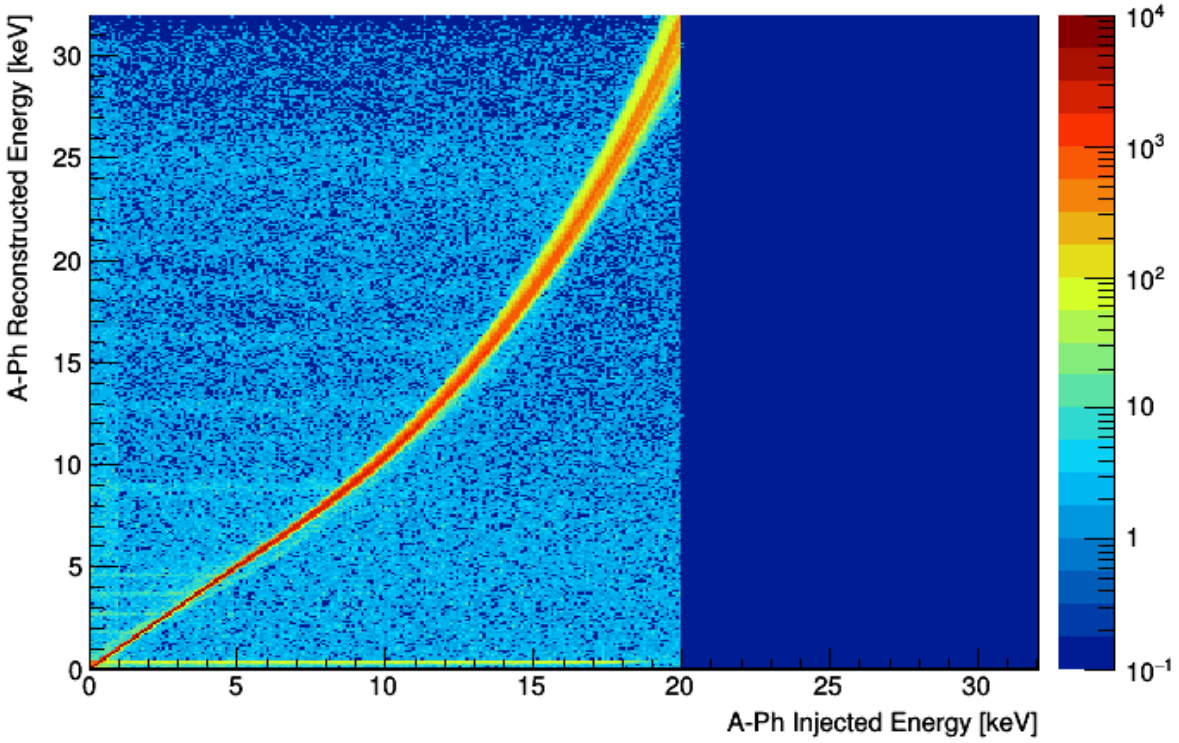

Figure 5.34: Reconstructed versus injected energy for the continuous stream simulation performed for the phonon channel of detector A. Only events NOT surviving the selection criteria are considered.

Figures 5.35, 5.36, 5.37 and 5.38 show the survival probability of simulated signal events as a function of their energies after different cuts have been applied. In all detecors, the trigger efficiency produces an error function (cf. Section 5.10) centered at the recoil energy threshold.

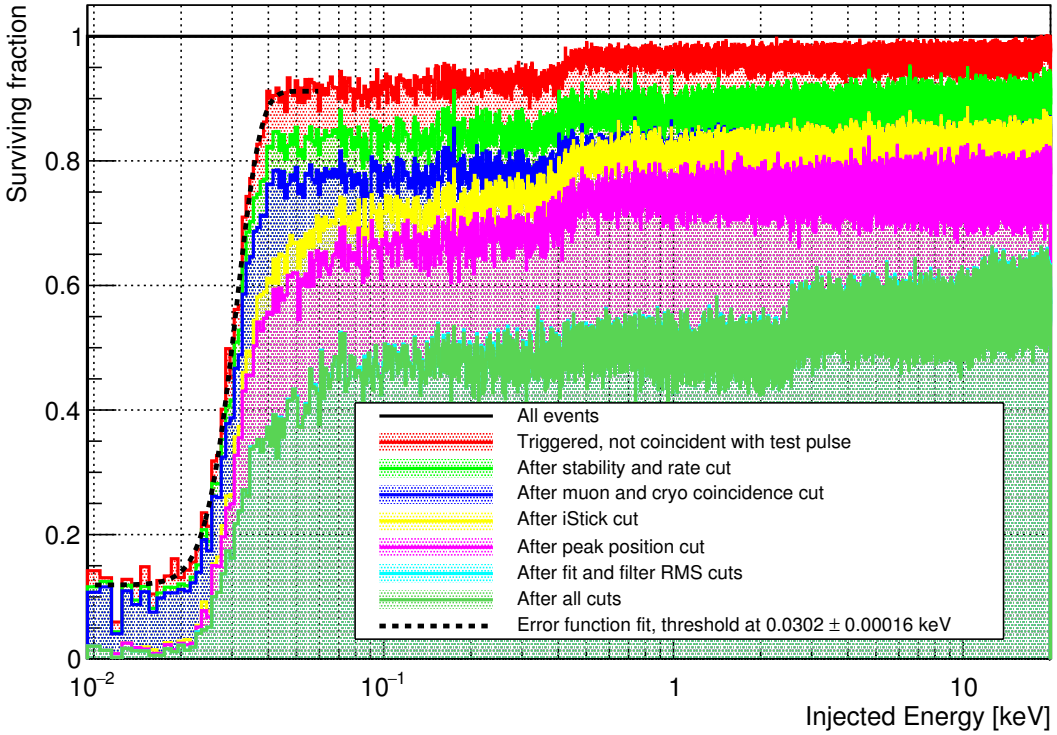

Figure 5.35: Survival probability of simulated events after different cuts for detector A. A continuous energy spectrum was simulated. Towards the detector threshold, which was extracted through a fit, the amount of triggered pulses (red curve) decreases sharply. For the bottom green curve ("After all cuts"), the following cuts were applied additionally: The voltage spike cut, the right-left baseline cut, the filter amplitude ratio cut, and the filter amplitude cutoff.

At ≈0.4 keV, a kink in the flat distribution of triggered pulses is visible for detector A (red curve in Figure 5.35); this is due to the influence of control pulses. In Figure 4.8, secondary maxima neighbouring the peak of each filtered pulse are visible. If a simulated event occurs near a recorded control pulse, and its filtered amplitude does not exceed the amplitude of the filtered control pulse's secondary maximum, the trigger algorithm will prefer the control pulse and the simulated pulse is lost. The effect is also present in other detectors, but the exact energy at which it sets in is not resolved by the discrete simulations. In fact, indications of multiple small steps are visible for B, E, and J, which can be attributed to test pulses of different amplitudes having a similar effect on the filtered stream. Generally, the simulation of a flat energy spectrum for detector A is able to resolve smaller details in the survival probability distribution, which is to be expected and strongly argues against only simulating a discrete set of amplitudes.

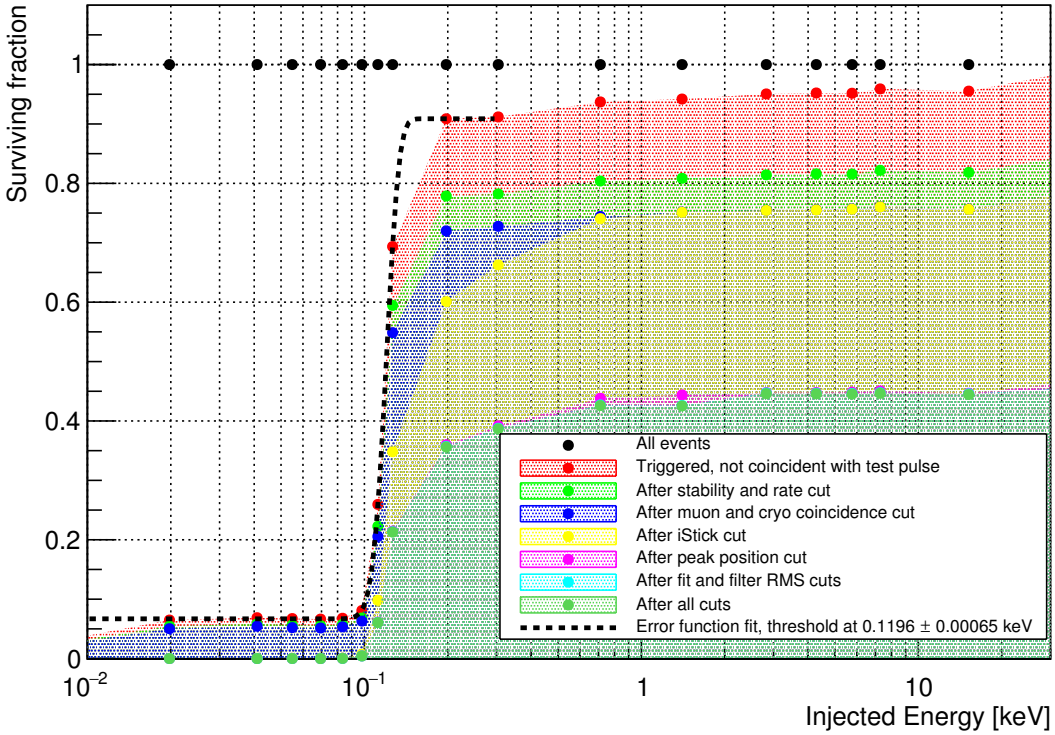

Figure 5.36: Survival probability of simulated events after different cuts for detector B. A discrete set of amplitudes was simulated. Towards the detector threshold, which was extracted through a fit, the amount of triggered pulses (red curve) decreases sharply. For the bottom green curve ("After all cuts"), the following cuts were applied additionally: The voltage spike cut, the filter amplitude ratio cut, and the filter amplitude cutoff.

In all detectors, the peak position cut removing pile-up events has a strong impact and removes up to 30 % of the events (detectors B, E in figures 5.36 and 5.37). Stability and rate cut remove a large portion of the pulses in detector J, which suffers most from "jump" events and thus periods of high rate (Figure 5.38). The effect of the iStick veto is almost non-existent at higher energies, and strongly pronounced at low energies for all detectors. Fit and filter RMS cuts mostly affect detector A, and produce an energy dependent structure in the survival probability (Figure 5.35). In the phonon channel of detector E, the cutoff due to the maximum reconstructable filter amplitude is clearly visible at 29 keV in the difference between the light blue and the dark green curve. This detector also shows a strong effect of the filter amplitude ratio and right-left baseline cuts.

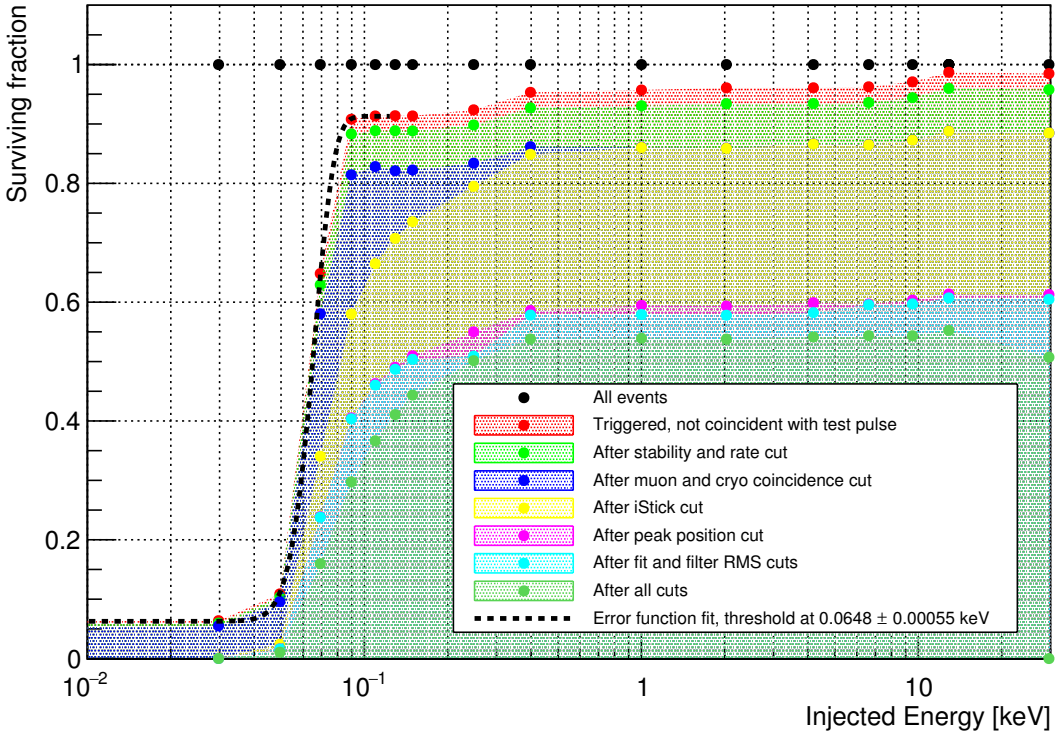

Figure 5.37: Survival probability of simulated events after different cuts for detector E. A discrete set of amplitudes was simulated. Towards the detector threshold, which was extracted through a fit, the amount of triggered pulses (red curve) decreases sharply. For the bottom green curve ("After all cuts"), the following cuts were applied additionally: The voltage spike cut, the right-left baseline cut, the filter amplitude ratio cut, and the filter amplitude cutoff. The latter is visible at 29 keV.

For detectors E and J (figures 5.37 and 5.38), the survival probability directly above threshold is reduced to ≈30 % due to the pulse shape cuts, which remove a large part of the signal, as the discrimination becomes worse. At higher energies above ≈1 keV, the signal fraction which survives all cuts is approximately constant in all detectors. Generally, the rate and stability cuts, as well as the iStick and peak position cuts and the muon veto randomly remove a constant fraction of the signal, while RMS cuts result in an energy-dependent survival probability. For detector J, the effect of the parametric fit rise time cut is visible via the difference between the light blue and the light green curve.

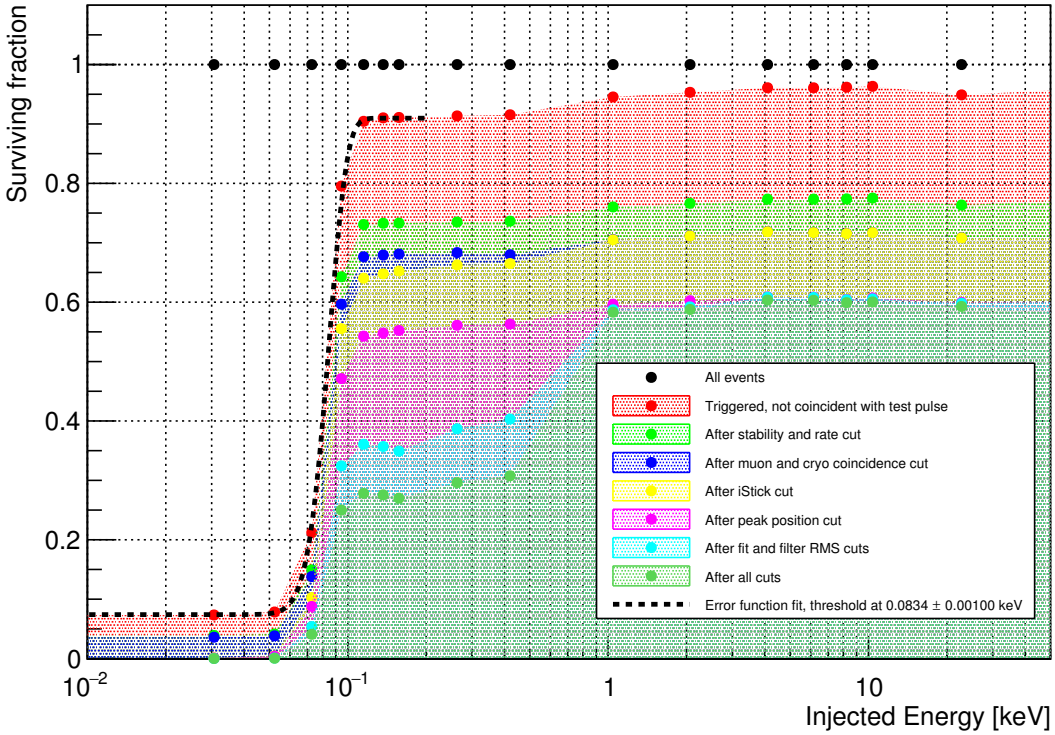

Figure 5.38: Survival probability of simulated events after different cuts for detector J. A discrete set of amplitudes was simulated. Towards the detector threshold, which was extracted through a fit, the amount of triggered pulses (red curve) decreases sharply. For the bottom green curve ("After all cuts"), the following cuts were applied additionally: The voltage spike cut, the right-left baseline cut, the filter amplitude ratio cut, and the filter amplitude cutoff.

In this detector, the chosen energy range of the simulation actually limits the reconstructable energy range, which was discovered only after finalizing the analysis for this detector; the maximum reconstructable filter amplitude would allow energy reconstruction up to ~100 keV.

5.10 Resolutions and Thresholds

In spite of lower resolution compared to detector A, the simulations for E, B and J are still sufficient to extract detector thresholds. This is done via the fit of an error function, to model the trigger turn-on curve as a convolution of the ideal step function with a Gaussian detector resolution. This function f of the injected energy E_{inj} is highlighted in Equation 5.2, and includes four parameters: The threshold p_{thresh}, the resolution p_{res} at threshold, the pedestal due to pile-up $p_{\text{pile-up}}$ and the maximum height of the distribution p_{scale}.

$$f(E_{\text{inj}}) = \frac{p_{\text{scale}} - p_{\text{pile-up}}}{2} \cdot \text{erf}\left(\frac{E_{\text{inj}} - p_{\text{thresh}}}{p_{\text{res}} \cdot \sqrt{2}}\right) + \frac{p_{\text{scale}} + p_{\text{pile-up}}}{2} \tag{5.2}$$

Due to coincidence with test pulses, the trigger efficiency will never reach 100 %, and p_{scale} will not be 1. In order to avoid the additional filter effect of these test pulses, which was explained in the previous section, only the low-energy region is used in each fit. Analysis cuts may introduce an additional energy dependence and cause a deviation from Equation 5.2, therefore all thresholds in this work are determined before cuts.

The resulting recoil energy threshold is indicated in the respective figure for each detector, and a summary is given in Table 5.10. With (30.21±0.16) eV, module A features the lowest phonon channel threshold, while B-Ph lies just above the design goal of 100 eV. For modules B, E, and J, larger uncertainties arise due to the small amount of simulated amplitudes; although each amplitude was simulated with sufficient statistics, only a few points are available for the fit. The resolution of each detector is determined according to Section 4.4; however, simulated particle pulses near threshold are used instead of injected heater pulses, and the converted filter amplitude (cf. Section 5.5) is used as energy estimator. For detector A, an additional simulation is performed here, while for B, E, and J, the same simulation as in Figures 5.35-5.38 is used. Table 5.10 shows that all resolutions obtained via this method are lower than the resolutions resulting from the survival probability fit discussed before. This may be due to the remaining effect of secondary (or tertiary) test pulse filter maxima; it can also be explained by the energy dependence of the resolution, which has not been accounted for in the fit.

Channel	Threshold [eV] (surv. prob. fit)	Resolution at threshold [eV] (surv. prob. fit)	Resolution at threshold [eV] (sim. pulse at threshold, converted filter amplitude)
A-Ph	30.21 ± 0.16	5.35 ± 0.20	4.81 ± 0.05
B-Ph	119.6 ± 0.65	10.29 ± 0.71	7.31 ± 0.12
E-Ph	64.76 ± 0.55	9.62 ± 0.48	7.90 ± 0.05
J-Ph	83.38 ± 1.00	11.66 ± 0.82	10.35 ± 0.06

Table 5.10: Recoil energy thresholds for the phonon channels of modules A, B, E, and J as extracted from the error function fit in Figures 5.35, 5.36, 5.37, and 5.38. The right column gives the result of a fit to the Gaussian distribution of reconstructed amplitudes for a simulated particle pulse near threshold.

Module	Light detector resolution at phonon threshold [eV]
A	132.7± 0.2
B	244.7± 3.2
E	285.2± 0.5
J	197.9± 0.4

Table 5.11: Resolutions of the light detectors in modules A, B, E and J at phonon channel threshold; for A, E, and J, the resolutions were determined via a simulation of events on the continuous stream. For detector B, the resolution of 2 mV test pulses was used.

The resolutions of the light detectors at the threshold of their corresponding phonon detector were also determined from simulated pulses on the continuous stream. For detector B, this simulation was not performed, and the resolution of 2 mV test pulses close to the threshold was used instead. The broader pulse shape of test pulses is more easily recognizeable than a particle event with the same pulse height, therefore the resolution obtained via this method overestimates the "real" resolution for signal-like events.

5.11 Dark Matter Exclusion Limits

Although the spectra shown in Section 5.8 all show a dark matter-like signal at very low energies, the different characteristics of the excess in each detector make a DM origin very unlikely, as will be discussed in Section 5.12.1. Therefore, upper limits are calculated according to Section 3.5. For Yellin's optimum interval approach, the acceptance region is defined in the following way: The 50 % line of the O band marks the upper border, while the lower border is given by the lower 99.5 % line of the W band, i.e. the lower boundary light yield above which 99.5 % of W recoil events are expected. This is illustrated in Figures 5.21, 5.23, 5.25 and 5.27 in yellow. These borders are chosen prior to unblinding in accordance with earlier CRESST analyses, in order to allow for better comparability. They provide a reasonable compromise between reducing leakage of electrons and γs at low energies, including as much as possible of the nuclear recoil bands, and exploiting event discrimination at medium to high energies.

5.11.1 Spin-Independent Results

Figure 5.39 shows the resulting upper limit on the cross section for spin-independent, elastic scattering of dark matter particles off nuclei for each detector as a function of assumed dark matter particle mass. Due to its extremely low recoil energy threshold, detector A provides the strongest constraints down to a mass of 167 MeV/c^2, although the exclusion limit obtained with detector J is lower than that of detector A in a small mass interval. 'Kinks' in a limit are due to two effects: The change of the dominant target material from W at higher masses to Ca and then O at lower masses, and events with low LY located in the acceptance region. The latter case is visible in detector J, where events from the feature at 6 keV have a strong impact above masses of ~5 GeV/c^2. Multiple 'intersections' of several limits already provide a strong indication that the signal-like excess spectra in all modules (cf. Section 5.8) are not compatible with a particular dark matter particle mass and cross section. Instead, multiple different masses are "mimicked" in each detector module. Nevertheless, each strongly suffers from the excess at low energies.

In Figure 5.40, the resulting Yellin limit for detector A is compared to results from Xenon1t [52], Xenon100 [53], Panda-X [54], DarkSide [55], LUX [56, 57], EDELWEISS [58, 59], SuperCDMS [60], CDMSlite [61], DAMIC [62] and CDEX-10 [63], COSINE-100 [64], Collar [65], NEWS-G [66] and PICO [67], as well as positive evidence from CDMS-Si [60] and CoGeNT [68]. CRESST-II results obtained with the detectors TUM40 [69] and Lise [70] are also shown. New parameter space is explored below dark matter particle masses of 1.6 GeV/c^2 in comparison to Lise and CDMS Lite; the original projection for CRESST-III [98] assuming 50 kgd of exposure and a

threshold of 100 eV is shown as a light red band. The theoretical cross section for elastic neutrino-nucleus scattering off $CaWO_4$ [72] marks the upper border of the gray area; this process would provide a background which is not distinguishable from dark matter recoils on event-by-event basis.

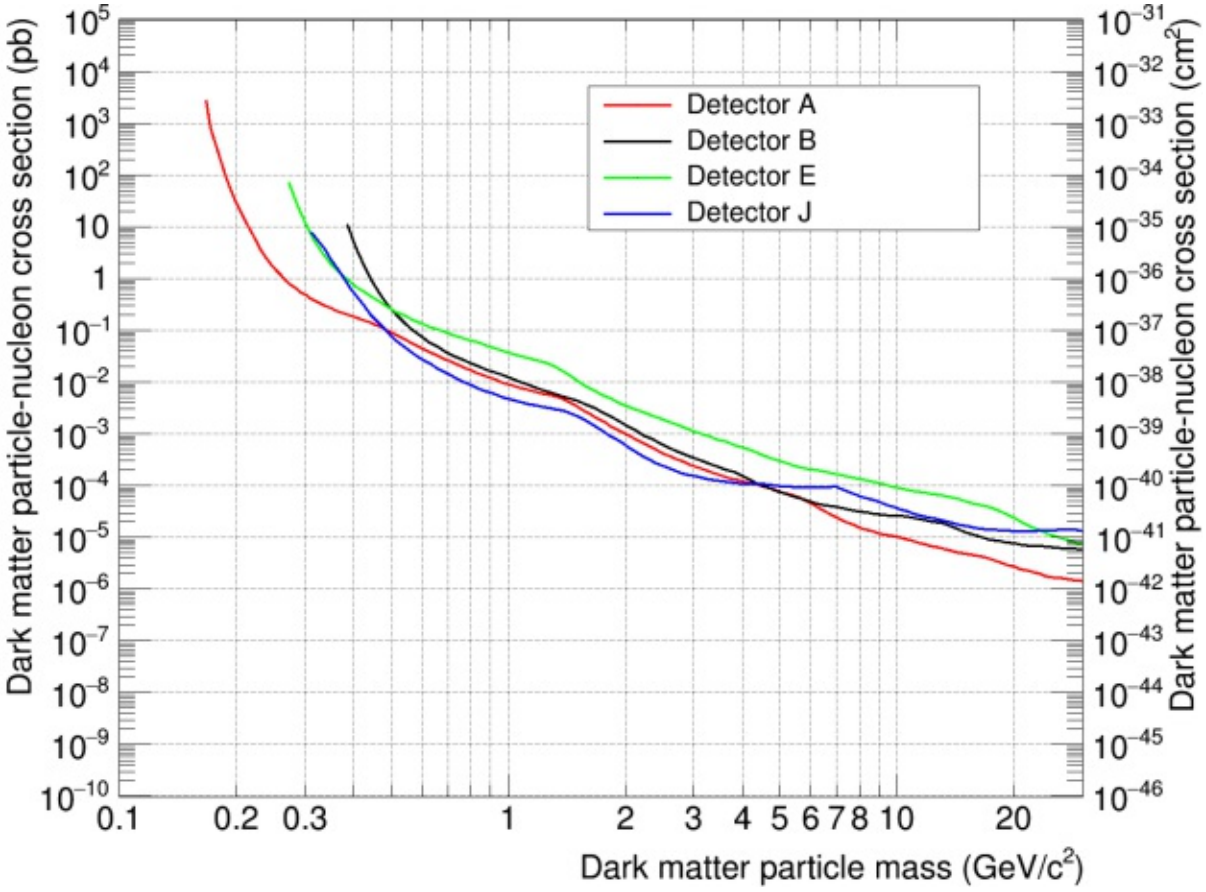

Figure 5.39: Upper limits on the cross section for spin-independent scattering of dark matter particles off nulcei as a function of dark matter particle mass obtained with detectors A, B, E and J via Yellin's optimum interval method.

Although detector B features the highest nuclear recoil energy threshold of the modules presented in this work (119.6 eV), it provides a significantly stronger bound than detector E (64.76 eV) over the mass range above 0.5 GeV/c^2. The same is true for detector J (83.38 eV) with a threshold comparable to that of E; in both cases, this is caused by the background spectrum near the threshold in detector E, which is relatively flat and extends to higher energies (see Figure 5.31).

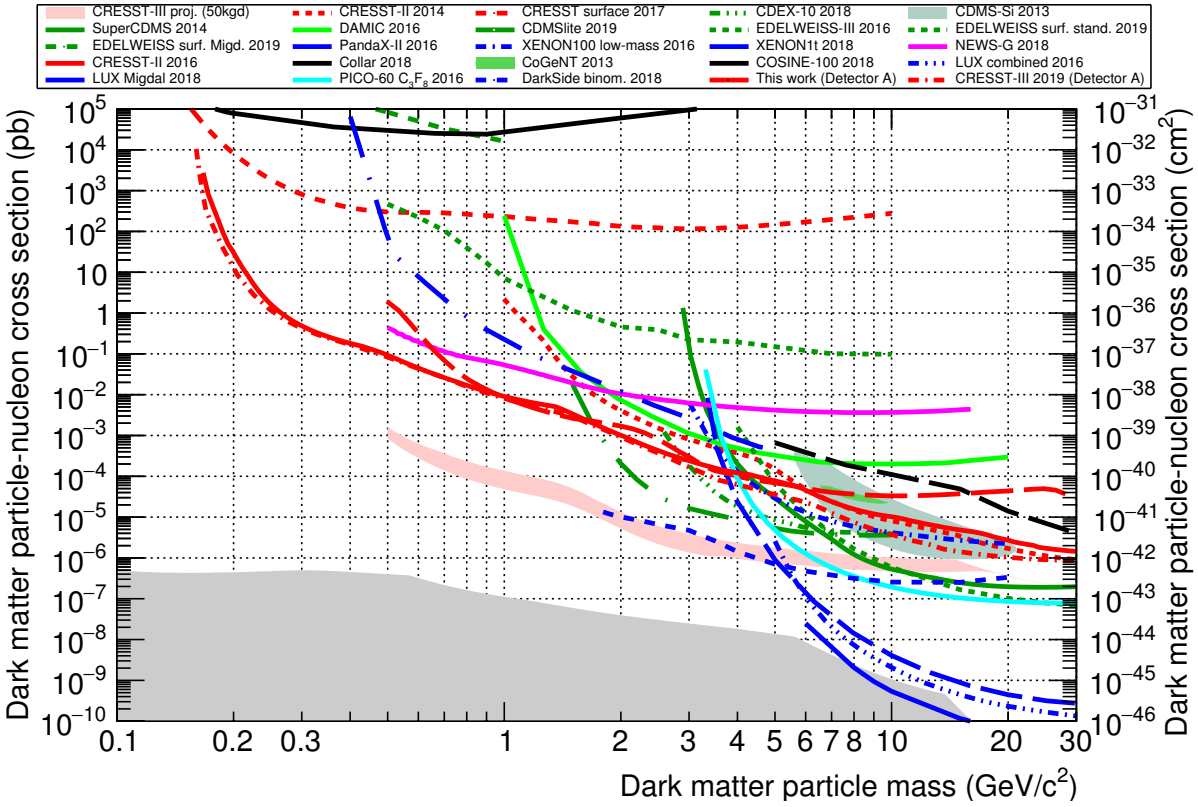

Figure 5.40: Upper limit on the cross section for spin-independent elastic scattering of dark matter particles off nuclei as a function of assumed dark matter particle mass, obtained with the full dataset of detector A via Yellin's optimum interval method (solid red line), in comparison to limits from Xenon1t [52], Xenon100 [53], Panda-X [54], DarkSide [55], LUX [56, 57], EDELWEISS [58, 59], SuperCDMS [60], CDMSlite [61], DAMIC [62] and CDEX-10 [63]. Liquid noble gas experiments based on xenon or argon are represented by blue colors, while silicon or germanium based solid state detector experiments are depicted in green. Results from COSINE-100 (NaI, dashed black line) [64], Collar (H, black line) [65], NEWS-G (Ne + CH_4, magenta) [66] and PICO (C_3F_8, cyan) [67] are also shown, along with positive evidence reported by CDMS-Si [60] and CoGeNT [68]. Previous results from CRESST-II obtained with detectors TUM40 [69] and Lise [70] are depicted as red dashed lines; the top red dotted line corresponds to a surface measurement performed with a gram-scale Al_2O_3 detector [71]. The dash-dotted red line marks the result of another analysis performed for the same detector and dataset published in [113]. All results represent upper limits at 90 % confidence level, apart from the CoGeNT(99 %) and CDMS signals. A red shaded area gives the initial projection for CRESST-III [98]. The gray area indicates the cross section below which background events due to coherent scattering of neutrinos off $CaWO_4$ are expected [72].

Figure 5.40 also shows the results of a second analysis performed for the same dataset [113]. It yields a comparable limit over the whole mass region, but gives a somewhat stronger constraint for particle masses above ~3 GeV/c^2. This is due to slightly different analysis cuts; in particular, the energy dependent cut on the standard event fit RMS is different and removes a few events from the acceptance region which survive in this work. At low masses below

~0.2 GeV/c^2, differences between the energy reconstruction chains start to have an influence; the signal simulation used in this work was originally adapted to [113], and thus gives a more precise signal estimation for the latter analysis. In particular, the pulses were simulated on the stream with a standard event different from that used for reconstruction in this work. This also explains the slightly lower resolution of 4.6 eV reported in [113], compared to 4.8 eV in this work. A better signal description and resolution allow for stronger constraints in case of lower statistics of surviving events near the detection threshold.

5.11.2 Spin-Dependent Results

Three stable isotopes are present in the target material $CaWO_4$ which have an odd nuclear mass number and a single unpaired neutron; these isotopes are ^{17}O ($J = +5/2$), ^{43}Ca ($J = -7/2$), and ^{183}W ($J = -1/2$). Using the natural abundances of 0.0367 %, 0.135 %, and 14.31 % [120], respectively, the exposures for each detector are calculated according to table 5.12. For ^{17}O, the minimum abundance quoted in literature is used, resulting in a more conservative estimate of the exposure.

Module	^{17}O [gd]	^{183}W [gd]	^{43}Ca [gd]	Combined [gd]
A	0.464	502.394	1.034	503.896
B	0.462	499.752	1.028	501.347
E	0.482	521.544	1.073	523.101
J	0.341	368.592	0.758	370.1

Table 5.12: Exposures for the spin-dependent analysis of several modules; all exposures were calculated from the total exposure (see table 5.1) using the natural abundances of ^{17}O, ^{183}W, and ^{43}Ca. Note that all exposures are given in gd instead of kgd.

These exposures can now be used to calculate exclusion limits on spin-dependent elastic scattering of dark matter particles off nuclei. The software used to extract these results is a modified version of [105] [121]; it uses the spin matrix elements $\langle S_n \rangle = 0.5$ for ^{17}O and ^{43}Ca [122], and $\langle S_n \rangle = -0.17$ for ^{183}W [123]. For ^{43}Ca and ^{183}W, the chosen values give the maximum absolute respective value for $\langle S_n \rangle$ compatible with literature; this provides a more conservative limit as the cross section increases with $\langle S_n \rangle^2$.
The resulting upper limits for Yellin's optimum interval method are given in Figure 5.41. Again, detector A provides the strongest constraint, while detector E yields the weakest. For some masses however, detector J provides a slightly stronger limit than detector A. With only the

signal expectation changed in comparison to the previous section, and thus mainly the cross section, this seems logical.

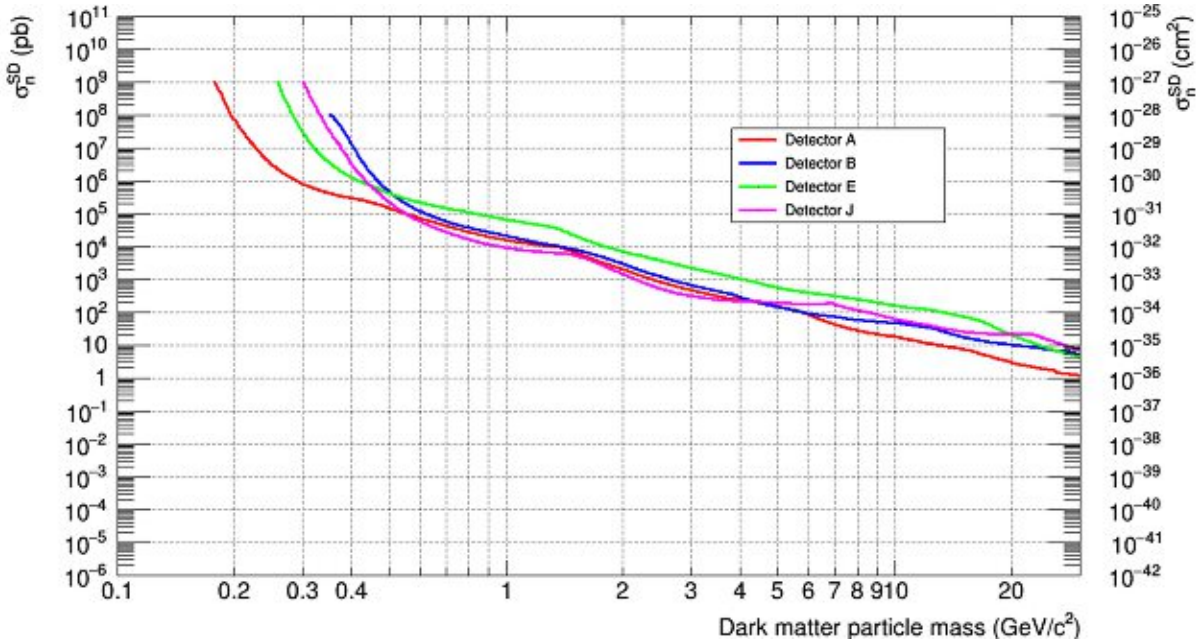

Figure 5.41: Upper limits on spin-dependent scattering of dark matter particles off unpaired neutrons for the isotopes ^{17}O, ^{43}Ca and ^{183}W for detectors A (red), B (blue), E (green), and J (magenta). Detector A provides the best upper limits over most of the DM particle mass range.

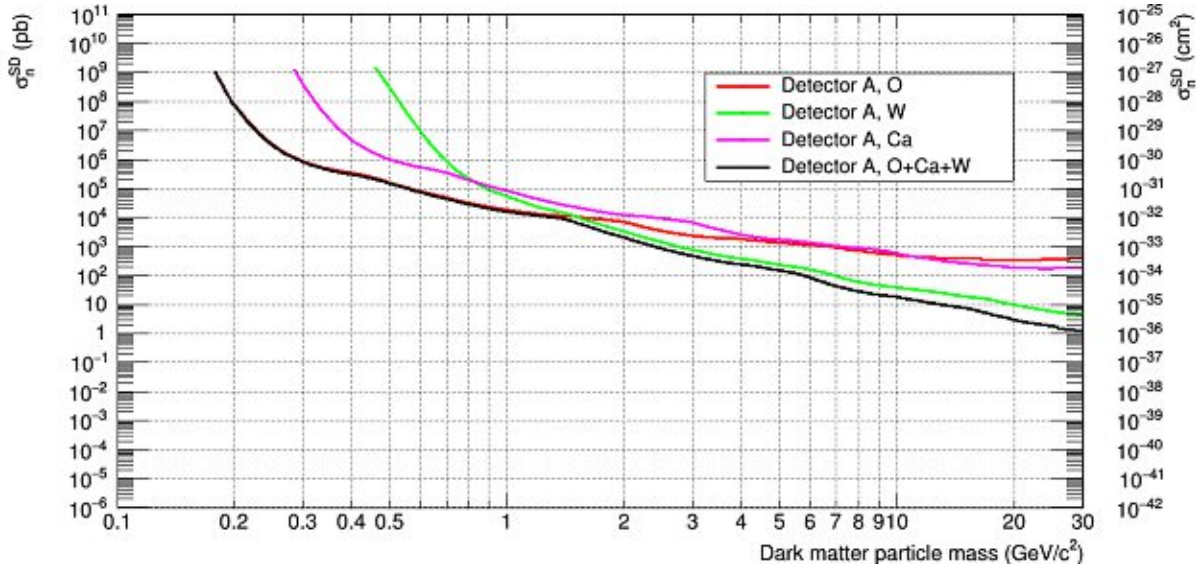

Figure 5.42: Upper limits on spin-dependent elastic scattering of dark matter particles off unpaired neutrons obtained with detector A and using Yellin's optimum interval method; limits from scattering off ^{17}O only (red), ^{183}W only (green) and ^{43}Ca only (magenta) are compared to the combination of the three isotopes (black).

The effect of different isotopes is highlighted in Figure 5.42 for detector A, where the calculation is repeated for recoils off each individual isotope only with the exposure varied according to table 5.12. At higher dark matter particle masses above ~2 GeV/c^2, the effect of ^{183}W recoils on the limit calculation dominates over ^{17}O recoils because of its higher abundance. While ^{43}Ca contributes to the sensitivity over the whole mass range, the other two isotopes are far more important.

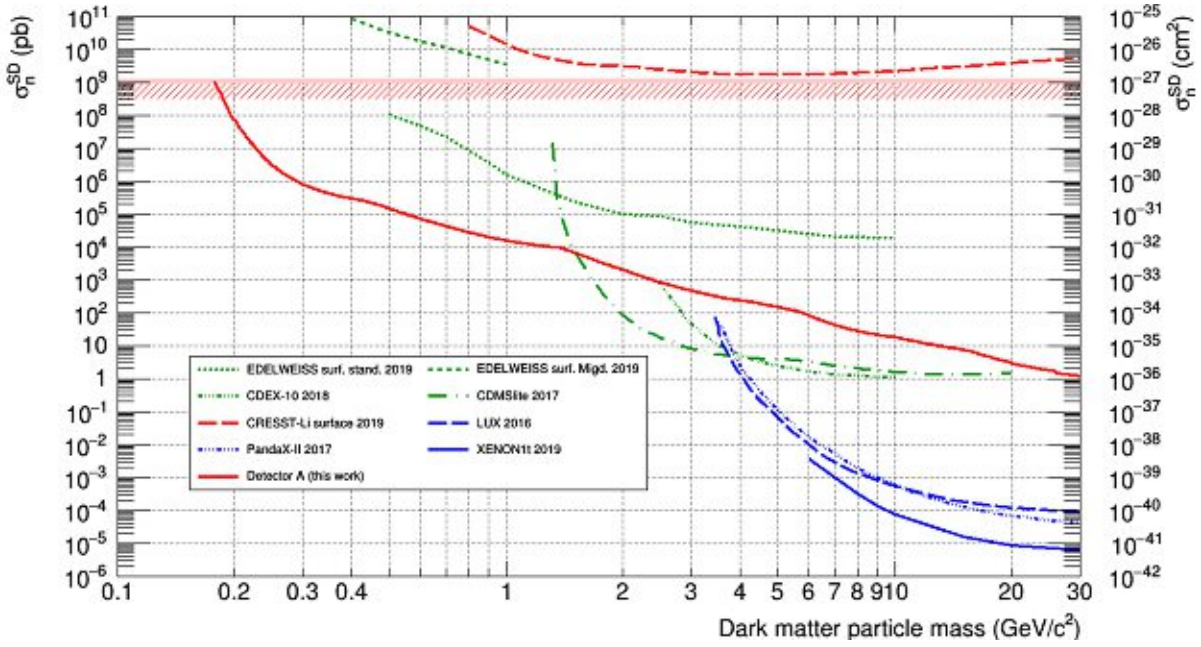

Figure 5.43: Upper limits on spin-dependent elastic DM-neutron scattering obtained from detector A in comparison with results from other direct detection experiments: CDMSlite [124], EDELWEISS [59], and CDEX-10 [63] (^{73}Ge), as well as LUX [125], Panda-X [126] and XENON1t [127] (^{129}Xe and ^{131}Xe) are shown. A ^{7}Li above-ground result from CRESST [88] is depicted as a dashed red line. The red shaded area shows the maximum detectable cross section at the Gran Sasso underground lab, obtained via considerations of earth shadowing [113].

Figure 5.43 compares the limit obtained with detector A to spin-dependent upper limits from other experiments such as CDMSlite [124], EDELWEISS [59] and CDEX-10 [63], featuring ^{73}Ge as target, and LUX [125], Panda-X [126] and XENON1t [127], which employ ^{129}Xe and ^{131}Xe. An above-ground result from CRESST [88] using ^{7}Li as target is also shown. Below a dark matter particle mass of 1.4 GeV/c^2, detector A yields the leading limit, and opens up the parameter space down to 167 MeV/c^2. In [113], a calculation was performed according to [128]: Taking into account the rock composition of the LNGS overburden [129], dark matter particles with a cross section greater than 10^9 pb would not be able to reach the underground laboratory. This effect is also called "earth shadowing" or "earth shielding".

5.11.3 Minimum Detectable Dark Matter Particle Mass

In case of an analytic description of the detector resolution and the expected signal spectrum, the limit calculation needs to be truncated manually. Otherwise, deviations in the tail of the real detector resultion from the Gaussian analytic model have a large influence for low-energy signal events, and result in an unrealistic amount of expected events above the detection threhold. For detectors E, B and J, the limit calculation was only performed down to the theoretical minimum dark matter particle mass able to deposit an energy above threshold in a recoil off O. This mass is given by the sharp cutoff in the signal spectrum due to the escape velocity (cf. Section 3.2). The nominal minimum mass is listed for each detector in table 5.13; for detector A, an upper limit is extracted for a mass as low as 167 MeV/c^2, where the corresponding maximum recoil energy lies 1.6 σ below the threshold. This limitation comes from the criterion that simulated and reconstructed event energies should not deviate by more than 5 % (introduced in Section 5.9). As the continuous spectrum simulation for detector A already accounts for the resolution, the limit calculation automatically stops as soon as zero events are expected above threshold. A detailed comparison of both methods (analytic and simulated signal spectrum) is the subject of ongoing research [130] [121].

Module	Minimum DM particle mass [GeV/c^2]	Recoil energy threshold [eV]
A	0.189	30.21
B	0.380	119.6
E	0.278	64.76
J	0.316	83.38

Table 5.13: Minimum detectable dark matter particle mass for a measured O recoil energy at threshold in detectors A, B, E and J.

5.11.4 Systematic Effects due to Varying Energy Calibration

Extremely low activities of the cosmogenically induced Hf lines which are used for the final energy calibration result in an uncertainty on the voltage to energy conversion in every detector. This is also evident from the comparison of the bandfit results in table 5.14 to literature values of the Hf peaks; the L1 line which should be at 11.27 keV varies by a few percent. To estimate the effect of this uncertainty on the exclusion limit, the Yellin limit calculation for detector A was repeated for the spin-independent scenario with the energy of each recorded event increased and decreased by 10 %, respectively.

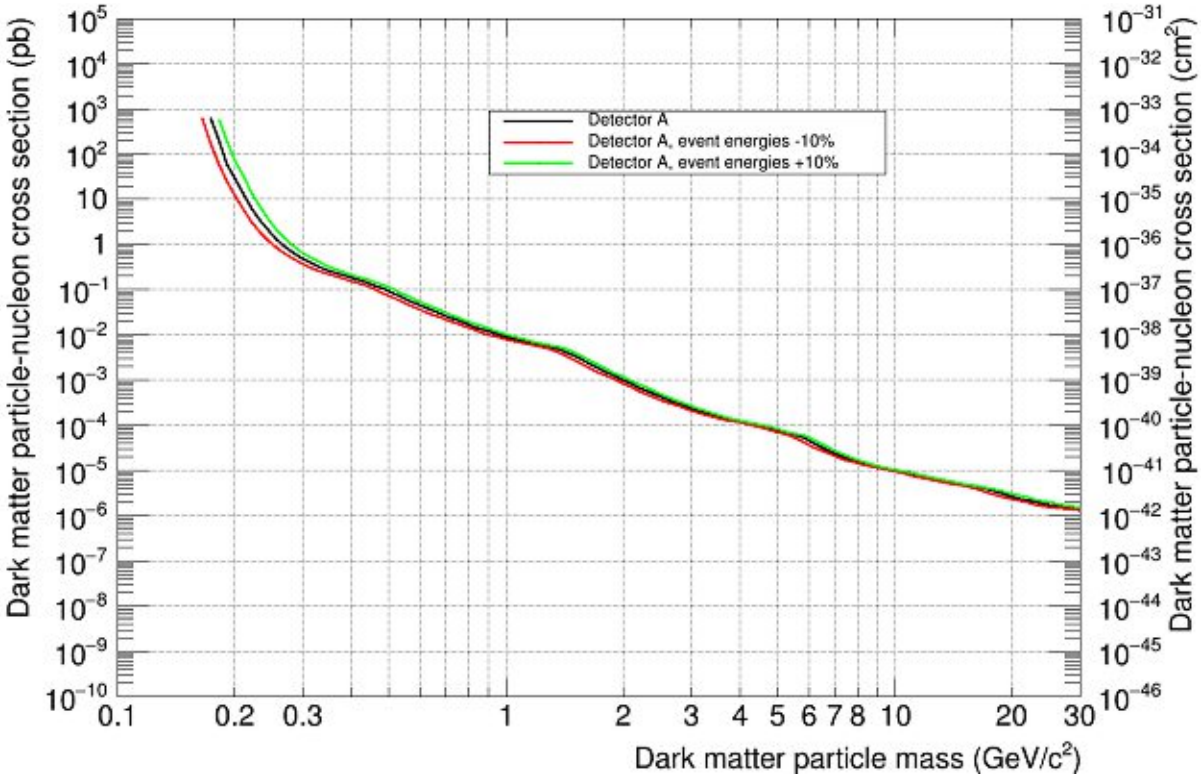

Figure 5.44: Optimum interval exclusion limit for spin-independent scattering obtained with detector A (black). The green limit was calculated with event energies increased by 10 %, while the red limit was obtained using event energies decreased by 10 %.

Figure 5.44 shows the resulting exclusion curves; the effect of the varied energy calibration is small, and only visible at very low masses. As described in Section 4.5, defining the phonon energy as the total energy of an event results in a slight overestimation of at most 6.6 %; from Figure 5.44, it becomes evident that this approximation results in a more conservative exclusion limit.

5.11.5 Likelihood Limits

Using the framework from [105], which was discussed in Section 3.5.2, a likelihood exclusion limit is calculated for detector A. It is depicted in Figure 5.45 in comparison to the optimum interval limit. At low particle masses, both methods yield the same result; at higher masses, the Yellin limit produces a stronger constraint. This was already observed in [105], and is due to the explicit background model in the likelihood function, which does not allow for an exponential background and explains the observation with signal. Yellin's optimum interval makes no assumption on the background spectrum, and basically ignores the low-energy recoil spectrum for higher dark matter particle masses (see [105] for a detailed discussion).

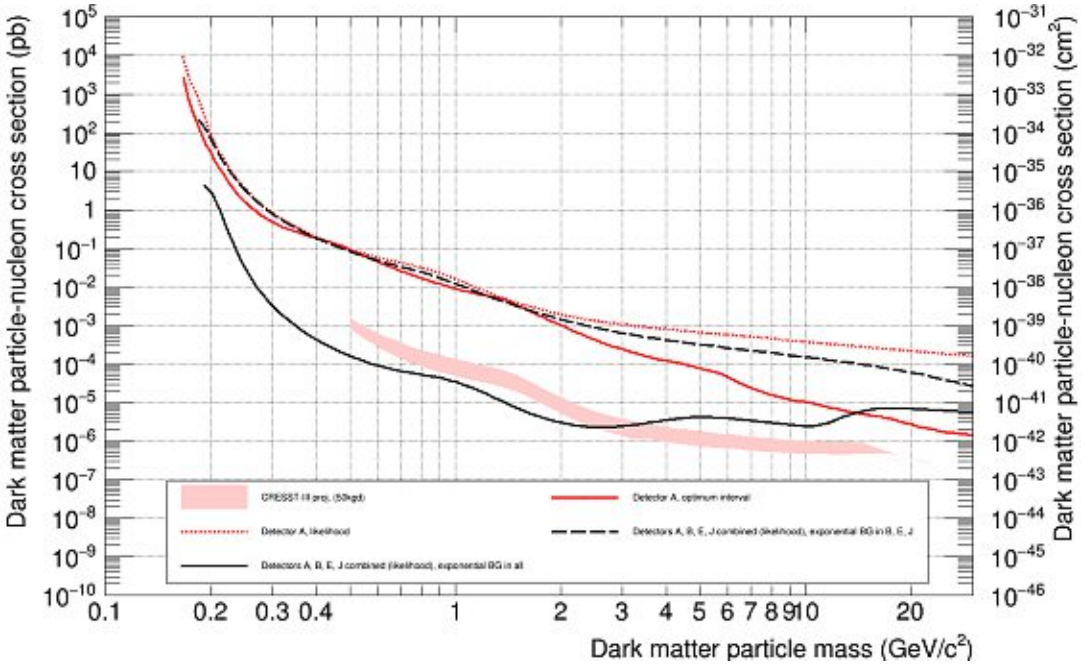

Figure 5.45: Likelihood limit for detector A (red dashed line) compared to the optimum interval limit (red line). A combined likelihood exclusion limit for detectors A, B, E and J is also shown (dashed black line), where an exponential background spectrum was allowed in the likelihood function for B, E, and J. If this is also allowed for detector A (solid black), the signal-like exponential excess is mostly ignored, and the resulting upper limit is compatible with the CRESST-III projection (red shaded area).

Arguably, a dark matter interpretation for low energy excess events is disfavored, since the excess appears differently in each detector module. By adding an additional exponential component to the expected differential recoil energy spectrum in the background model discussed in 3.4.1,

$$\frac{dN_{ex}}{dE}(E) = F_e \exp(-\frac{E}{D_e}), \text{ [121]} \tag{5.3}$$

the exponential excess can be accounted for as background in the likelihood function [130]. Another free parameter L_{lee} describes the mean light yield of these events. For the detector with the lowest threshold, the possibility of a dark matter signal is not excluded by any of the other modules; therefore the excess in detector A may be due to dark matter. However, the fact that an exponential background is present for every other detector makes this interpretation very doubtful. Using the likelihood ratio test, an upper limit is extracted for this hypothesis: For detectors B, E and J, an exponential background component is allowed, while for A it is not. The resulting exlusion limit is depicted in Figure 5.45 (dashed black line) in comparison to the Yellin and likelihood limits from detector A alone. While an improvement with respect to the combined limit is achieved at higher masses, the Yellin limit still provides the strongest bound.

The likelihood approach also allows assessing the limitation in terms of sensitivity due to excess events, and Figure 5.45 shows another modified upper limit (solid black line), where an exponential excess is allowed in all detectors. It is important to note that this result is not physically motivated; it simply shows the potential of the detector modules under the assumption that a different exponential background spectrum is present in each detector without giving an explanation for it. Compared to the combined likelihood limit, the upper limit cross section is decreased by one to three orders of magnitude. At masses above ~20 GeV/c^2, the Yellin limit from detector A is still lower. This is due to the surviving events in the acceptance region with recoil energies significantly above the exponential excess, which strongly influence the likelihood calculation, while the very low recoil energy range is not relevant for the Yellin method at these masses. No neutron background was allowed in the likelihood function, which is a conservative choice; a non-zero expectation would greatly enhance the exclusion limit from the likelihood calculation [121]. Additionally, a single exponential might not be a good fit for the excess in the likelihood function. Due to all these considerations, this limit should not be considered a projection for a background-free experiment. The initial projection for CRESST-III, assuming a threshold of 100 eV and an exposure of 50 kgd, is also depicted in Figure 5.45. A comparison to the exponential background likelihood limits clearly highlights the importance of the nuclear recoil energy threshold, which proves to have more impact than increased exposure, since only 20 kgd were used in this work.

5.12 Surviving Events

In the Yellin approach, each event in the acceptance region which has survived all selection criteria is considered a dark matter candidate. It is therefore reasonable to take a closer look at these events, and verify that they do not originate from detector baseline artifacts or misreconstructed background events.

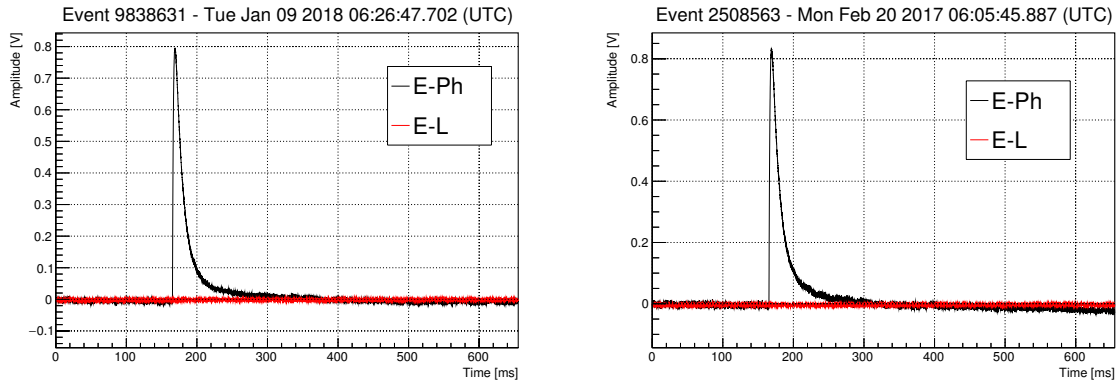

Figure 5.46: No-light events in the full dataset which survive all cuts. The two depicted events are the highest in energy which have no light.

Figure 5.46 shows the most energetic surviving events in detector E; they show no significant deviation in phonon pulse shape and no signal in the light channel at all, which is exactly what one would expect for dark matter recoils. Apart from the latter, neutrons could also produce these events. In [131], it was shown via simulation that $\sim 10^{-3}$ neutron events per kgd are expected, where a significant contribution is not due to natural radioactivity in the rock overburden, but instead caused by fission in the lead shield. This low number cannot explain the observed events, and their origin is not clear.

5.12.1 Low Energy Excess

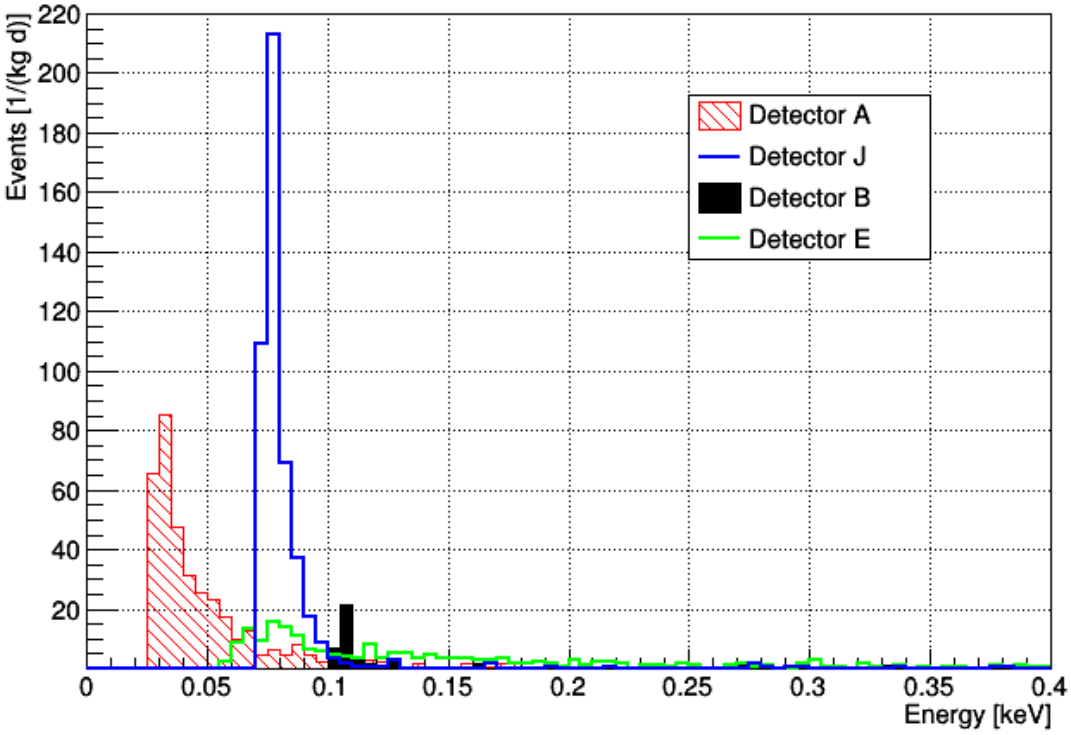

Figure 5.47: Phonon energy spectra for detectors A, B, E and J below 0.4 keV. An exponential rise of the event rate towards the threshold is visible for all detectors.

Figures 5.47 and 5.48 show a zoom to the low-energy region below 0.4 keV for the spectrum of each detector. A light yield cut of ±15 was applied, to include events within the e^-, γ and neutron bands and account for the widening of the bands at low energies. Each spectrum has been corrected, i.e. divided by the cut efficiency. For every detector, a rising event rate is visible at lowest energies just above the recoil energy threshold. The different spectra are inconsistent, i.e. the starting energy and amplitude of this excess varies in each detector, which suggests a systematic effect due to the detector setup. A particle physics origin is difficult to reconcile with the different measured spectra.

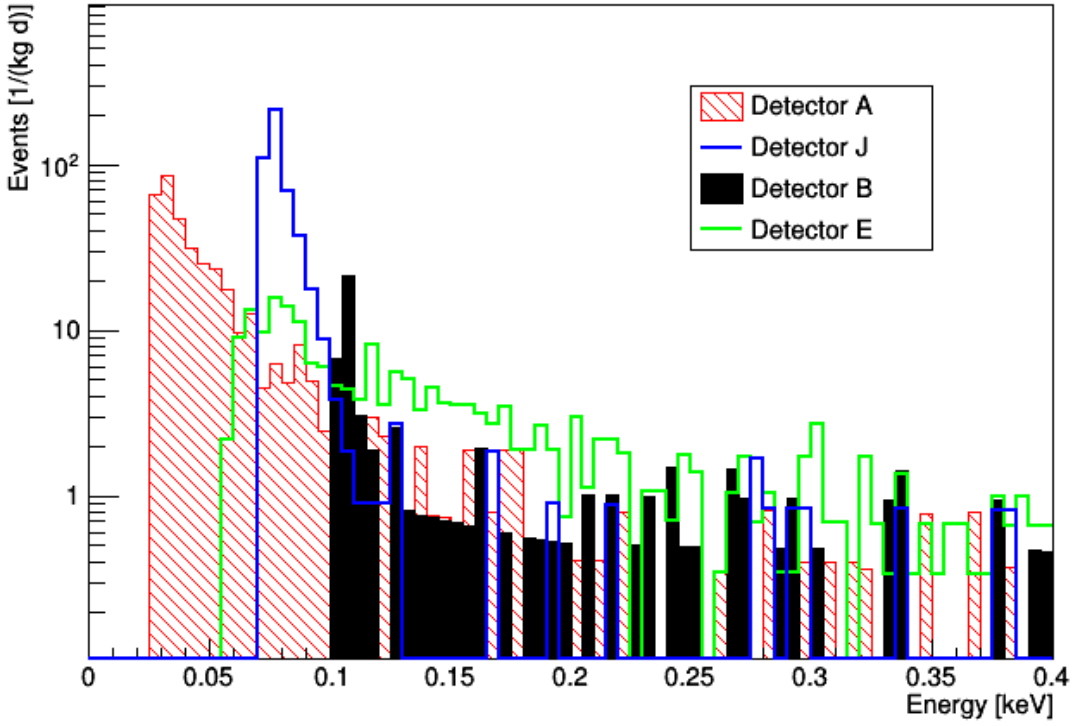

Figure 5.48: Phonon energy spectra for detectors A, B, E and J below 0.4 keV. A logarithmic y scale was chosen to highlight differences between the spectra.

5.12.2 Time Distance Analysis

In an earlier CRESST measurement [132], events due to mechanical stress were observed due to a very tight holding scheme for the target crystals, which was realized via plastic clamps. Special care was taken to reduce the applied tension to the crystal by using either $CaWO_4$ holding sticks or metal clamps, and it was shown in [133] that bronze clamps and sticks result in lower stress at a comparable level. However, as the recoil energy spectrum of the above events was found to be exponential in shape, they might provide an explanation for the low energy excess observed in this work. The so-called "crack" events were found to cluster in time [132]; one "big" event would be followed by several events with smaller amplitudes. If measured events in a dataset are distributed according to a Poisson process, i.e. if the rate per time interval is constant and events are not correlated, the time between two *arbitrary* events is random[2]. Correlated events (in particular a radioactive decay with a decreasing rate) will produce a deviation from a flat distribution of this quantity. The time distance distribution is

[2]This is not to be confused with the "waiting time" between two consecutive events.

calculated for the dark matter dataset of detector A after cuts; since the exponential excess of events is not only visible in the acceptance region, but across the whole e^- and γ bands, and a similar excess appears at higher light yield, different data subsets are compared. This is illustrated in Figure 5.49. Additionally, the time difference distribution for simulated events is shown.

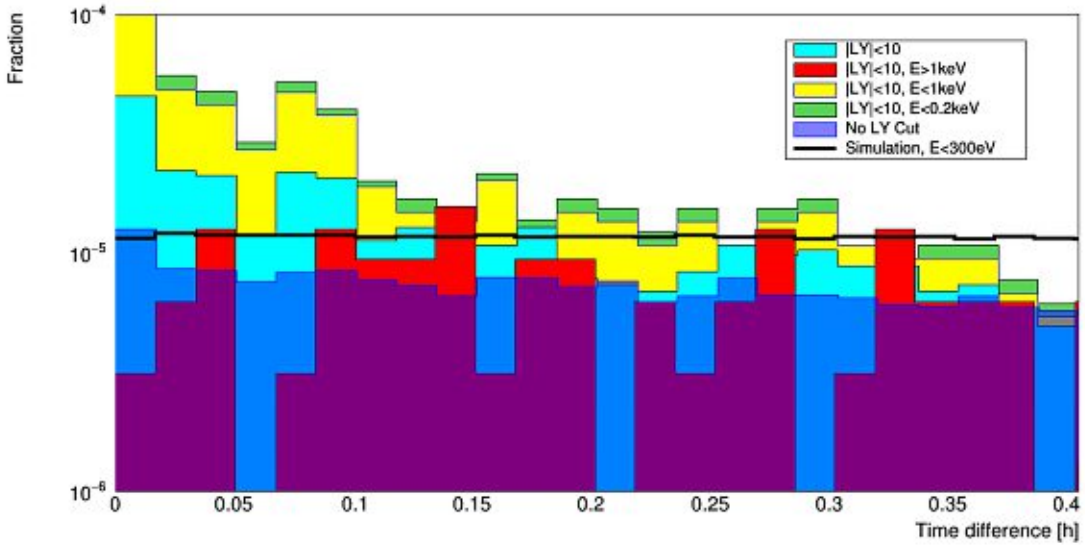

Figure 5.49: Distribution of the time interval between two arbitrary events selected from the dark matter dataset of detector A. Results for different subsets of the experimental data after cuts as well as simulated events are displayed.

For the simulation, the distance in time between two events is distributed flatly; for background events with energies above 1 keV, the same is true, while a correlation (i.e. an increase towards smaller time differences) is visible for events at low energies and with an absolute light yield below 10, i.e. events from the low energy excess. However, only a small fraction of events shows a correlation, and the "crack" hypothesis cannot account for the excess.

5.13 Background Components

In this section, different observed background components are discussed. Values for the background spectrum in each module resulting from the spectral fit discussed in Section 4.1.3 are listed in Table 5.14, where each resulting activity is given in µBq/kg and in counts per (kg d). The fit considers a flat background, a fraction linearly decreasing with energy, and several γ peaks, where the total number of peaks is not free, but was defined manually before each fit. In contrast to earlier CRESST phases, the Cu fluorescence line at 8 keV is only visible during the neutron calibration in detector E; its position is consistent with the literature value.

	Literature value [keV]	A	B	E	J
Constant (1/(keV kg d))	-	4.14	4.72	4.53	8.064
Linear factor (1/(keV^2 kg d))	-	-	-	-	-0.131
Hf K	65.350	-	-	-	71.80
A [1/(kg d)]		-	-	-	4.9
A [µBq/kg]		-	-	-	56.71
Hf L1	11.271	11.115	11.3107	11.4498	11.53
A [1/(kg d)]		5.33	11.85	7.69	6.30
A [µBq/kg]		61.67	137.17	89.02	72.90
Hf L2	10.739	10.9101	10.1769	10.9	10.9
A [1/(kg d)]		2.47	8.98	1.89	1.52
A [µBq/kg]		28.55	103.94	21.93	17.54
Hf L3	9.561	9.556	-	-	9.62
A [1/(kg d)]		0.80	-	-	0.49
A [µBq/kg]		9.20	-	-	5.68
Hf M1	2.601	2.65686	2.91286	2.8999	2.93
A [1/(kg d)]		2.66	11.96	11.30	4.30
A [µBq/kg]		30.76	138.41	130.83	49.79
Hf N1 (?)	0.538	0.556	-	0.7527	0.7525
A [1/(kg d)]		2.03	-	5.89	26.58
A [µBq/kg]		23.51	-	68.20	307.64
^{210}Pb	46.54	-	-	-	49.48
A [1/(kg d)]		-	-	-	3.87
A [µBq/kg]		-	-	-	44.80
Cu K$_\alpha$ (neutron calibration)	8.05	-	-	8.1745	-
A [1/(kg d)]		-	-	1.60	-
A [µBq/kg]		-	-	18.48	-

Table 5.14: Background components in modules A, B, E and J obtained from the spectral- and bandfit.

5.13.1 Flat Background

In this work, the flat background rate is around 4.5 counts / (keV kg d) for detectors A, B, and E. For the detector TUM40 operated in the previous stage of CRESST [134], 3.51 counts / (keV kg d) in the energy range between 1 and 40 keV have been reported as background level, which includes the activity of γ peaks. A band- and spectral fit with the method presented in [105] and also used in this work yields a constant background of 4.40 counts / (keV kg d) and a decreasing term of -2.56/ (keV^2 kg d) for TUM40 [121]; the mean value in [1,40]keV is 2.6 counts / (keV kg d). While a strongly falling component of the spectrum is not observed in A, B, or E, the constant background obtained with the fit is almost exactly the same for TUM40. The mean background rate in TUM40, however, is almost a factor two lower. This remaining discrepancy can be reduced when considering the origin of the background, which is thought to be partially due to impurities of surrounding copper parts [91]. In the low energy range, electrons and photons are very unlikely to penetrate deep into the crystal; therefore the background rate can be expected to scale with the surface area of the detector, and not its volume or mass. Since the mass of each target crystal is almost exactly ten times lower than the mass of the TUM40 target crystal (248 g), this yields a relative factor $10^{-\frac{3}{2}} \approx 0.215$ for the surface, which is two times higher than the factor 0.1 expected for volume scaling. If one third of the background scales in this way [91], the expected mean number of counts per (keV kg d) would be 3.61 which is closer to the values obtained with most detectors in this work. Detector J shows a significantly higher constant background rate of 8 counts / (keV kg d), which is mostly due to the line at 6 keV. Additionally, this detector features a decrease of the event rate with increasing energy: Above ~20 keV, the resulting rate is compatible with the other detectors.

5.13.2 Cosmogenic Activation

Before entering the underground laboratory, each target crystal was exposed to surface-level cosmic radiation. This results in the activation of the detector material and subsequent contamination with radioactive isotopes. To be measured in the underground lab, the half-life of such a process needs to be sufficiently long; a prominent example is the reaction

$$^{182}\mathrm{W} + \mathrm{p} \rightarrow {}^{179}\mathrm{Ta} + \alpha,$$

which is due to protons from cosmic radiation. The subsequent decay of the unstable isotope ^{179}Ta has a half-life of 1.82 y and thus occurs during the measurement phase.

$$^{179}\text{Ta} \xrightarrow{\text{EC}} {}^{179}\text{Hf}^{*} + \nu_e, \qquad {}^{179}\text{Hf}^{*} \rightarrow {}^{179}\text{Hf} + \gamma.$$

The observed γ energies correspond to the electron binding energies of ^{179}Hf; in previous CRESST phases, the K, L1, L3 and M shells were observed, and the ratio L/K was calculated to be compatible with theoretical expectations as well as experimental measurements [91] [135]. While both the positions of the Hf M1 and L1 line are consistent for detector A, a significant deviation is visible for the M1 line in modules B, E and J, where the reconstructed energy is higher than the literature value. The M1/L1 ratios in Table 5.15 also do not match the reference value; to account for the low statistics of the L2/L3 lines and their proximity to L1, an M1/$\sum_L$ ratio is calculated. However, the ratio still only matches in detector A. It is therefore unclear whether the deviation can be attributed to a non-linearity in the energy calibration, or whether the M1 line was in fact misidentified for other modules. Adjusting the energy calibration using this line may result in too low phonon energies, and is only justified for detector A. Leaving out this modification results in a more conservative upper limit. It should also be noted that no measured literature values are available for the M1/L1 or M1/$\sum_L$ ratios, but only theoretical values.

Ratio	Literature Value [135]	A	B	E	J
L/K	0.808	-	-	-	1.285
M1/L1	0.281	0.499	1.009	1.470	0.683
M1/$\sum_L$	0.246	0.341	0.574	1.179	0.551
N1/M1	0.272	0.764	-	0.521	6.178

Table 5.15: Ratios between different observed γ lines due to the decay ^{179}Ta $\xrightarrow{\text{EC}}$ ^{179}Hf + γ in comparison to calculated theoretical values [135].

In [99], a background analysis was performed for the target crystals of A, B, and E based on the degraded iStick signals propagated from the main absorber. It yields activities for L1 of (149.48±49.62) µBq/kg, (250.67±101.14) µBq/kg, and (150.36±57.07) µBq/kg, respectively. While these values lie significantly higher than those listed in Table 5.15 (but are still compatible given their uncertainies), the difference can be explained in part by the fact that the L2 line was not considered separately in [99]. If both activities (L1 and L2) from this work are added, closer values are obtained: 90.22 µBq/kg, 241.11 µBq/kg, and 110.95 µBq/kg.

5.13.3 Interpretation of Low-Energy Lines

An additional line below 1 keV is compatible with the Hf N shell (538 eV) in detector A; this line is not observed in detector B (cf. Table 5.14). For detectors E and J, a similar line is visible, but has a higher energy, which is almost exactly the same in both modules. In the analysis of detector A, the discrepancy between the expected number of 2-3 events from the Hf N line at 538 eV, and the observed number of more than 10, clearly points to a different origin of these events. The same is true for the other detectors, where both the activity and the position of the line do not match. An alternative explanation for these lines is fluorescence of the detector materials O and Ca: The $K_{\alpha,1/2}$ lines of O and $L_{\beta,3/4}$ lines of Ca lie at $E_{O,K_{\alpha,1/2}}$=0.525 keV and $E_{Ca,L_{\beta,3/4}}$=0.412 keV, respectively. Still, a preceding excitation of the materials must be motivated. If the exponential excess is caused by physical events, this could be an explanation; especially a photon or electron flux could interact with the detectors. However, there is no known source of such a particle flux.

5.13.4 Internal and External Contaminations, Decay Chains

Radioactivity which is not caused by activation of the detector material, but by intrinsic contaminations of either the target material, the near surroundings or the detector housing, was studied in detail in [91]. Although the complete background model described in that work accounts for a large portion of the flat background in the low-energy range, no prominent γ lines apart from the Hf lines discussed in the previous sections are to be expected. No statement about other contaminations can be made on the basis of the dataset analyzed in this work. The next section focuses on an improved fit method, which attempts to account for saturation and make the medium to high energy range accessible again.

6 Description of Saturation

Ideally, the transition of a TES is described by a sigmoid function, i.e. an S-shaped curve. The most general analytic form of such curves is the *generalized logistic function* or *Richard's curve*

$$Y(x) = A + \frac{K-A}{(C+Qe^{-Bx})^{1/\nu}} \text{ [136]}, \tag{6.1}$$

with A the lower asymptote, K the upper asymptote if C=1, and B the growth rate. ν affects near which asymptote maximum growth occurs, and Q is related to the value $Y(0)$. The upper asymptote can be obtained from the value of C via $A + \frac{K-A}{\sqrt[\nu]{C}}$. $Y(x)$ is displayed in Figure 6.1 for A=0, K=1, B=3, Q=ν=0.5, M=0, and C=1. The effect of varying parameters is illustrated in Figure 8.13 in the appendix.

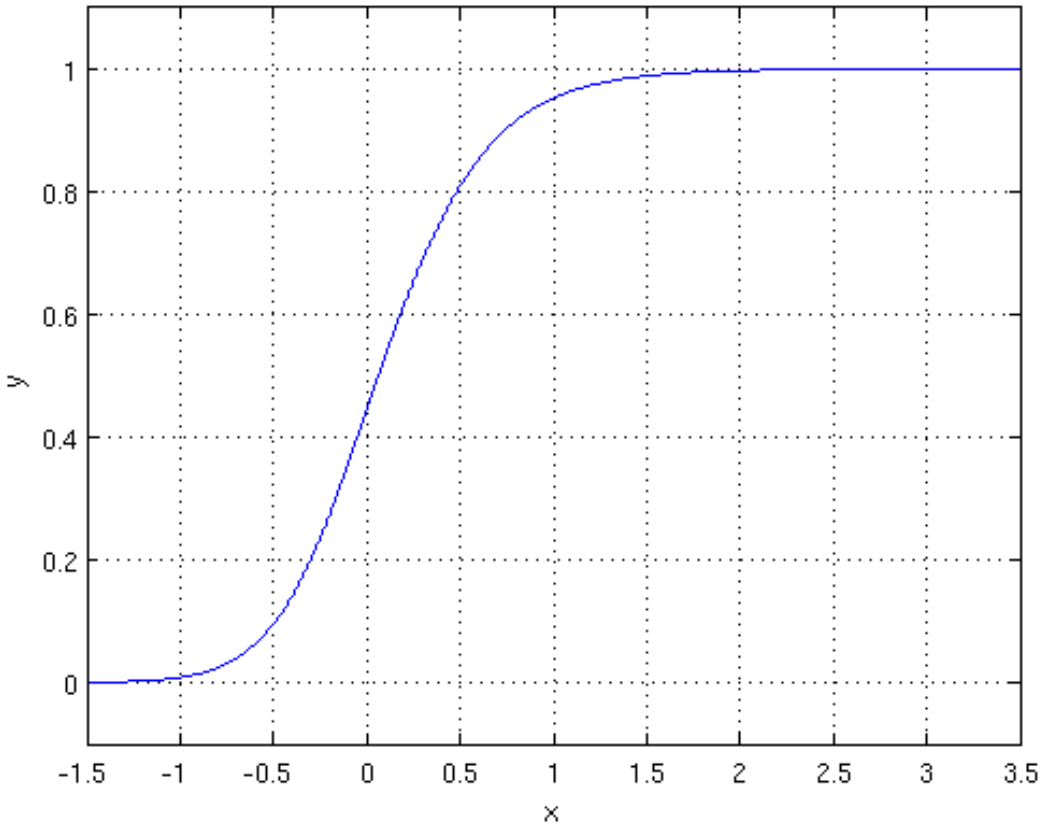

Figure 6.1: Generalized logistic function $Y(x)$ for A=0, K=1, B=3, Q=ν=0.5, and C=1 [137].

Requiring that $Y(\Delta T = 0) = 0$, one obtains

$$-A(C+Q)^{1/\nu} = K - A \Rightarrow K = A(1-(C+Q)^{1/\nu}). \tag{6.2}$$

This yields the form

$$Y(x) = A \cdot \left(1 - \left(\frac{C+Q}{C+Qe^{-Bx}}\right)^{1/\nu}\right) \tag{6.3}$$

which is now used for an empirical description of the transition. Since the structure of the transition itself is independent of time, one can just replace x by the pulse shape of the signal $\Delta T(t)$, either obtained from a parametric description or via interpolation between the samples of an averaged pulse. In the following, we assume a parametric description. The parametric pulse model $\Delta T(t)$ is obtained from a fit to the standard event (Figure 6.2); three components instead of two are used to achieve an optimal description of the pulse shape. This approach is empirical, and the third, long-lived component is not physically motivated;

it serves to describe the tail in each standard event. While the tail may be due to a physical effect, it is more plausible that the baseline model used during the creation of the standard event (a polynomial of first order) was insufficient, and effects of decaying baselines were propagated to the standard event; no such long-lived signal component was measured in previous stages of CRESST. The modified pulse model and resulting fit parameters are given in Section 8.3 in the appendix.

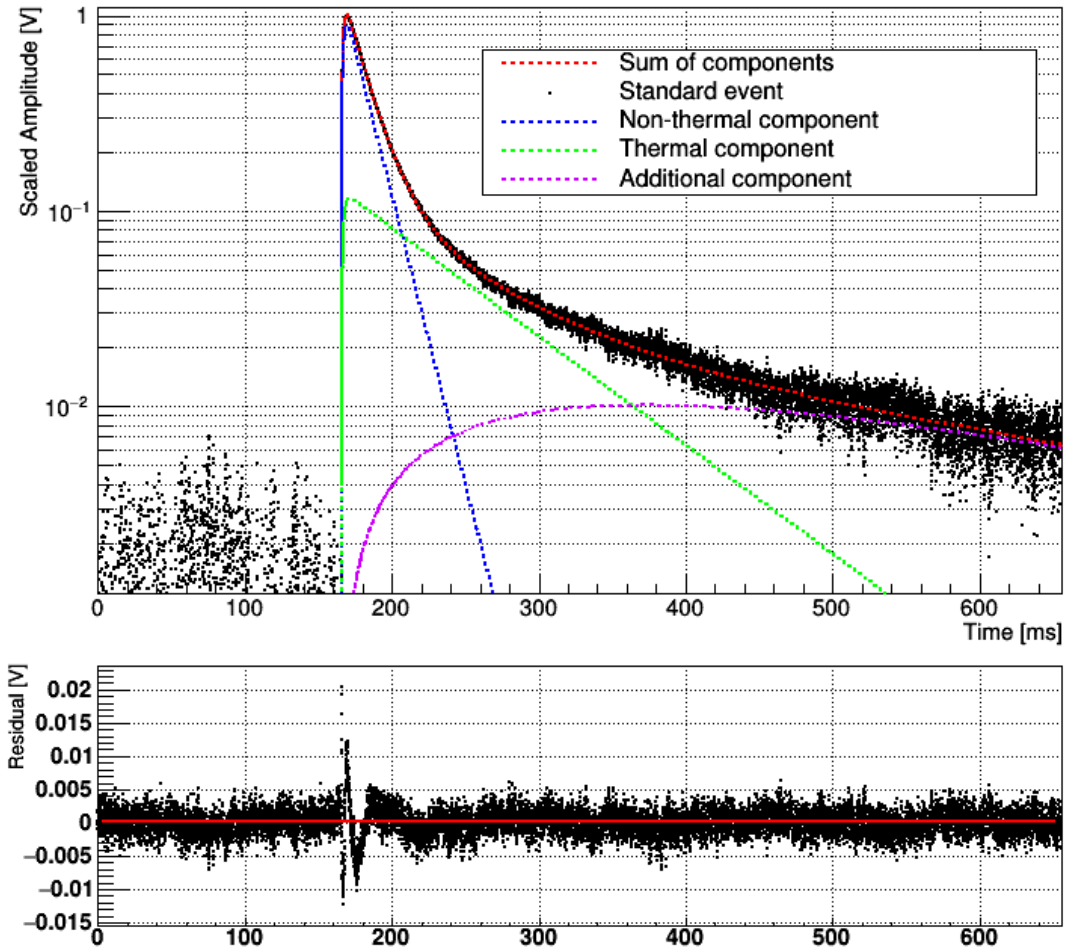

Figure 6.2: Parametric fit to the standard event for the phonon channel of detector A in CRESST-III, Phase One. A calorimetric pulse model was used (cf. Section 4.2.2) which features an additional third component (cf. Section 8.3). The standard event was scaled such that its maximum amplitude is 1 V.

One can now obtain the parameters of the transition by fitting a saturated signal pulse. This pulse must have an energy sufficient to reach the maximum (voltage) value observed in the data, but needs to return to the linear range, i.e. the range where the original pulse model correctly describes the pulse shape, within the record window. Alternatively, one can extend

the record length until the linear range is included. To describe the energy of the pulse, the signal is multiplied by a linear scaling factor n. The fit function is thus

$$Y(t) = A \cdot \left(1 - \left(\frac{C+Q}{C+Qe^{-BnA\Delta T(t,O)}}\right)^{1/\nu}\right), \tag{6.4}$$

where the parameters of $\Delta T(t,O)$ are fixed apart from the onset O of the pulse. To further constrain the transition fit, n is also fixed here using the result of a truncated fit (cf. Section 4.2.1) with the same pulse shape. The resulting truncated fit amplitude is divided by the truncation limit (TL) and n is fixed to that value, such that the saturated fit model will reproduce the correct constant pulse shape for values of n below 1. Figure 6.3 shows the fit for a saturated pulse in the phonon channel of detector A in CRESST-III Phase One. Figure 6.5 shows the resulting transition $Y(x)$, and the obtained parameters are listed in Table 6.1.

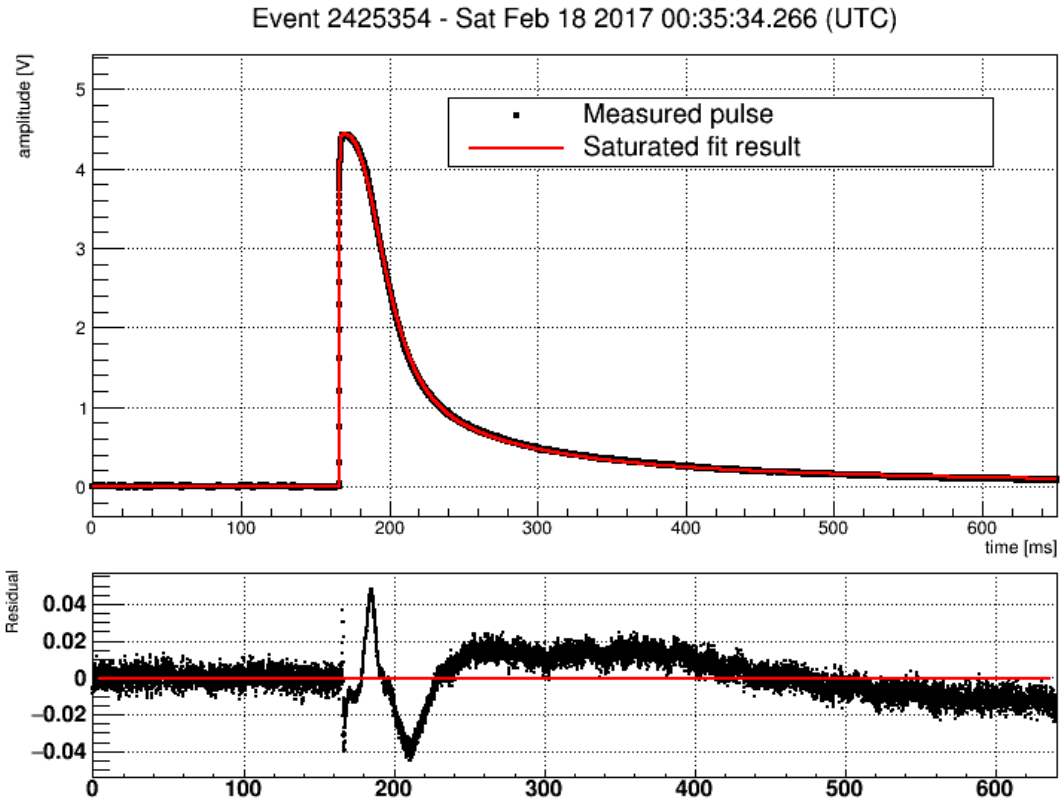

Figure 6.3: Saturated fit in the phonon channel of detector A: The red line in the upper panel shows the saturated fit model, while the black dots correspond to the measured pulse. The lower panel gives the residuals. This pulse was used to obtain the parameters of the logistic function.

Parameter	Value
A	39.5669
C	0.161914
Q	0.308122
B	0.383843
ν	9.97737

Table 6.1: Transition parameters obtained from the saturated pulse fit. Equation 6.4 was used.

After obtaining the transition parameters, they can be fixed in the fit, and only the onset and the scaling parameter n remain free. Since the linear range of the transition was fixed using the truncated fit, $n \cdot \mathrm{TL}$ should equal the truncated fit result at least for each pulse with an amplitude below the TL. It is important to note here that fixing n in the transition fit is an optimization step to improve the resolution in the low-energy and thus linear range. Not fixing it may improve energy resolution in the medium to high-energy range; then the conversion factor from n to energy has to be obtained from a known peak and cannot be inferred from the truncated fit amplitude. Using background peaks at higher energies, one can also use the saturated fit method to obtain a calibration factor, if only the truncation limit is known, but not the energy scale.

6.1 Comparison of Resulting Transition

The parametric transition obtained from the saturated fit model can now be compared to the "real", i.e. the measured transition of the phonon channel TES of detector A. Since the transition shape also varies with the applied bias current, applying the same bias current during a transition measurement which is used for the data taking campaign is a necessity for this comparison. However, no dedicated transition measurement is available with the applied bias current, and a heater sweep will be used instead (Figure 6.4); this sweep was initially used to optimize the operating point of the detector and was already explained in Section 3.3.3. In this case, the reconstructed pulse height of a 10 V control pulse is used to reconstruct the transition curve. The relation between injected DAC (digital to analog converter) heater power V_{DAC} and reconstructed amplitude (running average pulse height in V) is linear in the immediate vicinity of the operating point (indicated in green); the same is true for the relation between reconstructed amplitude and injected heater amplitude for test pulses V_{TP}. In order to convert DAC heater power to injected test pulse amplitude, a linear fit

can thus be used to obtain the necessary factor. It was measured to be:

$$\zeta \approx 218 \frac{V_{TP}}{V_{DAC}}$$

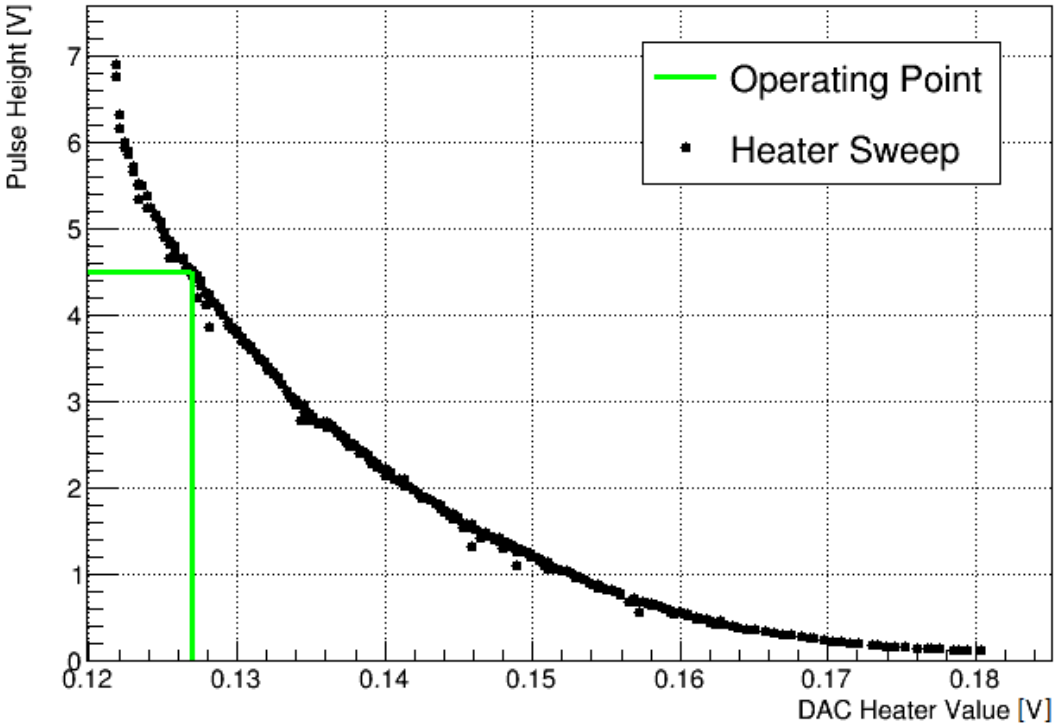

Figure 6.4: Measured height of a control pulse with an injected pulse height of 10V as a function of applied heating power. The operating point of detector A's phonon channel is indicated by green lines.

Figure 6.5 shows the reconstructed transition curve, where (x,y)=(0,0) corresponds to the operating point at a heater value of 0.127 V. Figure 6.6 gives a logarithmic y scale to better illustrate deviations from the "real" transition.

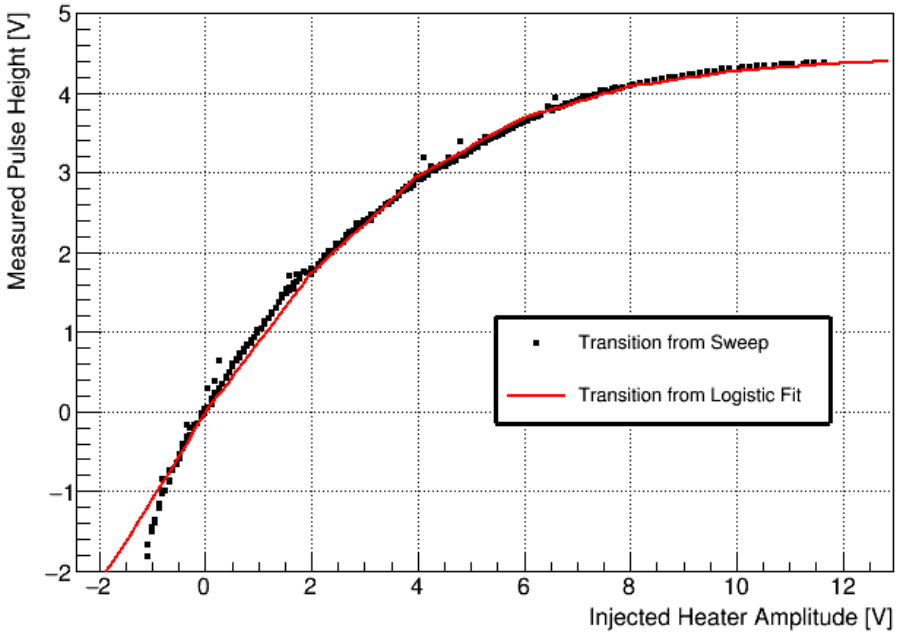

Figure 6.5: Transition obtained from Figure 6.4 (black dots) compared to the transition resulting from the saturated fit model (red).

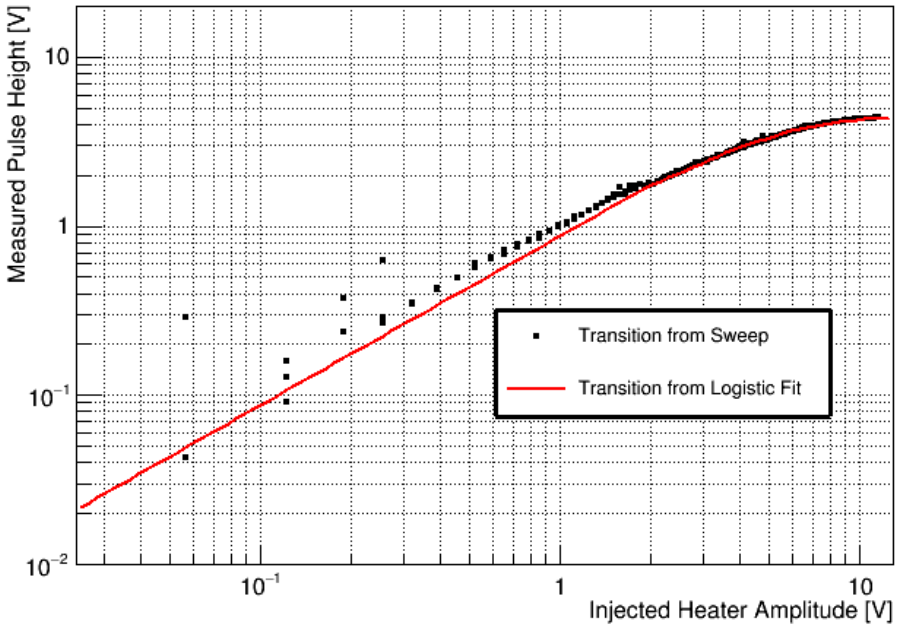

Figure 6.6: Transition obtained from Figure 6.4 (black dots) compared to the transition resulting from the saturated fit model (red); logarithmic y axis.

The agreement between the two transitions varies over the injected voltage range. Below the operating point, the fit had no information at all, since an energy deposition can only increase the temperature, but not decrease it. Thus, the logistic function does not describe the real transition well here. However, this region is not relevant for the analysis. At large injected voltages, the agreement is quite good, while in the intermediate range the measured voltage is first slightly under-, and then overestimated. The choice of the saturated pulse from which the fit transition is extracted arguably determines where the best agreement is achieved; the pulse used in this case already shows strong saturation and therefore results in a better description of the real transition for higher injected pulse heights. Since the primary advantage of the saturated fit method is an extension of the energy range to higher values, this choice seems reasonable.

It should be emphasized that the transition model used here is purely empirical; it does in particular not account for any hysteresis, which may be introduced by electrothermal feedback in the TES. Such effects could be studied by comparing two transitions obtained only from the rising and the falling flank of a pulse, respectively. Since there are always much more samples in the falling flank, it will determine the resulting transition, if the whole pulse is used in the fit. This is the case for the transition shown above.

6.2 Medium-Energy Range Results

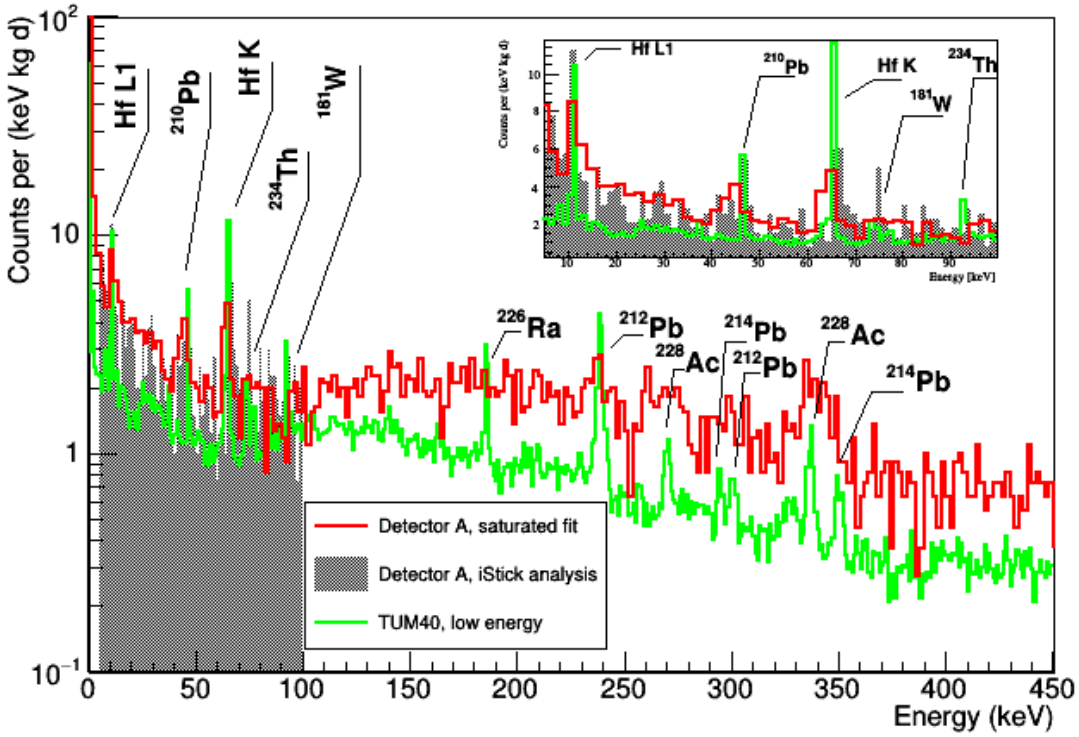

Figure 6.7: Comparison of an energy spectrum obtained from a saturated fit to the dataset of detector A in CRESST-III, Phase One (red), and a the spectrum of TUM40 (CRESST-II) for the low-energy range (green) [91]. The black spectrum was taken from [99] and rebinned by a factor of 2. It uses degraded signals detected in the instrumented holding sticks of detector A. The inlet shows a zoom to the range below 100 keV.

Figure 6.7 shows the results of a saturated fit to the full dataset of detector A. Apart from an amplitude-dependent cut on the fit χ^2, no quality cuts were applied, and the same raw exposure of 5.5 kgd as before was assumed. The spectrum is compared to the spectrum of TUM40, a detector operated in CRESST-II, in terms of activity [91]. Additionally, the results of an iStick analysis of detector A are shown [99], which is limited to a maximum energy of ≈100 keV. Two known peaks from TUM40 were used to set a rough energy scale for detector A via a second degree polynomial: the 11.27 keV Hf line and the 338.32 keV ^{228}Ac β^- decay. Zero amplitude is assumed to correspond to zero energy. Peaks which appear in the now calibrated spectrum include the ^{210}Pb and ^{212}Pb β^- decays at 46.5 keV and 238.63 keV, and the Hf K shell at 65.35 keV. The resolution degrades drastically with increasing energy, which is to be expected. While the TUM40 spectrum ends at ~500 keV, the highest energy reconstructed

with this method is ~2 MeV; although a medium-energy dataset is available for TUM40, which is based on a different analysis, the low statistics in detector A do not allow for a meaningful comparison. A zoomed out version of Figure 6.7 showing the full energy range is given in Section 8.4.2 in the appendix. The total background level is roughly compatible for the iStick analysis and the saturated fit; in both analyses, the level is much higher than in TUM40 in the low energy region. Over the whole energy range, the event rate in the saturated fit spectrum is roughly a factor 2 higher than in TUM40. In comparison to [91], the ^{226}Ra peak at 186 keV is not visible at all. It is attributed to external radiogenics as part of the ^{238}U decay chain, together with ^{214}Pb peaks at 295 keV and 352 keV. Neither of the latter is strongly pronounced (the ^{210}Pb line at 300 keV comes from a different decay chain). These observations point to a lower ^{238}U concentration in surrounding parts of the setup, which could be due to the position of detector A in the detectour carousel differing from that of TUM40. Additionally, the different module design might have an effect: While detector A is completely enclosed by a Cu housing, TUM40 featured a Cu structure covered with scintillating foil.

7 Conclusion

Four detectors from CRESST-III Phase One were analyzed in this work, and it was confirmed that three of them achieved a threshold ≤100 eV, while one lies slightly above the design goal. This was done using a signal simulation on the complete recording stream, and via processing of these simulated pulses in the analysis chain. A survival probability for signal events was extracted as a function of their nuclear recoil energy, and the effect of each analysis cut was studied (Section 5.9). For one detector, the simulation of a continuous energy spectrum was used instead of a finite set of amplitudes; this allows for the resolution of smaller features in the survival probability, and highlights systematic effects due to cuts. An upper limit on the dark matter particle-nucleus elastic scattering cross section as function of dark matter particle mass was extracted for each detector (Section 5.11), both for the spin-independent and for the spin-dependent interaction case, showing that new parameter space could be covered with all detectors, while detector A provides the strongest constraints over most of the dark matter particle mass range. For this detector, an exclusion limit for a minimum dark matter particle mass of 167 MeV was extracted. Each detector module shows an exponential excess near the threshold, where the exact shape of this excess varies; the origin of the excess could not be determined, although a time difference analysis was performed, which provides some indication of an underlying Poissonian process. Via inclusion of the exponential excess as background in a likelihood calculation, it was shown that CRESST-III would achieve and even surpass its projected sensitivity (Section 5.11.5) in the absence of this feature.
The results of Section 5.13 emphasize the need for a reliable energy calibration method at low energies; calibration peaks used in previous CRESST iterations are now above the linear range of detectors, and activities in the observed low-energy cosmogenic Hf lines are extremely small. Using the latter for calibration purposes thus requires long measuring times. However, it was also shown in Section 5.11.4 that a relative uncertainty of the event energy of about 10 % has little impact on a resulting exclusion limit. The resulting Hf activities were shown to be compatible with an analysis performed for the same detectors which uses the iStick signal. It was observed that the reconstructable energy range of each phonon channel is limited

due to the optimum filter reconstruction method and saturation effects. A simple method to fit saturated pulses was presented, which allows reconstruction of energies at least up to 500 keV; it was shown that this yields a result consistent with the aforementioned iStick analysis, and known medium-range γ lines from a previous CRESST phase were observed. The resulting transition was shown to approximate the measured transition reasonably well. CRESST-III demonstrates that cryogenic calorimeters with a target mass as small as 24 g and measuring recoil energies of several tens of eV can be reliably operated as extremely sensitive dark matter detectors. In future analyses, studies of the exponential excess may be performed by lowering detector thresholds even further, and including noise triggers in the likelihood model. Thereby, differences between the background population and an exponential dark matter signal may become visible, and additional sensitivity can be gained.

8 Appendix

8.1 Conversion Functions from Filter Amplitude to Fit Amplitude

The energy range in each detector is limited by saturation of the filter amplitude used for reconstruction (cf. Section 4.2). To better illustrate these cutoffs, the conversion functions from filter amplitude to equivalent standard event fit amplitude are illustrated here.

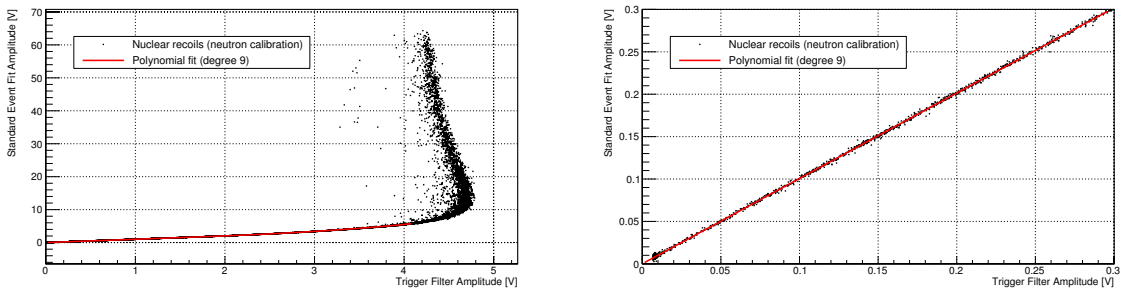

Figure 8.1: Conversion from trigger filter amplitude to standard event fit amplitude for the phonon channel of detector A. A polynomial of ninth order is used, and the maximum reconstructable filter amplitude is given by the fit range. A zoomed version is shown on the right.

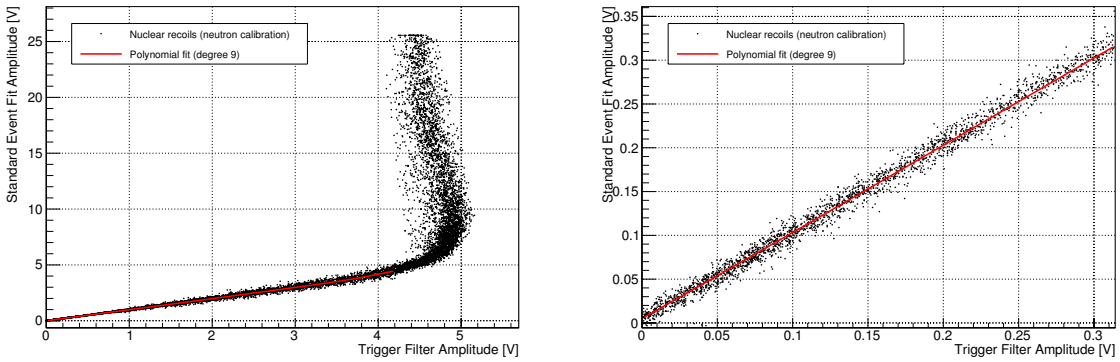

Figure 8.2: Conversion from trigger filter amplitude to standard event fit amplitude for the phonon channel of detector B. A polynomial of ninth order is used, and the maximum reconstructable filter amplitude is given by the fit range. A zoomed version is shown on the right.

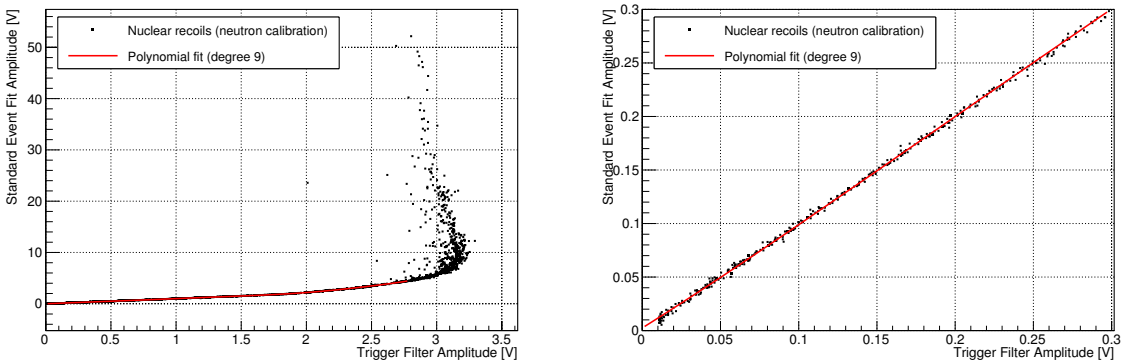

Figure 8.3: Conversion from trigger filter amplitude to standard event fit amplitude for the phonon channel of detector E. A polynomial of ninth order is used, and the maximum reconstructable filter amplitude is given by the fit range. A zoomed version is shown on the right.

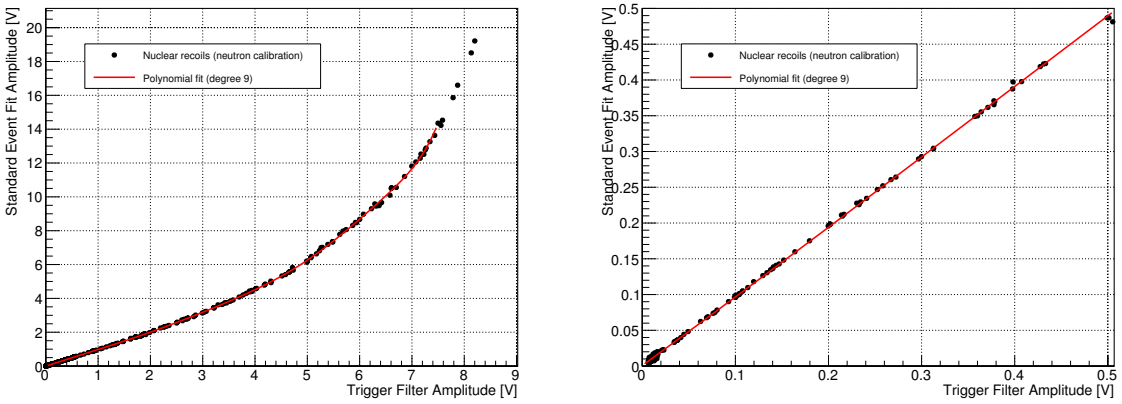

Figure 8.4: Conversion from trigger filter amplitude to standard event fit amplitude for the phonon channel of detector J. A polynomial of ninth order is used, and the maximum reconstructable filter amplitude is given by the fit range. A zoomed version is shown on the right.

8.2 Bandfit Results

Band parameters for each detector module obtained with the fit are listed in Table 8.1; Table 8.2 gives the spectral parameters. Each parameter is explained in sections 3.4 and 5.11.5. The bandfit was carried out in two steps: A first fit to neutron calibration data, while fixing the gamma peak activities to zero, gives the electron band parameters L_0-L_4, the energy dependent light resolution parameters S_1 and S_2, the factor ε, and the neutron spectra $(D_i, F_{i,NCal})$ for the neutron calibration. These are subsequently fixed. In a second step, the background dataset is fitted and gives the activities and mean values $A_{\gamma,i}$ and mean values $E_{\gamma,i}$ of the γ peaks, the γ band quenching parameters $Q_{\gamma,1}$ and $Q_{\gamma,2}$, as well as the background electron recoil spectrum (P_0,P_1). The energy dependent part of the phonon energy resolution $\sigma_{P,1}$ and the excess light density (El_{amp}, El_{dec}, El_{width}) are also determined in this step. The constant phonon and light energy resolutions $\sigma_{P,0}$ and $\sigma_{L,0}$ are preset and fixed input parameters (results from Section 5.10), together with the exposure for each module in (kg d) and the recoil energy threshold E_{thr}. For the likelihood calculation with exponential background allowed, the parameters F_e, D_e, and L_{lee} are determined from the background dataset, an then fixed in each respective module; for a calculation without exponential background, they are set to zero. The additional parameters for background neutrons $F_{i,BG}$ are fixed to zero. In Section 5.7, a second fit was motivated for detector J, accounting for the effect of a feature at ~6 keV. Only the neutron calibration data was fitted in this case in order to cross-check the resulting e^- band parameters.

Parameter	Det. A	Det. B	Det. E	Det. J	Det. J ("gap")
L_3	3.63244	31.373	3.19889	0.939424	0.000100841
L_2	0.409785	0.367779	0.303902	1.01034	0.513045
L_0	1.13716	1.85077	0.855921	1.00109	0.962369
L_1	0.00746888	0.00739509	0.00999058	0.00288431	0.00385691
$\sigma_{L,0}$	0.132706	0.244682	0.285171	0.197904	0.197904
S_1	0.397838	0.950377	0.462827	0.502502	0.526477
S_2	0.0301889	0.00171765	0.0279763	0.0488077	0.0457869
El_{amp}	127.302	59.3899	116.198	88.027	84.0102
El_{dec}	5.82999	12.6177	8.48132	6.0353	7.10804
El_{width}	11.9874	24.7088	21.0769	12.209	11.1159
$\sigma_{P,0}$	0.0048	0.00731439	0.00790374	0.0103483	0.0103483
$\sigma_{P,1}$	0.000168043	0.015831	0.00136323	0.00190453	0.0121976
$Q_{\gamma,1}$	0.798821	0.787192	0.803435	0.753872	1
$Q_{\gamma,2}$	0.00377637	0	0.000935179	0.00205675	0
ε	0.572568	0.516759	0.591197	0.651133	0.639568
kg d	5.49666	5.46775	5.70617	4.03274	4.03274
E_{thr}	0.030145	0.1196	0.064666	0.082968	0.082968

Table 8.1: Results of the bandfit for different detectors - band parameters. For detector J, two results are listed, where the latter was obtained with a modified survival probability excluding the feature at ~6 keV (cf. Section 5.7).

Parameter	Det. A	Det. B	Det. E	Det. J	Det. J ("gap")
P_0	93.49	217.325	148.806	141.32	108.725
P_1	0	0	0	0.171646	1.10163
F_e	669454	7387.64	67421.2	863983	3347.16
D_e	0.0216728	0.230957	0.104334	0.00852286	1.7175
L_{lee}	0.034038	0.0512691	0.0263744	0.0383693	0.0484408
$A_{\gamma,1}$	14.6068	65.3883	64.5007	17.3471	-
$M_{\gamma,1}$	2.65686	2.91286	2.8999	2.92768	-
$A_{\gamma,2}$	0	0	0	1.9801	-
$M_{\gamma,2}$	8.08814	8	9.50403	9.62488	-
$A_{\gamma,3}$	13.5295	49.1008	10.8098	6.1133	-
$M_{\gamma,3}$	10.9101	10.1769	10.9	10.9	-
$A_{\gamma,4}$	29.2878	64.8015	43.8868	25.3989	-
$M_{\gamma,4}$	11.1151	11.1729	11.4498	11.5285	-
$A_{\gamma,5}$	11.1634	0.00782661	9.11325	15.6066	-
$M_{\gamma,5}$	0.55642	0.757928	8.17454	49.4857	-
$A_{\gamma,5}$	4.37103	0.0603522	33.6254	107.189	-
$M_{\gamma,5}$	9.55641	9.89677	0.752748	0.752527	-
$F_{O,BG}$	0	0	0	0	0
$F_{Ca,BG}$	0	0	0	0	0
$F_{W,BG}$	0	0	0	0	0
$F_{O,NCal}$	111.182	367.324	273.473	133.97	254.487
D_O	79.826	42.1736	43.9367	110.9	38.3378
$F_{Ca,NCal}$	1283.43	7479.11	2538.61	1105.82	9092.64
D_{Ca}	3.19753	0.419453	2.24684	4.80406	0.216743
$F_{W,NCal}$	4944.04	1934.85	74950.4	8601.71	1e+07
D_W	0.373236	3.21383	0.0660448	0.416772	0.0206953

Table 8.2: Results of the bandfit for different detectors - spectral parameters. For detector J, two results are listed, where the latter was obtained with a modified survival probability excluding the feature at ~6 keV (cf. Section 5.7).

8.3 Parametric Fit Results - Two versus Three Components

If another component is added to the parametric pulse model discussed in Section 4.2.2 (either calorimetric or bolometric), described by an amplitude A_3 and two time constants τ_3 and τ_4, a more accurate description of the pulse may be obtained:

$$\widetilde{\Delta T} = \Delta T + A_3 \cdot \left(e^{-\frac{t-t_0}{\tau_3}} - e^{-\frac{t-t_0}{\tau_4}} \right) \tag{8.1}$$

The comparison for two and three components is shown in Figures 8.5 to 8.12 for all phonon channels, and the resulting parameters are given in tables 8.3 and 8.4 for each respective fit.

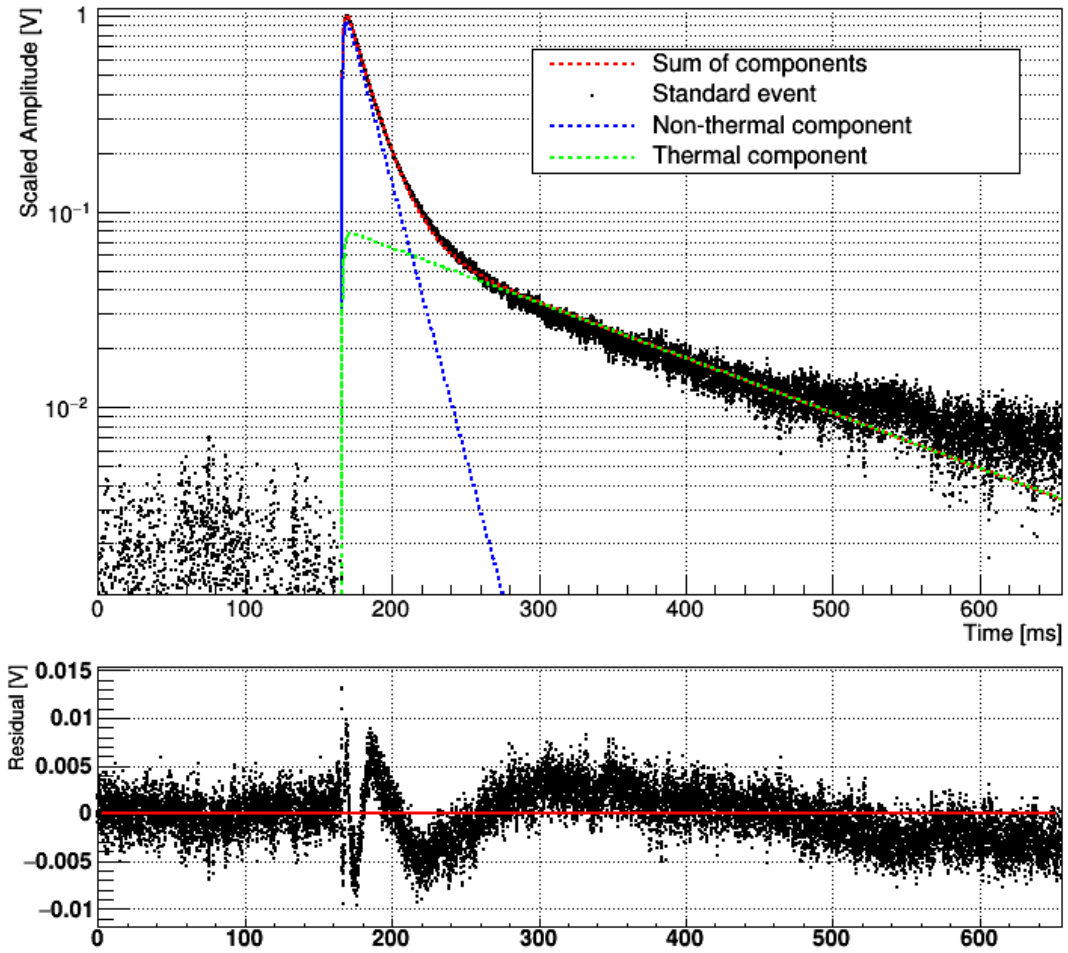

Figure 8.5: Two-component calorimetric fit to the standard event used in the analysis of detector A. The y scale is logarithmic to highlight deviations from the model in the pulse tail. The standard event was scaled such that its maximum amplitude is 1 V.

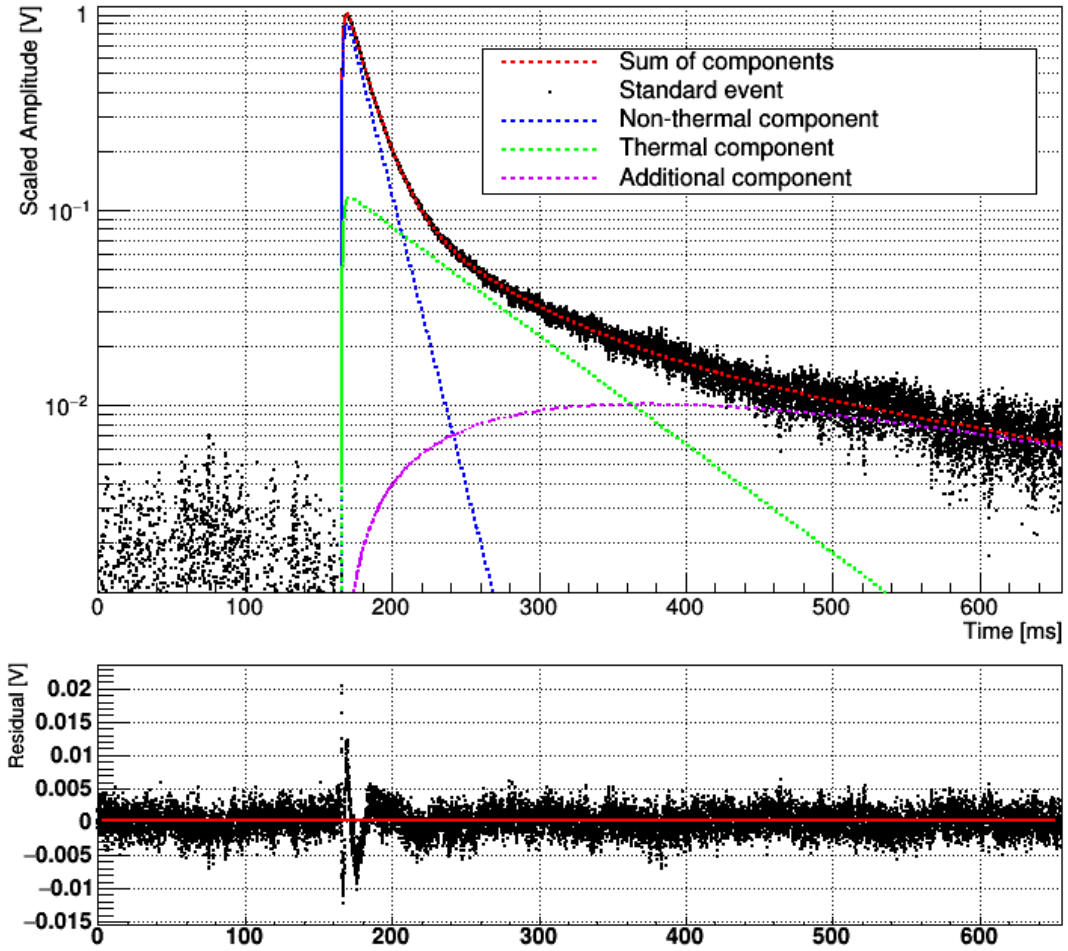

Figure 8.6: Three-component calorimetric fit to the standard event used in the analysis of detector A. The y scale is logarithmic to highlight deviations from the model in the pulse tail. The standard event was scaled such that its maximum amplitude is 1 V.

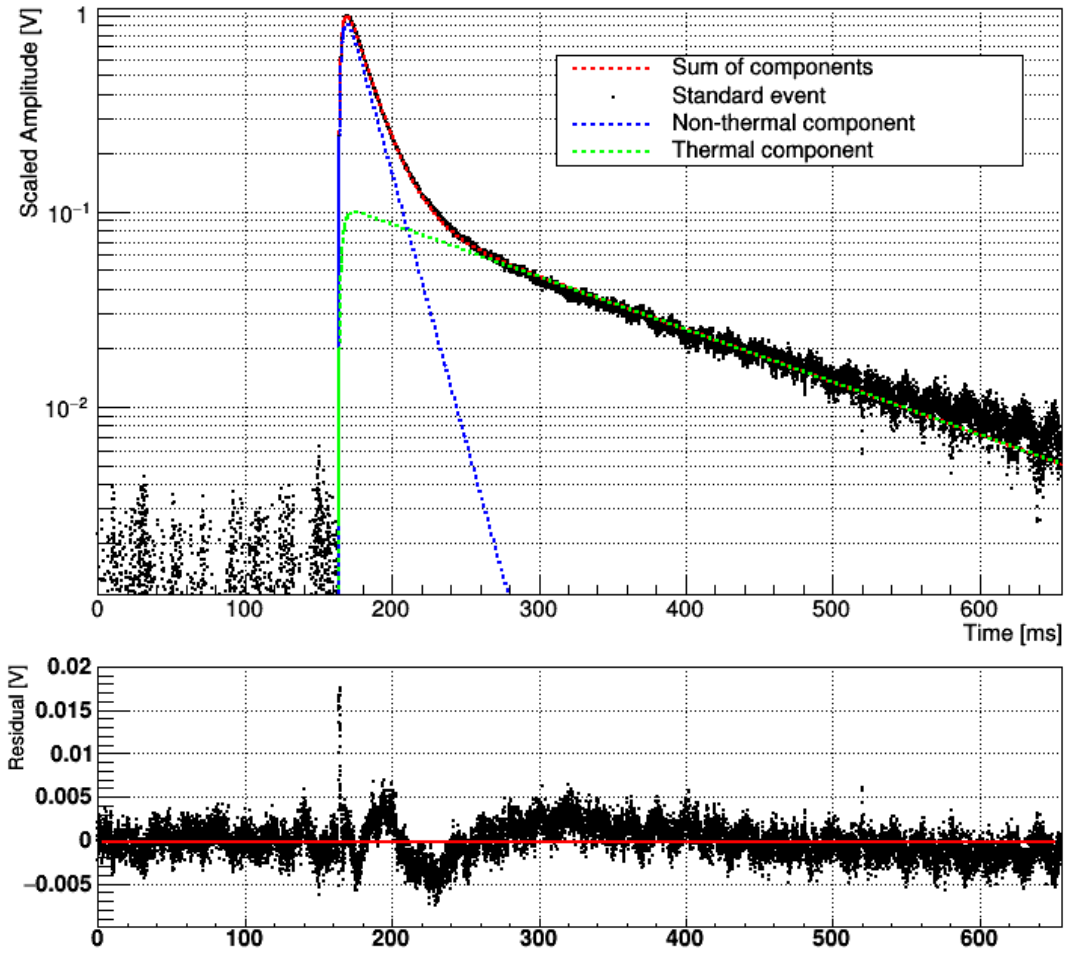

Figure 8.7: Two-component calorimetric fit to the standard event used in the analysis of detector B. The y scale is logarithmic to highlight deviations from the model in the pulse tail. The standard event was scaled such that its maximum amplitude is 1 V.

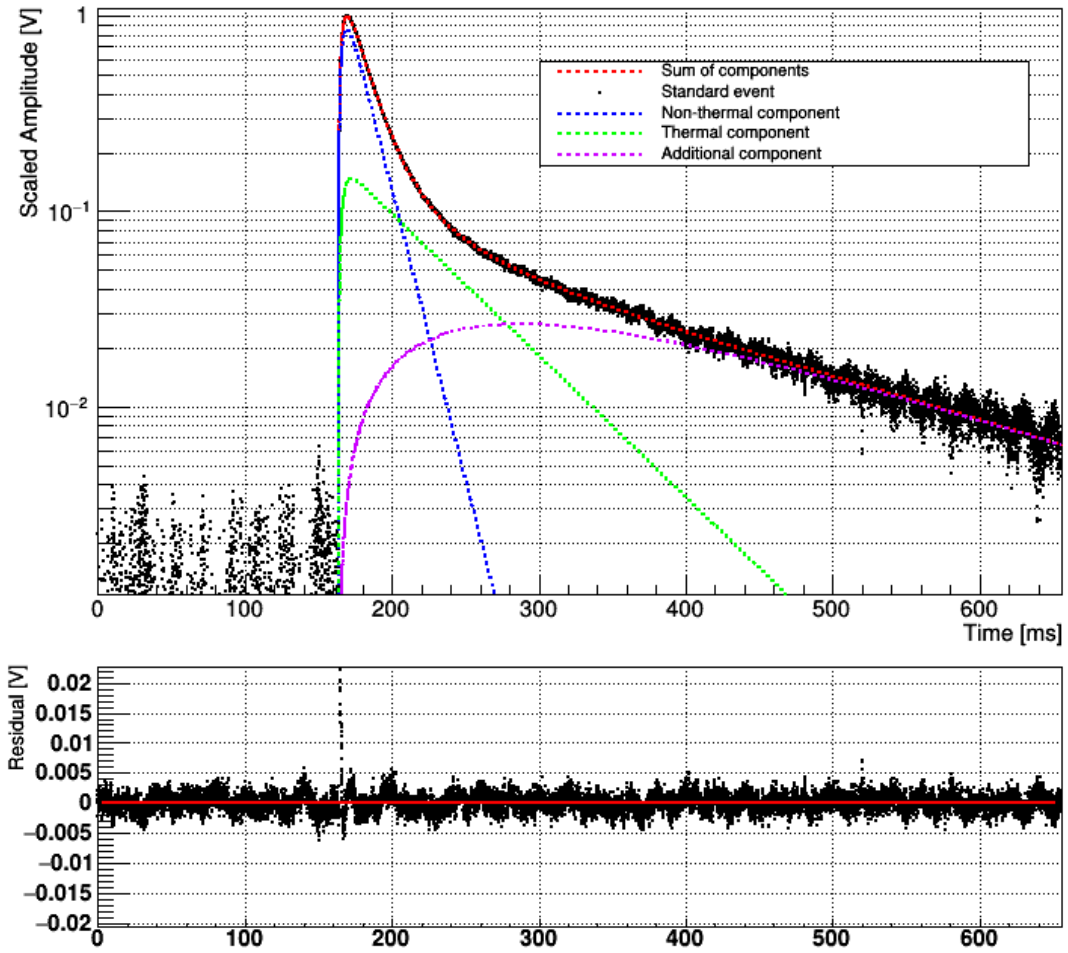

Figure 8.8: Three-component calorimetric fit to the standard event used in the analysis of detector B. The y scale is logarithmic to highlight deviations from the model in the pulse tail. The standard event was scaled such that its maximum amplitude is 1 V.

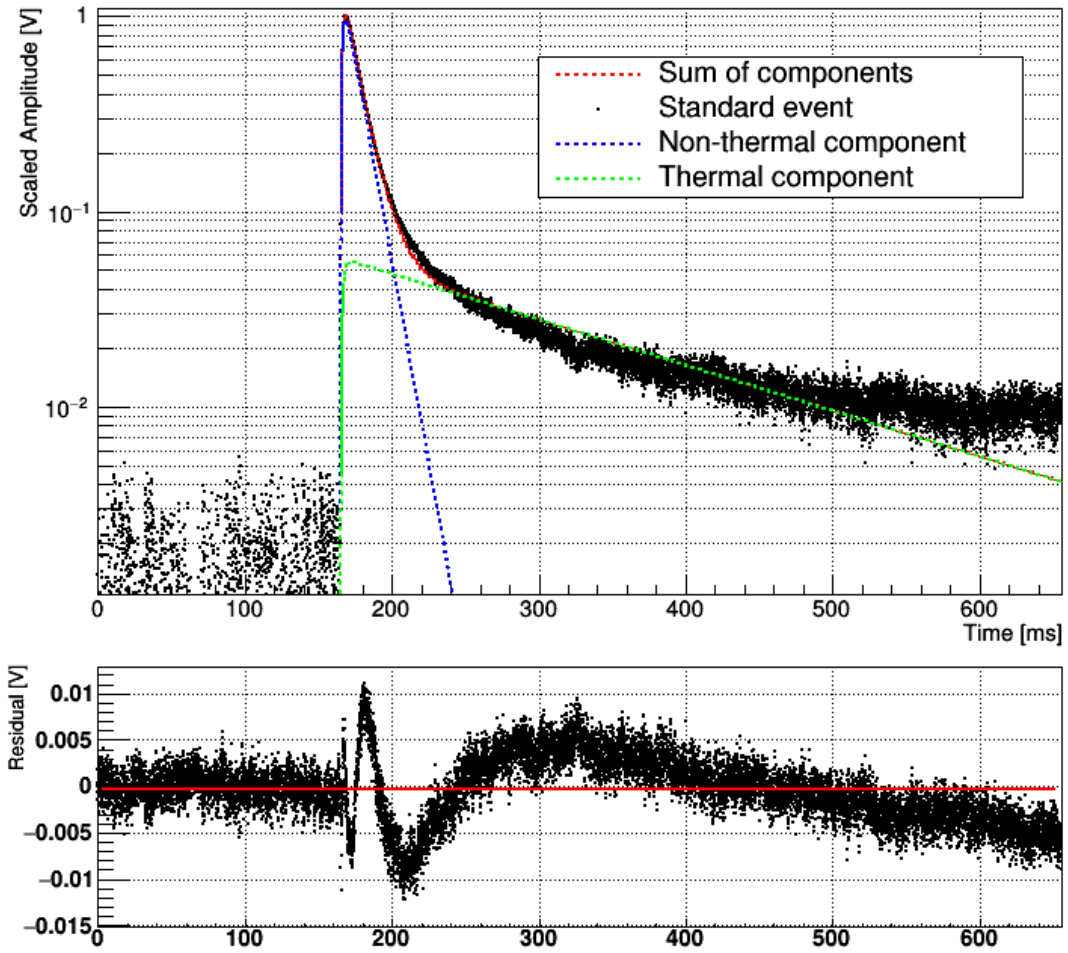

Figure 8.9: Two-component calorimetric fit to the standard event used in the analysis of detector E. The y scale is logarithmic to highlight deviations from the model in the pulse tail. The standard event was scaled such that its maximum amplitude is 1 V.

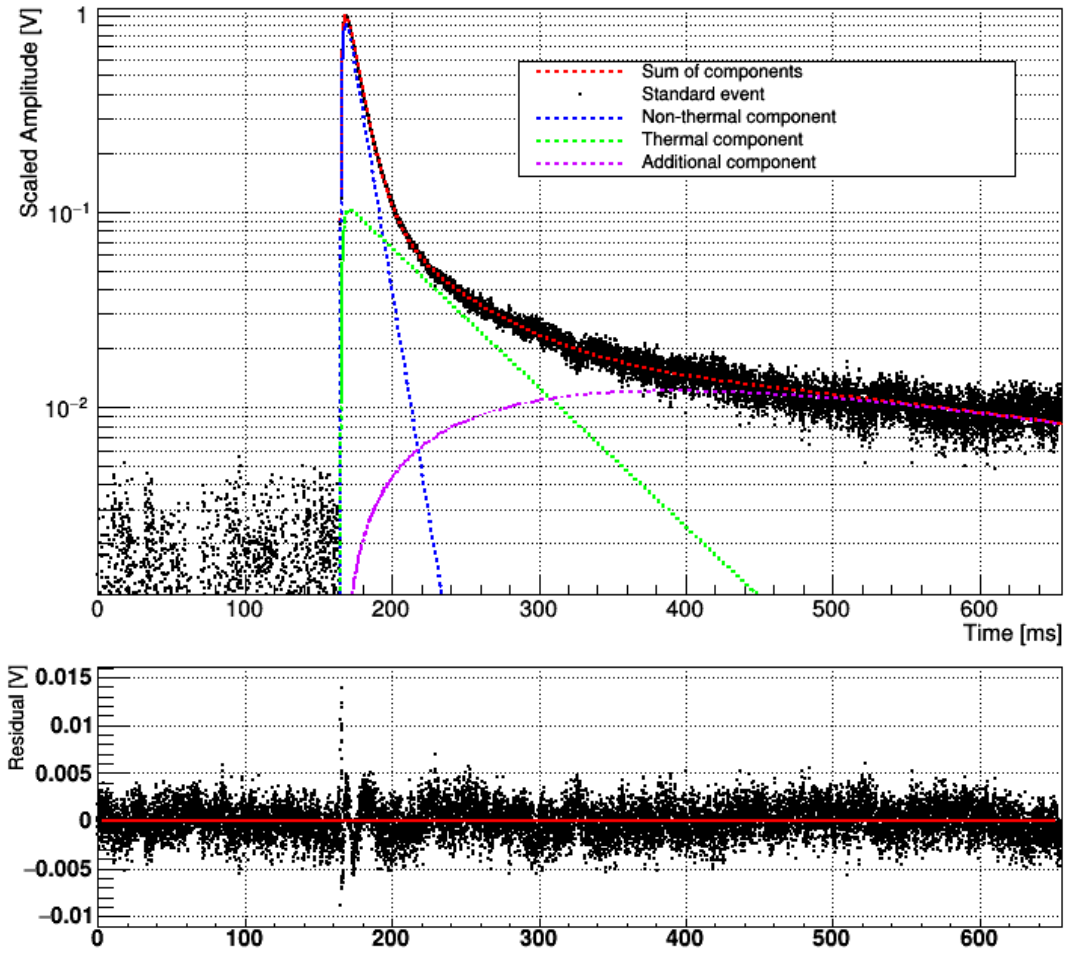

Figure 8.10: Three-component calorimetric fit to the standard event used in the analysis of detector E. The y scale is logarithmic to highlight deviations from the model in the pulse tail. The standard event was scaled such that its maximum amplitude is 1 V.

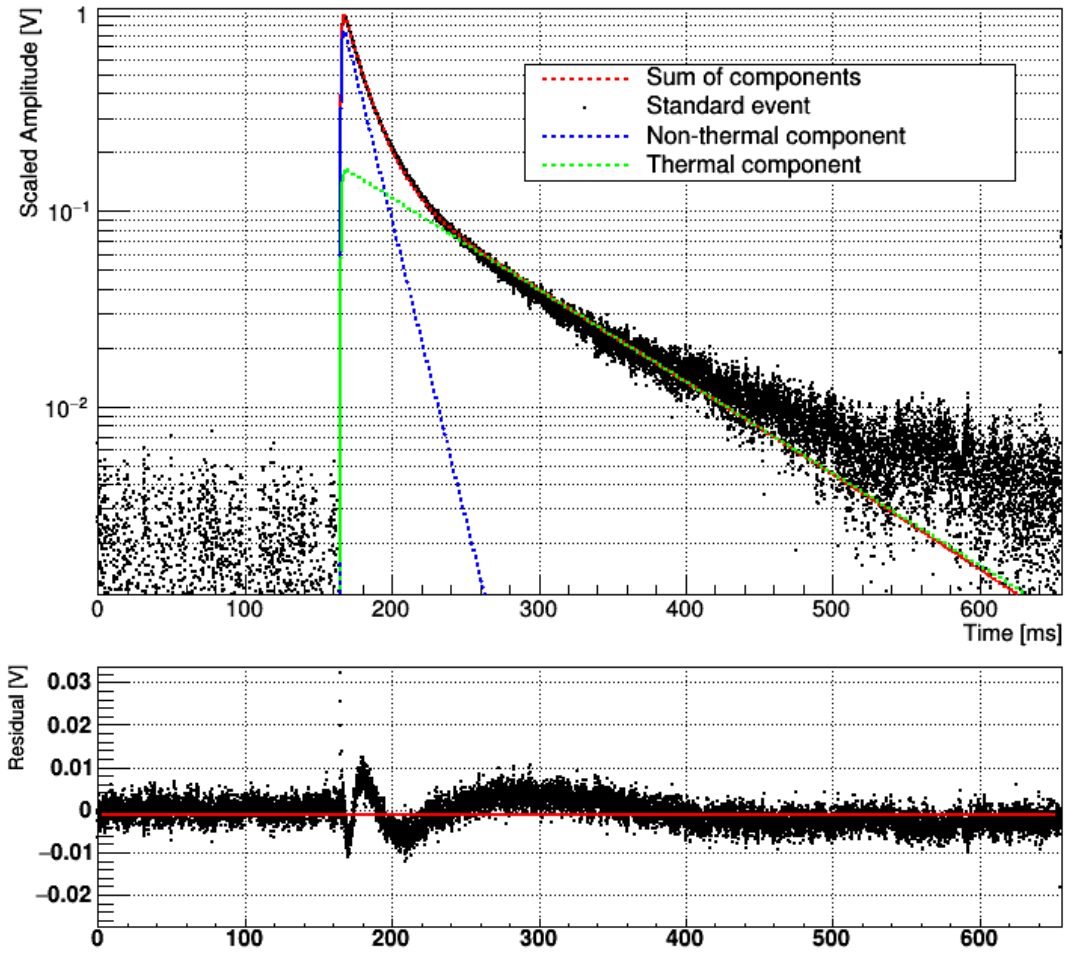

Figure 8.11: Two-component calorimetric fit to the standard event used in the analysis of detector J. The y scale is logarithmic to highlight deviations from the model in the pulse tail. The standard event was scaled such that its maximum amplitude is 1 V.

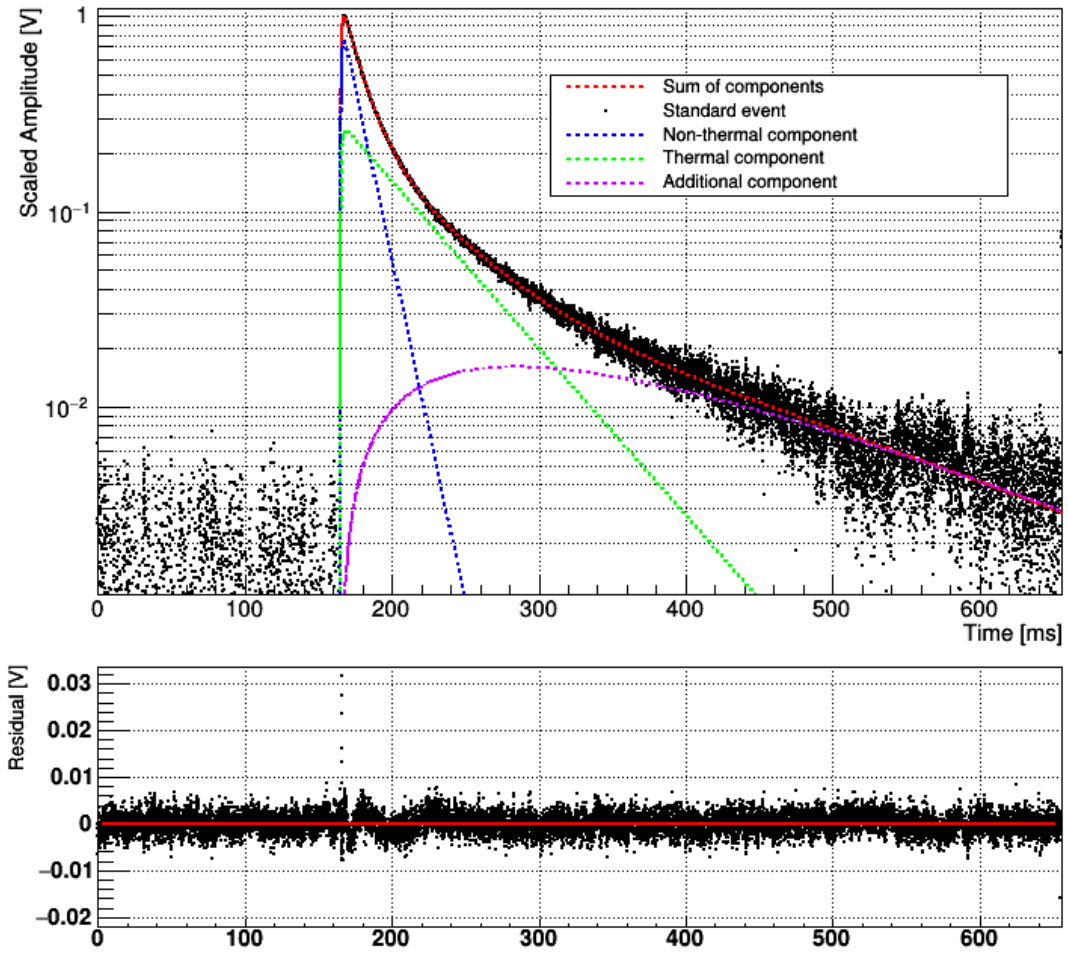

Figure 8.12: Three-component calorimetric fit to the standard event used in the analysis of detector J. The y scale is logarithmic to highlight deviations from the model in the pulse tail. The standard event was scaled such that its maximum amplitude is 1 V.

Channel	A-PH	B-PH	E-PH	J-PH
Onset [ms]	165.724	163.897	165.400	165.152
τ_{in} [ms]	15.562	15.913	10.541	14.274
τ_n [ms]	1.382	2.590	1.482	0.775
A_n [V]	0.775	0.926	0.914	0.628
τ_t [ms]	154.084	161.220	185.922	92.352
A_t [V]	0.049	0.065	0.035	0.102

Table 8.3: Two-component parametric fit results for standard events of different detector channels.

Channel	A-PH	B-PH	E-PH	J-PH
Onset [ms]	165.715	163.787	165.364	165.089
τ_{in} [ms]	14.643	14.635	9.474	12.404
τ_n [ms]	1.430	2.789	1.617	0.863
A_n [V]	0.764	0.938	0.944	0.584
τ_t [ms]	78.104	59.880	60.842	50.770
A_t [V]	0.076	0.107	0.069	0.171
τ_3 [ms]	225.378	181.111	256.235	128.910
A_3 [V]	0.099	0.061	0.082	0.166
τ_4 [ms]	190.794	88.326	201.536	110.141

Table 8.4: Three-component parametric fit results for standard events of different detector channels.

8.4 Saturated Fit

8.4.1 Effect of varying Parameters in Richards' Curve

Figure 8.13 shows the effect of varying each parameter of the generalized logistic function. For convenient comparison, Richards' Curve is given again here:

$$Y(x) = A + \frac{K - A}{(C + Qe^{-Bx})^{1/v}}$$

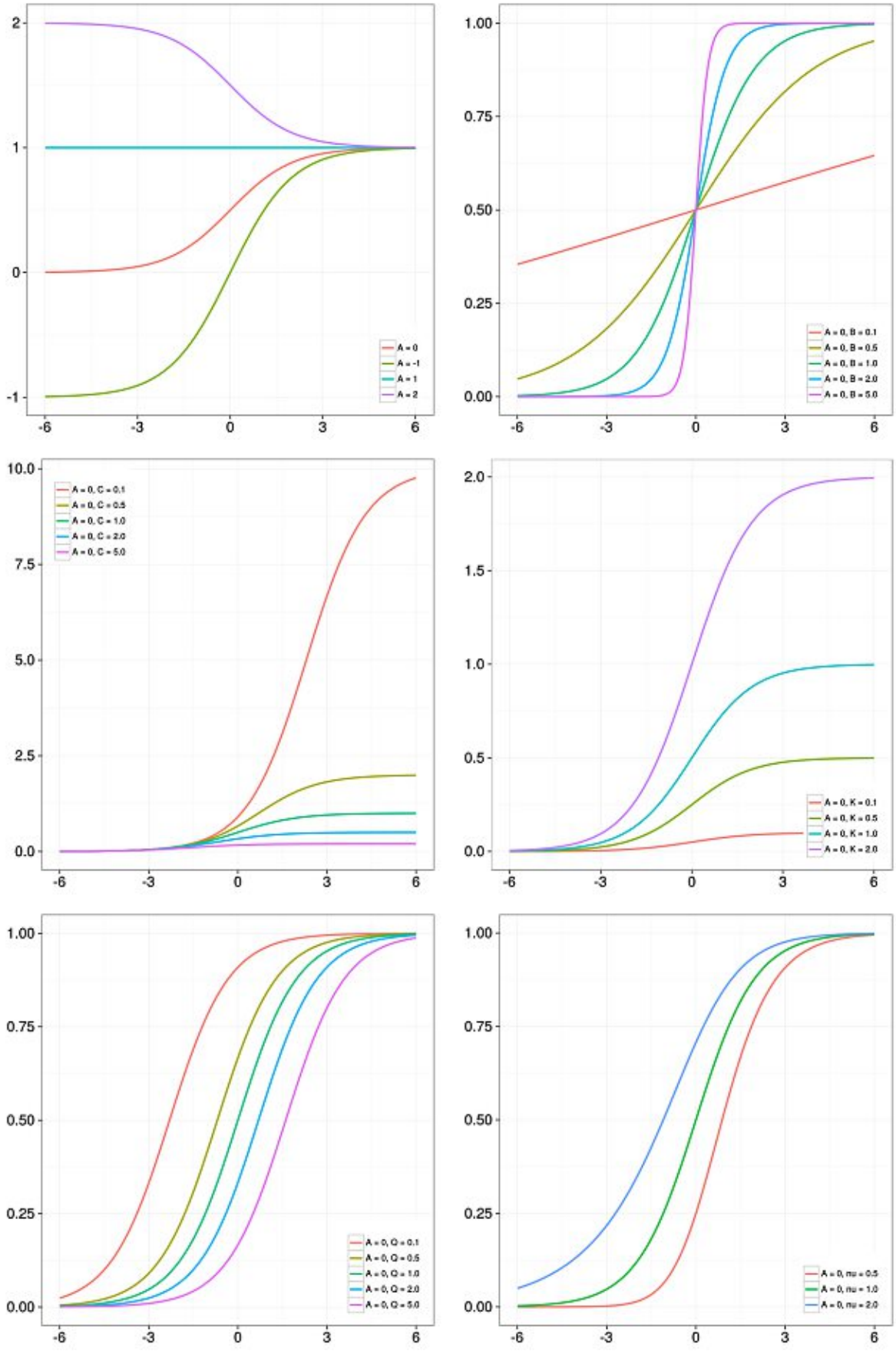

Figure 8.13: Effect of varying parameters in the logistic function $Y(x)$. In each image, one parameter is varied while the others are kept constant. Unless A is the varied parameter, A=0, and all respective other parameters are 1. Figures taken from [137].

8.4.2 Full Energy Range of Detector A

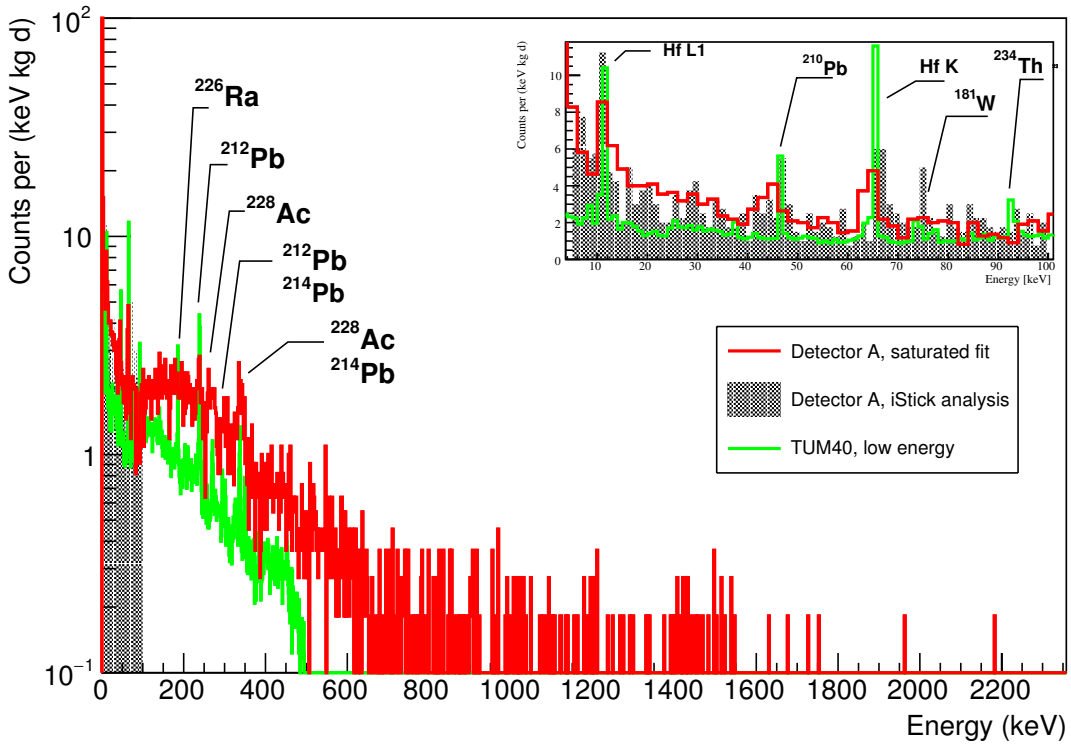

Figure 8.14: Comparison of an energy spectrum obtained from a saturated fit to the dataset of detector A in CRESST III, Phase One (red), and a the spectrum of TUM40 (CRESST II) for the low-energy range (green) [91]. The black spectrum was taken from [99] and rebinned by a factor of 2. It uses degraded signals detected in the instrumented holding sticks of detector A. The inlet shows a zoom to the range below 100 keV.

The high energy range of the spectrum obtained via the saturated fit shows events reaching up to 2 MeV; In comparison to [91], three clusters between 900 and 1000 keV may be indications of three known ^{228}Ac lines at 911.2 keV, 964.766 keV and 988 keV, and the cluster above 1400 keV could correspond to the β^+ and electron capture decay of ^{40}K at 1460.83 keV, but no definitive answer can be given due to the low statistics.

8.5 Generation of Artificial Baselines

It was shown in [138] that by using the NPS of a given detector baseline, artificial time series can be produced which correctly describe the behavior of the channel in absence of a signal, if correlations between noise frequencies are neglected. This is very useful if the amount of empty baselines obtained via hardware readout is limited; high statistics are advantageous for analysis techniques based on machine learning, and for the signal survival probability simulation described in Section 4.1.2. Following [138], the method is sketched here shortly. For a given time series $n(t)$, expressed as a superposition of k randomly delayed components with the same shape $f(t)$ and coefficients a_k

$$n(t) = \sum_k a_k f(t - t_k), \tag{8.2}$$

the NPS $N(\omega)$ is related to the power spectrum $P_f(\omega)$ of $f(t)$ in the following way:

$$N(\omega) = \alpha P_f(\omega) = \alpha |\hat{F}(\omega)|^2, \tag{8.3}$$

Here, $\hat{F}(\omega)$ is the fourier transform of $f(t)$, and α is a normalization constant.

8.5.1 Fourier Sampling

The power spectrum can be formulated as an ensemble average of discrete fourier transforms $\mathscr{F}(f_L[k])$ of sequences $f_L[k]$ with finite length L :

$$P_f[k] \simeq < |\mathscr{F}(f_L[k])|^2 > \tag{8.4}$$

An easy solution is found by using the experimentally sampled noise power spectrum $N[k]$ and adding a random phase Θ_k for each frequency sample. We define

$$F[k] \equiv \sqrt{N[k]} \cdot e^{i\Theta_k}, \quad \Theta_k \in (0, 2\pi) \tag{8.5}$$

from which the "raw" time series $f[k]$ can be calculated via an inverse discrete fourier transform

$$f[k] = \mathscr{F}^{-1}(F[k]). \tag{8.6}$$

A symmetry condition $F[k] = F^*[-k]$, with $F^*[k]$ the complex conjugate of $F[k]$, has to be imposed to ensure the realness of $f[k]$. According to equation 8.2, we can now generate

an artificial baseline using the time shifts t_k and amplitudes a_k. Assuming a Poissonian process for t_k, and introducing the overlap rate of the signals λ, the time shifts are calculated iteratively:

$$t_k = t_{k-1} - \frac{\ln(1-R)}{\lambda}, \tag{8.7}$$

R is uniformly distributed between 0 and 1. If the density function from which the amplitudes a_k are drawn has a variance given by

$$|a|^2 = \frac{\alpha}{\lambda T}, \tag{8.8}$$

where T is the length of the time series in seconds, this function can be randomly chosen and the relation 8.3 always holds (cf. [138]). In this work, a Gaussian distribution of amplitudes is used.

8.5.2 Results for Detector A

Following the previous section, artificial baselines are generated for the phonon channel of detector A. λ is set to the frequency base of the NPS; α is calculated according to equation 8.3 and generating random phases Θ_k between 0 and 2π. Then $|a|^2$ is calculated, and the series of amplitudes a_k is drawn from a Gaussian distribution with variance $|a|^2$ centered around 0. The time shifts t_k are drawn according to 8.7. $f(t-t_k)$ is then evaluated for each t_k, multiplied by a_k and summed over according to equation 8.2. Figure 8.15 shows a real baseline from the data set used to create the NPS on the left side, and an artificially created baseline on the right side.

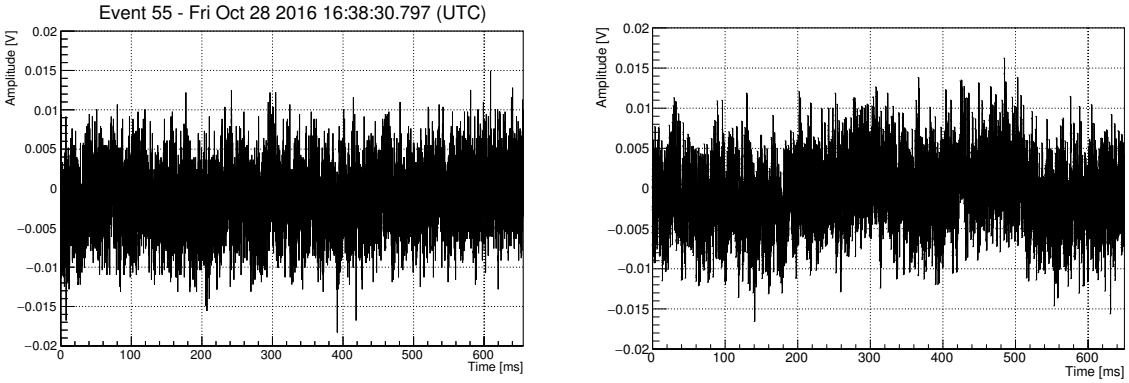

Figure 8.15: Left: Real detector baseline for the phonon channel of detector A; Right: Artificially created baseline

By eye, both baselines appear very similar, and even the contribution from the prominent 50 Hz peak due to the electric supply is visible. A straightforward test to determine the accuracy of the produced time series is the comparison between the original NPS and an NPS obtained from artifical baselines. This is illustrated in Figure 8.16, where a good agreement over four orders of magnitude in frequency is observed. The fit of a constant value to the difference between both NPS in the lower part of the Figure gives a value of ≈0.993, with a χ^2/ndf of 1.107.

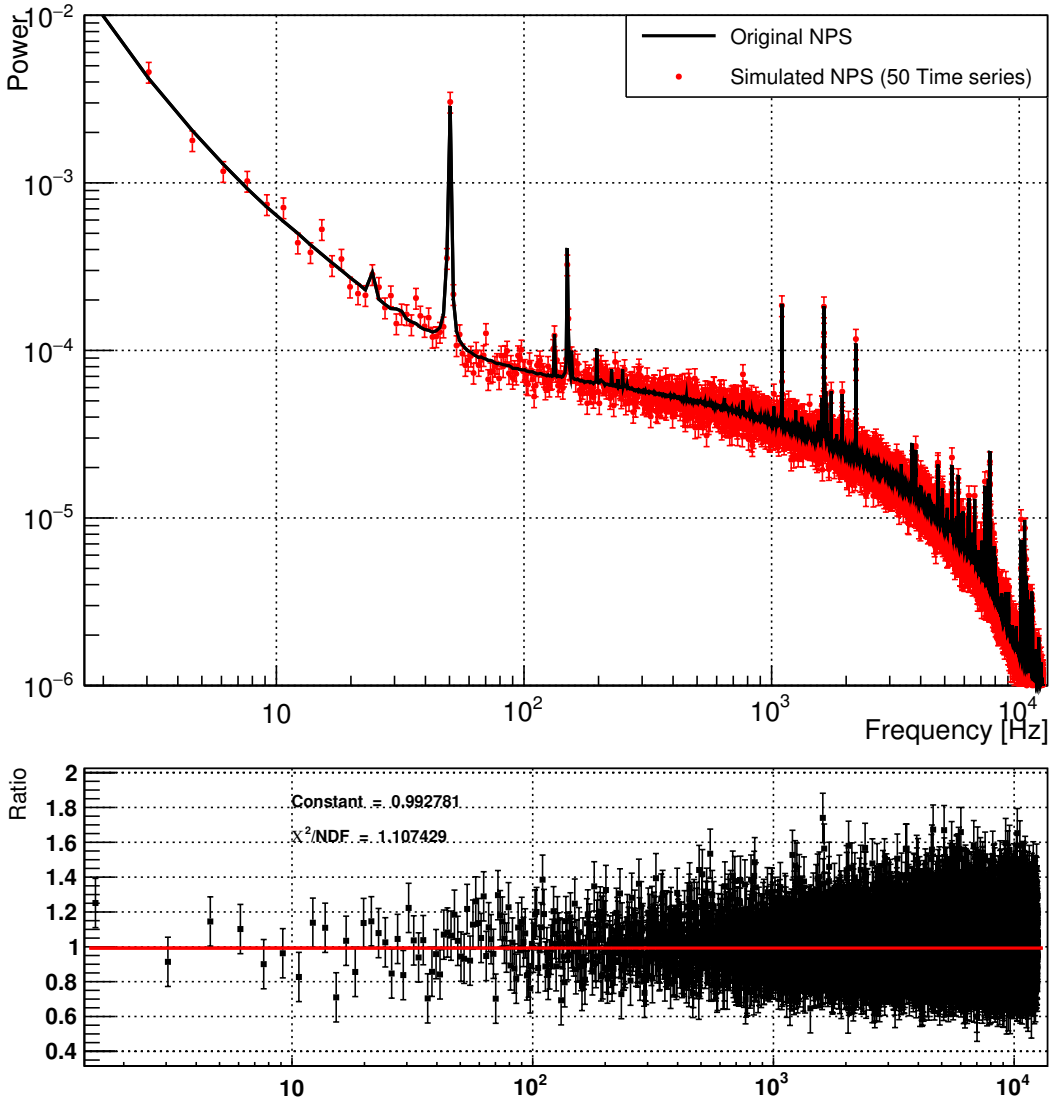

Figure 8.16: Comparison of the original NPS for detector A (black) and an NPS obtained from 50 simulated time series (red). Uncertainties are assumed to be poisson-distributed. The lower part shows the difference between both distributions on a zoomed-in scale, fitted with a constant.

8.5.3 Comparison of Simulated and Real Baselines

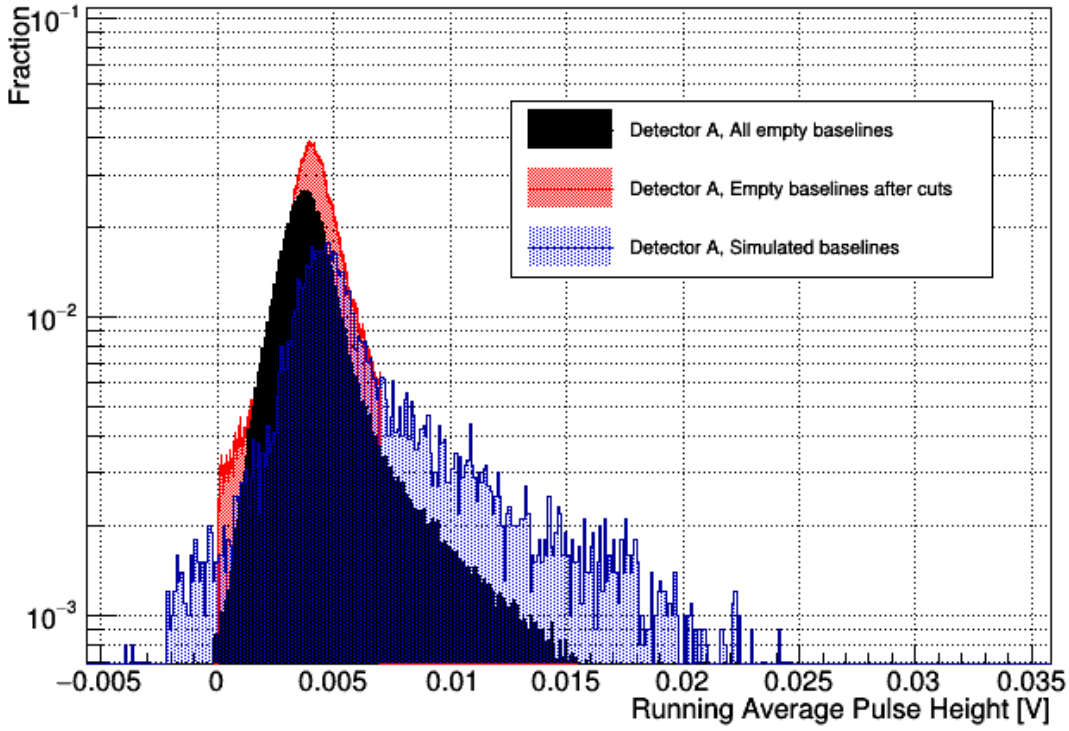

Figure 8.17: Comparison of the running average pulse height for real (red) and simulated (blue) baselines; the black histogram shows the distribution for all baselines. The red dataset was used to extract the noise power spectrum. Each distribution was normalized to one.

In Figures 8.18, 8.17, and 8.19, three parameters are compared for simulated (blue) and real baselines (black and red), respectively. The maximum pulse height (calculated via a 50 samples running average) of simulated baselines is shifted to higher values, and the distribution shows a different shape (Figure 8.17); in the baseline RMS parameter, the simulated pulses systematically display lower values (Figure 8.18). Both of these characteristics may be due to correlated frequencies in the noise power spectrum, in particular 50 Hz and the corresponding harmonics. In [138], no correlated components are considered, but only white noise, and the relative phase difference between correlated components is lost. If fluctuations of high frequency components over time were limited by the correlated lower frequencies, variations of the baseline on small time scales would be reduced, which would result in a narrower pulse height distribution and a lower pulse height on average. At the same time, constructive interference between correlated components would increase the RMS system-

atically. A possible approach to consider this aspect is to correlate frequency amplitudes and introduce non-random phases when simulating a time series; the problem here is that the relation between different frequencies may not be constant over time. Alternatively, filtering out these frequencies from the NPS and also from measured empty baselines should improve the agreement in parameter distributions. This has the obvious disadvantage that no "realistic" baselines can be produced. An intermediate solution to the problem might be the generation of multiple noise power spectra for small time intervals instead of just one for an entire measurement campaign; for each NPS, the correlation can then be considered constant, and be accounted for during baselines simulation.

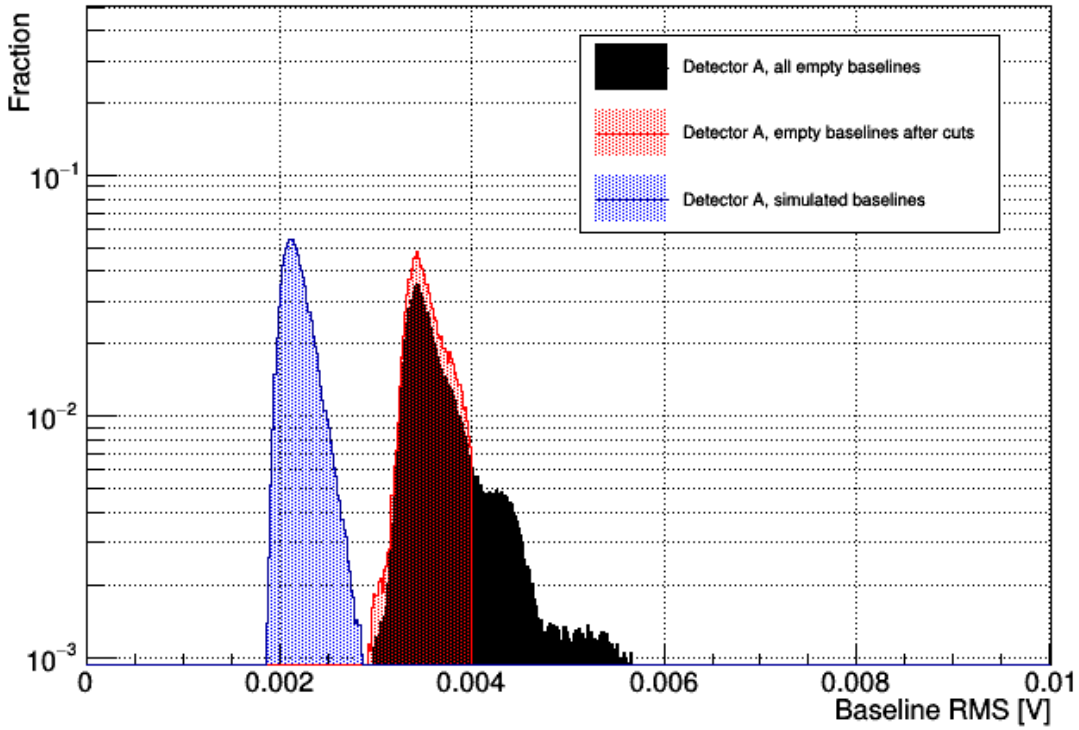

Figure 8.18: Comparison of baseline RMS for real (red) and simulated (blue) baselines; a linear baseline model with an offset was used. The black histogram shows the distribution for all baselines. The red dataset was used to extract the noise power spectrum. Each distribution was normalized to one.

Figure 8.19 gives the peak position parameter for each dataset; this parameter is the relative position of the highest pulse sample within the record window (after averaging) in ms. Before cuts, most of the real empty baselines show a peak position at the beginning of the record window (see Figure 8.19), which is to be expected, since many randomly extracted

baseslines coincide with the decaying flank of a recorded pulse. After the selection criteria have been applied, most of these baselines are removed, and only two "bumps" around 100 ms and around 500 ms remain (red dataset). This feature is caused by baseline oscillations with extremely low frequencies, where the oscillation period is roughly the same as the record window size. The right-left cut (cf. Section 5.3.3), which is one of the quality cuts used to clean the baseline dataset for the NPS, then acts like a phase filter. For simulated baselines, the distribution is completely flat, as one would expect in the absence of signal; the aforementioned oscillations cannot be resolved in the NPS.

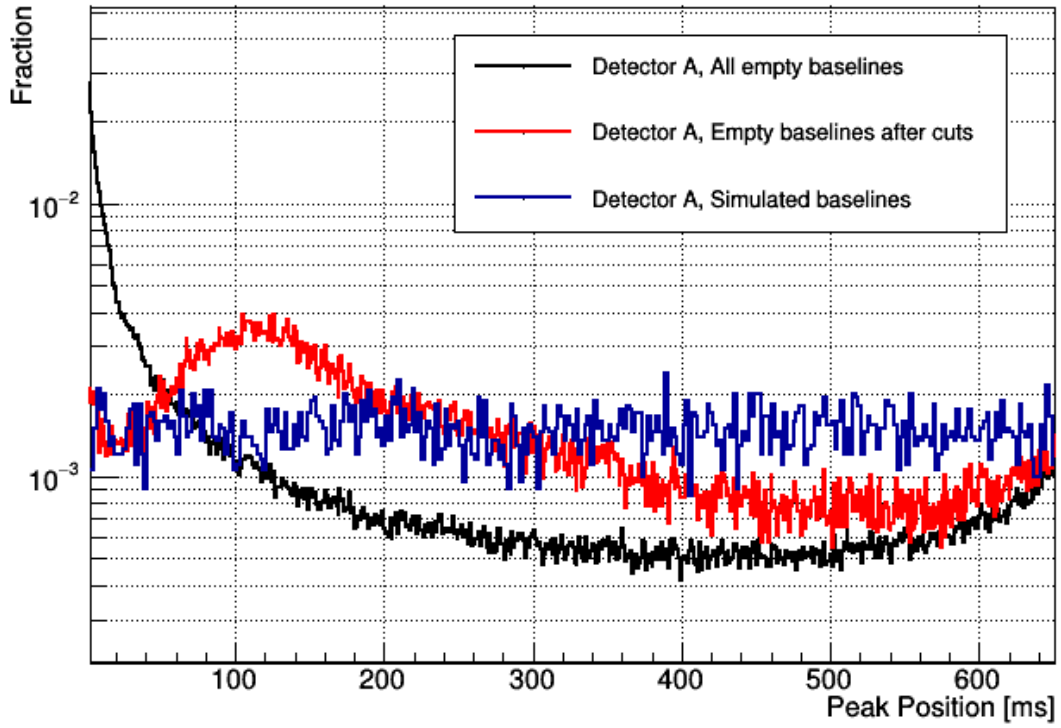

Figure 8.19: Comparison of the peak position for real (red) and simulated (blue) baselines; the black histogram shows the distribution for all baselines. The red dataset was used to extract the noise power spectrum. Each distribution was normalized to one.

List of Figures

List of Tables

References

[1] C. Montgomery, W. Orchiston, and I. Whittingham, Journal of Astronomical History and Heritage **12**, 90 (2009).

[2] J. Michell, Philosophical transactions of the Royal Society of London , 35 (1784).

[3] W. Thomson and L. Kelvin, *Baltimore Lectures on Molecular Dynamics and the Wave Theory of Light* (C.J. Clay and Sons, 1904).

[4] H. Poincare, Popular Astronomy **14**, 475 (1906).

[5] J. H. Oort *et al.*, Bulletin of the Astronomical Institutes of the Netherlands **6**, 249 (1932).

[6] E. Hubble, Proceedings of the national academy of sciences **15**, 168 (1929).

[7] F. Zwicky, Helvetica Physica Acta **6**, 110 (1933).

[8] V. C. Rubin and W. K. Ford Jr, The Astrophysical Journal **159**, 379 (1970).

[9] V. C. Rubin, W. K. Ford Jr, and N. Thonnard, The Astrophysical Journal **238**, 471 (1980).

[10] K. Begeman, A. Broeils, and R. Sanders, Monthly Notices of the Royal Astronomical Society **249**, 523 (1991).

[11] G. Bertone, D. Hooper, and J. Silk, Physics reports **405**, 279 (2005).

[12] J. F. Navarro, C. S. Frenk, and S. D. White, The Astrophysical Journal **490**, 493 (1997).

[13] D. Clowe, A. Gonzalez, and M. Markevitch, The Astrophysical Journal **604**, 596 (2004).

[14] M. Bradač *et al.*, The Astrophysical Journal **652**, 937 (2006).

[15] M. Markevitch *et al.*, The Astrophysical Journal **606**, 819 (2004).

[16] NASA, `https://www.nasa.gov/mission_pages/chandra/multimedia/photos06-096.html`, Accessed: 2019-08-23.

[17] NASA, http://www.cfht.hawaii.edu/en/news/DarkMatterCore/A520-mass+xray+lum-4up-m-1.jpg, Accessed: 2019-07-23.

[18] P. A. Ade *et al.*, Astronomy & Astrophysics **594**, A13 (2016).

[19] N. Aghanim *et al.*, arXiv preprint arXiv:1807.06209 (2018).

[20] Particle Data Group, M. Tanabashi *et al.*, Physical Review D **98** (2018).

[21] G. R. Blumenthal, S. Faber, J. R. Primack, and M. J. Rees, Nature **311**, 517 (1984).

[22] D. N. Spergel *et al.*, The Astrophysical Journal Supplement Series **148**, 175 (2003).

[23] A. McKellar, Publications of the Dominion Astrophysical Observatory Victoria **7** (1941).

[24] A. A. Penzias and R. W. Wilson, The Astrophysical Journal **142**, 419 (1965).

[25] D. Fixsen, The astrophysical journal **707**, 916 (2009).

[26] J. A. Peacock *et al.*, Nature **410**, 169 (2001).

[27] V. Springel *et al.*, nature **435**, 629 (2005).

[28] The TNG project, http://www.tng-project.org/about/, Accessed: 2019-07-18.

[29] J. Schaye *et al.*, Monthly Notices of the Royal Astronomical Society **446**, 521 (2015).

[30] M. Furlong *et al.*, Monthly Notices of the Royal Astronomical Society (2016).

[31] G. Bertone and D. Hooper, Reviews of Modern Physics **90**, 045002 (2018).

[32] J. L. Feng, Annual Review of Astronomy and Astrophysics **48**, 495 (2010).

[33] C. collaboration *et al.*, arXiv preprint arXiv:1704.07781 (2017).

[34] G. Aad *et al.*, The European Physical Journal C **76**, 259 (2016).

[35] C. Baker *et al.*, Physical Review Letters **97**, 131801 (2006).

[36] K. M. Zurek, Physics Reports **537**, 91 (2014).

[37] J. D. Bekenstein, Physical Review D **70**, 083509 (2004).

[38] B. Famaey and S. S. McGaugh, Living reviews in relativity **15**, 10 (2012).

[39] L. Baudis, Annalen der Physik **528**, 74 (2016).

[40] J. Liu, X. Chen, and X. Ji, Nature Physics **13**, 212 (2017).

[41] T. Emken, R. Essig, C. Kouvaris, and M. Sholapurkar, Journal of Cosmology and Astroparticle Physics **2019**, 070 (2019).

[42] R. Essig, J. Mardon, and T. Volansky, Physical Review D **85**, 076007 (2012).

[43] J. B. Birks, *The theory and practice of scintillation counting: International series of monographs in electronics and instrumentation* (Elsevier, 2013).

[44] E. Aprile *et al.*, New Astronomy Reviews **49**, 289 (2005).

[45] D. Akerib *et al.*, Nuclear Instruments and Methods in Physics Research Section A: Accelerators, Spectrometers, Detectors and Associated Equipment **704**, 111 (2013).

[46] H. Zhang *et al.*, SCIENCE CHINA Physics, Mechanics & Astronomy **62**, 31011 (2019).

[47] XENON Collaboration, E. Aprile *et al.*, Journal of Cosmology and Astroparticle Physics , 027 (2016).

[48] Homepage of the XENON Dark Matter Search, http://www.xenon1t.org, Accessed: 2020-01-16.

[49] T. Alexander *et al.*, Astroparticle Physics **49**, 44 (2013).

[50] C. Aalseth *et al.*, The European Physical Journal Plus **133**, 131 (2018).

[51] C. Amole *et al.*, Physical Review D **100**, 022001 (2019).

[52] XENON Collaboration, E. Aprile *et al.*, Physical Review Letters **121**, 111302 (2018).

[53] XENON Collaboration, E. Aprile *et al.*, Physical Review D **94**, 092001 (2016).

[54] PandaX-II Collaboration, X. Cui *et al.*, Physical Review Letters **119**, 181302 (2017).

[55] DarkSide Collaboration, P. Agnes *et al.*, Physical Review Letters **121**, 081307 (2018).

[56] LUX Collaboration, D. Akerib *et al.*, Physical Review Letters **118**, 021303 (2017).

[57] LUX Collaboration, D. Akerib *et al.*, Physical review letters **122**, 131301 (2019).

[58] L. Hehn *et al.*, The European Physical Journal C **76**, 548 (2016).

[59] EDELWEISS Collaboration, E. Armengaud *et al.*, Physical Review D **99**, 082003 (2019).

[60] SuperCDMS Collaboration, R. Agnese *et al.*, Physical Review Letters **112**, 241302 (2014).

[61] SuperCDMS Collaboration, R. Agnese *et al.*, Physical Review D **99**, 062001 (2019).

[62] DAMIC Collaboration, A. Aguilar-Arevalo *et al.*, Physical Review D **94**, 082006 (2016).

[63] CDEX Collaboration, H. Jiang *et al.*, Physical Review Letters **120**, 241301 (2018).

[64] G. Adhikari *et al.*, Nature **564**, 83 (2018).

[65] J. Collar, Physical Review D **98**, 023005 (2018).

[66] Q. Arnaud *et al.*, Astroparticle Physics **97**, 54 (2018).

[67] P. Collaboration, Physical Review D **93**, 052014 (2016).

[68] C. E. Aalseth *et al.*, Physical Review D **88** (2013).

[69] R. Strauss *et al.*, The European Physical Journal C **75**, 1 (2015).

[70] CRESST Collaboration, G. Angloher *et al.*, The European Physical Journal C **76**, 1 (2016).

[71] G. Angloher *et al.*, The European Physical Journal C **77**, 637 (2017).

[72] A. Gütlein *et al.*, Astroparticle Physics **69**, 44 (2015).

[73] M. Ackermann *et al.*, The Astrophysical Journal **840**, 43 (2017).

[74] C. Karwin, S. Murgia, T. M. Tait, T. A. Porter, and P. Tanedo, Physical Review D **95**, 103005 (2017).

[75] P. J. Fox, R. Harnik, J. Kopp, and Y. Tsai, Physical Review D **85**, 056011 (2012).

[76] T. A. Collaboration, Atlas feature: Dark matter, Accessed: 2019-08-23.

[77] A.-C. Eilers, D. W. Hogg, H.-W. Rix, and M. K. Ness, The Astrophysical Journal **871**, 120 (2019).

[78] P. de Salas, K. Malhan, K. Freese, K. Hattori, and M. Valluri, Journal of Cosmology and Astroparticle Physics **2019**, 037 (2019).

[79] M. Perelstein and B. Shakya, Journal of High Energy Physics **10** (2011).

[80] D. Mihalas and J. Binney, *Galactic astronomy: Structure and kinematics* (WH Freeman and Co., San Francisco, CA, 1981).

[81] K. Freese, M. Lisanti, and C. Savage, Reviews of Modern Physics **85**, 1561 (2013).

[82] J. D. Lewin and P. F. Smith, Astroparticle Physics **6**, 87 (1996).

[83] R. Bernabei *et al.*, Universe **4**, 116 (2018).

[84] M. C. Smith *et al.*, Monthly Notices of the Royal Astronomical Society **379**, 755 (2007).

[85] R. H. Helm, Physical Review **104**, 1466 (1956).

[86] J. M. Schmaler, *The CRESST Dark Matter Search - New Analysis Methods and Recent Results*, PhD Thesis, Technische Universität München, 2010.

[87] M. Bravin *et al.*, Astroparticle Physics **12**, 107 (1999).

[88] CRESST Collaboration, A. Abdelhameed *et al.*, The European Physical Journal C **79**, 630 (2019).

[89] M. Ambrosio *et al.*, Physical Review D **52**, 3793 (1995).

[90] A. Garai *et al.*, Review of Scientific Instruments **90**, 096104 (2019).

[91] A. Abdelhameed *et al.*, The European Physical Journal C **79**, 881 (2019).

[92] A. Erb and J.-C. Lanfranchi, Cryst. Eng. Comm. **15**, 2301 (2013).

[93] R. Strauss *et al.*, Nuclear Instruments and Methods in Physics Research Section A: Accelerators, Spectrometers, Detectors and Associated Equipment **845**, 414 (2017).

[94] G. Angloher *et al.*, Astroparticle Physics **31**, 270 (2009).

[95] S. Henry *et al.*, Journal of Instrumentation **2**, P11003 (2007).

[96] F. Pröbst *et al.*, Journal of Low Temperature Physics **100**, 69 (1995).

[97] R. Strauss *et al.*, The European Physical Journal C **77**, 506 (2017).

[98] R. Strauss *et al.*, Journal of Physics: Conference Series **718**, 042048 (2016).

[99] A. Münster, *High-Purity $CaWO_4$ Single Crystals for Direct Dark Matter Search with the CRESST Experiment*, PhD Thesis, Technische Universität München, 2017.

[100] N. Ferreiro Iachellini, *Increasing the Sensitivity to Low Mass Dark Matter in CRESST-III with a New DAQ and Signal Processing*, PhD Thesis, Ludwig Maximilian Universität München, 2019.

[101] F. Reindl, *Exploring Light Dark Matter With CRESST-II Low-Threshold Detectors*, PhD Thesis, Technische Universität München, 2016.

[102] C. Arpesella *et al.*, Nucl. Physics. B (Proc. Suppl) A **28** (1992).

[103] K. Rottler, *Muons in the CRESST Dark Matter Experiment*, PhD Thesis, Eberhard Karls Universität Tübingen, 2014.

[104] R. F. Lang, *Search for dark matter with the CRESST experiment*, PhD Thesis, Technische Universität München, 2008.

[105] D. Schmiedmayer, *Calculation of Dark Matter Exclusion Limits using a Maximum Likelihood Approach*, Master's Thesis, Technische Universität Wien, 2019.

[106] R. Strauss *et al.*, The European Physical Journal C **74**, 1 (2014).

[107] R. F. Lang *et al.*, arXiv:0910.4414 (2009).

[108] S. Yellin, Physical Review D **66**, 032005 (2002).

[109] S. Yellin, arXiv:0709.2701 (2007).

[110] J. Orear, Notes on statistics for physicists, 1958.

[111] R. Barlow, Nuclear Instruments and Methods in Physics Research Section A: Accelerators, Spectrometers, Detectors and Associated Equipment **297**, 496 (1990).

[112] M. Mancuso *et al.*, Journal of Low Temperature Physics **193**, 441 (2018).

[113] A. Abdelhameed *et al.*, Physical Review D **100**, 102002 (2019).

[114] G. Angloher *et al.*, Astroparticle Physics **23**, 325 (2005).

[115] E. Gatti and P. F. Manfredi, La Rivista del Nuovo Cimento (1978-1999) **9**, 1 (1986).

[116] S. D. Domizio, F. Orio, and M. Vignati, Journal of Instrumentation **6**, 02007 (2011).

[117] G. Angloher *et al.*, The European Physical Journal C **74**, 1 (2014).

[118] P. Bauer, *Preliminary title: Data Analysis for the CRESST Experiment*, PhD Thesis, Technische Universität München, 2020.

[119] P. Bauer and N. Ferreiro, Private Communication.

[120] N. E. Holden *et al.*, Pure and Applied Chemistry **90**, 1833 (2018).

[121] D. Schmiedmayer, private communication.

[122] V. Bednyakov and F. Šimkovic, Physics of Particles and Nuclei **37**, 106 (2006).

[123] V. Bednyakov and F. Šimkovic, Physics of Particles and Nuclei **36**, 131 (2004).

[124] SuperCDMS Collaboration, R. Agnese *et al.*, Physical Review D **97**, 022002 (2018).

[125] LUX Collaboration, D. Akerib *et al.*, Physical Review Letters **116**, 161302 (2016).

[126] PandaX-II Collaboration, C. Fu *et al.*, Physical Review Letters **118**, 071301 (2017).

[127] XENON Collaboration, E. Aprile *et al.*, Physical Review Letters **122**, 141301 (2019).

[128] D. Hooper and S. D. McDermott, Physical Review D **97**, 115006 (2018).

[129] H. Wulandari, J. Jochum, W. Rau, and F. von Feilitzsch, Astroparticle Physics **22**, 313 (2004).

[130] D. Schmiedmayer, (2020), in preparation.

[131] S. Scholl and J. Jochum, Journal of Physics: Conference Series **375**, 012020 (2012).

[132] J. Åström *et al.*, Physics Letters A **356**, 262 (2006).

[133] K. J. Schäffner, *Study of Backgrounds in the CRESST Dark Matter Search*, PhD Thesis, Technische Universität München, 2013.

[134] R. Strauss *et al.*, Journal of Cosmology and Astroparticle Physics **2015**, 030 (2015).

[135] R. B. Firestone and V. S. Shirley, *Table of isotopes, 2 volume set* (Wiley-VCH, 1998), p. 3168.

[136] F. Richards, Journal of experimental Botany **10**, 290 (1959).

[137] Wikipedia, `https://en.wikipedia.org/wiki/Generalised_logistic_function`, Accessed: 2019-12-13.

[138] M. Carrettoni and O. Cremonesi, Computer Physics Communications **181**, 1982 (2010).

Danksagung

Viele Menschen haben zur Entstehung dieser Arbeit beigetragen, und dürfen hier nicht unerwähnt bleiben: Professor Dr. Jochen Schieck hat die Arbeitsgruppe für Rare-Event-Searches am HEPHY in Wien begründet, und mich überhaupt erst für das Forschungsgebiet der Dunklen Materie begeistern können. Als mein Betreuer und Doktorvater warst Du trotz zahlreicher anderer Verpflichtungen zu jeder Zeit erreichbar, stets geduldig und hilfsbereit, und hast mein Projekt von Anfang an unterstützt - vielen Dank dafür!
Dr. Florian Reindl stand als Analysekoordinator und Ansprechpartner für alle Fragen rund um CRESST-Datenauswertung zur Verfügung. In seiner Funktion als eifriger Korrekturleser hat er so manchen Fehler gefunden, und mich stets motiviert. Lieber Florian, danke für deinen unermüdlichen Einsatz und die viele Zeit, die Du geopfert hast; durch die Zusammenarbeit mit Dir habe ich unglaublich viel gelernt.

Dr. Achim Gütlein hat in seiner Zeit am HEPHY das Software-Framework entworfen und begonnen, das ich für meine Analyse weiterentwickelt habe - ohne ihn wäre ich wohl nicht sehr weit gekommen. Die Likelihood-Resultate in der Arbeit wären ohne die Software von Daniel Schmiedmayer nicht möglich gewesen, der auch als last-minute Korrektor eingesprungen ist, und viele hilfreiche Anmerkungen beigesteuert hat. Ich bedanke mich bei Dr. Holger Kluck, der nicht nur als Leidensgenosse bei ROOT-Problemen stets ein offenes Ohr hatte, und zusammen mit Dr. Cenk Türkoglu als Background-Experte fungierte. Dear Cenk, thank you for keeping me company during all the work evenings! You were the "dark" in "dark office". Am HEPHY darf Dr. Valentyna Mokina nicht fehlen, der ich für eine Menge Nervennahrung und ihr unempfindliches Gehör danke - sorry Valentyna, but this is hard to translate.

Der CRESST-Gruppe am Max-Planck-Institut in München möchte ich für zahlreiche hilfreiche Diskussionen und Anregungen danken, insbesondere Dr. Nahuel Ferreiro, der die Eventsimulation sowie den Triggeralgorithmus auf dem kontinuierlichen Stream entwickelt und implementiert hat, und Dr. Franz Pröbst, der ein geradezu unheimliches Wissen über jeden Aspekt von CRESST besitzt. Ich danke Philipp Bauer, der einen großen Teil zur Software

beigetragen hat, für die konstruktive Zusammenarbeit, auch bei der Analyse, und die vielen gründlichen cross checks.

Meine Familie hat mich in diversen Phasen des Stresses ertragen müssen und mich trotzdem immer wieder unterstützt und aufgebaut, wenn ich aus dem fremdartigen Ausland zu Besuch war. Ihr vier seid meine Inspiration und mein Ruhepol. Schließlich danke ich der Person, die mehr als nur die Hälfte meines Klaviers besitzt, und die wohl den meisten Frust abbekommen hat - Du hast mir gerade in der Endphase auf so viele verschiedene Weisen entscheidend geholfen, dass ich gar nicht weiß, wo ich anfangen soll.